Manufacturing and Evaluation of a Biologically Inspired
Engineered MAV Wing Compared to the
Manduca Sexta Wing Under Simulated Flapping Conditions

THESIS

Nathanial E. DeLeón, Second Lieutenant, USAF

AFIT/GAE/ENY/11-M07

DEPARTMENT OF THE AIR FORCE
AIR UNIVERSITY

AIR FORCE INSTITUTE OF TECHNOLOGY

Wright-Patterson Air Force Base, Ohio

AFIT/GAE/ENY/11-M07

Manufacturing and Evaluation of a Biologically
Inspired Engineered MAV Wing Compared to the
Manduca Sexta Wing Under Simulated Flapping Conditions

THESIS

Presented to the Faculty

Department of Aeronautics and Astronautics

Graduate School of Engineering and Management

Air Force Institute of Technology

Air University

Air Education and Training Command

In Partial Fulfillment of the Requirements for the

Degree of Master of Science in Aeronautical Engineering

Nathanial E. DeLeón, B.A.S.

Second Lieutenant, USAF

March 2011

APPROVED FOR PUBLIC RELEASE; DISTRIBUTION UNLIMITED

AFIT/GAE/ENY/11-M07

Manufacturing and Evaluation of a Biologically
Inspired Engineered MAV Wing Compared to the
Manduca Sexta Wing Under Simulated Flapping Conditions

Nathanial E. DeLeón, B.A.S.
Second Lieutenant, USAF

Approved:

_____   _____
Dr. A. N. Palazotto, PhD (Chairman)   date

_____   _____
Maj A. J. Lofthouse, PhD (Member)   date

_____   _____
Dr. R. G. Cobb, PhD (Member)   date

AFIT/GAE/ENY/11-M07

Abstract

In recent years, researchers have expressed a vested interest in the concepts surrounding flapping wing micro air vehicles (FWMAVs) that are capable of both range and complex maneuvering. Most research in this arena has found itself concentrated on topics such as flapping dynamics and the associated fluid-structure interactions inherent in the motion, however there still remains myriad questions concerning the structural qualities intrinsic to the wings themselves. Using nature as the template for design, FWMAV wings were constructed using carbon fiber and Kapton and tested under simplified flapping conditions by analyzing 'frozen' digital images of the deformed wing by methods of photogrammetry. This flapping motion was achieved via the design and construction of a flapper that emulates several of the kinematic features that can be seen in naturally occurring flyers. The response to this motion was then compared to the inspiring specimen's wings, the North American Hawkmoth (*Manduca Sexta*), under the same flapping conditions in order to identify some of the key features that nature has deemed necessary for successful flight.

In order to consider the comparison between the wings, vector analysis was used to examine both the angular displacement of the leading edge and the torsional displacements/deformations in several locations about the spanwise direction. Results show that though the engineered wing compared well to the biological wing in terms of mass and first bending mode, it failed to emulate the behavior concieved by the biological wing when subjected to flapping motion in both air and vacuum, especially in terms of torsional deformations. In addition to the comparision of engineered wing to biological, this study also served to shed light on the behavior of the biological wing. The results suggest that aerodynamics play a key role in the wing's behavior (as opposed to its behavior being dominated by inertial properties).

Acknowledgements

I have been immensely fortunate to have been surrounded by such a strong support structure during my career at AFIT. Two of the most influential people in my life are my parents, who showed unrelenting support and care through all the trials that came as a result of earning a Master's degree. I would like to especially thank my mother, who having endured similar enterprise was able to lend both an ear and advice to both me and my friends (not to mention a good sense of humor).

At the Air Force Institute of Technology (AFIT), I was fortunate to have been surrounded by a myriad of peers who in short 'carried' me through the process (despite my often reluctance to accept). I would like to thank Captain Sarah Summers and Renato Jelic. Sarah, who had the fortitude to be both my friend and mentor, proved to be one of the most influential individuals in my life, always willing to offer good advice. Renato provided much needed support and guidance even though he often employed creative methods.

One of the most important people in my career at AFIT, and possible my future career in the Air Force, was Major Ryan O'Hara, whose lack of sentiment and willingness to push me to do what was complete and correct provided me with the mental tools neccessary to carry out this study. His patience and guidance through my processing of important concepts, proved to be crucial during the times in which were most stressful.

I would also like to extend a great deal of thanks to my committee members, Dr. Richard Cobb and Major Andrew Lofthouse. Dr. Cobb provided my on-going investigation with a great deal of guidance, along with Dr. Reeder, whose invaluable insight into the theories and concepts greatly influenced my research. Major Lofthouse was very instrumental in supplying guidance into the methodology and the 'programming mind' , which pointed my research into the non-fluids realm. This opened up to me

new opportunities for inquiry in ways I had not considered before. He never lost faith in my research and his insight and support havebeen sincerely appreciated.

I would also like to thank an undergraduate professor of mine, Dr. Jack McNamara, from The Ohio State University who provided me with the important foundation for my thinking and questioning when it came to the area of research.

It is important to note that none of my research could have taken place without the important sponsors for this project: Dr. Doug Smith of the Air Force Office of Scientific Research (AFOSR), and Dr. Richard Snyder of the Air Force Research Lab (AFRL), who even took the time to become personally involved in my research.

Lastly, and possible most importantly, I would like to thank my advisor, Dr. Anthony Palazotto. From the moment I stepped onto the Air Force Institute for Technology (AFIT) campus, his knowledge, guidance, patience, wisdom, and sense of humor provided me with a support system that has been instrumental in my journey through this program. Dr. Palazotto was very tolerant of me in my efforts to grasp the world of structures and aeroelasticity. Through this process he has provided me with the important tools to complete the method of inquiry that has lead to the completion of this thesis. I will forever be thankful for his guidance and support.

<div align="center">Nathanial E. DeLeón</div>

Table of Contents

List of Figures

xiii

xiv

List of Tables

List of Abbreviations

Manufacturing and Evaluation of a Biologically Inspired Engineered MAV Wing Compared to the *Manduca Sexta* Wing Under Simulated Flapping Conditions

I. Introduction

1.1 Introduction of The Research Topic

Overall, the goal of this research is to examine the response of engineered flapping MAV wings as compared to the specimen from which the constructive inspiration was gained. The means by which inspiration is gained is the *Manduca Sexta*, or as it is more commonly known, the North American Hawkmoth. Upon realizing the existence of a myriad of factors that would influence the dynamic behavior of a flapping wing, it became necessary to make an attempt at constructing a wing; paying close attention to a few of the factors associated with the most obvious features. Previous research indicates that modal analyses were conducted [1] [6] [7], however this comparison leaves much to be desired due to the fact that small displacements are not a part of the life of these intended flying machines. It was determined that characterization and comparison of these wings would be better suited in the arena of flapping itself, as the constructed wing would be subjected to such motion throughout the course of its operational life. The objective of this thesis is to fully establish manufacturing and experimental systems to evaluate if an engineering wing duplicates the flapping motion of the actual *Manduca Sexta* wing. The process of arriving at design iterations will include as much as possible of the physics, kinematics, and mathematics related to components within the design.

The Defense Advanced Research Projects Agencies's (DARPA's) current vision of the optimal MAV motivates this research. This MAV's dimensions are less than 15 cm [6 inches], and has a range and speed of 1 km and 15 m/s [8]. The realization of practical MAV applications is possible due to the ever-decreasing size and weight
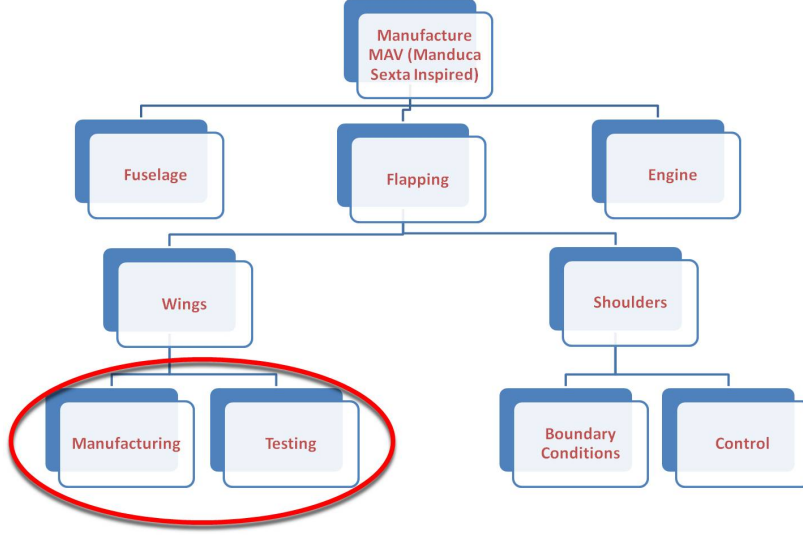
Figure 1.1:   Flowchart of Current MAV Research

of payload components such as video cameras, chemical sensors, and autopilots [9]. Figure 1.1 indicates that there are several pertinent aspects of achieving this goal, however it has been discovered that the study of MAV mechanics has been concentrated mainly on the fluid-structure interactions associated with flapping wings, and the structural aspects of the wings themselves have been vastly ignored [1].

These interactions between structure and the surrounding fluid are both pertinent and necessary areas of investigation due to the fact that the wings flap at frequencies that range ($\cong$25-40) Hz and move freely. These qualities complicate the solving of problems associated with unsteady and low Reynolds number flow fields [10]. However the medium of flight to consider other than the fluid present, is the physical wing itself. It can thus be deemed crucial that in order to fully consider the fluid structure interactions (FSI), the characteristics within the structures themselves must also be fully investigated.

Figure 1.1 points towards the fact that the overall goal of this research is to engineer a flapping MAV. Through an assembly of various components, to include the manufacturing of engineered wings, this goal of artificial creation can in fact be achieved. In order to test and characterize all wings investigated, it became necessary

2

MAV production cycle
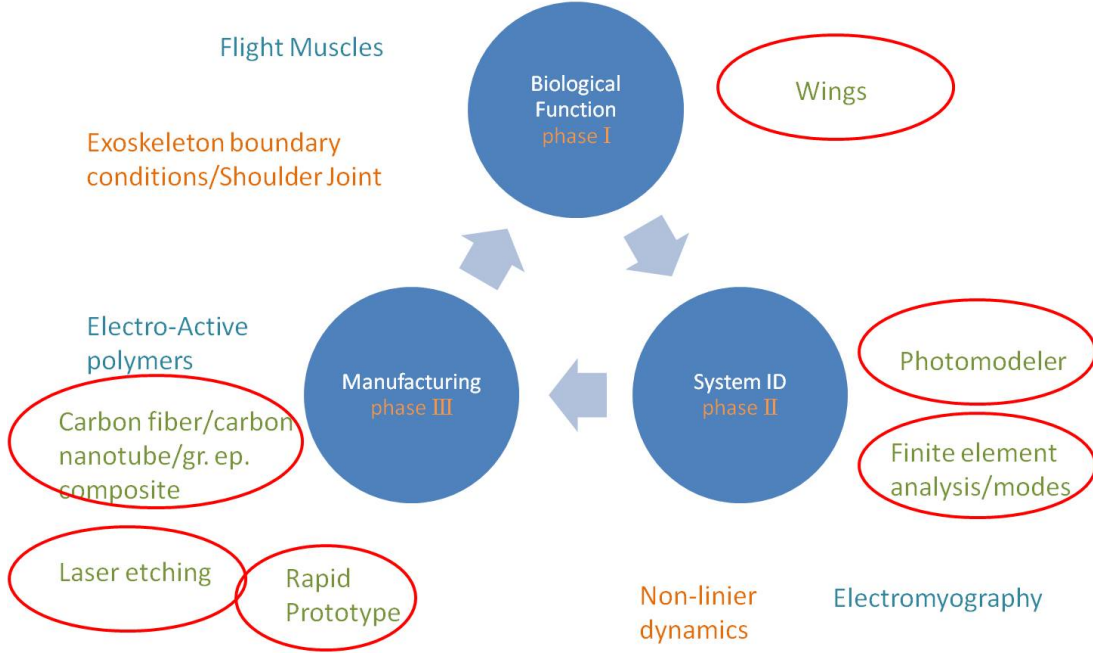
Figure 1.2:   Detailed Flow Chart of MAV Manufacturing Process

to devise a method of verification and investigation. The final method devised incorporated performing a dynamic analysis using a Scanning Laser Vibrometer (SLV) of both the biological specimen and the engineered specimen. Following this comparison, it became necessary to perform an analysis of larger displacements. It was decided that simulating large displacements and deformations could be achieved by simulated flapping motion. The deformations were characterized by effectively "freezing" the test subjects during the flapping motion using strobes. These frozen images could then be plugged into Photomodeler^{TM} [1] which allows for three dimensional modeling of the deformed specimen. These could then be compared to each other under the same conditions (flapping frequency and phase) for the effective characterization of the engineered specimen with respect to the biological specimen.

These engineered wings are to be created using a wide range of materials that attempt to mimic the dynamic response and material properties of the Hawkmoth.

3

Similar to Figure 1.1, Figure 1.2 grants an in-depth look into the iterative nature of the intended research. The red circles denote the specifics associated with this portion of the design process, beginning with the wings, moving to the characterization of the biological specimen, and finally characterizing and comparing the engineered specimens in hopes to make the loop again, iterating on the more effective and useful design.

1.2 Motivation Background

As warfighters are taxed with ever increasingly difficult situations, it is crucial that they be made aware of what is to come; whether it be over a hill, in a cave, or in a room of an unknown building [11]. Recent years have found a vested interest in the realm of 'hide in plain sight' in that a craft should be able to observe a situation without hiding, which can hinder observational functions. Currently, exciting and innovative research is taking place concerning the incorporation of micro air vehicles into the warfighter's arsenal of intelligence and reconiassance equipment. [12]

DARPA's vision is to create a small, lightweight and relatively inexpensive solution to the problem: a MAV. This machine would allow warfighters to infiltrate hostile or unreachable areas without risking human lives while still gathering quality information that would aid in the successful execution of the given mission. The MAV will be capable of a multitude of close quarter reconnaissance tasks, ranging from battlefield operations to safety inspections of civilian structures [4]. These 'insect sized' aircraft would be nearly indistinguishable from the surrounding insect population, with hopes to perhaps hide within a swarm avoiding visual detection. DARPA has published a list of constraints that can be viewed in Table 1.1

Here it can be seen that the constraints that define a successful MAV are very specific. These 'bug sized' machines must be usable and cheap. It is incumbent for engineers, regardless of resources or funding, to create and implement their MAVs with as little cost as possible, a daunting task for such specifications as those listed in Table 1.1. Many find it necessary and sufficient to attempt to achieve these goals using

Table 1.1:   MAV Design Requirements [4]

Specification	Requirements	Details
Size	$< 15.24cm$	Max Dimension
Weight	~100 g	Objective GTOW*
Range	1-10 km	Operational Range
Endurance	60 min	Loiter Time on Station
Altitude	$< 150m$	Operational Ceiling
Speed	15 m/s	Max Flight Speed
Payload	20 g	Mission Dependent
Cost	$1,500	Max cost, 2009 USD**

*GTOW-Gross Takeoff Weight
**USD-United States Dollars

conventional flapping theory and engineering physics, however little has come of this approach and the field of flapping wing MAV's is still in its infancy [13]. Conventional aircraft have large, fixed wings and require a rotor or some form of forward locomotion. The MAV, as required by DARPA, should have the ability to negotiate small spaces and perhaps even hover within close quarters; a near impossible feat for a vehicle that requires forward motion. When indoors, slower is better [14].

It can be said that it is perhaps necessary to turn to nature for answers as it has already found the ability to create small, agile flying machines. Particular interest is found within insects due to the fact that the wings themselves are rigid and are passively controlled. Norris *et al* [1] stated that prior to the mid 1990's there was no serious research on flapping wing fliers. Instead, most research concentrated on jet and rocket propulsion. Current research finds a vested interest in this *flapping wing MAV (FWMAV)*, however science is compelled to mimic the elegant (and perhaps efficient) designs that nature has already employed for its flapping wing design [1]. Nothing in nature exhibits fixed wing flight behavior or propeller driven thrust, rather it is flight through flapping that perhaps is the key to the successful creation of the MAV [14].

Figure 1.3 shows some of the recent developments within the realm of MAVs. What is important to note here is that many methods of locomotion and body styles.
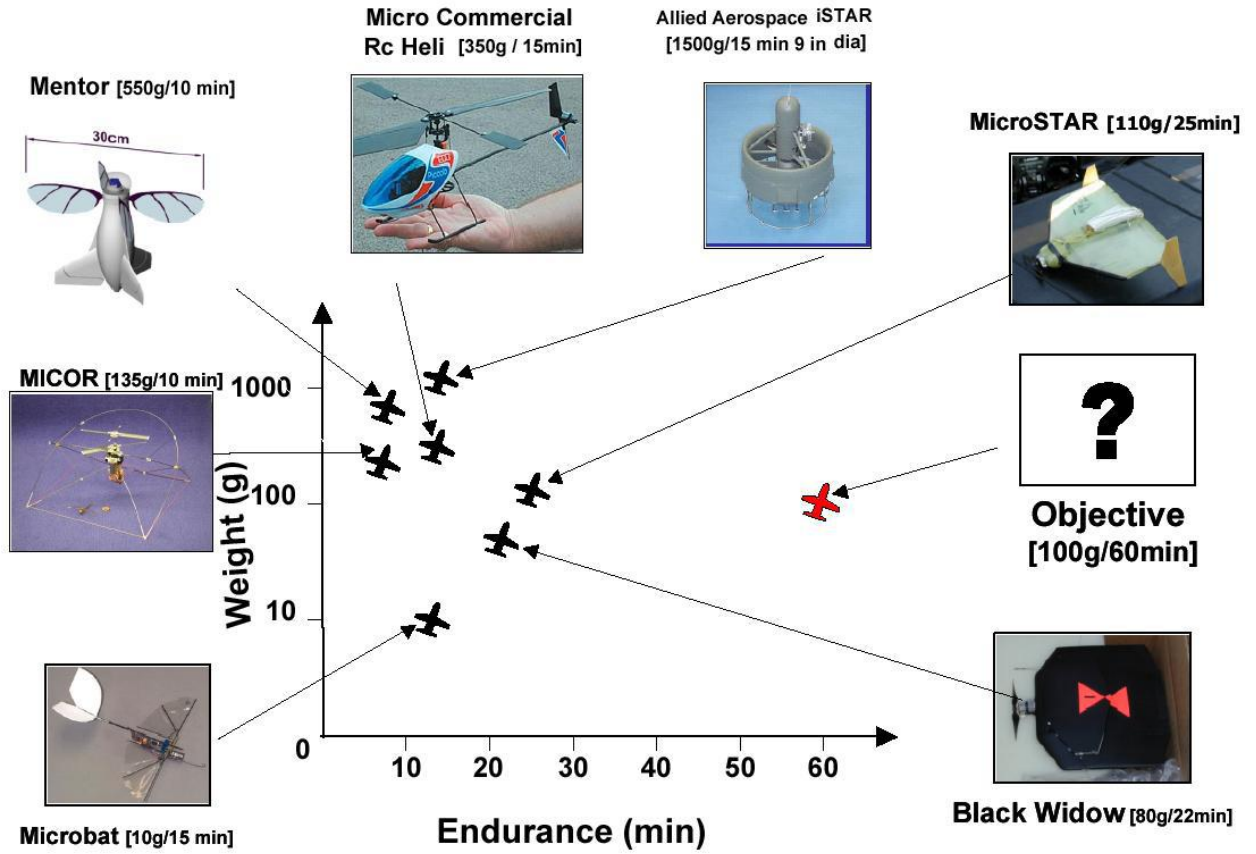
Figure 1.3:   View of Recent MAV Developments [15]

Clearly however, the red data point has not yet been seen in the world of MAV creation.

1.3 The Inspiring Specimen

The *Manduca Sexta* is the perfect candidate for study due to its size and availability [1] [4]. The Hawkmoth is readily available in the United States (its larval stage is known as the tobacco worm, and is considered a pest), and its dimensions remain within DARPA's constraints listed in Table 1.1. The Hawkmoth is also very docile and easy to handle, remaining dormant whenever there is 'day-like' light present. Figure 1.4 shows a picture of an adult female *Manduca Sexta*. A great many of the
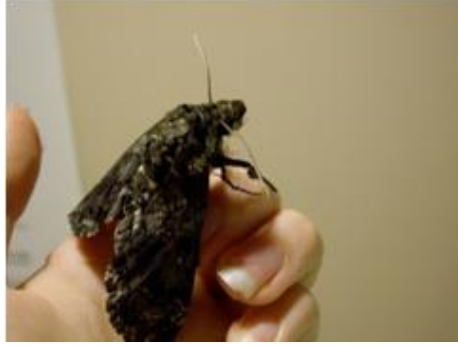
Figure 1.4:   Adult Female *Manduca Sexta*

Hawkmoths were provided for this research by Dr. Mark Willis of Case Western Reserve University.

> *The* Manduca Sexta *wing beat proved to be remarkably consistent. Significant intra specific variation has been reported for many insect groups including butterflies and flies. However, the variation in kinematics between successive wing beats and also between individuals, was small in the current study* [5].

This consistency in parameters allows for more accurate study in the realm of the behaviors to be mimicked. Sims [4] mentions that even though the *Manduca Sexta* is a four wing flapper, studies have shown that the insect is capable of flying in the absence of the two rear wings. Furthermore Willis [16] mentions that the presence of the hind wings are purely for aerobatic purposes in that the rear wings are passively controlled until being engaged for sharp turns or evasion. The basic two wing setup drastically simplifies the analysis of the bio-inspired MAV.

1.4   The True Boundary Conditions

The fact that the inspiration is biological, leads to an interesting set of boundary conditions presented for investigation and possible mimicking. The main function of any biological being, or any flying object for that matter is to transmit force to the external environment during flight in order to become airborne without risking damage to the flight vehicle itself in the form of bone or muscle damage [17]. This unique

7
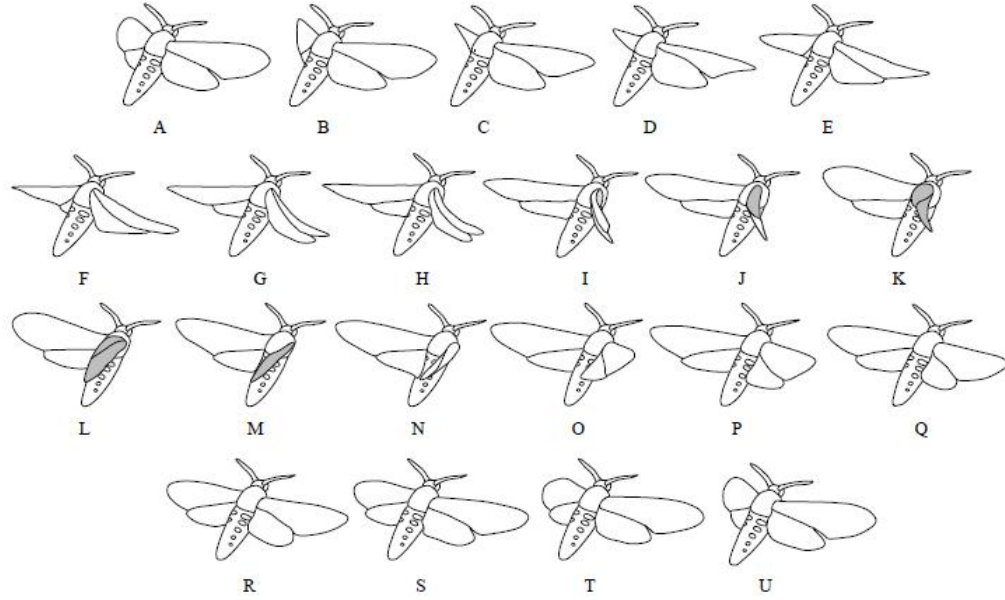
Figure 1.5:   *Manduca Sexta* Wing Outlines Traced From High-Speed Video Sequence [5]

limitation of flapping fliers leads to a number of interesting boundary conditions including both a flapping orientation and a wing beat frequency. Figure 1.5 [5] sheds light on the complex movements associated with the hovering flight of a *Manduca Sexta*.

It can be seen in Figure 1.5 that the wings do not remain at a constant angle of attack, nor do they travel in a straight line, rather they pronate and supinate (flap up and down, constantly changing their angle of attack with respect to both free stream and the 'flapping stream' which is the path that the wing takes relative to a stationary observer) through several angles of rotation along with movement to both the posterior and anterior positions. These movements, while distinct and observable, are immensely complicated and unusual in that little is known about the controls inherent in successful flapping flight. Characterization is extremely complex without some form of simplification, which is possible if not all factors of flight are taken into account. In other words, given reliable information about bodily dimensions and wing-stroke parameters, the method of simplification enables one to quickly arrive

8
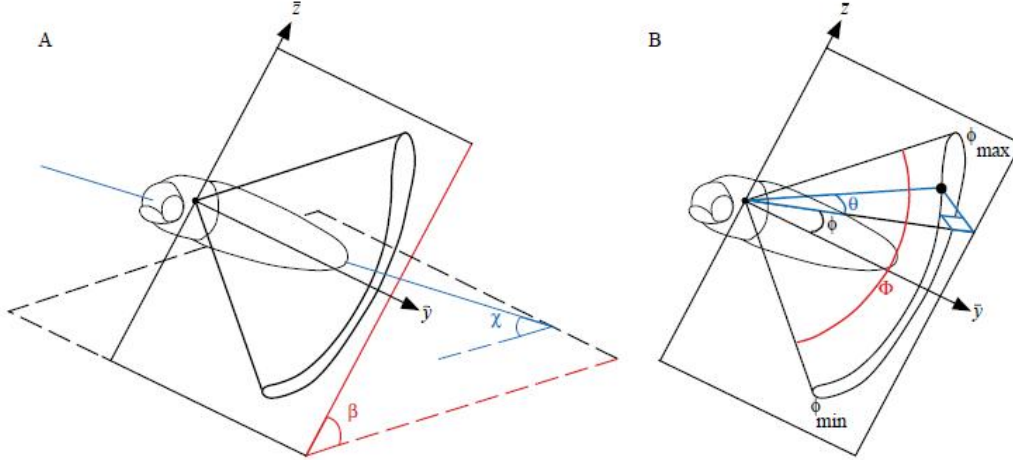
Figure 1.6:   Summary of Kinematic Parameters of *Manduca Sexta* [5]

at a first-order approximation so as to assess whether the animal makes use of well-established mechanisms or employs unusual or novel principles [18].

Willmont and Ellington of the University of Cambridge attempted to characterize the flight kinematics of the Hawkmoth using high speed cameras. Figure 1.6 was used to describe the kinematic parameters associated with the wing beat cycle of the flapping Hawkmoth. Special attention should be paid to the parameter of ϕ which describes the amplitude of the wing beat stroke (from ϕ_{min} to ϕ_{max}) taken from the **y** axis. It was noticed that "Symmetry between the left and right wing couples was good " [5] during straight and level flight, and asymmetry was only exhibited during maneuvering [18]

Their most noticeable results to be mimicked are the wing beat stroke amplitude ϕ and the average flapping frequency for forward flight. These are as follows in Table 3.2 [5]:

Table 1.2:   Average Parameters of *Manduca Sexta* Flight Kinematics [5]

Parameter	Symbol	Range
Wing beat Frequency	n	24.8-26.5 Hz
Hovering Stroke Amplitude	ϕ_h	115-120 degrees
Forward Flight Stroke Amplitude	ϕ_f	100-105 degrees

9

When the flapping motion is considered, the parameters mentioned above are the most prominent. The seemingly simple oscillating 'up and down' motion require a considerable amount of complex kinematics due to the fact that unlike birds or other flying vertebrates, insects lack extra control surfaces. This fact forces the rigid insect wings to serve as both locomotion *and* stability and control [19]. To accomplish this, the three parameters mentioned in Table 1.2 are coupled with the rest shown in Figure 1.5 to create a complex movement that translates into a substantial control problem. Evident from Figure 1.5, one may also notice that the wings undergo a considerable amount of twisting during flapping as well as translation. Figure 1.7 provides side views of the wingtip paths relative to the wingtip base at varying speeds. This attempts to connect the tip path of the flapping wings with the varying speeds of flight (shown). Here, the downstroke is plotted in red and the upstroke is in blue.

After an extensive literature search, it was discovered that little is known about the overall make up of the shoulder joint that allows for such complex movements [1] [16]. It would be very difficult to attempt to accurately mimic the twist and elevation angle θ shown in Figure 1.6. Future studies may in fact yield more prominent and usable conclusions as to the best method to mimic this movement.

1.5   *The Wing: The Materials and Structures to be Considered When Manufacturing*

It should be of no surprise that nature integrates varied methods of construction when it comes to the fabrication of materials used as support structures. Figure 1.8 shows both the top view of a *Manduca Sexta* Wing, along with a cross-sectional view of the wing at the half chord [1]. The general shape of the wing is similar to that of other biological beings in the Insecta class, such as the dragonfly and cicada, both of which can be considered model fliers for MAV application. [20]

---

[1]images gained from computed tomography (CT) scan courtesy of the Air Force Materials Directorate
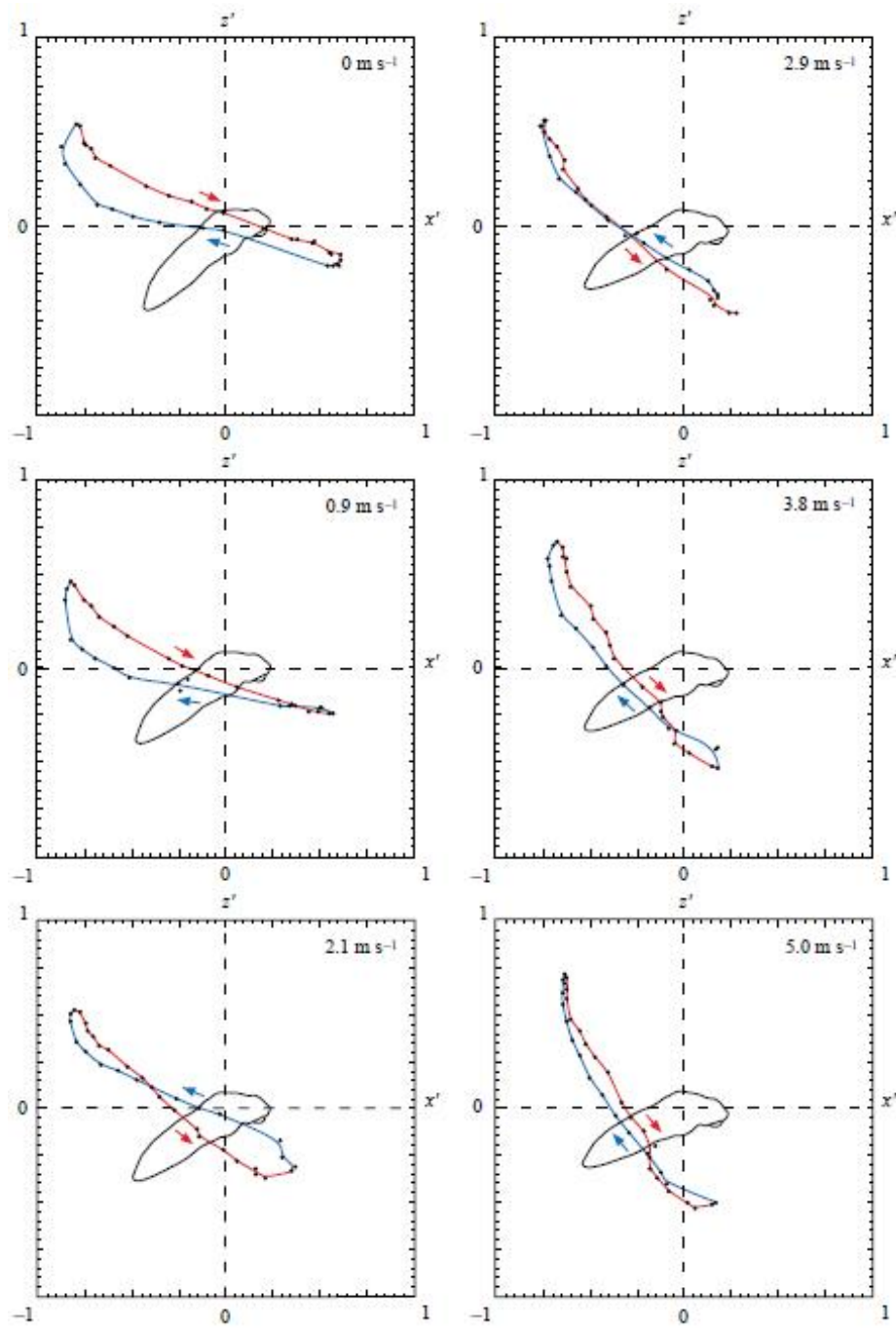
Figure 1.7:   Side View of Wingtip Paths of *Manduca Sexta* [5]

11
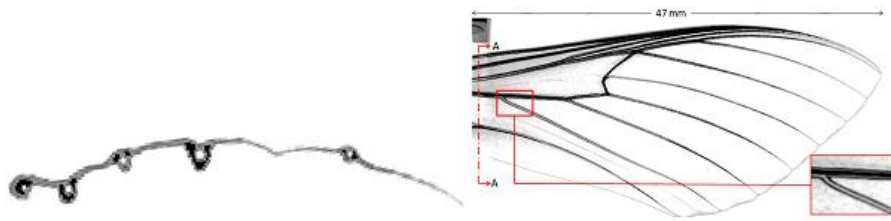
Figure 1.8: CT Scan Images of *Manduca Sexta* Forewing

Figure 1.8 sheds light on one very important concept: There exists at least two separate partitions in structure, albeit there are the presence of a 'membrane' that acts as a matrix between 'vein' elements. The veins primarily are made out of a material known as *cuticle* which is a fibrous composite material. The fibrous component consists of micro fibrils of *chitin*, a polysaccharide, and the matrix is protein. Wooton [19] mentions that the chitin is generally chemically uniform throughout the insect world, but the matrix of protein varies greatly, disallowing the assumption of universal insecta material properties.

> *In the outer layers of certain areas the proteins are strongly covalently cross linked - 'sclerotised' - giving the familiar rigid, horny plates, annuli, tubes, rods, hairs, spines and scales of the skeleton. The degree and nature of the cross-linking, and the consequent stiffness, may vary locally, as may the relative thickness of the sclerotised layers and the local thickness of the cuticle as a whole. Elsewhere the cuticle remains unsclerotised, giving areas and bands of pliant membrane between the rigid components and allowing their relative movement by a range of articulations and joints with different degrees of freedom. In some areas, the cuticle may be rich in resilin, a protein elastomer with high rebound resilience, capable of storing and releasing energy elastically and efficiently at loading frequencies within the flapping frequency range of many insects [19].*

It can thus be said that few assumptions can be made when attempting to characterize and model the wing of the *Manduca Sexta* due to the fact that nature has allowed for a large variation in material properties via the nature of composite materials. The extraordinary versatility of the insect cuticular material is likely beyond the reach of mankind, however with a careful selection of materials (composites and/or polymer materials) movement can be achieved by possibly mimicking the kinematic

properties inherent in the flapping, thus leading to the possibility of flapping flight for mankind [19]. Due to the variability and clear lack of standardization from insect to insect, system identification may seem near impossible when testing multiple specimens. The only way to curb this issue is to obtain specimens whose condition of development (standardized upbringing) can be considered constant. In order to to this, it was conceived that a standard supplier of specimens had to be introduced to the experimental method. This would eliminate some of the versatility associated with the varying developments seen within same-species specimens.

1.6   The Concept of Biological Inspiration

There is no doubt that mankind has often looked to that which surrounds him for inspiration into the realm of flight. The Wright Brothers themselves examined the structures emulated by the birds of the sky to eventually influence the creation of the Wright Flyer. It is easy to stray away from something that already works and apply what mankind believes to be 'appropriate' according to the knowledge and theories of scientists and scholars before them. Many academics find themselves in an almost 'species-centric' frame of mind when it comes to influences other than those which they already 'know' works. This way of thinking however carries the possibility of folly, and many previous studies find themselves effectively reinventing the wheel, expending time and resources to gain knowledge into what is already known.

This concept of mankind's tendency of 'species-centric' thinking was realized by Aaron Norris *et al* [1]. His research focus lay firmly rooted in the concepts of flapping flight and through his research found that an astounding *lack* of literature was present in the area of bio-inspired flight, especially those studies focused on insect inspired flight. Research in the field, he found, was present in the area of jointed flapping wings such as birds and bats [1] however, little was present concerning the rigid flapping flier. Furthermore, an astounding lack of structural analysis had been performed on the actual wings (See Figure 1.9 [1]).
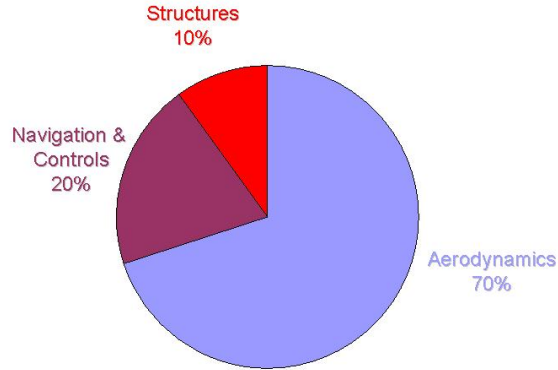
Figure 1.9:   Current Research Interest of Flapping Flight [1]

Aaron Norris' overall goal was to delve further into the realm of the structural dynamics incorporated by nature, specifically that of the *Manduca Sexta* due to its availability and size. It was Norris who was responsible for introducing this creature to AFIT. He found that it was necessary to identify the key factors/elements that remained consistent from moth to moth. If he could pinpoint the similarities between completely different creatures, he believed that he could effectively unlock the secrets that nature has been using to attain flapping, rigid (flexible but passively controlled) winged flight. Norris' system identification began at the modal level; he believed that the wing beat frequency of 26 Hz was the primary forcing frequency acting on the wing, thus providing a metric for the relative nature of the wing's *dynamic stiffness* [1]. With that in mind, he utilized a scanning laser vibrometer (SLV) to identify the mode shapes of 'liberated' [2] or separated wings under small displacements in both air and vacuum. Figure 1.10 depicts the mode shapes of the Hawkmoth's forewing as attained by Norris' analysis.

_____

[2]a term coined by Norris in his work

14
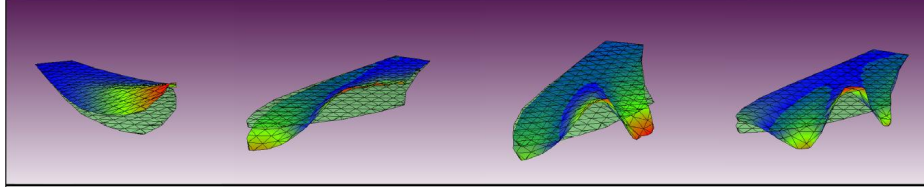
Figure 1.10:   First Four Modes of a Hawkmoth's Forewing [1]

It can be seen in Figure 1.10 that the four mode shapes are distinct and identifiable from each other. Norris *et al* identifies these as the *flap, feather, saddle,* and *bisaddle* modes respectively, in order of ascending frequency (Hz) [1]. The eigenvalues can be seen in Table 1.3[3][4]

Table 1.3:   Summary of the Modal Parameters of a Hawkmoth's Forewing in Air and Vacuum   [1]

Mode	Structural Behavior	Name	Avg Freq** (Air) [Hz]	Avg Freq* (Vac) [Hz]	MR** (Air) [–]	MR* (Vac) [–]	Damp (Air) [%]	Damp (Vac) [%]
1	SW Bending	Flap	60	85	1.0	1.0	5.0	2.5
2	SW Torsion	Feather	84	105	1.4	1.3	5.0	2.5
3	CW Bending	Saddle	107	138	1.8	1.6	5.0	2.5
4	CW Torsion	BiSaddle	142	170	2.4	2.2	5.0	2.5

*Based off of 10 wings tested in vacuum
**Based off of 50 wings tested in air
Modal Ratio (MR)
Spanwise (SW)
Chordwise (CW)

Interestingly enough, though the sample size tested was notably large, the values shown in Table 1.3 remained remarkably consistent (although not exact) from specimen to specimen, illustrating definite trends. Norris speculated that the slight scatter of values may lead to such conclusions as the naturally occurring wing emulates a certain degree of 'robustness' in which "close is good enough" [1] allowing for the wing design to be somewhat varying from specimen to specimen. This finding

---

[3]*Based off of 10 Wings tested in vacuum
[4]**Based off of 50 wings tested in air

is a substantially powerful point to consider for those who wish to design wings and emulate the traits of the Hawkmoth in that it is not necessary for the Hawkmoth to have 'wings to exact specifications' to still be flightworthy. Furthermore, Norris hypothesized that this robustness would allow a creature to sustain damage to their wings without their flight abilities being completely disabled; an important trait for a MAV.

Norris found throughout his testing that the Hawkmoth wings tested were time dependent. Unfortunately, the wings would dry out within 3 hours after being removed from the specimen, adding yet another variable to consider when testing. A 'freshly removed' wing would behave in a different manner than that of one that had been allowed to sit out and dry. Additionally, a wet wing inserted into a vacuum chamber would most definitely dry faster as the air was removed, perhaps altering gathered data. To counter these issues, Norris standardized the timetable of testing by continually running his analyses on wings that were no more than 20 mins from removal.

In addition to his analysis of the Hawkmoth wing, Norris elected to perform cursory analyses on several other flapping fliers in the insect world such as the damselfly, skipper, and butterfly. Though some species yielded little conclusions of note, Norris along with others [6] did find several similarities to the overall eigenstructure of the separate species, to include the Hawkmoth. This discovery in similarity left Norris with far more questions than answers concerning the important aspects of the structure of a flapping flier. Norris found himself questioning the validity of his tests/procedures due to the fact that they yielded such overwhelmingly similar results, even trans-species. Fortunately he tested a paper wing of the exact same dimensions as the Hawkmoth with the scanning laser vibrometer (SLV) and found a stark difference in the behavior of the paper wing. This stark difference was an important finding due to the fact that concern was expressed in the area of validity in the experimental method. As mentioned, this trans species similarity came as a surprise, so naturally questions were raised as to the nature of the discovery and whether or

16
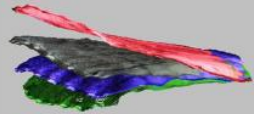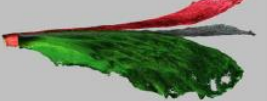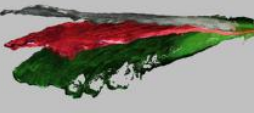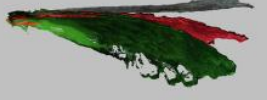
not the test equipment was producing false results. It was this paper wing however that eradicated the skepticism associated with Norris' findings in his mind, however as will be discussed, the lack of camber associated with the paper wing that may have played a crucial role in the modal response and therefore provides the rationale for this study.

Once the experimental procedure was verified and the validity was confirmed, Norris' tests continued in the area of modal analysis of several different samples. These tests lead to one of the most notable and fundamental results from Norris' work, which was not so much the eigenvalues themselves, rather it was the ratio of the first bending mode to the second bending mode gained from the testing of each of the specimens. Norris observed a remarkable trend of consistency in this ratio, which ended up being a value of 1.85. Though hesitant and skeptical of this fact, Norris was able to conclude that it was this ratio that held the key to unlocking engineered flapping flight.

Inspired by the works of Combes and Daniel of the University of Seattle, Norris decided that the aeroelastic response of the wing was a necessary area of investigation. In order to do this, Norris constructed a flapper of his own design that would emulate the flapping motion of a Hawkmoth. This flapper allowed for a 26 Hz flapping frequency. In order to capture the response of the wing, the flapping wing was strobed to create a 'frozen in time' image that could be applied to Photomodeler for a 3D view of the deflected flapping wing. It is clear that this process provided the inspiration of the research to be performed here.

His results unfortunately did not lead to any profound conclusions in this particular area, however the concept is what is most important here. Figure 1.11 displays a pictorial representation of the results gained from using Photomodeler and his test set up.

In Figure 1.11 the red wing represents flapping in ambient condition, the green wing was flapped in vacuum, and the grey wing is a static, undeflected wing (used

Sweep Angle	Rear View	Front View	Isometric View
27° DS (τ = 0.40)			
0° DS (τ = 0.50)			
-34° US (τ = 0.76)			

Downstroke(DS), Upstroke(US)

Figure 1.11:   Photomodeler Output of Flapping Deflected Wings [1]

as reference). It is important to note that each wing emulates stark differences in deflection relative to the other; a notable fact for this particular project.

Norris provided a basis of study for others to follow. It is important to realize that though no conclusions were made about the aeroelastic response of the wing, this realization of the concept of study will provide the underlying theme for the rest of this project.

1.7   The Finite Element Approach

Following closely in the footsteps of Aaron Norris, Travis Sims [11] wished to examine more closely the validity of the findings of Aaron Norris; more specifically he desired to delve further into the realm of modal analysis from a finite element (FE) approach in an attempt to identify the key factors that influence the modal behavior explained by Norris. The objective of his work was to produce a finite element model of a *Manduca Sexta* forewing grounded in experimental vibration testing [11].

Throughout the model creation process, there were two competing requirements: 1. maximizing geometric simplifications to ensure tractability, and 2. minimizing unnecessary deviation from the physical structure to preserve the accuracy of results [4].

18

Testing was accomplished in air and vacuum, to observe potential aeroelastic effects. Second, a finite element model capable of representing the observed modal behavior was developed and analyzed. Geometric dimensioning is accomplished via computed tomography (CT) imaging methods [11].

Clearly, Sims followed Norris' train of thought in that the structural aspects of the Hawkmoth's forewing was worthy of study. It is important to realize that his work used both experimental and analytical data, with research and testing being firmly rooted in structural theory. To begin, he observed that which Aaron Norris had begun and felt that theory should be more closely examined. What was revolutionary about this work was the extensive use of computed tomography (CT) scanners to inspire the digital model of the specimen (as seen in Figure 1.8). With a clear view of the inspiring specimen, Sims was able to recreate the model shown in Figure 1.12.
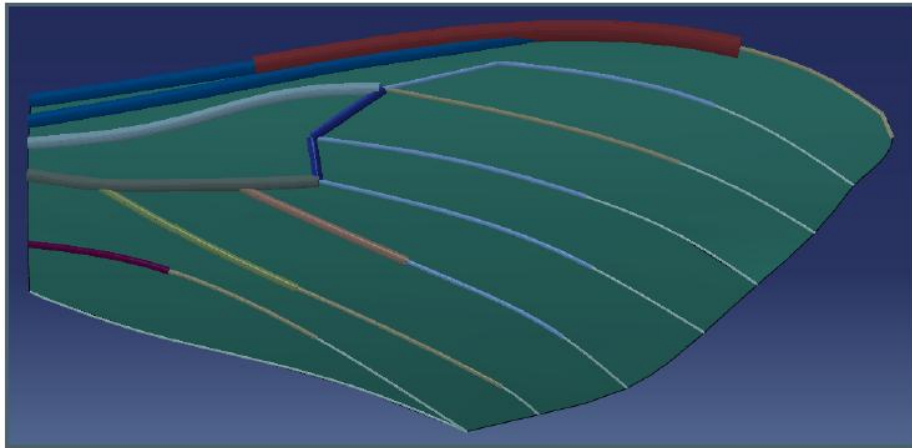
Figure 1.12:   Finite Element Model of Forewing [4]

The Sims model yielded results similar to those of the experiment as seen in Table 1.4, save for the third mode. He offers little explanation as to the reason for this aberrant behavior, however he does state that though the frequency is in stark difference to the experimental results, the 'saddle' mode shape prevails, similar to what Aaron Norris' research concluded (see Figure 1.10) Sims however did not feel that his results were simply obtained in that there were several factors that had to be

adjusted. His research lead him to examine the **Aeroelastic Question**: What are the parameters that influence the dynamic behavior of the Hawkmoth forewing?

Table 1.4:   Natural Frequency Results Generated by Sims [4]

	Experimental (Hz)	FE Model (Hz)	Minimum Difference
ω_1	86 ±2	84.6	0.0 %
ω_2	106 ±2	106.1	0.0%
ω_3	155 ±2	317.7	102.4%

Original analyses obtained from Combes and Daniel stated that it was the material properties that influenced the behavior of the wing, specifically the flexural stiffness (to be discussed). Travis however felt that there were three main areas of interest to this question:

1. The material properties

2. The geometry/shape of the wing; specifically the vein patterns/structure

3. The natural, unique camber of the wing

Sims was able to investigate several sources, but like Norris he too was unsuccessful in finding adequate data to reveal the actual material properties of the *Manduca Sexta*. He was,however, able to take the properties from that of the cicada, as the material properties of the vein structures and the membrane. Due to observed behavior however, Sims found it necessary to reverse the properties for application to the Hawkmoth [11]. These properties can be seen in Figure 1.13. The importance of these properties cannot be ignored, mainly due to the fact that these represented the basis of investigation and provided the 'first iteration' of characteristics used in the eventual application to MAV wings.

Due to the nature of his research and experimentation, Sims was able to easily change these properties, and the results he produced proved to be contrary to those before him. His most stunning discovery was that of the three properties listed above, it was in fact the **camber** that had the most profound effect on the natural frequencies produced by the FEA results. Figure 1.14 shed light on one of the most important
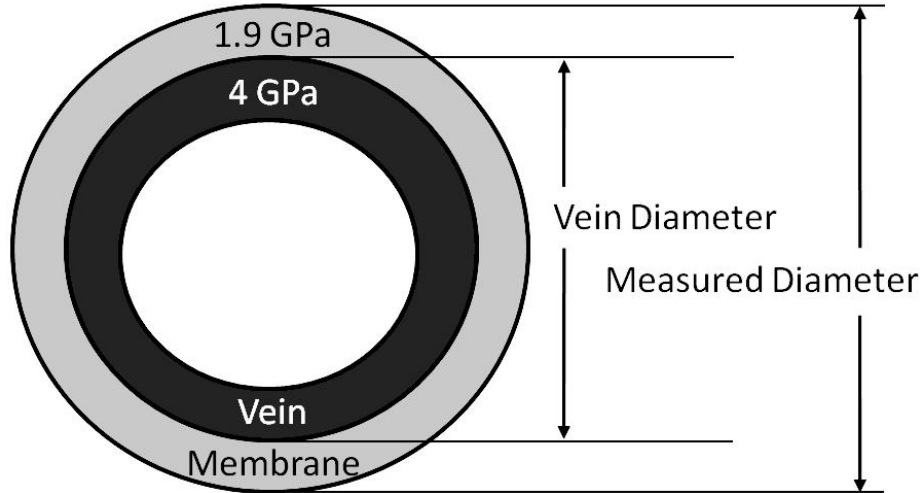
Figure 1.13:   Material Properties Used to Simulate Hawkmoth Properties as Used By Sims [11]

conclusions that Sims drew from his work which is proving that the challenge of mimicking material properties perhaps is not as critical as once was believed.
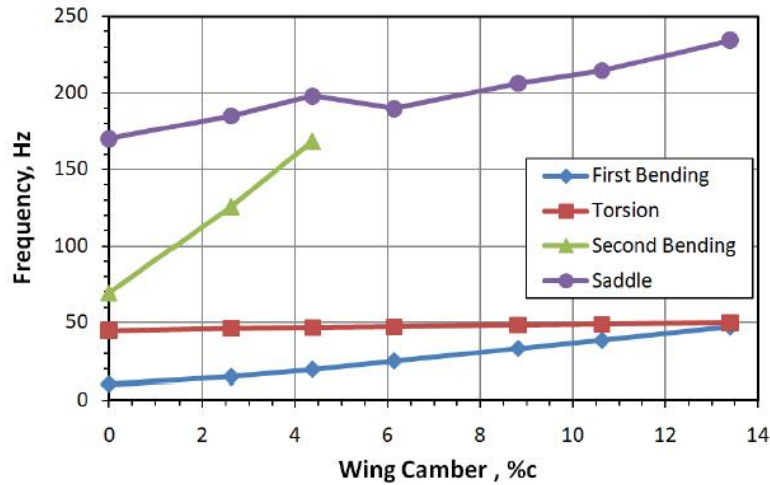
Figure 1.14:   Effect of Camber on ω_n [11]

Though ground-breaking, it is important to note that Sims introduced his camber by applying the wing outline to a constant camber cylinder which does not accurately represent the camber of the biological specimen. Furthermore the constant arc length is "...severely under predicts the natural camber associated with the biological specimen" [21]. Work done by O'Hara at Air Force Institute of Technology utilized

21

reduced CT data to effectively model the camber inherent in a dry *Manduca Sexta* wing as seen in Figure 1.15 [21].
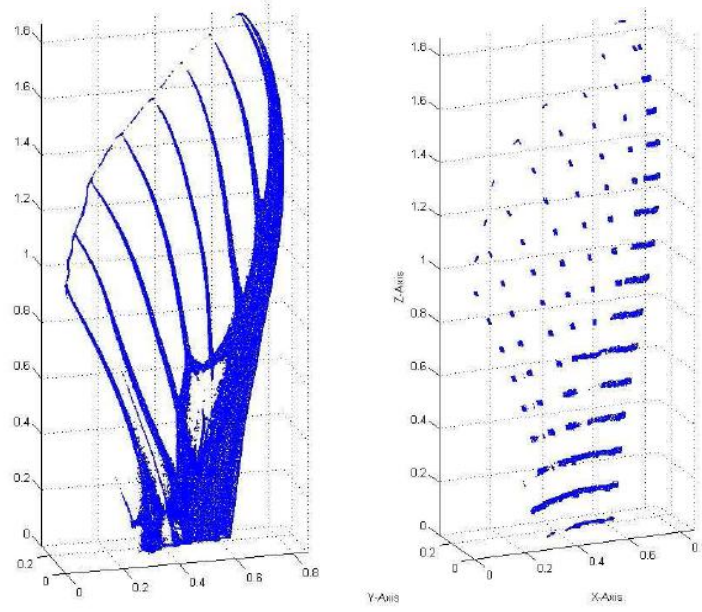
(a) Original CT Data   (b) Reduced CT Data
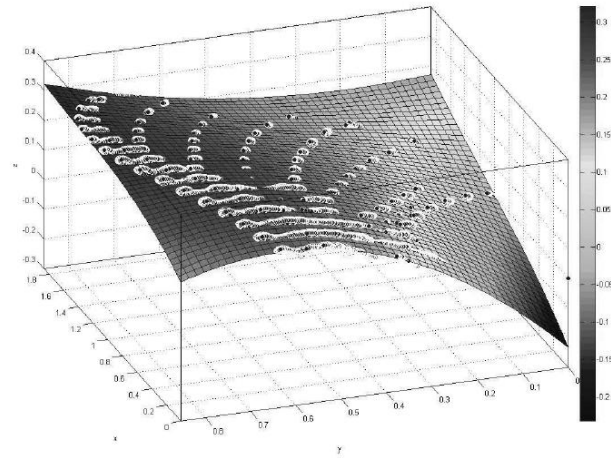
(c) Planar Fit Reduced CT Data

Figure 1.15:   O'Hara's CT Data and Planar Fitted Data [21]

O'Hara felt that Sims' conclusions were both interesting and crucial to MAV development, however they lacked in overall numerical validity and thus felt it necessary

22

to gain a numerical representation of the plane that would boast the most accurate camber modeling. Using the reduced CT points displayed in Figure 1.7, O'Hara was able to produce a planar fit of the data seen in Figure 1.7. He confirmed that Sim's applications of the constant cylindrical camber lacked the necessary complexity required to adequately model the camber properties of the wing. Using MATLAB as the primary generator of the 3 dimensional polynomial planar fit to the CT data, O'Hara was able to yield the following equation to describe the camber of the biological wing [21]:

$$f(x,y) = p00 + p10*x + p01*y + p20*x^2 + p11*x*y + p02*y^2 + \quad (1.1)$$
$$p30*x^3 + p21*x^2*y + p12*x*y^2 + p03*y^3$$

Equation 1.1 further confirms the complexity of the 3 dimensional wing shape. Empirical testing found that this representation was authentic in terms of 'goodness' for the application to future iterations of the wing, as many have failed to attempt to model per Norris' research. Both O'Hara and Sims believed that if one could impart this camber to a wing, it may be yet another key to the unlocking the complexity of the optimal MAV wing.

1.8 A Word on Flexural Stiffness: A Biologist's Opinion

Both Sims and Norris found themselves influenced by the works of Combes and Daniel, a group of biologists at the University of Washington. These experimentalists have observed that during insect flight the wings would undergo large-scale deformations and believed that they were controlled by the architecture of the wings [6] [7]. This hypothesis represents the exception to Norris' findings that little efforts were being made at investigating the structural aspects of the wings.

> *The structure of the insect wings thus appears to permit certain beneficial passive deformations while minimizing detrimental bending that would compromise force production* [6].

What is most important about the above statement by Combes and Daniel is that they recognized that the flexion of the spanwise rigid wings is *deliberate.* In fact, this deliberate flexion can be considered a method of energy storage, making the spanwise rigid wings more efficient than those of birds and bats who actively manipulate the spanwise length of their wings during flight– requiring both the presence of extra driving/control muscles and weight for flight.

The parameter that these two decided was the most important to investigate was that of the **flexural stiffness** which they define as "the composite measure of the overall bending stiffness of a wing; it is the product of the material stiffness (E, which describes the stiffness of the wing material itself) and the second moment of area (I, which describes the stiffness generated by the cross-sectional geometry of the wing)". This parameter is represented in the mathematical model for a beam as shown below [6]:

$$EI = \frac{FL^3}{3\delta} \tag{1.2}$$

Here, the parameter [L] is the effective beam length, δ is the wing displacement at the given position of force application, and [F] could be considered an applied force. The term I can be described as follows for the wing:

$$I = \frac{wt^3}{12} \tag{1.3}$$

Where [w] is the width and [t] is the thickness of the wing. They found it necessary to test this parameter from both an experimental and finite-element based investigation (similar to Sims'). The setup of these two investigations can be pictorially represented in Figure 1.16

In Figure 1.16a, Combes and Daniel depict the experimental setup; wherein a point force was applied to a freshly removed (within 30 mins) *Manduca Sexta* wings (separately that were glued at the wing base and along the leading edge). This method in theory could be used to gain insight into the flexural stiffness of the wing

|(a) Wing Displacement|(b) Finite Element Representation|
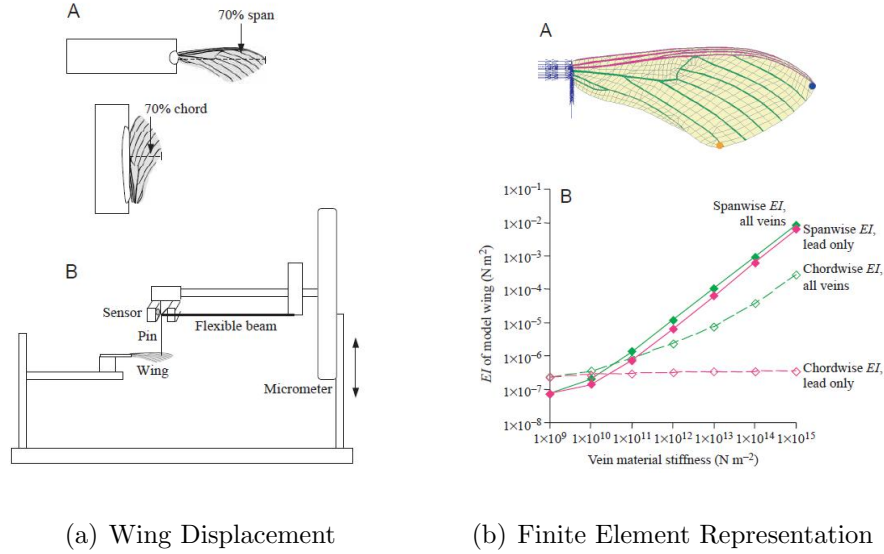
Figure 1.16:   Combes and Daniel's Initial Flexural Stiffness Investigations [6]

as a function of the distance from the base/leading edge. Combes and Daniel found it necessary to standardize the location of the applied force to 70% of the span and chord length (simply because the needle would slip off). The finite element model depicted in Figure 1.16b represented a simplified version of the Sims analysis in that Combes and Daniel did not attempt to recreate the 3 dimensional characteristics of the wing [6], rather their goal was to investigate the effects of vein stiffness on the overall flexutral stiffness, and thus did not find it pertinent to include changes in vein/membrane thickness but instead modeled the wing as a flat plate of uniform thickness. This is what they termed as a 'general' model of the wing, however it can be inferred this certainly is not the case due to the fact that, as was seen with the work of both Sims and Norris, the three dimensional nature of the wings shape is crucial in the eventual understanding of the Hawkmoth wing for MAV applications.

Though the model presented by Combes and Daniel could be considered overly simplified, it does serve as the basis of investigation into the aforementioned characteristics. It is important to note that even though the veins modeled by Combes and Daniel were flat plates, they did take into account the fact that the biologically constructed veins were hollow, blood filled tubes, granting them a higher second moment

of area [I] (in some cases several orders of magnitude higher) than that of a flat plate. To account for this fact in the results of the FEM, Combes and Daniel felt it necessary to adjust the material stiffness [E] associated with the veins. This would in turn aid in determining the overall flexural stiffness as compared to the physical experiment (described in Figure 1.16a). The following properties for the wing were suggested for the FEM analysis by Combes and Daniel, based off of their own literature reviews:

Table 1.5: Summary of the Material Properties of Insect Wings as Presented By Combes and Daniel [6]

Parameter	Value
ν	0.3-0.49
ρ	$1200 kg\ m^{-3}$
E_{Vein}	$1x10^9$-$1x10^{15}N\ m^{-2}$
E_{Mem}	$1x10^9 N\ m^{-2}$

An interesting result of this study indicated that the utilized Poison's Ratio ν had little effect on the flexural stiffness values and thus its value was considered negligible [6]. Results obtained for several species are depicted in Figure 1.17. These indicate that the size of the specimen has a profound effect on the flexural stiffness exhibited by the sample. What is most influential for the project to be executed here is that this fact indicates that it may be wise to **standardize the size** of the sampled specimens tested. There is not a lot that can be done to control the size of the tested biological wings in this project, however variability in results when comparing specimens can be eliminated by attempting to mimic both the size and geometry of the *Manduca Sexta* wing. The construction process of the tested specimens will be detailed in Chapter 3.

"The strong correlations between wing size and flexural stiffness suggest that size scaling is the dominant factor [in] determining overall flexural stiffness." Sims too recognized the possible importance of this parameter, mentioning it himself in his thesis [4]. Combes and Daniel recognized that the venation pattern may not affect overall stiffness, rather it could be considered an influential factor in determining the way in which stiffness varies throughout the wing [6]. This statement sheds light
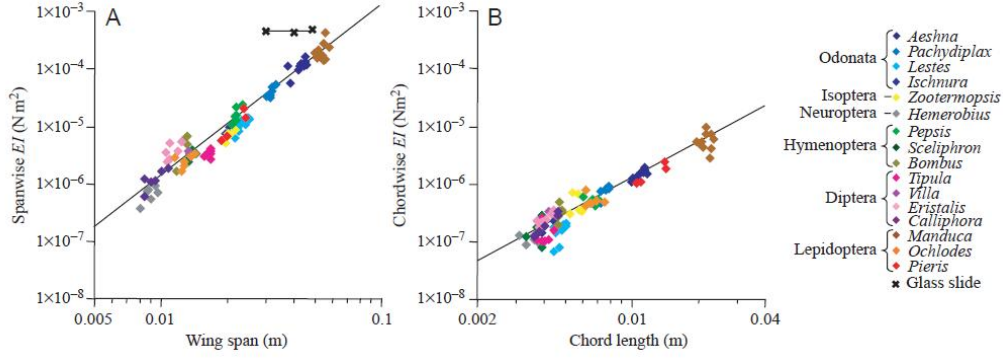
Figure 1.17: Results of Combes and Daniel's First Attempt at Measuring Flexural Stiffness [6]

on these individual's core belief that the geometry matters little in the arena of wing behavior during a dynamic response (at least for their particular study). Furthermore, this initial study done by Combes and Daniel speaks towards spanwise-chordwise anisotropy exhibited in all insects, in that most flying insects exhibit the 'thickened' leading edge, and the anisotropy in the vein properties would serve to strengthen the wing from bending in the spanwise direction, yet allowing for chord wise deformation (perhaps for aerodynamic purposes) [6] [22].

The experiments detailed in Figure 1.16 were reinvestigated in a manner similar to what will be shown in this report; moving from tangible sensors to a method that utilizes procedures similar to that of photogrammetry. Instead of using a micrometer as was shown in Figure 1.16a, laser lines were projected onto the deflected wing, and using a camera, the displacement of the wing relative to the original position of the lines could be measured, to be indicative of the desired flexural stiffness. An example of these photos can be seen in Figure 1.18 where the [A] and [B] are the deflected and undeflected images respectively. The basic method here is one of comparison. The images of the laser lines of the undeflected wing were clearly different than those of the deflected ones. These could be compared to each other and conclusions could be drawn about the total deflection.
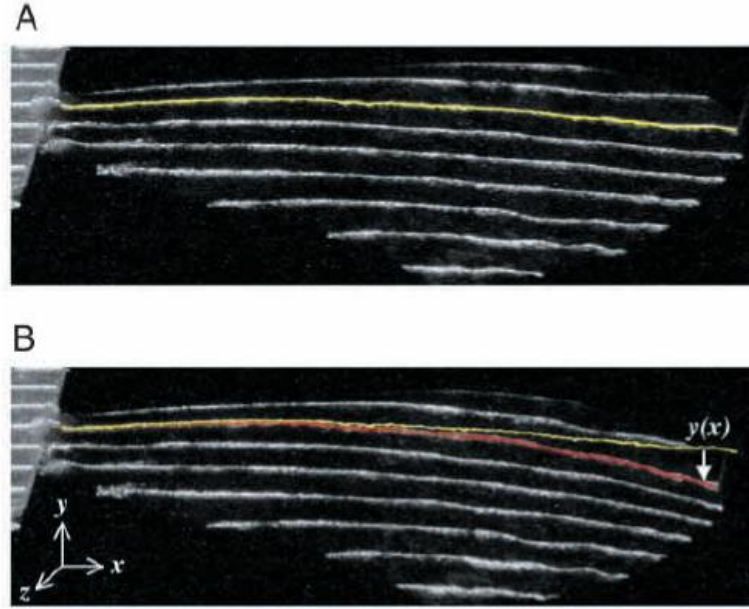
Figure 1.18:   Laser Marking of Deflected *Manduca Sexta* Wing [7]

In order to further investigate the effects of flexural stiffness in the arena of aeroelasticity, Combes and Daniel found it necessary to employ tactics similar to those to be shown. Combes and Daniel had already recognized that the purpose of wings was to accelerate masses of air to support body weight while resisting possible damage incurred by that action [7], and thus found it necessary to examine the actual dynamic response of the wing. To do this, the finite element model that was mentioned in their first study was flapped (computationally) at a frequency of 26 Hz at 108 degrees based on the information gained by Willmont and Ellington [5]. Due to the fact that the FE software did not incorporate air into its calculations, Combes and Daniel found it necessary to apply a computational 10% damping coefficient to the system, which according to the findings of Norris et al [1] (see Table 1.3) is too high. One important fact to consider when examining the consideration of air however is that Norris obtained results using small displacements, not large ones as were simulated in the work by Combes and Daniel. For this investigation, it was not so much the behavior of the wing itself that was of interest, rather it was the

behavior of the viens. Combes and Daniel investigated two different cases when the vein stiffness was considered:

1. The veins themselves are of homogeneous properties, in that their stiffness does not change with respect to span

2. The vein stiffness decreases exponentially as a function of span

This consideration is crucial in the development of a structure that would accurately mimic the characteristics put forth by the Hawkmoth. There are a number of ways that this can be achieved both material wise (composites) or geometrically (vein tapering and lofting as described by Wooton [19]). Figure 1.19 depicts the result of the FE flapping study, where the (blue) wings represent the homogeneous stiffness veins, and the (red) wings represent the exponentially decreasing stiffness veins.
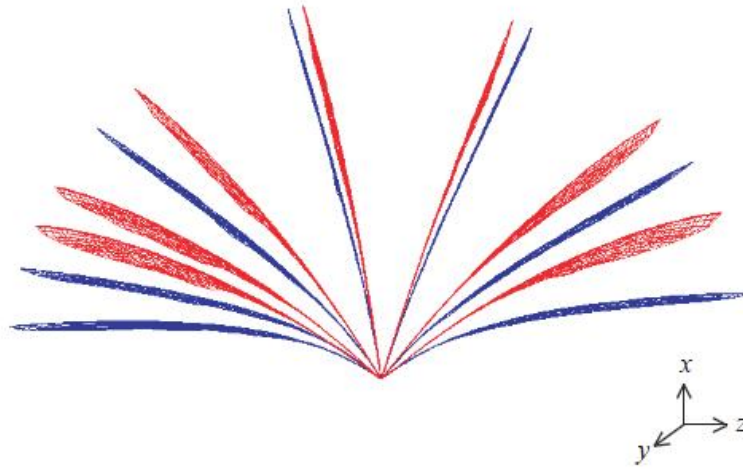
Figure 1.19:   FE Model of Flapping *Manduca* Wing [7]

These results led Combes and Daniel to make a rather interesting, and perhaps important conjecture based on the findings of Wooton [23]; the veins of the *Manduca Sexta* may contain one-way hinges or other micro-structural features that facilitate asymmetric bending as in other insect wings [7]. This conjecture would be convenient for an engineer to ignore due to the fact that constructing a micro structural member

29

capable of such behavior would prove itself difficult, however, new technologies grant further possibilities in manufacturing and fabrication. Despite this however, Combes and Daniel did conclude from this particular study that:

> ...the sharply declining stiffness measured in real wings helps maintain rigidity near the wing base (despite larger bending moments), while localizing bending to the tip and trailing edge, which are regions of particular importance in controlling aerodynamic force production [7].

The conclusion stated here call into consideration the subject area of the fluid structure interaction inherent in the motion of these flapping wings; furthermore it facilitates an aura of wonder on the particulars associated with the structure-fluid interaction. Norris, Combes and Daniel, and (as will be discussed) Willmont and Ellington all grasped at the same concepts concerning the large displacements associated with the flapping motion. The only logical path to take is through controlled experimental simulation. Combes and Daniel, along with others in the scientific community, have taken action to investigate this concept. Combes and Daniel specifically considered the concept of aerodynamic vs. inertial loading in that one should dominate the other. They themselves cite Ennos [24], who estimates that spanwise bending moments due to inertia of flapping wings are twice as large as those due to aerodynamic forces. This, according to Ennos, is the cause of the complex rotation associated with that of Figure 1.5, which is described in [25] as being a result of the wing being decelerated at the end of the beat due to the conservation of angular momentum. This suggests that the anisotropic wing would serve to strengthen the wing from bending in the spanwise direction [6], granting the ability to lead the associated twist inherent in the flapping wing. This is one of the most deterministic factors for this particular study, since it brings to the front some of the most important behaviors associated with the design and manufacturing of the engineering wings to be tested.

To shed light on the discussion of the dominance of aerodynamic and inertial effects, Combes and Daniel devised an experiment similar to that seen in Norris *et al* [1] wherein wings were removed from anesthetized Hawkmoths at the base and

were flapped using the mechanism seen in Figure 1.20. The difference between the Norris experiment and the experiment described by Combes and Daniel [26] is the fact that instead of tracking the wing as a whole, reference points were marked on the wing using white paint that weighed 1.5% of the total wing mass on both the dorsal and ventral sides on the wing tip, trailing edge, and leading edge. The marked wing was then attached at the base to a brass rod that could be rotated by an oscillator constructed from a pen motor and amplifiier of a Gould chart Recorder [26]. This entire system was placed inside a plexiglass box in which allowed for both isolation from noise, but also a change in atmosphere.
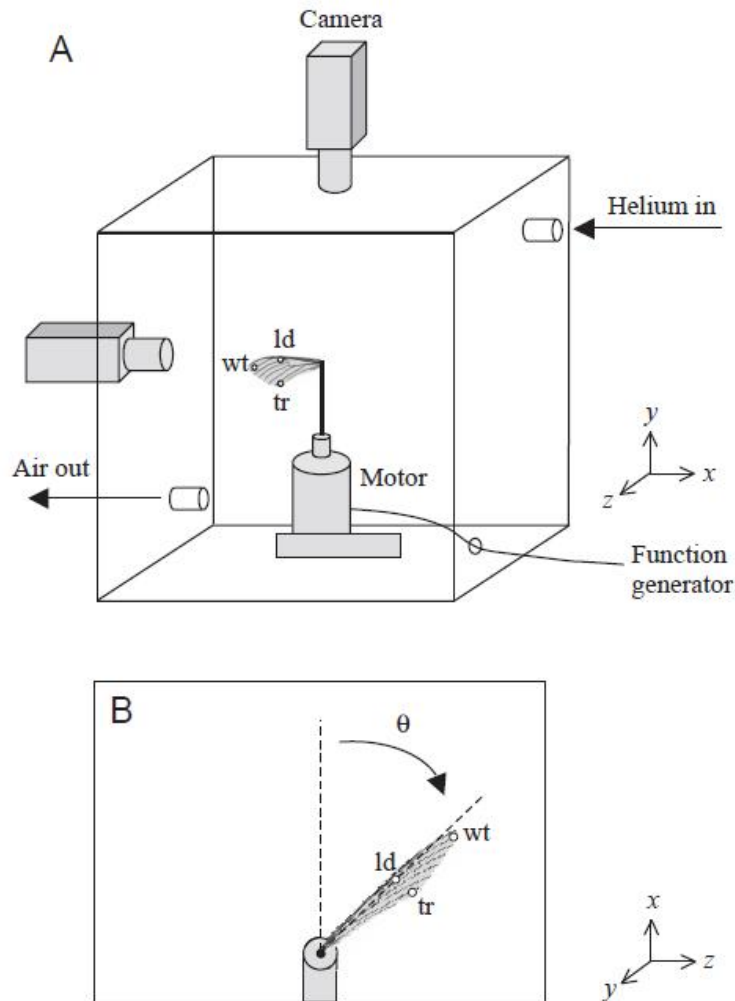
Figure 1.20:   Combes and Daniel Flapping System [26]

Where Norris had the ability to flap in vacuum, Combes and Daniel were limited and thus used helium to execute their experiments, in addition to flapping in air. To observe the deformations inherent in the wings that were flapped at an amplitude of 107-110 degrees at 26 Hz about the dorsal ventral axis in both air and helium. This motion was filmed using the three cameras depicted in Figure 1.20 in order to observe the deformation of the wing. They analyzed frames from three complete flaps in the middle of each filming sequence, to avoid bending artefacts at the onset of motion [26]. A Matlab program was developed to identify the exact coordinates of the wing tip as it moved for corresponding frames– thus being able to back out three-dimensional coordinates in much the same manner as Photomodeler. The trajectory of the wing could then be observed and a Fourier analysis was performed on the wing bending data in order to gain the dominant frequencies of wing motion [26]. This data could then be compared to the aforementioned FEM data. Results are shown in Figure 1.21.

Results shown in Figure 1.21 lead Combes and Daniel to the conclusion that measurements of regional wing bending of flapping Manduca wings undergo significantly more dynamic bending at the wing tip and trailing edge than along the leading edge, confirming previous static measurements of regional flexural stiffness as was seen in [7]. Additionally, Combes and Daniel found that flapping in helium attained similar behavior to that of flapping in air, however the far less dense properties of helium did not damp the deflection/bending of the wing as was in air. Observed deflections of the helium filled experiment had a higher amplitude (though similar behavior) than those of the experiment in air, agreeing with Norris *et al.* [1]. Relating to the work presented for this particular report, Combes and Daniel make the following statement about their experiment that proves itself both relatable and pertinent to this research:

> *The experimental work and dynamic modeling in this study were based on a relatively simple kinematic pattern, in which the wing was rotated around only the dorsalventral axis of the wing hinge. In most insects, muscular forces transmitted to the wing base not only propel the wing with large amplitude motions such as these, but also rotate the wing around*
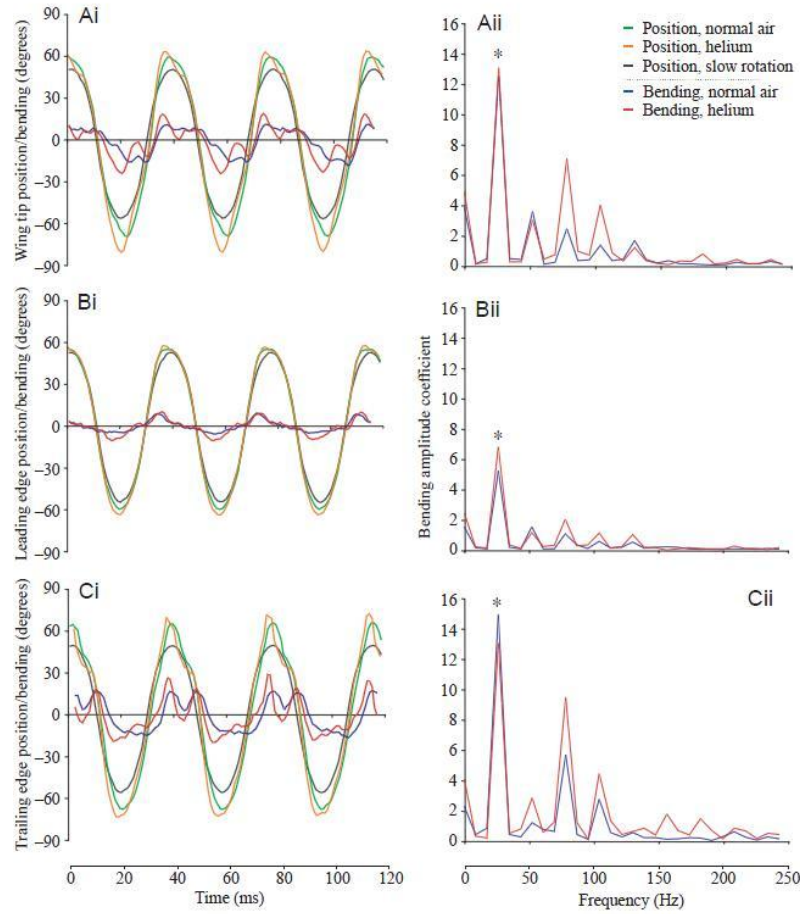
Figure 1.21:   Results of Combes and Daniel Flapping System Experiment [26]

its leading edge, controlling the angle of attack of the wing and, in some cases, causing significant spanwise twisting [26].

What was most important and inspirational about the work performed by these individuals was the fact that though they realized that they were not exactly representing the biological specimen, they did find it necessary to standardize testing procedures by eliminating room for error. This was done by eliminating the complexity of their models while still retaining their ability to have confidence in their findings.

1.9 Willmont and Ellington: Flapping and Photogrammetry

Perhaps two of the most influential individuals within the realm of the flight of the Hawkmoth are Alexander P. Willmott and Charles P. Ellington. Most of their works have been cited by anyone who wishes to delve into the arena of the biologically inspired MAV. Biologists they may be, their data concerning the *Manduca Sexta* holds great value when examining the abstract behavior of flapping motion. One of their most notable experiments that relates to the topic of dynamic characterization of the *Manduca Sexta* forewing undergoing large rotation/translation and the use of photogrammetry to reconstruct three dimensional images from the two dimensional images. Their overall goal in [27] was to characterize the angle of attack of the insect in flight. What is interesting about their first methodology however is that they neglected asymmetric flapping and assumed that the left wing was the same as the right, thus granting them two images of the same wing. This is what they coined as 'The Symmetry Method' [27] and it reduced the amount of data to be taken by the high speed cameras that they used to photograph the wing. The obvious issue with this is that the flapping would be dependent solely on an uncooperative insect and it can be seen that often times the flapping motion is not always symmetric. The only issue that they found with this method was when the wing margins were parallel to each other in the images [27]. Here, they found it difficult to back out the positions of the wings due to limitations in visibility. They also found that their assumption concerning the symmetric flight lead to unacceptable errors.

Their most successful method was known as the 'Landmarks Method' in which instead of using assumptions such as symmetry, noticeable 'landmarks' were considered on the wing and measured from the base of the undeflected wing to create a reference for a deflected one. Landmarks included vein intersections, other natural features, along with physically marked, artificial features added by the researchers.

The true distance of each mark from the wing base is measured directly for the untwisted wing... In an individual frame, the position of each landmark in turn is digitized and its apparent distance from the wing base

*is calculated. The third coordinate is found from the known length of the
line between the points by Pythagoras' theorem.* [27]

Willmont and Ellington admitted that this method's accuracy was largely dependent on the size and shape of the landmarks themselves– and a total lack of standardization between species did in fact have its effects. Willmont and Ellington found that this method was impractical for a fully intact *Manduca Sexta*, simply due to the fact that the scales cover many of the natural features, and those features that were discernible showed poorly in the high speed video sequences. Several attempts were made to add artificial landmarks, using enamel paints, white correction fluid, silver paints, and a range of fluorescent powders and paints, all of which met with failure due to the following reasons:

- The presence of wing scales and their tendency to be shed during flight meant that the landmarks were often lost very rapidly after marking

- None of the materials adhered readily to either the wing cuticle or the scales

- Spots large enough to track were often too heavy and would affect the behavior of the wing by changing the distribution of wing mass

Though troublesome, this landmarks method "has great potential owing to its simplicity, absence of assumptions, and requirements for only one wing outline" [27]. They do state that the main drawback however is the possibility of the landmarks having an effect on the response of the wing is ever present, especially if the wing is light. Additionally, they state that the marks should be as small as possible to increase accuracy of the photogrammetry– and due to the fact that the biological wing often refuses any type of marking, control of the size of the marks may prove problematic.

1.10 Conclusion to the Literature Review

The objective of this work is to evaluate and execute a method of characterizing and evaluating the response and subsequent behaviors of both engineering and bio-

logical wings subjected to both large displacements and deformations as well as small ones. The inspiring specimen for this work (*Manduca Sexta*) has many complicated features that may not be duplicated in the engineering model, therefore an initial attempt at characterization of the fundamental features is being attempted in this area of inquiry. There are several more variables that need to be considered when trying to exactly mimic the species:

- The actual materials

- The naturally occurring boundary conditions

- The three dimensional geometry

- The interfaces between the separate materials

- The time dependent material characteristics and their effects

- The possibility of unconsidered factors that deal with the natural wing itself, such as the presence of scales and their aerodynamic/inertial effects

This research will attempt to recreate portions of many other projects, combining features from each into one concise, standardized, and repeatable experiment. The mission here is the elimination of variability to the highest degree possible. Though simplified and seemingly unrealistic, the experiments that will be shown in this research will be comparable to each other, which is the crux of this entire project.

In conclusion, the methods of wing construction and evaluation will be investigated here in order to more fully understand and appreciate the factors that are associated with the construction and implementation of biologically inspired FWMAVs. System ID will pull from previous experiments to include modal analyses for both the separated biological wings and the engineered wings; allowing for the validation of Norris' work [1]. Furthermore, all wings will be subjected to standardized flapping in both air and vacuum, and the response of such motion will be identified using Photomodeler; granting the ability to compare and contrast the separate responses of the wings. This will also shed light on the **Aeroelastic Question** (the question of the

dominance of air or mass distribution in the wing motion during flapping) mentioned by Norris [1], Sims [4] [11], Ennos [24], Combes and Daniel [6] [7] [26] and others.

This thesis will attempt to characterize the flapping motion of both a biological and engineered wing. This document will first outline the underlying theory concerning the tools that will be used to carry out the experiments (Chapter 2). Chapter 3 will discuss the manufacturing of both the wings that will be tested and the flapper, which was used as an evaluation tool. Chapter 4 will outline the testing and data gathering procedure, to conclude with the data handling that was used to obtain the results. The results will be shown in Chapter 5. Conclusions to this study will be shown in Chapter 6.

II. Theoretical Development

This section serves to demonstrate an understanding of the mathematics associated with the experimental processes that are to be performed for this project. The two main areas of focus include the design of a new AFIT Flapper as inspired by Norris et al. [1] and a brief discussion on the concepts harnessed by PhotoModeler ©as will be implemented in the experimental methods to be presented in the future.

2.1 Introduction to the Flapper

The AFIT Flapper was originally conceived by Aaron Norris [1]. The purpose of this device was to simulate the flapping motion exhibited by the *Manduca Sexta*. The original device can be seen in Figure 2.1 which was composed of a simple, single 4-Bar mechanism as is defined by conventional mechanics. Though innovative and unique, the Norris Flapper proved itself as an all too simplified version of the flapping behavior, failing to exhibit qualities that would mimic the actual flapping angles and neglecting the possible effects of gravity when simulating the motion; an important factor when examining the argument of inertial vs. aerodynamic influences as presented by Combes and Daniel [26] and Ennos [24]. It was conceived that the Norris Flapper would have to be redesigned to perhaps incorporate more of these aforementioned qualities. The Norris Flapper represents the first iteration towards accurately simulating the flapping motion of the biological specimen that grants the inspiration for eventual MAV applications.

The objective of these flappers, as mentioned, are to simulate the flapping conditions inherent in the flapping flight of the Hawkmoth. Little concern is shown at this point for direct application into a flying machine, thus it is not pertinent to take size or mass into consideration when constructing these devices. Figure 2.1 represents the next iteration towards the successful simulation of the boundary conditions exhibited by the inspiration. The DeLeón Flapper's objective was to simulate a few more of the flapping parameters discussed by Willmont and Ellington [5] to include the correct flapping angles and magnitudes, and the effects that gravity may have on

38
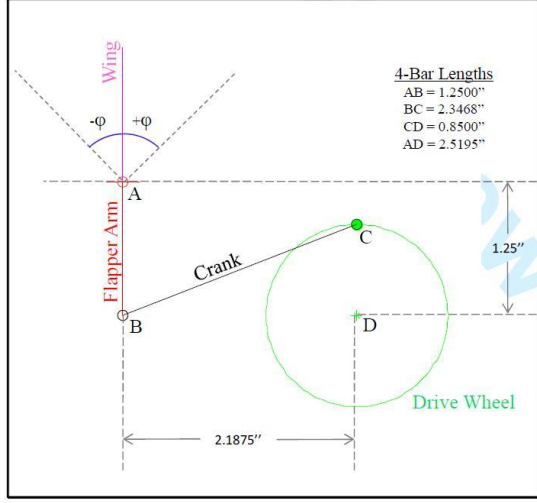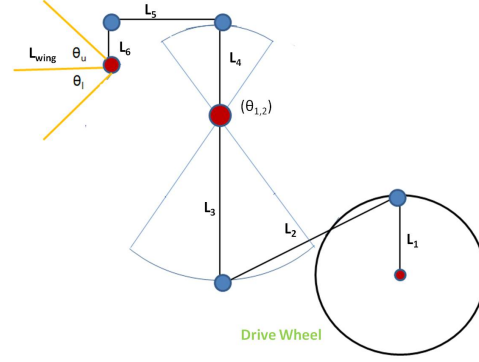
(a) Norris Flapper   (b) DeLeón Flapper

Figure 2.1:   The AFIT Flappers as Conceived by the Palazotto Group

the wing itself. This design was partially inspired by the work done by Anderson [28] who incorporated piezo actuators into a simple four bar mechanism to simulate the flapping conditions.

2.2 Original Design Considerations: The Geometric Formulations and Process of Design

As mentioned in Table 1.2 in Section 1.4, the flapping angle amplitude and the flapping frequency were taken as the most necessary parameters to mimic for this current study. Little consideration was taken for the flapping frequency as it could be easily controlled by a speed controller on the driving motor/mechanism. The flapping angle amplitude presented itself as the most influential in terms of flapper design. Previous designs of the flapper allowed for uneven accelerations. Figure 2.2 below was produced by Norris et al. [1] to illustrate the behavior of the several different results as gained by observing mechanical behavior of flapping.
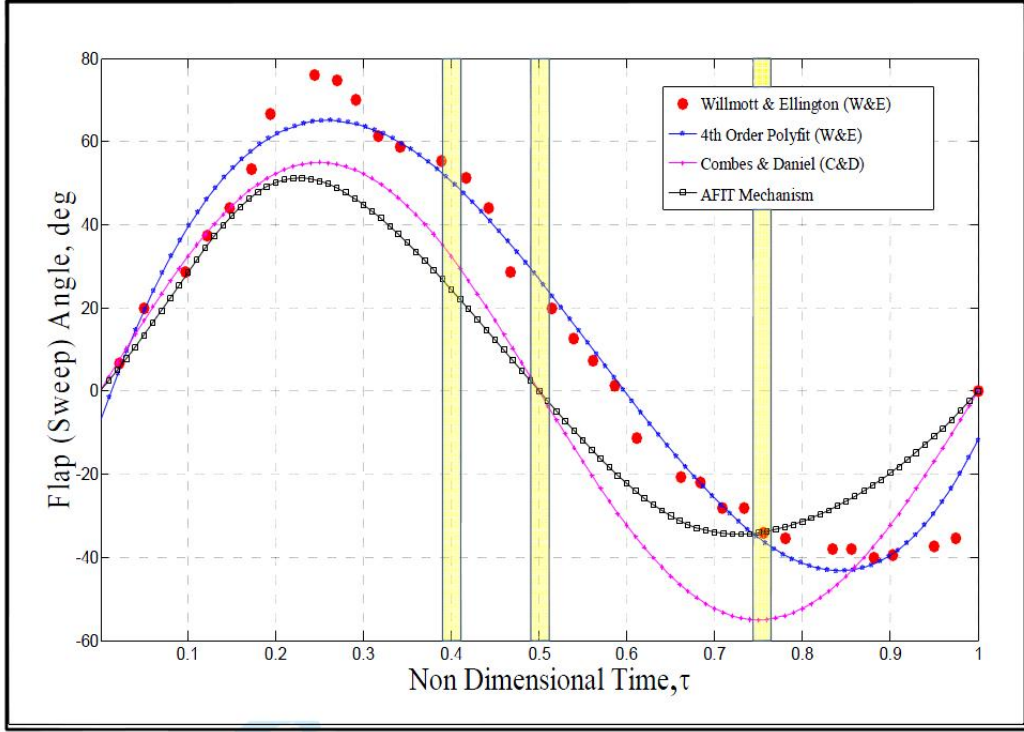
Figure 2.2:   Variable Angular Displacements as Gained by Several Researchers [1]

Figure 2.2[1], which is taken directly from Norris' work [1], sheds light on some of the fundamental differences inherent in the original flapper- especially when compared to that of the inspiring specimen presented by Willmont and Ellington. Needless to say, it can be seen that the flapper conceived by Norris left plenty to be desired in the fact that the overall magnitude of the the angular displacement was short by about 17° as well as the fact that the biological specimen's angular displacement is not symmetric with respect to the '0' horizontal axis; rather it is offset with a bias upwards. This 'bias' in the upper portion of the stroke may in fact lead to some important behaviors when considering the dynamic response of the wing; and for this study it was deemed pertinent to take this into consideration.

To begin the overall design process however, the aforementioned bias was not initially considered, rather priority was granted to obtaining the correct stroke am-

---

[1]Yellow bars on the plot represent the phases in the stroke that Norris examined in Photomodeler for his preliminary experiments

plitude as mentioned in Table 1.2. Various linkage designs as conceived from the *Manduca Sexta* can be seen in Figure 2.3.

(a) Inspiring Design

(b) Slider Simulation

(c) Four Bar Simulation
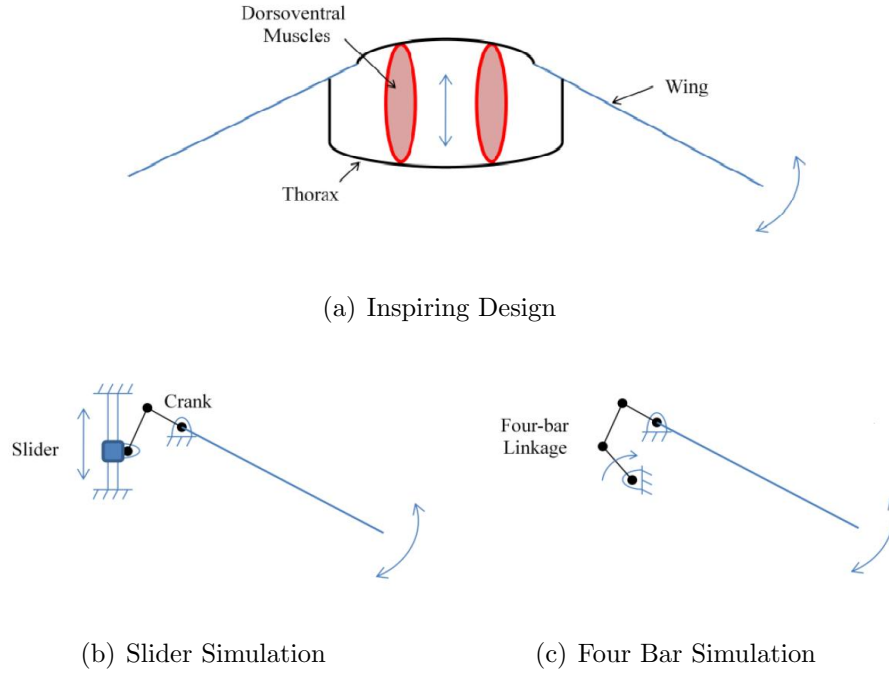
Figure 2.3:   Flapping Simulation Conceived as Linkages [28]

Since the crux of this project is biological inspiration in engineering, it is necessary to study Figure 2.3 in order to obtain a full understanding of the motivations behind the design parameters to be discussed. Figure 2.3a depicts a simplified representation of the naturally occurring flier. The oval shapes in the middle are representative of muscles that expand and contract. This motion allows for the upper and lower portions of the solid thorax (depicted as black curved lines) to oscillate. This motion translates to the wings allowing them to flap up and down. The most important concept to take from this is that the specimen has employed a mechanical advantage in the form of a linkage system in order to amplify the small motion generated by the flight muscles into a much larger motion as seen by the beating wings. This mechanical efficiency can best be described by Figure 2.3b which is a slider. As the slider is allowed to move up and down, the small displacement of the slider is amplified by the attached linkage system to generate a much larger displacement of

the attached wing. Furthermore, Figure 2.3c depicts a four bar mechanism known as a Crank-Rocker mechanism. Here, the angular displacement of the bottom, pinned bar is amplified via the attached links to recreate the flapping motion that can be seen by the inspiring specimen.

A similar setup was realized by Norris et al. [1] who constructed the four bar mechanism depicted in Figure 2.1. As mentioned, his hope was to mimic the motion achieved by the Hawkmoth, however this oversimplified version left plenty to be desired as can be seen in Figure 2.2. It was thus necessary to fully utilize the already existing mechanism that nature had suggested to essentially 'tweek' the existing AFIT flapper designed by Norris in order to more fully realize the potential of biologically inspired flapping motion. This Crank-Rocker mechanism depicted in Figure 2.3c provides a start to the beginning of a mechanism design. Due to the fact that this study is not concerned with the total flapping mechanism- it was necessary to consider only the mechanical piece (aka not the driving piece). Using the work done by Norris [1] and Anderson [28] as a guide, a four bar mechanism was realized as detailed in Figure 2.4.

Anderson [28] used a piezo to run his experiments wherein the vertical line in Figure 2.4b is allowed to deflect back and forth. This small motion is amplified by the linkage as is seen in the inspiring specimen in Figure 2.3. The same basic motion can be achieved without the use of a piezo by simply allowing the leftmost linkage in Figure 2.4c to move back and forth, rotating about the red (fixed) frictionless hinges. This motion can be achieved by a motor attached to yet another Crank-Rocker mechanism. As long as the simulated 'piezo stick' (leftmost linkage in Figure 2.4c) exhibits the back and forth motion achieved by the piezo- it can be considered a similar design. Additionally, this setup has the potential to remove some of the possible issues associated with non-rigid body motion such as the effects of aerodynamic/inertial loading on the 'deflecting' pieces. This aforementioned setup can be seen in Figure F.1 in its entirety.

(a) From Inspiration   (b) Anderson Flapper

(c) Four Bar Simulation
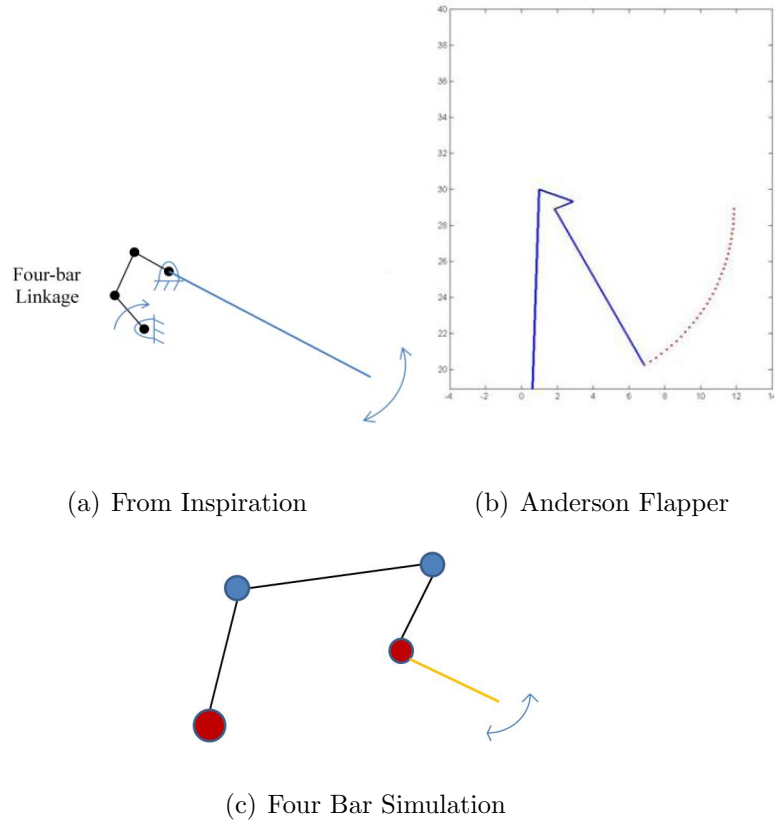
Figure 2.4:   Flapping Simulations Conceived as Linkages [28]

2.3   Comparison of DeLeón Flapper with Others

In order to verify the comparison of the DeLeón Flapper to the data gathered by
Willmont and Ellington, it was necessary to carry out a careful kinematic analysis; a
process that is shown in detail in Appendix F. This demonstrated the understanding
of the 'design blueprint' before the construction of the flapping mechanism, which will
be discussed in Chapter 4.

The results of the angular displacement analysis of the flapper seen in Appendix
F can be compared to the inspiring specimen, along with previously conceived flap-
ping mechanisms. Before the comparison was physically made, the data from Figure
2.2 had to be gathered as clearly as possible. This was done by examining the indi-
vidual curves and picking off the coordinate points with the use of a program called
GraphClick^{TM} to show that which was found in Norris' work [1] and Willmont and

Ellington's [5]. An issue was discovered concerning this data wherein the end point was misconstrued when gathered by Norris in Figure 2.2 as he tried to shift the data. This shift lead to innacuracies in the data representation that showed the Willmont and Ellington data as being shifted to the right. It was necessary to correct this issue by correcting for this shift. Once the point data was gathered and corrected, the following could be plotted using MatLab.
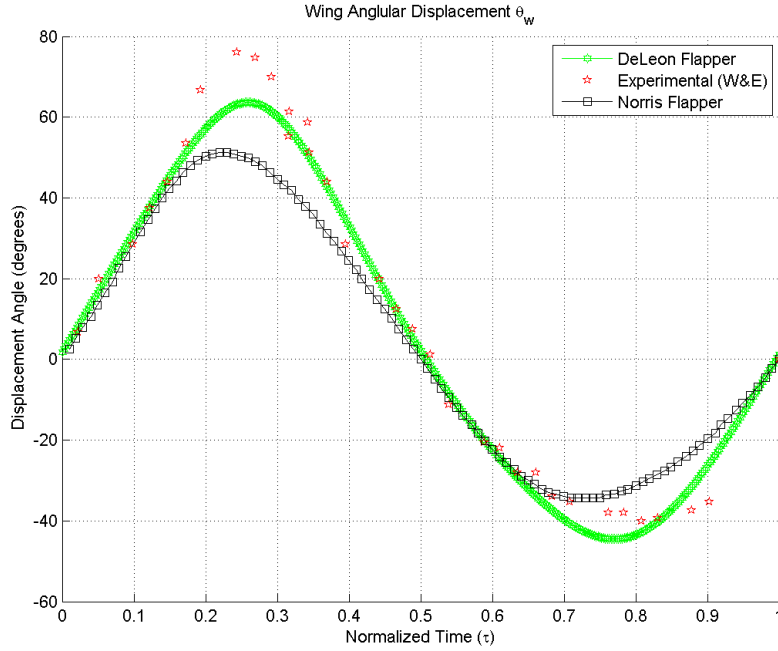
Figure 2.5:   Comparison of the Displacement Flapping Kinematics

The data presented in Figure 2.5 sheds light on what will be currently applied to the dynamic analysis of the wing to what has been done; most importantly however this analysis depicts the experimental data forged by Willmont and Ellington [5]. A few of the shortcomings of previous designs can be seen here as often they do not achieve the full amplitude of flapping nor do they exhibit exact behavior of the slopes (as will be seen). It would appear upon close inspection that the DeLeón Flapper achieves the closest to matching the experimental amplitudes as exhibited by the inspiring specimen. The next section will perform an analytical comparison of this claim.

In addition to the angular displacement analysis, a velocity analysis was carried out (in Appendix F) and compared to the differentiation of the 6th order polyfit of both the Willmont and Ellington data and the Norris Flapper data.
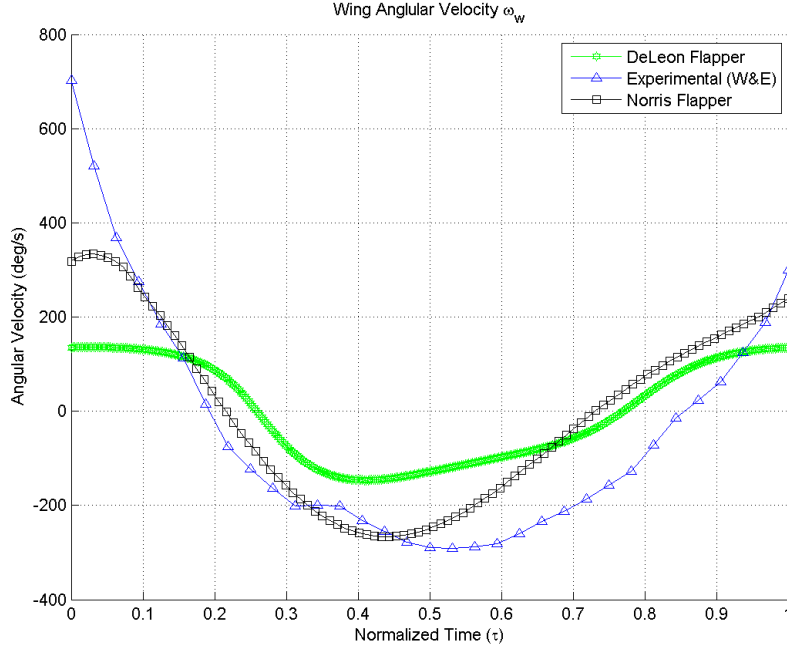
Figure 2.6:   Comparison of the Angular Velocities of the Flappers

It can be seen in Figure 2.6 that the DeLeón flapper does not quite match the experimental data in magnitude, but the associated behavior inherent in the newly conceived flapper appears to most closely mimic that which is seen by the *Manduca Sexta*. It is clear here that perhaps the earlier designs emulate the biological displacements in the angular velocity spectrum as their magnitudes most closely conform to the experimental data.

The final comparison dealt with the angular accelerations produced by the analysis. Figure 2.7 sheds light on the comparison between the 'theoretical' data, original AFIT flapper, and the new AFIT flapper.

In the next section, a regression test will be presented wherein the new flapper will be compared in terms of displacement to the data gathered by Willmont and
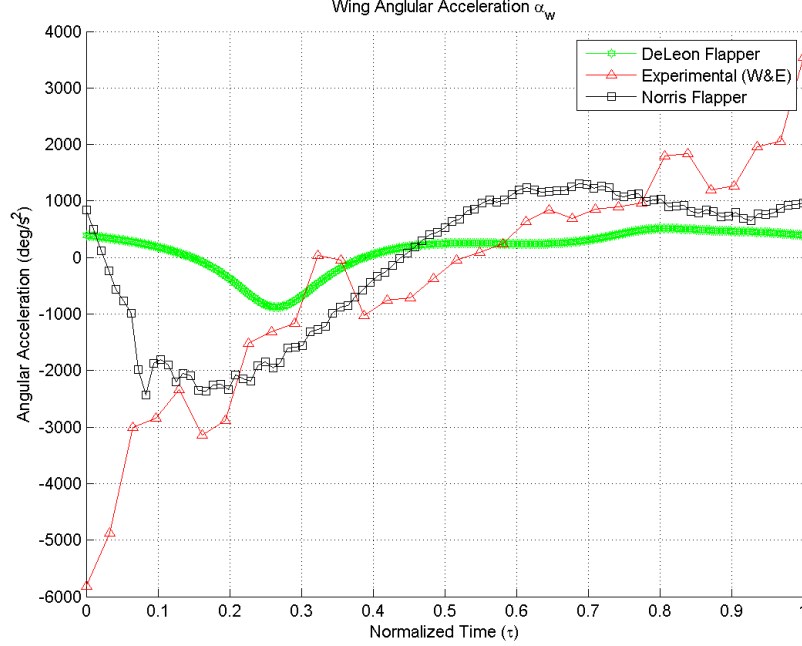
Figure 2.7:   Comparison of the Angular Accelerations of the Flappers

Ellington which has been fitted with a 6th order polyfit in order to illuminate the level of comparability to the new flapper.

2.4   Regression Analysis: How does the DeLeón Flapper Compare?

The purpose of this section is to take into consideration the data gathered by Willmont and Ellington to understand whether or not the new flapper truly does mimic the flapping motion of the biological specimen. This is pertinent considering that the whole motivation behind its design was in fact to emulate a few of the kinematic properties associated with the inspiring flapping motion.

Figure 2.8 sheds light on this regression analysis. The aforementioned polyfit applied to the Willmont and Ellington data was applied to the Combes and Daniel data, along with the Aaron Norris data. All of them were plotted using the same normalized time vector as that which was utilized in finding θ_w. In doing this– a point-to-point comparison could be executed for the magnitude of the difference between the experimental and calculated results. The results of this calculation produce the plots

46

seen in Figure 2.8 that shows the differences in angular displacement as a function of the normalized time. The goal of any of these flappers was to minimize the difference in magnitude.
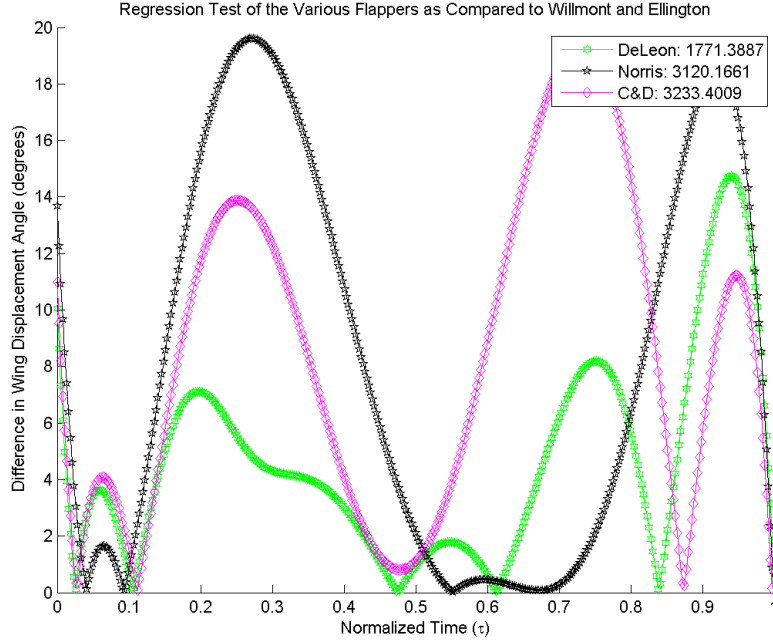
Figure 2.8:   Regression Test of the Angular Displacements (θ_w) of the Various Flappers

Though at a glance, this plot would appear to indicate that the DeLeón Flapper produces the least difference in magnitude, it was deemed pertinent to integrate the area under these curves to determine the 'overall agreement' of the regression analysis. The legend in Figure 2.8 displays the results of this operation, agreeing with the first conjecture that the DeLeón flapper holds the most accuracy when mimicking the angular displacement of the mechanism.

This same operation could be applied to the velocities and accelerations, as shown in Figures 2.9 and 2.10. As can be seen in Figure 2.9, the DeLeón Flapper does not perform quite as well as the others, however upon visual comparison, it may be safe to say that the values are close.

47
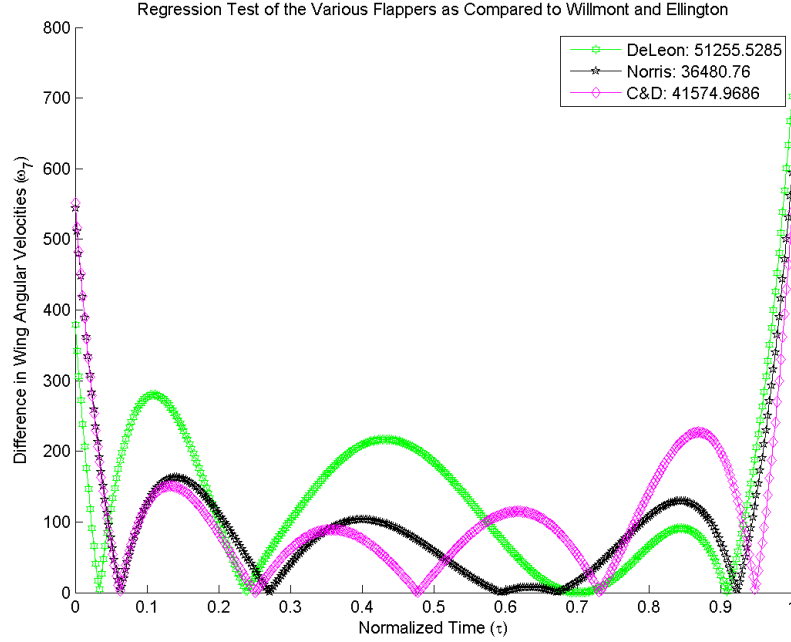
Figure 2.9:   Regression Test of the Angular Velocities (ω_w) of the Various Flappers

Though disconcerting, Figure 2.10 brings to the table some unfortunate news in that in the acceleration regime, the DeLeón Flapper fails in comparison to the rest.

Though for a true analysis this fact would be considered unacceptable, the DeLeón flapper was designed originally with only displacements in mind. Previous iterations of the design similar to that seen by Norris et al [1] experienced aberrant and uneven accelerations which proved too harsh on the wings tested. Luckily bench testing of the DeLeón Flapper indicated that modifications eliminated this issue instead of accelerations that were not exactly that of the inspiring specimen however did retain the qualities of 'wing survivability'. When observing Figure 2.7, it is clear that although different, the DeLeón flapper appears they exhibit acceleration qualities of a lower magnitude than those by the inspiring specimen and Norris. This may be advantageous as the DeLeón Flapper may in fact contribute to wing survivability by making the transitions and motions associated with flapping far less 'harsh' on a wing.
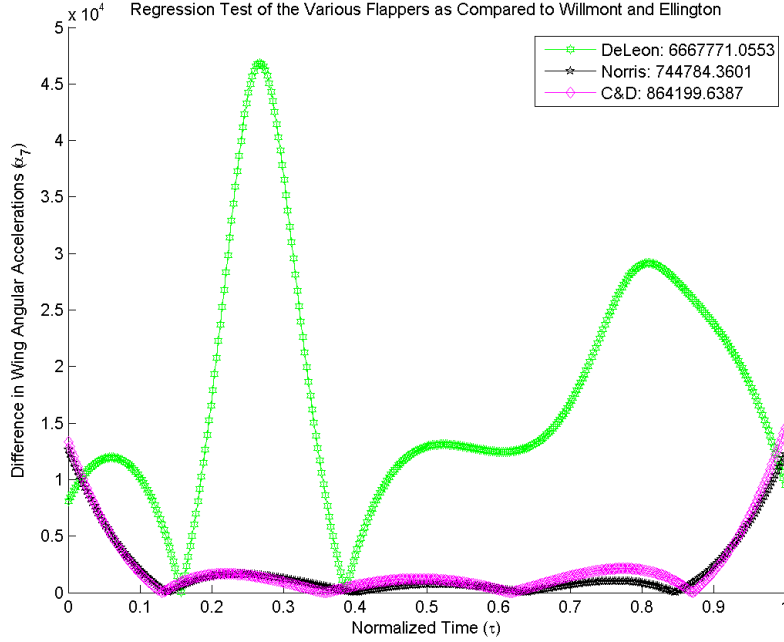
Figure 2.10: Regression Test of the Angular Accelerations (α_w) of the Various Flappers

In summary, the regression test revealed that in terms of displacements and velocities, the new AFIT Flapper compares well to the data gathered by Willmont and Ellington, however fails in the regime of accelerations. However in the long run this may aid in testing wings as they will be subjected to less overall force for most of the motion.

2.5 Force Analysis: Comparison of Crank-Rocker System to Biological Flapping Mechanism

Section 2.2 of this thesis shed light on some of the comparisons to the actual biological specimen to that of simplified linkage designs, in particular that of the Crank-Rocker (four bar) mechanism. It is necessary to consider some of the structural properties of this comparison. Figure 2.11 will aid in this discussion as it points out one of the more pertinent reasons for this analysis: the investigation of the muscular input of the Hawkmoth as compared to this Crank-Rocker System.

49
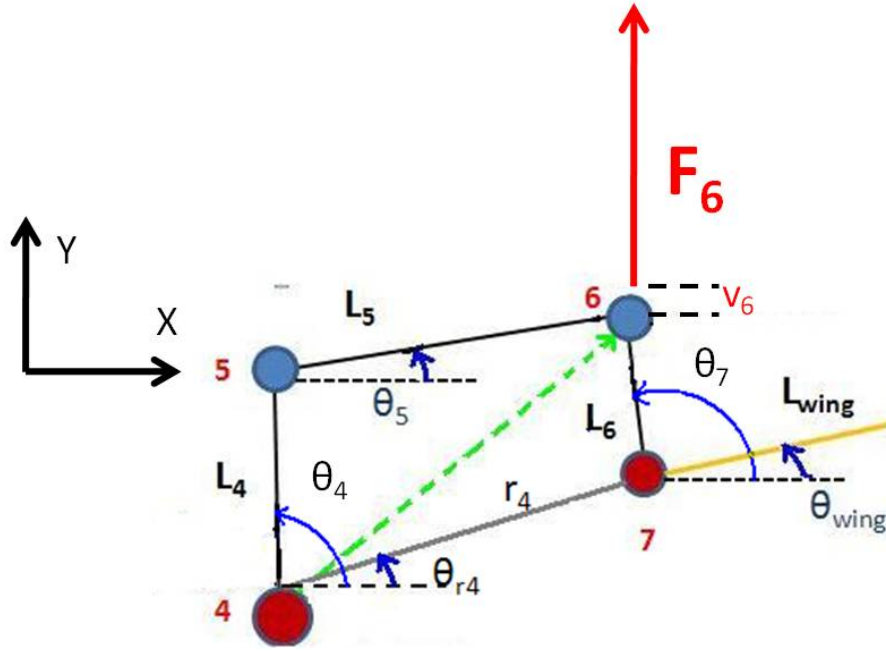
Figure 2.11:   Four Bar Mechanism as a Force Applied to Wing-Linked Node

To begin, it is pertinent to consider each of the linkages separately. Each link-age will have properties unique to themselves, especially in the construction of such a mechanism (which will be seen in Chapter 4). Knowing some of the material and physical properties will allow for this aforementioned 'force analysis'. The fundamental equation to understand here is the following:

$$[K_g]\{d\} = \{F\} \tag{2.1}$$

Where $[K_g]$ is considered the global stiffness matrix, $\{d\}$ is the vector of displacements associated with the moving/translating part. $\{F\}$ represents the force associated with the spring/stiffness due to that motion. Given a known displacement or a known force, one can back out any of the others. Figure 2.11 represents the investigative question: Knowing the displacement of the thorax mechanism (as seen in Figure 2.3) due to the force 'F', one theoretically could back out the displacement associated with the given four bar mechanism. Due to the kinematic analysis performed

50

above, every displacement will be known (using simple geometry and having known all of the angles of the linkages for all time). This allows for a direct comparison to the biological specimen, allowing for a juxtaposition of the displacements, essentially conveying yet another comparison of the Crank-Rocker to the thorax of the *Manduca Sexta*.

To begin, it is pertinent to first discuss the global stiffnesses of each of the linkage systems. Concerning the terminology to be used, one should note that $cs_4 = cos(\theta_4)sin(\theta_4)$ and $c_4^2 = cos^2(\theta_4)$. Additionally, the term [A] refers to the cross-sectional area of the linkage mechanism (to be pulled from SolidWorks from the given constructed mechanism as will be discussed in Chapter 3), [E] is representative of the Young's Modulus of the material used to construct the particular linkage, and the term [L] is the length of that linkage (shown in Table F.1).

In terms of the displacements, it is necessary to consider the terminology as well. u_4 and v_4 represent the displacement in the x and y directions (as defined by the global axis). Normally, the displacements are defined on a local-axis basis where the [u] terms represent displacements along the axial direction of the beam, and the [v] terms are defined normal to the longitudinal axis of the element. It is more conducive to the analysis however to explore these displacements in terms of this aforementioned 'global' system due to the fact that the main focus of this specific analysis is to investigate the effects of the presence of the displacements and forces associated with node 6 which are investigated along the **y-axis**. It should be noticed here that the [w] (rotational) displacements are ignored for this analysis due to the fact that the system described above is strictly two dimensional and rotations of the materials are considered negligible due to the assumed lack of friction in the mechanism construction (as will be discussed in the next section).

The properties of the linkages to be discussed are shown in Table 2.1

The first linkage to be discussed is that represented by L_4. The force associated with this linkage can be described as such:

Table 2.1: Properties of Top Crank Rocker Mechanism for Force/Displacement Analysis

Element	Length (m)	Young's Modulus (E) (GPa)	Area (m^2))
L_4	0.0254	2.87	2.903e-005
L_5	0.0381	70	1.3273e-006
L_6	0.0132	2.87	3.7287e-004

$$\frac{A_4 \cdot E_4}{L_4} \begin{bmatrix} c_4^2 & cs_4 & c_4^2 & -cs_4 \\ cs_4 & s_4^2 & -cs_4 & -s_4^2 \\ -c_4^2 & -cs_4 & c_4^2 & cs_4 \\ -cs_4 & -s_4^2 & cs_4 & s_4^2 \end{bmatrix} \cdot \begin{bmatrix} u_4 \\ v_4 \\ u_5 \\ v_5 \end{bmatrix} = \{F\} \tag{2.2}$$

However, in Equation 2.2, it can be inferred that by the design represented in Figure 2.11, the u_4 and v_4 terms are considered to be zero due to the fact that that end of the L_4 linkage is pinned. This allows for the elimination of the first two rows and columns of the matrix represented in Equation 2.2, to yield the following:

$$\frac{A_4 \cdot E_4}{L_4} \begin{bmatrix} c_4^2 & cs_4 \\ cs_4 & s_4^2 \end{bmatrix} \cdot \begin{bmatrix} u_5 \\ v_5 \end{bmatrix} = \{F\} \tag{2.3}$$

This now leads the the investigation of the L_5 linkage, which holds translation at both ends, so in the manner of the equation described in Equation 2.2, one can observe the following:

$$\frac{A_5 \cdot E_5}{L_5} \begin{bmatrix} c_5^2 & cs_5 & c_5^2 & -cs_5 \\ cs_5 & s_5^2 & -cs_5 & -s_5^2 \\ -c_5^2 & -cs_5 & c_5^2 & cs_5 \\ -cs_5 & -s_5^2 & cs_5 & s_5^2 \end{bmatrix} \cdot \begin{bmatrix} u_5 \\ v_5 \\ u_6 \\ v_6 \end{bmatrix} = \{F\} \tag{2.4}$$

Link L_6 is pinned at one end as well, but it is the opposite of that seen in Link L_4 and thus must be 'transformed' or treated differently than the other two by applying a different transformation matrix. Additionally, the angle considered (θ_7) is not on

the left hand side, rather it finds itself on the right. The following sheds light on the proper treatment and transformation of the force matrix for the L_6 link:

$$\frac{A_6 \cdot E_6}{L_6} \begin{bmatrix} c_7^2 & -cs_7 & c_7^2 & cs_7 \\ -cs_7 & s_7^2 & cs_7 & -s_7^2 \\ -c_7^2 & cs_7 & c_7^2 & -cs_7 \\ cs_7 & -s_7^2 & -cs_7 & s_7^2 \end{bmatrix} \cdot \begin{bmatrix} u_6 \\ v_6 \\ u_7 \\ v_7 \end{bmatrix} = \{F\} \qquad (2.5)$$

However, as was seen in 2.2, the displacement at node 7 is zero in both directions as it is a pinned boundary condition. The u_7 and v_7 rows and columns can be eliminated to produce the following:

$$\frac{A_6 \cdot E_6}{L_6} \begin{bmatrix} c_7^2 & -cs_7 \\ -cs_7 & s_7^2 \end{bmatrix} \cdot \begin{bmatrix} u_6 \\ v_6 \end{bmatrix} = \{F\} \qquad (2.6)$$

To consider the system in its entirety, it is necessary to consider the stiffness of the system as a whole. This can be expressed as such:

$$Kg = K_4 + K_5 + K_6 \qquad (2.7)$$

Combining Equations 2.3, 2.4 and 2.6 will allow for the treatment of the solutions. It should be mentioned that the theoretical displacements can be displayed as such:

$$d = \begin{bmatrix} u_5 \\ v_5 \\ u_6 \\ v_6 \end{bmatrix} = \begin{bmatrix} L_4 cos(\theta_4) - L_4 cos(\theta_4(t_1)) \\ L_4 sin(\theta_4) - L_4 sin(\theta_4(t_1)) \\ L_6 cos(\theta_7) - L_6 cos(\theta_6(t_7)) \\ L_6 sin(\theta_7) - L_6 sin(\theta_6(t_7)) \end{bmatrix}$$

53

If Equation 2.1 were to be carried out using these theoretical displacements, the resulting force vector would yield a vertical force at Node 6 for every point in time which can be seen in Figure 2.12.
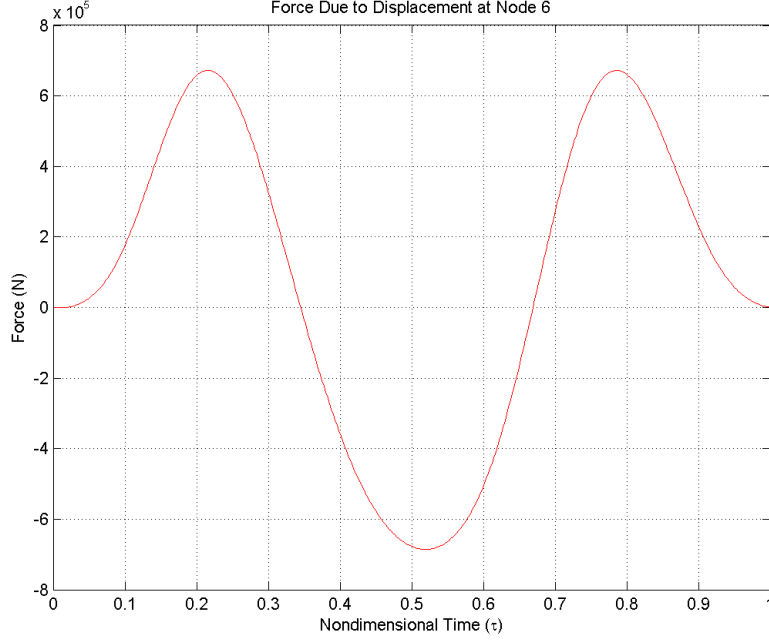
Figure 2.12:   Vertical Force Required to Move the Linkage at Node 6 for the Theoretical Displacements for All Time

Figure 2.12 shows what force is required for the vertical displacement. This is important for the comparison to the Hawkmoth since it will convey the level of emulation that the flapper possesses.

In order to compare the force to displacement that is exhibited by the inspiring specimen, it can be conceived that if one considers the force generated by the Hawkmoth muscles, and the displacement of the thorax, one could conceivably back out the displacement of the flapper under that force and compare it to that of the displacement associated with the flexing muscles. According to Tanner and Regnier [29], the maximum force that a Hawkmoth exerts during the flapping motion is:

$$F_{moth} = 1500 \ pN \tag{2.8}$$

54

The displacement of the thorax was measured via Photo-pixel measurement (discussed in the Residual Calculation section of this thesis) of a thorax that was still flapping after it was separated from the head and abdomen. The displacement associated is:

$$\Delta_{moth} = .29 \ mm \tag{2.8}$$

Placing F_{moth} into the force array at the position indicated in Figure 2.12 and keeping the displacement as a variable, the displacement of the flapper under that given force is:

$$\Delta_{flapper} = 2.466x10^{-9} \ m \tag{2.8}$$

Which is a far less from that of the Hawkmoth's displacement, indicating that the linkage presented in this study exhibits nearly no stiffness characteristics that can be seen by the inspiring specimen. This analysis does however bring to the forefront interesting characteristics concerning the boundary conditions associated with the possible FWMAV, or at least it is indicative of a suggestion of possible method. Though the DeLeón flapper does not mimic these characteristics, these results should not infer a 'de-validation' of the methods to be employed in this study as the displacement and kinematic properties were the crux of the flapper creation, and its construction was not meant for direct application.

2.6   PhotoModeler Methods

As mentioned in Chapter 1, the objective of this study is to capture the differences between deformed biological and engineered wings under simulated flapping conditions. The methods of comparison or quantification however proved to be a problem due to the fact that one cannot simply compare by 'looking at the picture' without some form of assurance that the observations made are quantifiable. The aim

of this study is to make the results measurable and repeatable; and the methods of data gathering should be standardized and easy to mimic. The methods employed by Willmont and Ellington [27] shed light on the concepts of image comparison, wherein several images were taken at various angles to effectively 'triangulate' the three dimensional position of the reference points on their wings. This study aims to execute a similar process of quantification, wherein images of flapping wings will be observed via several photos. Several reference points were applied to a flapping wing and their positions were triangulated via PhotoModeler to generate their three dimensional positions in space. This principle of triangulation is the fundamental principle of a method of three dimensional visualization from two dimensional images known as photogrammetry.

> By taking photographs from at least two different locations, so called "lines of sight" can be developed from each camera to points on the object. These lines of sight (sometimes called rays owing to their optical nature) are mathematically intersected to produce 3-dimensional coordinates of the points of interest [2]

These mathematical operations essentially create a model of the camera's "interior orientation parameters" which are quite a bit more complex than simply stating a range of real world tolerances and units related to manufacturing of cameras. In order to overcome this complexity, standardization of the camera's parameters is necessary, and this is done via a process known as **calibration** which derives these unseen parameters that the camera has inherent in its system so that the algorithms for visualization can determine and implement the qualities of 'how truly straight' the line in physical space is mapped to the camera's charge-couple device array (CCD array). The CCD array is essentially the light sensing device that the camera uses to convert images and lines in the physical world into intelligible images in the computational (camera's) world.

Simply stated, as light enters the camera, what was a straight line in physical space may not necessarily be a straight line on the CCD due to some distortions of a lense or camera misalignments. The process of camera calibration essentially will tell

56

a photogrammetry package how to "correct" for these distortions so that a straight line in the real (physical) space will be a straight line in the camera's computational space; effectively feeding the algorithm a detailed list of tolerances to be effectively accounted for during the 3D solution. This represents a transformation process from physical to CCD coordinates.

Though crucial, having a calibrated system is not enough to generate a three dimensional set of coordinates. It is inaccurate to simply judge an objects three dimensional characteristics with just two dimensional information. To account for this, it is possible to apply what is on one's face- be it that of the human eyes. Without two of them, depth perception is limited and the brain has trouble deciphering these three dimensional qualities inherent in an image. With two eyes however (binocular vision), one may gain insight into how the brain will back out depth by 'referencing' the same points from two different angles of perception (the separation of the eyes). The further an object is from an observer, the more difficulty they will have in deciphering the three dimensional characteristics.

Photogrammetry attempts to mimic this process of three dimensional processing by employing similar methods of characterization. The initial data input (i.e. 2D points or similar elements registered across multiple images) is then passed through a very sophisticated iterative statistical analysis known as free network bundle adjustment [3]. This process creates a final solution that has "accuracy qualities that are more than the number of pixels in the photographs" [3]. By taking multiple images at different angles as demonstrated in Figure 2.13, one may reference points of interest across the several photos taken. More than one reference point is necessary in order to fully determine the three dimensional characteristics. By referencing the points, the software will determine the position of the camera per picture. With these positions known, the photogrammetry software can back out the three dimensional positions of the reference points. Using these reference points as a 'skeleton' for the 3D image, it is possible to perform an operation known as dense surface modeling (DSM)) which will assign a 3D position to each pixel in each picture. It is safe to say that the more
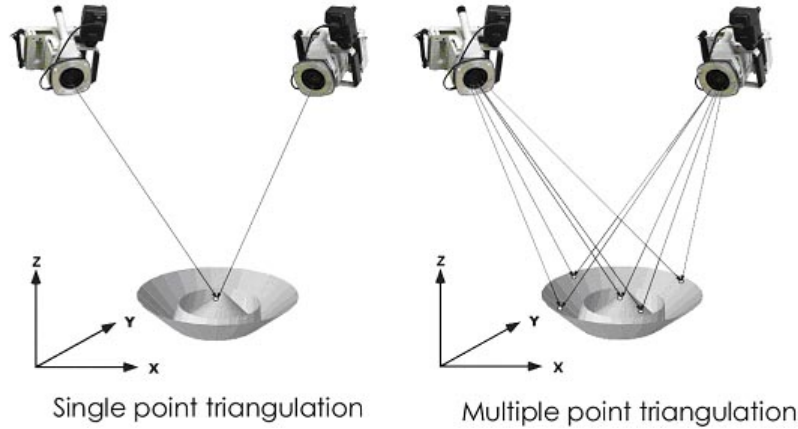
Figure 2.13:   Illustration of Triangulation [2]

pixels present in the system, the more points will be available for the 'point' could created from this process.

These methods were also seen in the work of Combes and Daniel [26] (See Figure 1.21) who inspired Aaron Norris [1] (See Figure 1.11) to make his move into the photogrammetry world. As is evident from Figure 1.21, Combes and Daniel were not required to 'determine' the camera positions as they were already known and standardized for their test. Aaron Norris took a different approach; for keeping the cameras in a fixed position severely limits the images that could be captured. This limit is imposed by the ability to see the aforementioned reference points- as in every photo their exists these points of reference- across multiple photos all reference points must be intelligible and identifiable. Combes and Daniel's fixed system disallowed them from capturing all images for a deflected wing as a deflection may hide the reference points placed on the wings. Norris [1] found it more pertinent to utilize a commercially available photogrammetry tool known as PhotoModeler©by Eos Systems Inc [3] (See Figure 2.14). This software includes all the aforementioned qualities of photogrammetry.

As can be seen from Figure 1.11, Norris employed the DSM features available through the program to generate his images. Norris found it pertinent to process 4 images to obtain a fuller view of the intended image set. Although more accurate,
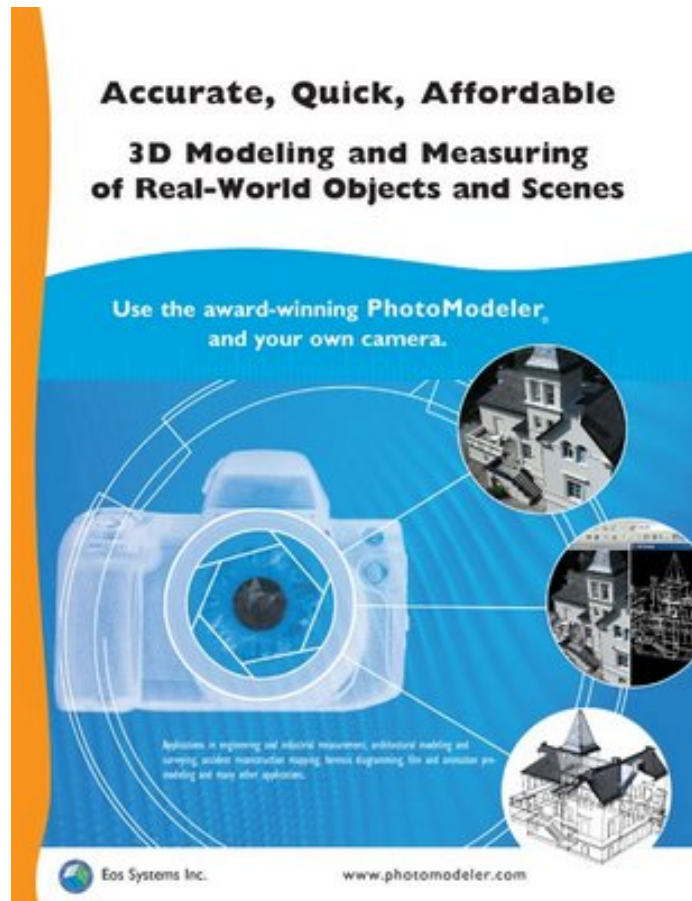
Figure 2.14:   PhotoModeler Scanner [3]

PhotoModeler claims that two pictures is often times sufficient for a solution; an in some cases, just one picture is necessary [3]. Norris' intent was to eliminate as much variability as possible, referencing the exact same reference points at close to exact phases, however there did exist one issue: Camera position. The camera position when an image is captured is crucial when performing tasks such as this. The DSM feature references the pixels inherent to an image- and even the slightest change in lighting or angle of capture will essentially shift the pixels. When the point cloud was generated; and three dimensional image was in fact generated however the standardization of specific points associated with the DSM cloud is almost nonexistent due to the sensitivity of the pixel positions. Point 1 on one DSM cloud may not be in the same position as point 1 of nearly the same image if the camera was slightly

moved or conditions changed at all. Fortunately, the 3D images allowed Norris to make comparisons between deflections as seen in Figure 1.11, however quantitative comparisons were difficult to infer.

Instead of relying on the DSM cloud, for this particular study the three dimensional positions of the reference points attached to a flapping wing will be examined and analyzed. Reference point application will be discussed further in Chapter 4, however their presence and standardized locations mandates yet another aura of confidence in the values obtained due to the fact that no longer will the positions of quantitative data be based on 'computational estimates' based on a cloud of pixels. Examining the orientation and shape of a deformed object relative to both fixed (non-translating reference points on the base not associated with the wing) and moving (reference points attached to the wing) reference points allows for more direct comparisons with a higher confidence. This owes to the fact that their exists a certain element of control associated with the mandation of the reference points. This fact was realized by David Curtis [30] who used laser projection to create the reference points on his wings (eliminating the issues seen with Willmont and Ellington [27]) and eliminating the usage of DSM.

It should be noted that in photomodeler, the concept of **perspective** is crucial. This was an issue during preliminary tests wherein irregular or aberrant wing geometries and point orientations were observed. Figure 2.15 sheds light on the comparison. The only difference between Figures 2.15b and 2.15a is that Figure 2.15a was constructed using photographs that more accurately captured the resolution of both the longitudinal and latitudinal directions.

If one were to take several photos of a wing in a horizontal line, the resolution along that line (in the horizontal direction) will be high, to the point of perhaps even capturing twist and deformations, however the length of the wing would be incorrect as the program had no way to gage the distance in that direction. For this particular study, it became necessary to consider a compromise between accuracy and resolution
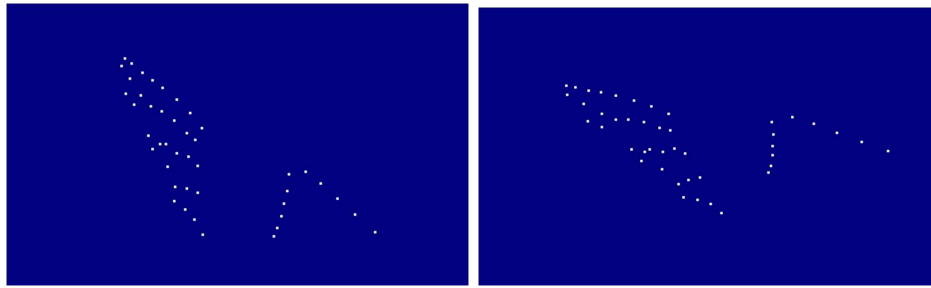
(a) Correct Perspectives   (b) Incorrect Perspectives (not enough)

Figure 2.15:   Examples of Different Perspectives in Photomodeler

in the following manner: There are to be 3 pictures taken instead of 4. This drastically reduces the amount of time required to spend with PhotoModeler as well as allows for resolution in all three dimensions. Figure 2.16 sheds light on what a typical data set would have to exhibit from an application standpoint.
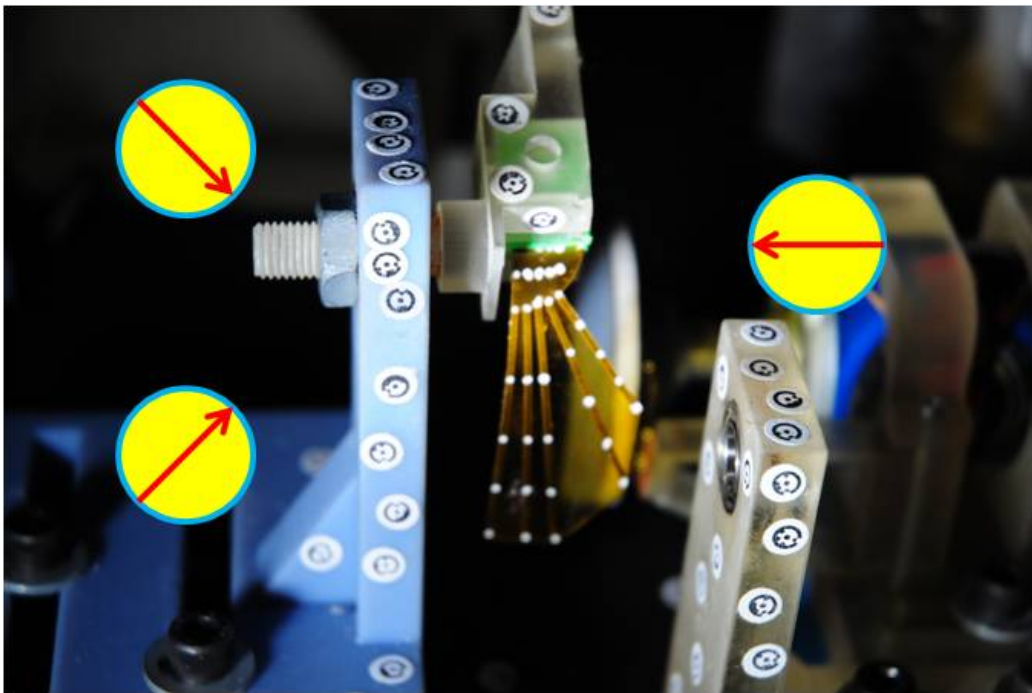
Figure 2.16:   Example of Necessary Photo Locations

In Figure 2.16, the yellow circles indicate the necessary locations for photo capture. The red arrows within the yellow circles indicate the direction of the lense

while the picture was taken. It can be seen that this method of data capture allows for resolution in all three dimensions; the left hand circles allow for depth of field and the right hand shot allows for resolution across the body of the wing and is essential in capturing twist. This in conjunction with the other two also allows for the capture of the depth/thickness qualities, which luckily for this study matter little since the objects of investigation are essentially flat.

It should be restated here that the purpose of this investigation is to characterize and compare the response of a manufactured wing as it compares to the inspiring specimen. The method of execution will require the investigation of the three dimensional qualities inherent in the deformed wings- and the tool to be used is photogrammetry of standardized positions along the flapping path. These images and their resultant three dimensional abilities will end up being the most conducive to the purposes of this project- capturing both response to flapping and the associated dimensions of the specimen in question.

2.7 A Word on the Effect of Reference Points on the Wing

As will be seen in the following chapters, reference points will be required to be placed on a wing for the purpose of the photogrammetry process mentioned in the previous section. It is necessary to consider the effects that these reference points will theoretically have on the structural properties of both the engineered wing and the biological wing. Combes and Daniel mention that in order to consider the presence of the reference points to be negligible, the overall weight of the applied points may not exceed 2% of the weight of the object in question. The effects of this addition cannot be ignored, so it is perhaps helpful to consider beam theory in terms of modal analysis.

The natural frequency of any linear beam (which is what the biological wing can be modeled as according to Norris et al [1] and Sims [4]) can be defined as such:

$$\omega_n = \sqrt{\frac{k}{m}} \tag{2.8}$$

Where [k] is the stiffness of the beam, and [m] is the mass. If one were to add 2% to the mass, the following effect would take place:

$$\omega_{nheavy} = \sqrt{\frac{k}{1.02m}} \implies \omega_n = .9901\sqrt{\frac{k}{m}} \tag{2.8}$$

Which has an effect of:

$$100 \cdot \frac{(\omega_n - \omega_{nheavy})}{\omega_n} = 0.9852\% \tag{2.8}$$

Thus adding a restriction of a 1% effect of the natural frequency of the object in question (if it is in fact linear).

2.8 Summary

This section served to convey a full understanding of the systems to be incorporated in this study. A new flapper was conceived in order to more closely mimic the kinematics of flapping inherent to that of the Hawkmoth by simulating the naturally occurring linkage design by replacing it with a Crank-Rocker four bar mechanism. The kinematics of this new mechanism were discussed as compared to the program used to design the flapper. Following this demonstration of the theory behind the rigid body analysis, the newly conceived flapper was compared to that of experimental data gathered from the flapping *Manduca Sexta* itself. A regression test was carried out in order to demonstrate the level of true resemblance as compared to previous flappers. As it turned out, the only area that the new flapper appeared to reign supreme was that of displacement. Velocities appeared close, however accelerations proved problematic.

In order to further verify the design of the flapper, the top four bar mechanism was compared to the muscular make up by executing an elemental force analysis; taking into consideration both the actual displacements and the force required to move them, and the biological as observed by a displaced thorax. This concept of the boundary condition proved an evermore daunting concept to consider as the interconnection between the rigid wing and the flapper, whether manufactured or biological, should attempt to closely mimic those exhibited by the true inspiring specimen. As Willmont and Ellington was the result of a visual observation of the angular displacement of the leading edge of the flapping wing with respect to a reference, this study will attempt to do the same. Needless to say, one can only consider the possibilities associated with the 'perfect' boundary conditions and the effect that their presence had on those observations.

The techniques associated with the topic of photogrammetry were discussed here, introducing the package known as Photomodeler as the tool for investigation. Following, the topic of the effect of adding mass to the investigated objects (wings) was considered, effectively quantifying the amount of 'leeway' associated with the addition of mass to the wings.

III. Manufacturing Methodology

This research is unique in that there are two separate areas that can be considered 'Methodology'. The first portion is the construction portion. The experiments associated with this research, though inspired by many (see Chapter 1) represents a completely new investigative process. Chapter 2 shed light on the concept of a biologically inspired flapping mechanism- which had to be constructed using modern methods of materialization. In addition to the construction of the flapping mechanism, a few of the test specimens had to be constructed and materialized. The construction of the test specimens re-introduces the concept of the 'iteration' that was seen in Chapter 1; specifically in Figure 1.2 wherein a circular patter can be seen when observing and identifying key components for the successful creation of a flappable/flyable FWMAV wing.

3.1 Initial Wing Materialization: 3D Printing

The initial method of production chosen to create the engineering wings was that of rapid prototyping. The first machine utilized was the Eden 500 and Connex 500 from Objet. Eden 3-D printing systems produce three dimensional models designed with most 3-D computer aided design (CAD) tools and with other job-specific 3-D applications [31] [20].

Material	Tensile Str (MPa)	E (MPa)
FullCure™720 Transparent	60	2870
FullCure™840 Vero Blue	55	2740

Figure 3.1:   Connex 500 Dual 3D Printer and Ink Properties

The process of 3-D printing begins with the three dimensional model, to be generated by a computer-aided design program. For this particular study, SolidWorks 2010^{TM} was chosen as the CAD program of choice. The designed object can then be introduced to the Objet software in order to generate a physical model of the designed structure. In order to do this, the printer itself is loaded with a variety of polymers (in the case of Objet products, the material is a resin photo-polymer) in liquid form that exhibit a variety of physical characteristics as shown in Figure 3.1. These liquid polymers can be mixed together in order to form composite materials to cater towards the specific structural needs [31] of the object to be generated. These polymers are then applied by the printer heads at a resolution of up to 16 μm, granting a high level of detail of the modeled objects. This high resolution is crucial, especially when dealing with small scale objects such as the engineering wings.

The layer of applied polymer is immediately cured via an ultraviolet light mounted on the printer head, in order that the 'ink' can be cured with every layer without sacrificing time to dry. This layer-by-layer process is an example of additive manufacturing with is both quick and affordable, thus making this process ideal for initial MAV wing manufacturing. Additionally, the ink itself can be considered isotropic- thus eliminating one element of complexity.

The first wing formed was designed with the inspiration in mind in both size and vein geometry, however it lacked the two dimensional geometry that can be seen in the vein structure; emulating a more simplified version. Figure 3.2 shows the basic structure and the picture of this wing.

It is evident from Figures 3.2a and 3.2c that the vein design is inspired by the biological vein design in that fillets were used to recreate/simulate the optimized- off set geometry. As it turns out, this design's moment of inertia is optimized for forces acting normal to it. The only issue with this design was that it was not hollow as is the biological veins, nor is it fluid filled. The only reason for this is that it was that the hollow design was both impractical and impossible for the manufacturing

66

(a) Biological Vein Design
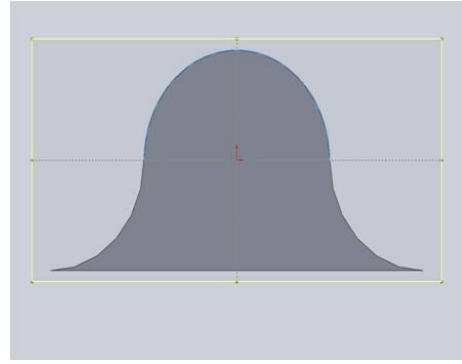
(b) Manufactured Vein Design
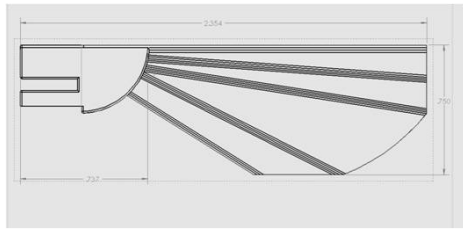
(c) Initial Wing Design
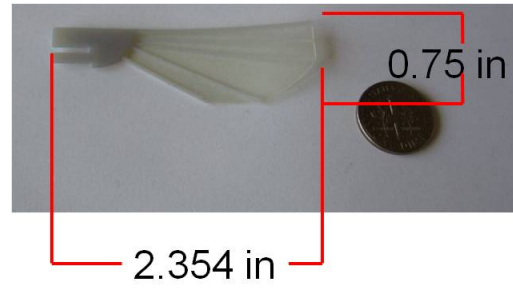
(d) Initial Wing

Figure 3.2:   Initial Wing Design

methods (which was the 3-D printer). Due to the capabilities of the Connex 500, dual materials were to be used in the construction of the wing. The materials used were the FullCure 720 Transparent (Membrane) and the FullCure 840 Vero Blue (Vein).

As can be seen from Figure 3.1, the materials in no way emulated those inherent in the biological design (See Figure 1.13). Additionally, these materials proved all too dense and thus the wing was not able to survive flapping. This contributes to the argument that Combes and Daniel [6] [7] [26], and Ennos [24] make that inertial properties have a far more significant effect on the deformations inherent in a wing than do aerodynamic. Unfortunately this wing was not subjected to flapping in vacuum as it would break in air; and according to Norris [1], the absence of air would further amplify the deflections exhibited by the flapping wing.

3.2 Wing Materialization: Laser Etching with New Materials

It was determined that the first attempt at the wing was an 'overstep' for the first iteration of manufacturing as it failed to survive flapping and it did not exhibit many of the characteristics of the inspiring design save for size and wing thickness. Additionally, the wing shown in Figure 3.2 had a mass of 183 mg; almost three times that of a freshly removed Hawkmoth wing. This high mass and lack of survivability lead to the conclusion that the first wing needed to be re-evaluated. It was determined that perhaps it was necessary to remove one of the characteristics of design in lieu of exploring new avenues of manufacturing. The first quality removed was its three dimensional characteristics, i.e. the vein geometry. Considering that the original design did not exhibit the hollow veins (nor the lofted vein geometry seen in Figure 1.8), it was determined that the filleted design contributed nothing but weight, making the wing 'too bulky' for actual application in a MAV.

Instead of printing on a 3-D Printer, where materials were limited and isotropic at all times, it was conceived that new avenues of application could be explored in the realm of laser etching. Cutting out geometries on a laser etcher is considered both controlled and exact; owing to the fact that provided a quality laser and standard input. Figure 3.3 depicts two of the iterations; a stainless steel wing and a carbon-fiber weaved wing. Both were cut out on an Epilog Fiber Mark 45 Watt CO_2 laser (provided by OHARARP LLC).

The cutouts depicted in Figure 3.3 represented the new step in the manufac-turing process. Both were covered with a Kapton tape (50 μm thick) that was used to represent the membrane. Though it in no way represents the material properties of the biological-protein based membrane found on the Hawkmoth, it proved easy to handle in that it did not melt when subjected to laser cutting. The only foreseeable issue with this however was the fact that one side was covered completely in the adhesive glue. This posed a problem since the mere presence of the glue added un-necessary weight to the wing, and in addition, the glue had the tendency to capture
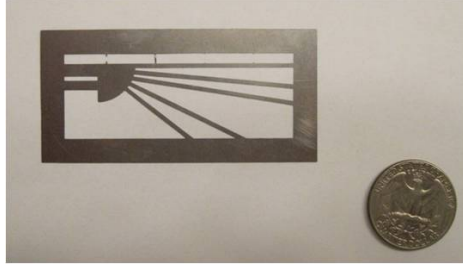
(a) Stainless Steel Wing
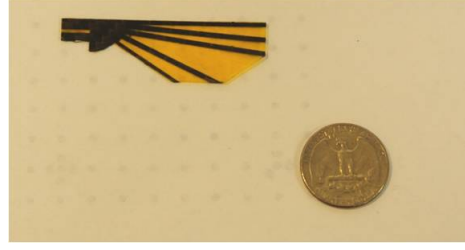
(b) Carbon Fiber Design
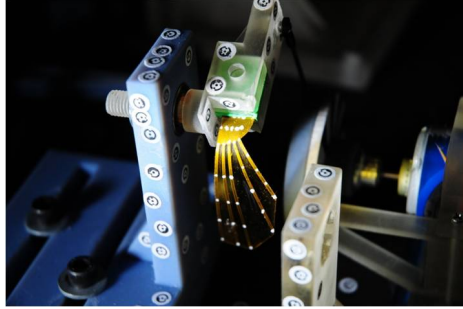
(c) Stainless at 12 Hz
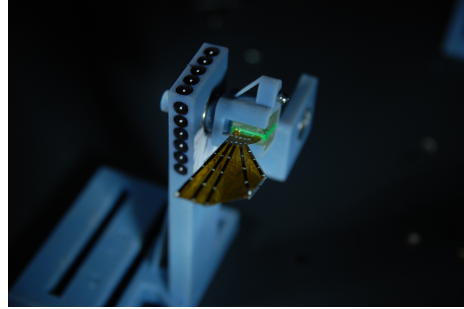
(d) Static Carbon

Figure 3.3:   2D Laser Cut Out Wings

small particles and oils after handling- making the weight of the wing change and essentially become heavier as time went on.

Both wings were subject to flap testing and their response in no way exhibited the response of the biological wing in that they were too heavy (225 mg for the stainless steel wing and ˜ 130 mg for the carbon fiber wing) and not stiff enough. In fact, the stainless steel wing had the tendency to plastically deform when subjected to flapping frequencies over 17 Hz. The carbon fiber wing appeared to survive the flap testing, but as it was already mentioned, it was too heavy and impractical for MAV applications.

With the stainless steel wing out of the picture, the carbon fiber wing's properties proved intriguing as it was the lightest of all previous attempts and it was able to survive flapping at 26 Hz in air. The natural frequency of the first mode for the carbon wing was $\cong$ 23 Hz, (See Figure 3.4) which is not stiff enough when compared

to the 60 Hz first bending mode (in air) of the biological wing. This material consideration paved the way into a new regime of manufacturing in that it was possible at that point in time to truly consider the level of inspiration gained from the inspiring specimen. It became apparent that far more could be considered in terms of the geometry exhibited by the Hawkmoth.

	FEA	EXP
Mode 1	25.3 Hz	26.75 Hz
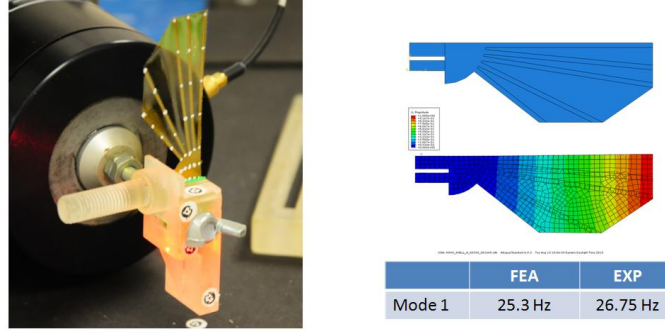
Figure 3.4:   Modal and FEA Analysis of Carbon Fiber-Kapton Wing

Combes and Daniel [6] suggested that the shape of the wings does not necessarily contribute to the stiffness, rather it contributes to its overall dynamic behavior. This of course re-opens the discussion of the aeroelastic question; as to whether or not the wing deformations in the naturally occurring-flapping fliers find themselves dominated by inertial or aerodynamic effects. Furthermore- initial flap-testing of these preliminary wings (which as aforementioned exhibited no dynamic qualities when compared to the inspiring specimen) brought into the picture yet another question: is the deformation of the wing observed on the insect while in flight actively or passively controlled? Logic would state the the shoulder joint on the insect flaps the wing in such a way that the 'paddling' motion seen in Figure 1.5 is actively controlled by some sort of special linkage or muscular input.

As it turns out, preliminary testing of a separated wing on the DeLeón flapper (which as will be seen exhibits a clamped boundary condition similar to that of Sims [4] and Norris [1]) observed the natural aforementioned motion seen on the biological specimen. This opened a new door that held within it considerations of the vein geometry. As was seen in Figure 1.5, the leading edge appears to lead the rest of the

wing as if the specimen was treading water. It was clear in the observations on the DeLeón flapper that the wing already exhibited this behavior (even in vacuum) placing even more emphasis on the overall 'vein geometry' issue. It was thus determined that the two dimensional geometry of the wings was worthy of emulation and consideration.

3.3 Wing Materialization of Final Design: Etching with Biologically Inspired Geometry

Norris *et al.* [1] found it pertinent to characterize wings by their natural frequencies (See Table 1.3) and he strongly felt that this method of characterization was crucial to the identification of the key parameters that would allow a wing to behave as it did. It was deemed pertinent to consider the same approach for the analysis of the engineered wings. Though Norris separated his wings further up than in this analysis (as this analysis takes into consideration the shoulder as well as the wing as seen in Figure 3.5) a Polytec Scanning Laser Vibrometer (SLV) was utilized in this analysis. The clamped boundary conditions employed by Norris will be the same in this analysis (to be discussed later) as was in his (which can be seen in Figure 3.6).

(a) Norris Cut Location [1]   (b) Shoulder Included
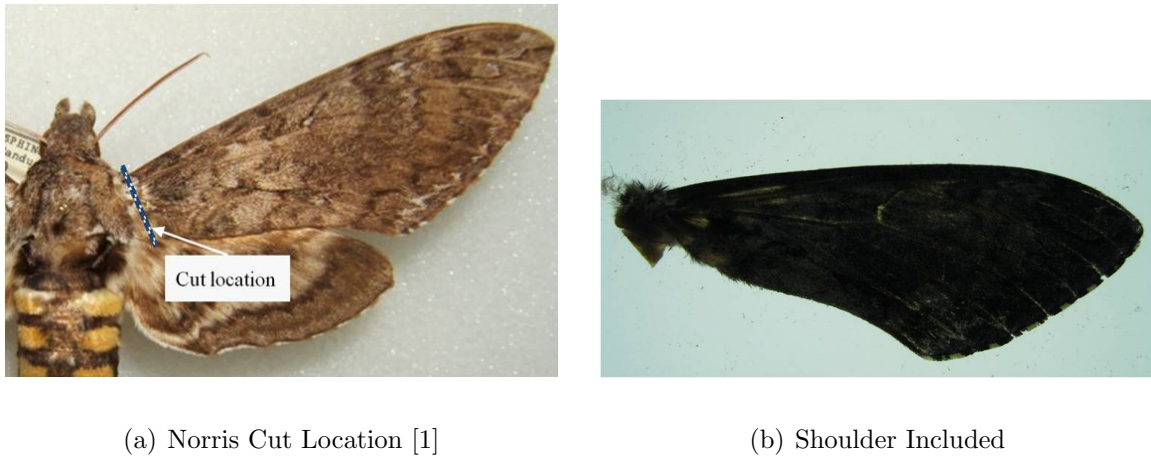
Figure 3.5:   Comparison of Wing Cut Locations

It was deemed necessary to perform a modal analysis on the wing to be tested. as will be discussed further later, the scales of the Hawkmoth wing were removed

71

Table 3.1:   Modal Analysis of Different Cut Points on Biological Wing (With Wing Scales)

Wing	1st Mode (Air)	2nd Mode (Air)	1st Mode (Vac)	2nd Mode (Vac)
Norris Wing	59.75 Hz	84.0 Hz	85.0 Hz	105.0 Hz
DeLeon Wing	46.86 Hz	84.38 Hz	84.4	152.5*

(which contributed to 4.8 mg of the mass of the wing according to testing) and reference points were applied. It was at this point where the vibrational analyses were carried out. The most basic results of this study are shown here*[1] in Table 3.4, which tabulates the modes as found for a biological wing freshly removed with wing scales still attached. Appendix E shows further results of the modal analyses for this study.
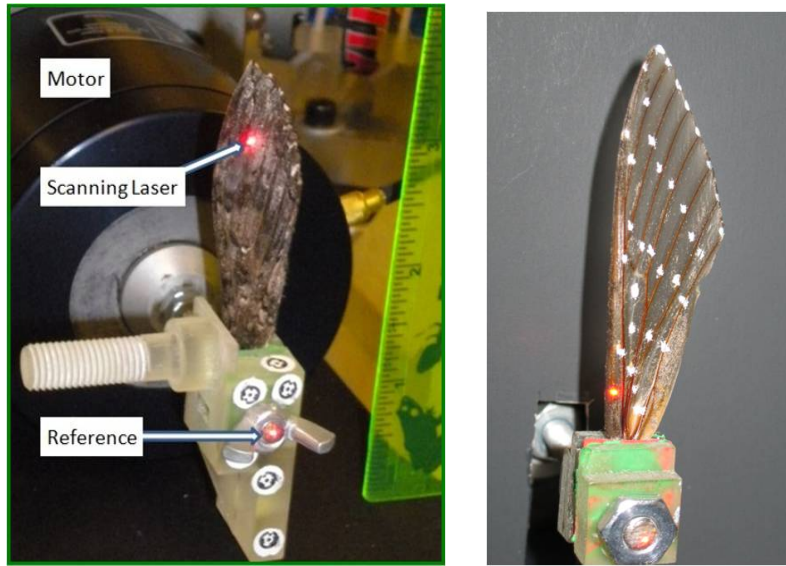
(a) Norris Modal Analysis [1]   (b) DeLeón Analysis

Figure 3.6:   Comparison of Modal Analyses

To consider the 2D geometry of the wing formation, it was necessary to employ digital photographs of removed *Manduca Sexta* wings; which gave a detailed repre-

---

[1]Mode 2 in vacuum of the shoulder-included wing is questionable as it lies far from the findings of Norris and exhibits qualities of the fourth mode (BiSaddle)

sentation of the vein geometries and formulations inherent to the natural design. In order to capture standardized and quantifiable data relating to the vein geometry, it was necessary to utilize a process employed by O'Hara [21] in which a MatLab program was written that allowed for the selection of vertices that corresponded to key points along the vein geometry. This process can be seen in Figure 3.7

(a) Original Wing Image

(b) Selected Points Along Vein
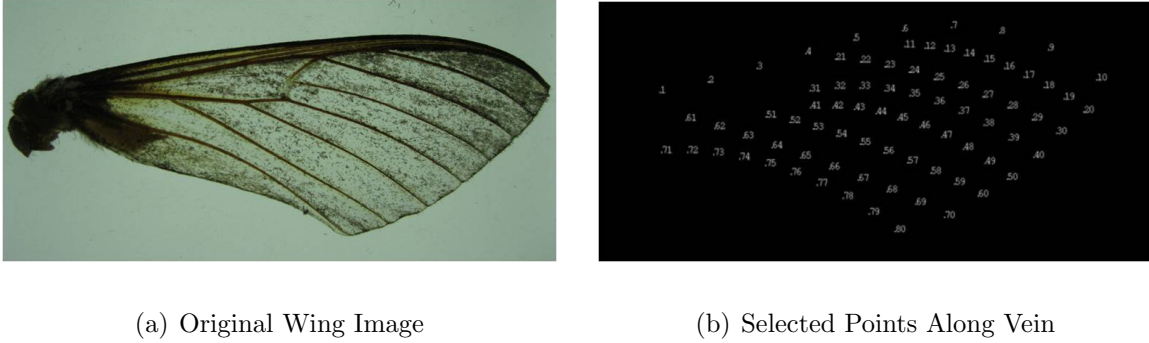
Figure 3.7:   Verticie Selection of 2D *Manduca Sexta* Forewing

These vertices could then be connected by third order spline-fitted lines (as that is the highest order allowed by MatLab)- which in turn created construction lines for more lines that would represent the varying/lofted vein thicknesses. This process can be seen in Figure 3.8 in which the lines have been connected from Figure 3.7b and then those were given thicknesses to form a total wing geometry.

(a) Connected Lines

(b) Thickened Lines
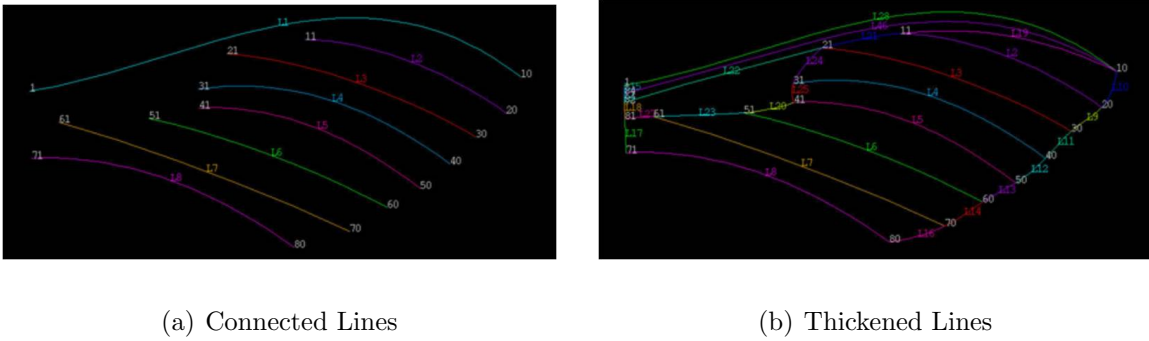
Figure 3.8:   Vein Formation of Hawkmoth Forewing

73

The newly formed wings could then be connected by a 'digital membrane' which would give an idea of what the wing would look like in its entirety. The information here could either be exported to Abaqus (for FEA analysis as was done by Combes and Daniel [7]) or into SolidWorks which could form a 3D representation of the newly formed vein geometry as is represented in Figure 3.3.

(a) Full Wing

(b) SolidWorks Vein Structure
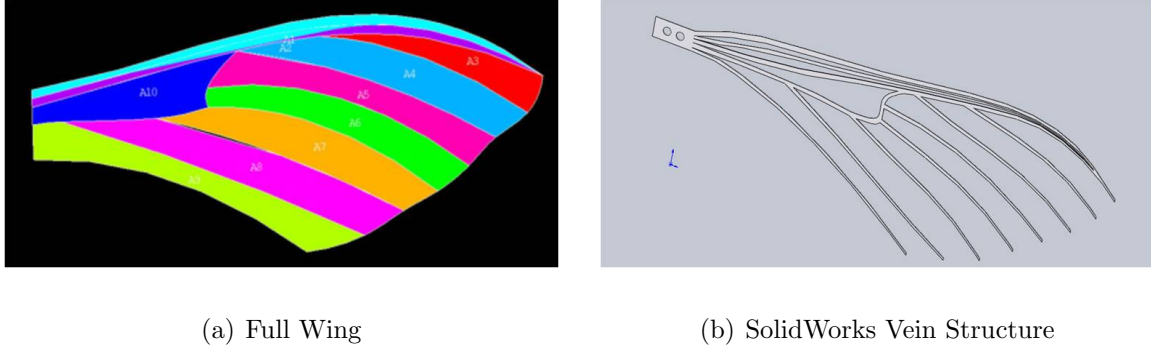
Figure 3.9:   Final Formations of Vein Geometry

The root formation of the newly formed wing proved to be rather problematic due to the fact that it was necessary to attempt to mimic the naturally occurring root that could be clamped without introducing any variability into the system. Figure 3.9b represents a preliminary attempt at this standardized formation. The holes at the bottom are meant to slide onto dowels that were created as a part of the clamp that would hold the wing during testing. This would disallow any rotation and it would ensure that the wings would be clamped at the same place every time. Figure 3.10 depict the clamped boundary condition that was held constant throughout the testing performed for this study.

The materials to be utilized for the final wing design included both carbon (single layer and multi layer) and stainless steel (despite its distinct lack of performance abilities observed on the previous wings). The wings were cut using lasers supplied by both OHARARP LLC (steel wing) and Mound Laser Figure 3.11 shows both of these wings that emulated this 'strictly biological' design. The material chosen for the membrane remained Kapton tape, however the thickness was only 40 μm. The

(a) Clamped Carbon-Kapton Wing (Top)
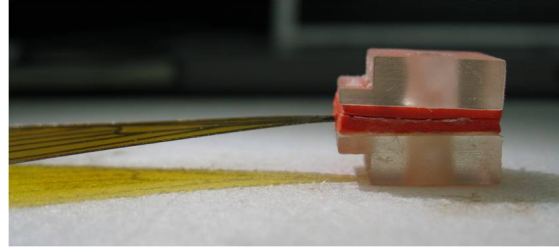
(b) Clamped Carbon-Kapton Wing (Side)

Figure 3.10:   Clamped Wing Boundary Conditions
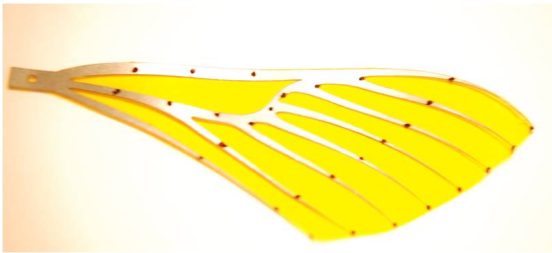
(a) Stainless Steel-Kapton Wing
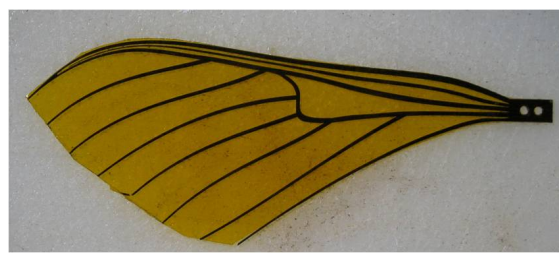
(b) 3 Layer Carbon-Kapton Wing

Figure 3.11:   Steel and Carbon Wing Formations

carbon wing was first constructed using a single layer of uni-directional cured carbon fiber. The fibers themselves ran the length of the wing in the span wise direction. Though light, this wing proved far too delicate for testing, and so it was determined that multi-layer carbon fiber was the most logical for application for this iteration of wing design.

All three layer carbon utilized for this study was arranged (and cured at 350 degrees) in a 0-90-0 formation and the total thickness was .25 mm (Carbon provided by Dr. Parker of AFRL/RB). This would in turn mimic the properties of an I-beam. Conveniently, the I-beam has similar properties as that of the original vein design in that the structural behavior of this formation allows for the most efficient design wherein the moment of inertia is optimized about the interface between the vein and membrane. The following table details some of the properties of the wings discussed

here. Each wing was marked with 27 randomly placed reference points on each side using hand-placed dots made with a silver $Sharpie^{TM}$:

Table 3.2:   First Biological Wing Properties

Wing	Weight (UnMarked)	Weight (Marked))	1st Mode (Air)
Carbon	71.3 mg	74.4 mg	43.43 Hz
Steel	160 mg	161.3 mg	30.00 Hz

As expected, the stainless steel wing was not able to perform well under flapping conditions as it would plastically deform and break at the base. Unfortunately, though the carbon-Kapton wing was both light and designed with bioinspiration in mind- it too proved to be too delicate for flapping and would break (as shown in Figure 3.12) when subjected to frequencies above 10 Hz in vacuum.
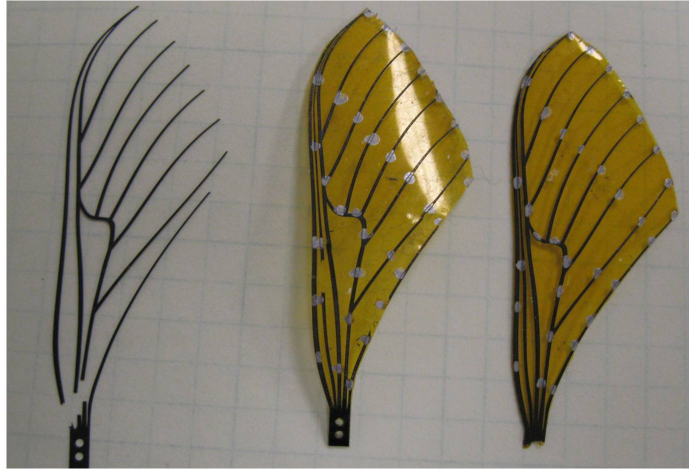
Figure 3.12:   Broken Carbon Fiber Wing

As can be seen in Figure 3.12, there existed some issues with the wing setup. First and foremost, the leading edge of the Hawkmoth wing, though it does in fact consist of three separate veins fused together (as can be seen clearly in Figure 1.8). It was determined that rather than separating these veins, it was possible to treat them as one. Secondly, as can be seen from the right most broken wing in Figure 3.12, the failure occurred where the clamp holes had been placed. Three separate wings of the exact same design were flap tested to produce the same resulting failure point: the point at which the first guide hole began. It was conceived that the presence of this

76

hole in the area of high stress had to be eliminated if these wings were to be able to flap successfully without sacrificing the previously discussed need for standardized positioning in the clamp. It became necessary to design a new base that would allow for this attribute. A third issue that is unrelated to the failure of the wings shown in Figure 3.12 was that of the geometry of the trailing edge. As can be seen in Figure 3.7a, the trailing edge of the biological wing does not end with the presence of a rigid vein, rather it ends with a flexible membrane. It was conceived that this may in fact contribute to some important dynamic attributes and thus the presence of the 'extra trailing edge membrane' was mandated. To do this, it was necessary to obtain measurements of the geometric properties associated with the trailing edge. Following, it was conceived that a 9th, removable vein would have to be placed at the trailing edge to act as a guide when constructing the wing- to be removed after the membrane was applied and cut out (using a hobby knife) to preserve the presence of the true trailing edge. Needless to say, the aforementioned changes were applied to a new (final) wing geometry, which can be seen in Figure 3.13
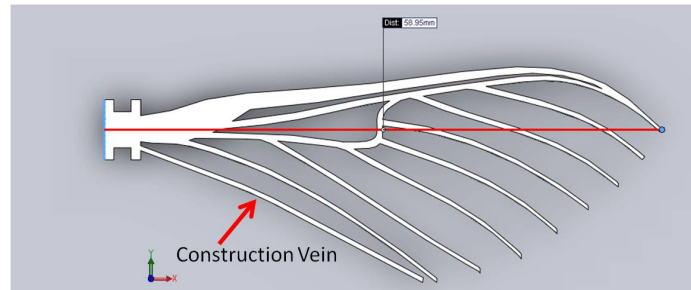
Figure 3.13:   SolidWorks Representation of Final Wing Design

This wing was cut out using an Epilog 30 Watt CO2 laser with the .25 mm 3-Layer carbon that was used to construct the last design. Furthermore, it was decided that new, thinner Kapton should be used in lieu of the Kapton tape- as the presence of the already applied adhesive added extra- unnecessary weight to the system. Instead, new 20 μm Kapton film was utilized. Several avenues for adhesion were explored from $Elmer's^{TM}$ glue to cyanoacrylate- both of which worked in adhesion, but failed to stay attached when the wing was subjected to flapping. It was discovered that the

most successful of adhesives was $3M^{TM}$ 45 spray on adhesive- that was sprayed into a small container and then applied by hand in thin layers via a painting brush along all of the veins on the carbon fiber. Not only did this method eliminate the need for extra-unused adhesive to be present on the membrane, but the adhesive also lasted flapping in both air and vacuum. Following adhesive application, the membrane was applied and cut out around all of the veins. Once this was completed, the extra construction vein was removed. This process can be seen in Figure 3.14

(a) Carbon Wings Cut Out on Laser
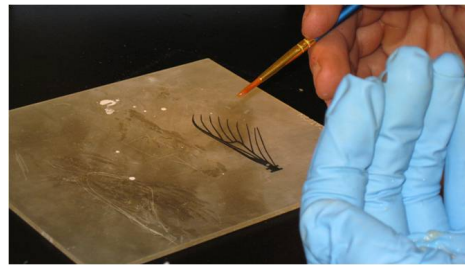
(b) Adhesive Application

(c) Membrane Application

(d) Removed Membrane

(e) Construction Vein Removal

(f) Finished Wing Without Reference Points

Figure 3.14:   Steps of Final Wing Construction

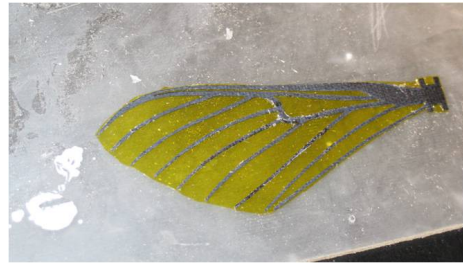It became apparent that in order to further eliminate variability in the experimentation, not only did wing construction methods need to be standardized, but also the placement of the reference points to be used in Photomodeler. It became necessary to construct a physical template or 'stencil' that would allow for consistent point placement on both the engineered wing as well as the biological wing. To do this, the Solidworks representation of the engineered wing was altered in that it also contained a sketch of where the marked points would go. This can be seen in Figure 3.15 wherein the red circles are where the eventual points would have to go. The stencil was cut out on piece of thicker, non-adhesive Kapton film on the Epilog 30 Watt Laser shown in Figure 3.3.
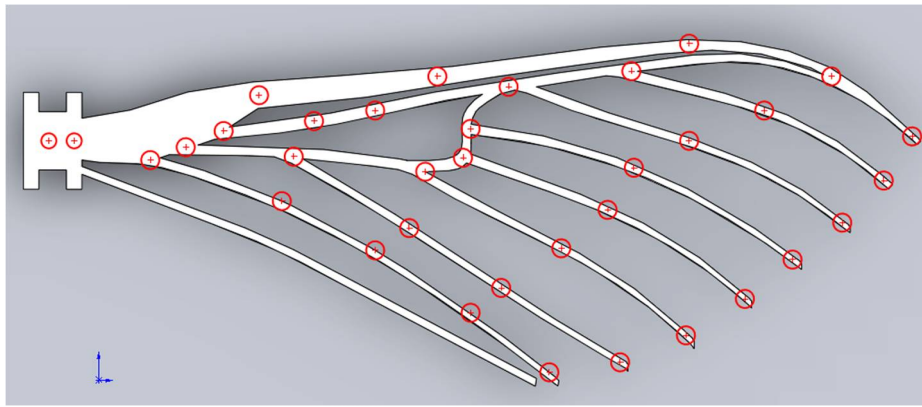
Figure 3.15:   SolidWorks Representation of Reference Point Placement

As was mentioned by Willmont and Ellington [27] in Chapter 1, the selection of reference point materials proved vexing in that a material had to be both light in color (for Photomodeler to recognize) yet it had to contribute to less than 2% of the total mass of the wing for their presence to be considered 'negligible' [26]. Additionally, a material had to be selected that would not only adhere to the Kapton and carbon, but also to the biological specimen- which was not an easy feat in and of itself. Needless to say, several avenues of reference point application were explored:

- Laser Dot Projection: Though this proved to be a non-intrusive form of reference point application (added no mass and thus did not effect modal response),

it would be difficult to accurately represent these points without having to re-adjust the position of the laser as the wing moved throughout the stroke amplitude. Curtis [30], who employed this method using high speed video to capture the displacement and movement of his flapping wings found it difficult to track all points on the wing during certain points of the flapping amplitude. Additionally, the reference points would translate on the wing surface as the wing moved due to the stationary nature of the projector (laser).

- Correction Fluid: White correction fluid ($WhiteOut^{TM}$) proved to be the most conducive for Photomodeler in that it was easiest for the program to recognize a marked point as a reference point. Though this was convenient for data gathering, often times these points weighed upwards of 5% of the weight of the wing (or on average about 3 mg) which pushes the overall validity of the experiment as the presence of the reference points would have too much an effect on the dynamic behavior.

- Fluorescence Dye: This dye responds to ultra violet light and is often used in the medical field, specifically in the realm of optometry, to observe corneal abrasions. When this substance is subjected to ultra violet light, or a black light, it reflects a 520 nm wavelength light which appears to glow. This would have been helpful to use since the due would dry out, contributing almost nothing to the mass of the system. The only issue was that there is no stroboscope that would omit a black light (that could be controlled) nor was there a lense that was big enough to act as a high-pass filter to only accept the aforementioned wavelength.

- Silver $Sharpie^{TM}$: This proved to be the least intrusive of the reference points as the marker has volatile properties that remove most of the mass of the marking upon drying. The only issue with this was that the solver was difficult to discern in the photographs for Photomodeler, leading to high, unacceptable residuals within the program. Additionally, the silver permanent marker still

found difficulty adhering to the veins of the biological wing and thus was deemed impertinent for application in this study.

- White $Sharpie^{TM} PAINT$ Pen: Similar to that of white correction fluid, this allowed for more control of the liquid as its delivery system was not in brush form rather it existed as a ball point similar to that of an ink pen. Unfortunately this material's behavior was similar to that of correction fluid in that it still proved to be too heavy and would often 'bleed' making the size of the reference points vary (often times making them too large for practical application). Additionally this paint would only adhere to the membrane of the biological wing, running off of the veins and refusing to adhere.

- $Pentel^{TM}$ WHITE 100WS Fine Point Marking Pen: This marking pen proved to be the only useful material for the marking of the reference points. Customer reviews state: "Perfect for creating eye-catching signs. Marks on nearly everything including metal, glass, plastic, rubber and most nonporous surfaces. Indelible and quick drying" which is an attractive quality for the purpose of marking. Additionally, this pen was not in the traditional form as it required small wooden 'nubs' that were included to act as the pen tip. This quality proved extremely useful and effective due to the fact that they could be sharpened for more precise marking. Additionally, these nubs worked through osmosis much like plants and required no movement across a surface as would a ball point pen- rather the ink was delivered as if dropped by a syringe. As marking progressed, the tips/nubs would become over saturated with the ink and dull- which required re-sharpening and/or replacement for more accurate reference point application. Figure 3.16 shows a picture of this product.

Luckily this style of marking adhered to both veins and membrane of the biological specimen. Furthermore, the ink had volatile properties much like that of the permanent markers, making it less intrusive to the dynamic qualities of the wings. As can be seen from Figure 3.15, there exists 33 points along the wing (on both sides) and this method of marking added a weight of on average 0.7

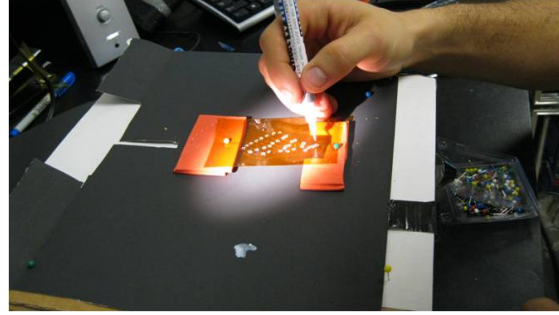**Figure 3.16:** $Pentel^{TM}$ WHITE 100WS Fine Point Marking Pen

mg. Though this was the lightest of all reference points (save for the permanent marker), none of the tested specimens weighed so little as to warrant concern with breaking the 2% limit for reference point mass.

Following the wing construction, it was necessary to lightly sand the completed wing. This was done in order to make the Kapton surface less reflective as this interfered in image processing in Photomodeler. Once sanded, the reference points could be applied. The Kapton stencil was suspended on pieces of red foam above the wing which lay flat on a solid surface. The suspension was necessary due to the fact that in previous attempts to apply the reference points, often excess ink would leak around the Kapton and spread onto the wing. The separation of the stencil film and the wing allowed the ink to stay attached to the stencil and not spread to the wing. This same process, which can be seen in Figure 3.17 was utilized for applying reference points to the biological wing- as it was necessary to do as much to compare to the engineered wing.

Though this wing proved itself when subjected to flapping, new carbon became available that was 25% thinner in three layers as the original 3 layer carbon (new carbon was .16mm thick as compared to the .25 mm thicker 3-layer carbon). Naturally, it was deemed neccessary to perform a vibrational analysis of the 'testable wings' to determine some of their intrinsic properties. The results of this would utimately

(a) Sanding of Completed Wing   (b) Reference Point Application

Figure 3.17:   Finishing of Wing Construction

Table 3.3:   Modal Analysis of Thick and Thin Carbon Wings

Wing	Weight) (UnMarked)	Weight (Marked)	1st Mode (Air)	1st Mode (Vac)
.25 mm Carbon	91.8 mg	95.3 mg	88.4 Hz	92.8 Hz
.16 mm Carbon	61.7 mg	62.0 mg	59.06 Hz	78.13 Hz
Biological (N)	N/A	N/A	59.75 Hz	85.0 Hz
Biological (D)	73.3 mg	68.5 mg	64.75 H Hz	120 Hz

(N)-Norris
(D)-DeLeón

determine whether or not is would be neccessary to stay with the thicker carbon or if the thinner carbon would more closely emulate the qualities seen by the inspirational specimen. Table 3.3 tabulates the comparison of these two different wings.

Considering the mass of a freshly removed and marked biological wing was found to be 63.3 mg and the first mode was 64.75 in air, it is clear that when considering Table 3.4 that the thinner wing comes closest to emulating the numbers seen for the biological specimen. Though the numbers are not exact, it is crucial to consider the aeroelastic question; that is the inherent effect of the presence of air as compared to that of its absence. When considering the biological wing, Norris found that there was a considerable change in modal behavior in the biological wing between air and vacuum. As seen in Table 3.3, the second, thinner wing appears to exhibit the same

Table 3.4:   Modal Analysis of Different Cut Points on Biological Wing

Wing	1st Mode (Vac)	2nd Mode (Vac)	1st Mode (% Effect)	2nd Mode (% Effect)
Without RP	58.13 Hz	80.31	-	-
With RP	57.81 Hz	80.63 Hz	.553	.397

air/vacuum dependency which leads one to believe that this is the closest as of yet to realizing the necessary structure for a FWMAV.
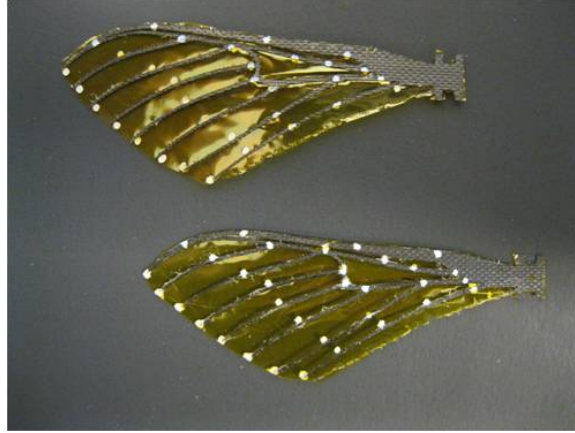

Figure 3.18:   Finished and Marked Carbon/Kapton Wing

In order to verify the lack of intrusion of the newly applied reference points, a modal analysis was carried out between the sanding and reference point application to yeild the following

This test in vacuum showed that the overall effect of the presence of the reference points on the wing was negligible per the discussion at the end of Chapter 2 ue to the fact that their effect yielded less than a 1% effect.

3.4   Biological Wing Separation Methods

In order to more accurately compare the response of the inspiring specimen to that of its engineered counterpart, it was necessary to standardize the methods associated with the removal of the wing. It is important to recall from Chapter 1 that there is a distinct time dependency associated with a removed wing. Both

Norris [1] and Combes and Daniel [6] [7] make mention of this issue in that the wing will essentially 'dry out' upon removal from the living creature. Both sources indicate that a wing can be deemed 'useless' within three hours of being removed in that its structural properties appear to stiffen and become more brittle, much like a tree branch that has been removed. Recent observations indicate that the wing actually begins to form an unnatural camber within 30 minutes of removal, which can be compared to that of a drying flower petal that curls when exposed to sunlight.

It can thus be stated that the methods of removal must be executed quickly in order to preserve the integrity of the wings properties. Opportunities present itself here for future study as to how to avoid such drying effects and/or preserve the wing's structural integrity after removal. In fact, attempts were made in this study to preserve said 'liberated' [1] wings by placing it into a moist environment; however this was met with failure (most likely due to the wing's natural tendency to repel water much like $Teflon^{TM}$). Needless to say, a standard time was set for the separation process in order to at least attempt to control/standardize these aforementioned time dependent effects. All following operations were executed within 30 mins- wherein flap testing began at the end of 30 minutes- as the following process took upwards of 23-26 minutes.

The first step in the removal process is one of humane treatment. Due to the fact that that the inspiring specimen is cold blooded and thus most of its functions/-consciousness is dependent on its surrounding temperature, it was deemed necessary to anesthetize the creatures in a freezer for 10 minutes. This did not kill the moth however it did place them into a dormant/unconscious state. This allowed for the removal process to be painless for the animal while still preserving the integrity of the wing. Figure 3.19a shows the anesthetized Hawkmoth. It can be noticed here that the moth has on it several hair patches on its thorax. It is necessary to remove these as it makes the dissection process much easier to control. Figure 3.19b shows the removed hair follicles- a process performed by carefully blowing compressed air at

(a) Anesthetized Hawkmoth   (b) Removal of Thoracic Follicles

Figure 3.19:   Dissection Preparation of Hawkmoth

the area of interest. Fortunately, the follicles blow off easily and offer little resistance to the compressed air.

Following this procedure, removal of the head and abdomen was necessary (as seen in Figure 3.20a). Head removal ensured that the animal was no longer living and the removal of the abdomen made the handling of the specimen far easier as the abdomen is coated with slippery, removable hair that made it difficult to secure. Unlike humans, though the head and abdomen were removed, functions within the thorax of the hawkmoth were still taking place- much like a lizard tail that twitches though it has fallen off. Though slowed by the cold temperatures, the nourishing functions performed by the thorax to the wings will continue for a short period of time, preserving the integrity of these wings. This small window was considered in order to remove the powder like scales that are present on the wing. Discussions in Chapter 1 revealed the difficulties associated with the presence of the scales in that they refused marking and often times would flake off during testing. In order to make yet another attempt at control, it was decided that the scales should be removed entirely from both sides of the wing. This was done by simply gently brushing the wings on both sides with a wet tooth brush. It was helpful to lay the wings on a flat surface while brushing the wings to ensure that the wing would not accidentally

(a) Removed Head and Abdomen   (b) Removed Wing Scales

Figure 3.20:   Dissection of Hawkmoth: Parts and Scales

break or fracture. Figure 3.20b illustrates the end of this process where both wings have been successfully cleared of the scales.

Following the scale removal, it was necessary to completely remove the wings from the thorax. This could be done by cutting the thorax in half with a dissection knife. Each half still contained both sets of wings (hind wing and forewing). The hind wing was removed from both halves of the thorax. The thorax halved could then each be halved themselves and then quartered- preserving the shoulder of the wing as shown in Figure 3.21a. Each wing was immediately rushed to an OHAUSE Voyager Pro Scale to be weighed. The weight was recorded for the right forewing, as that was the wing that would be investigated. Following this, the reference points were applied to the wing in the exact manner described in the previous section as shown in Figure 3.21b. The newly marked wing was then rushed back to the scale for another measurement of mass. This was done to ensure that the reference point presence did not contribute to the mass of the entire system more than 2%. If this were the case, the entire wing separation process would have to be repeated for a separate insect until the reference points were applied in such a manner as to not exceed the aforementioned limit. Immediately following, the Frequency Response Function (FRF) was obtained for the newly marked wing as seen in Figure 3.6 in air. It was concieved to obtain an FRF in vacuum, however the time it took for the

87

(a) Removed Wings   (b) Wing Marking

Figure 3.21:   Removal and Marking of Wings

system to reach a value under 1 TORR would have exceeded the time limit for the wing in question.

The final rendition of the wing was placed in the flapper for the rest of the experiment; to be flapped in vacuum and in air.
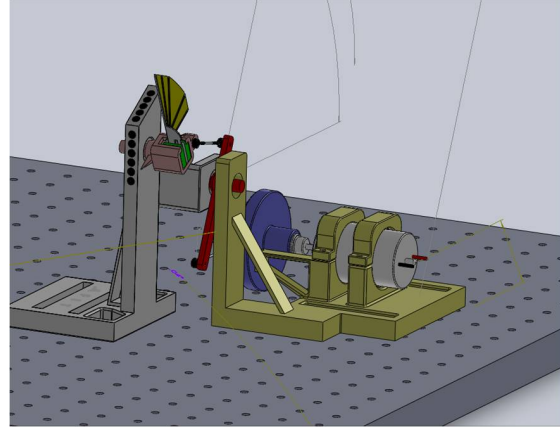

Figure 3.22:   Prepared Biological Wing

3.5   Construction of New AFIT Flapper

Chapter 2 shed light on the theory surrounding the construction of a new flapper that would attempt to mimic some of the kinematic parameters associated with the flapping of the inspiring specimen. It became necessary construct said system in order
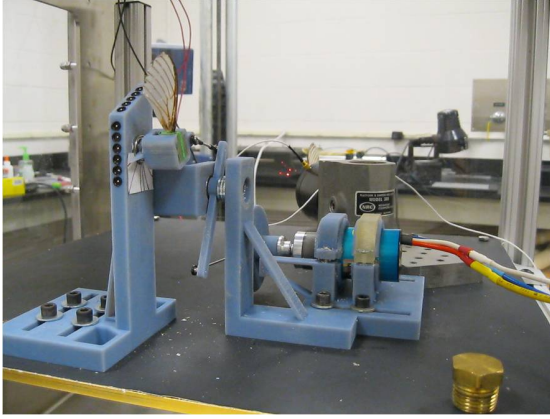
(a) Physical DeLeón Flapper

(b) Digital DeLeón Flapper

Figure 3.23:   Constructed AFIT Flapper

to carry out the operations of this study. To begin, it may be helpful to re-examine Figure 3.24 as it will aid in this discussion
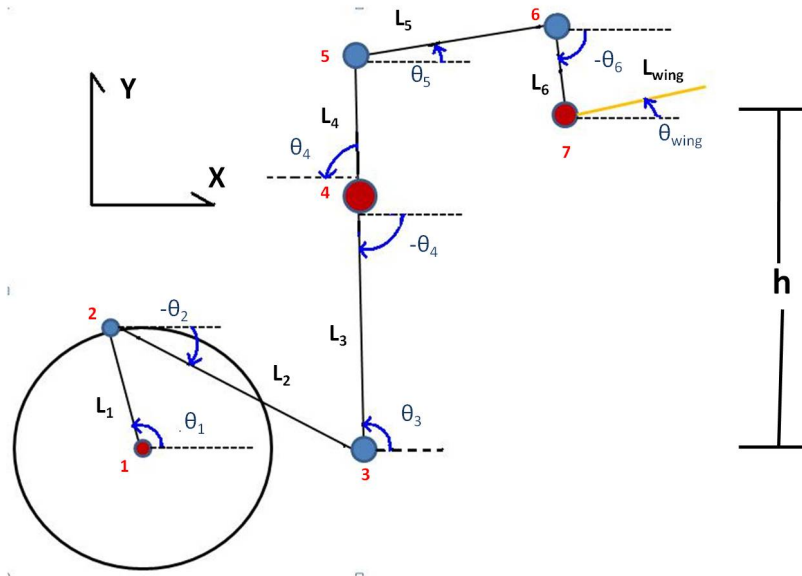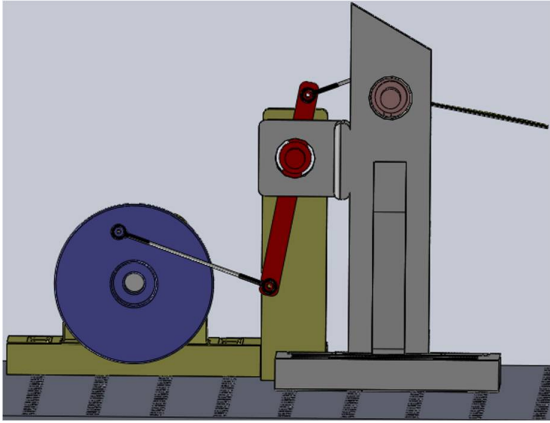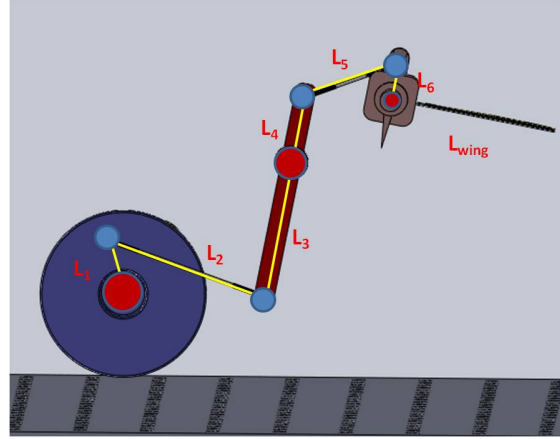

Figure 3.24:   Illustration of the Variables Associated With the DeLeón Flapper

Upon observing Figure 3.25, it may not be clear as to how the flapper may mimic the setup shown in Figure 3.24. Upon closer inspection, perhaps with the removal of some of the key pieces, it can become clearer that the flapper displayed in Figure

89

(a) Side View DeLeón Flapper   (b) Basic Annotated View of DeLeón Flapper

Figure 3.25: Side Annotated View of DeLeón Flapper

3.25 does in fact emulate the qualities that were discussed in Chapter 2. Figure 3.25a depicts a side view of the flapper displayed in Figure 3.25. Upon removal of some of the 'construction' braces and stands, an annotated view of the flapper components can be observed and compared to Figure 3.24. It is important to recall that the red points are fixed and are free to rotate but not translate. The blue dots are free to both rotate and translate.

Due to some unexplained features, it is necessary to describe each of these components in terms of their corresponding annotated names such as L_{wing} corresponds to the wing itself. The following discussion will progress in reverse order; shedding light on some of the features and properties associated with each of the flapper components.

To begin, it is necessary to discuss the top half of the four bar flapping mechanism. L_6, or at least the component that emulates the features required to exhibit the qualities of L_6 can be considered the wing holder. The clamp that holds the wing can be seen in Figure 3.26.

This clamp was discussed in the previous section and displayed in Figure 3.10 with the foam lining already attached. This foam was added originally by Aaron Norris to act as a less rigid boundary condition, allowing for some flexion at either
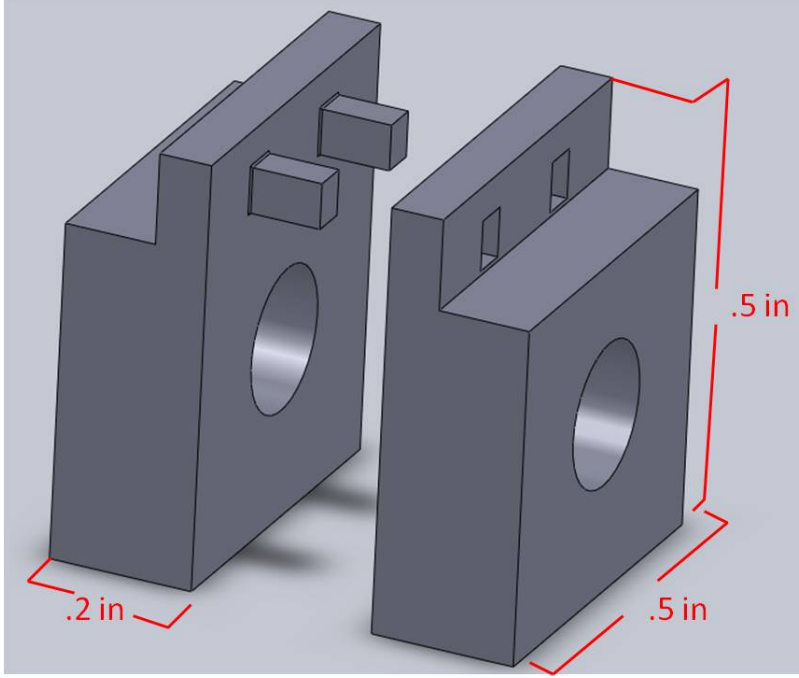
90

Figure 3.26:   Wing Holding Clamp (Without Foam)

side of the flap to preserve the integrity of the wing. Application of the foam included
the cutting out of the foam and and the associated holes to allow for the wing to be
braced on its base. The foam was secured by cyanoacrylate and was changed for every
wing's associated experiment as the foam would often exhibit wear as the wings were
flapped and vibrated. The wing clamp shown in Figure 3.26 was held in place by the
L_6 member shown in Figure 3.27.

The element representing L_6 may warrant some explanation. Chapter 4 will
discuss the experimental setup in more detail, but one may notice the needle-like
element extending from the bottom of the L_6 element. This was used for angle
calculation and visualization for the strobes as it was necessary to ensure the proper
angular treatments. The needle would point to the angular position of the flap during
the experiment, verifying that the stroboscopes were set to the correct phase delay.
A small piece of paper was attached to the supporting member that secured the L_6
element that depicted colored lines that corresponded to the investigated angles as
seen in Figure 3.28. Both the wing clamp and the L_6 elements were constructed
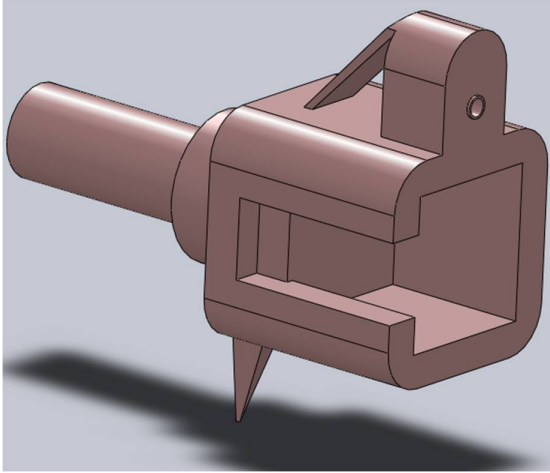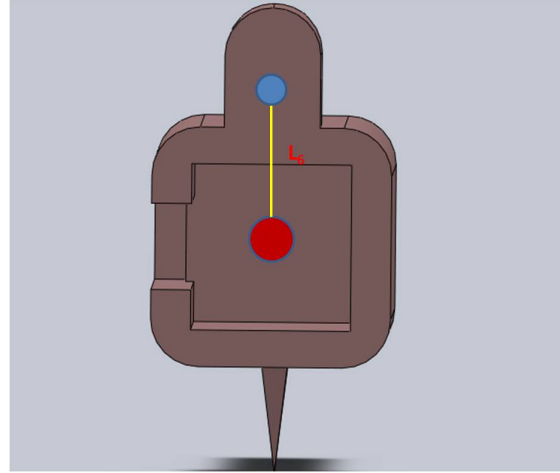
(a) Wing Clamp Holder   (b) L_6 Illustration

Figure 3.27:   Clamp Holder Shown as L_6

using the 3D printer discussed earlier and depicted in Figure 3.1 in the $VeroBlue^{TM}$ 'ink'. The next element to be discussed is the L_5 element (which was composed of the
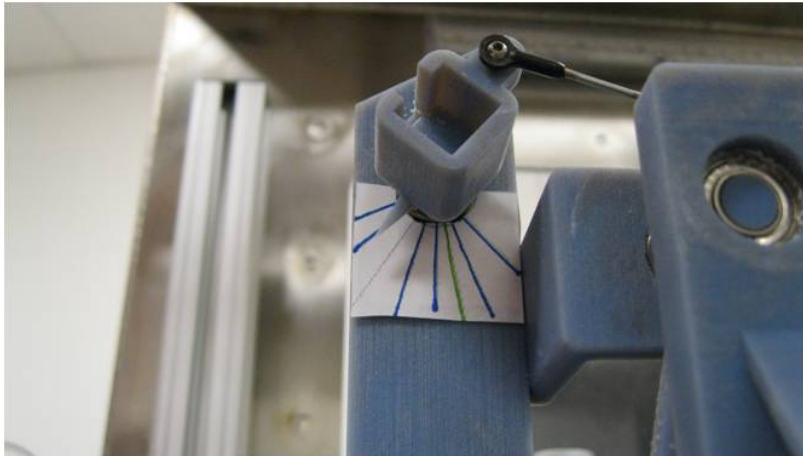

Figure 3.28: L_6 Element Pointer With Corresponding Paper Guide

same pieces to create the L_2 element). These were not composed of the 3D printer ink, rather these were composed of stainless steel push rods manufactured by $EFLITE^{TM}$ who specialize in remote control cars and aircraft. The black ends are designed to snap around metal ball joints (also purchased from the same company) as depicted in Figure 3.29b.
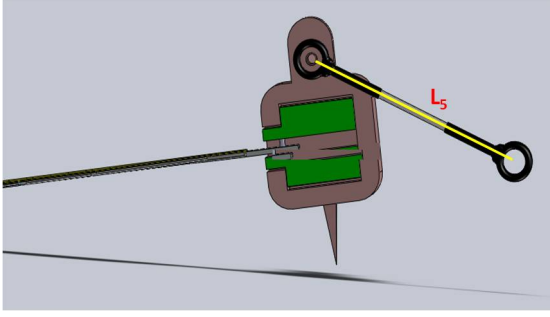
(a) L_5 Pushrod

(b) Physical Pushrod End

Figure 3.29:   Push Rod Shown as L_5

Following the push rod is the component that makes up lengths L_4 and L_3 as they rotate together. This component was fitted with the ball joints at either end so that the L_5 and L_2 push rods could be mounted to it. The center of the L_4/L_3 member remains fixed much like the center of the L_6 member, with its only degree of freedom being its rotation about the normal round pegs that extend symmetrically from either side. Figure 3.30 sheds light on this element, annotating the links that it represents and those that adjoin to it.

Attached to the L_2 push rod was a flywheel manufactured from the 3D printer. The radius of the center of rotation to the point at which a ball joint (that connected to the push rod) is representative of the L_1 linkage. This is considered the 'driving link' as this 'flywheel' is what is rotated by a motor to drive the whole system. Figure 3.31 depicts the flywheel along with the necessary annotations to link it to the kinematic analysis is Chapter 2.

In addition to the links that have just been discussed, it is necessary to consider the parts that hold the system together. There are two main parts that represent the 'fixed bases' that will essentially allow for motor placement and element rotation. The first part holds the wing clamp and the $L_4/L/3$ linkage. An addition to holding both parts, this piece also acts as the axis system for photomodeler. One may notice in Figure 3.32 that there exists several black marks with white centers. These exist in
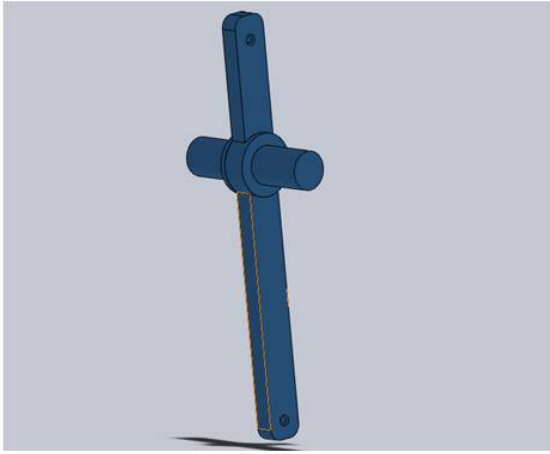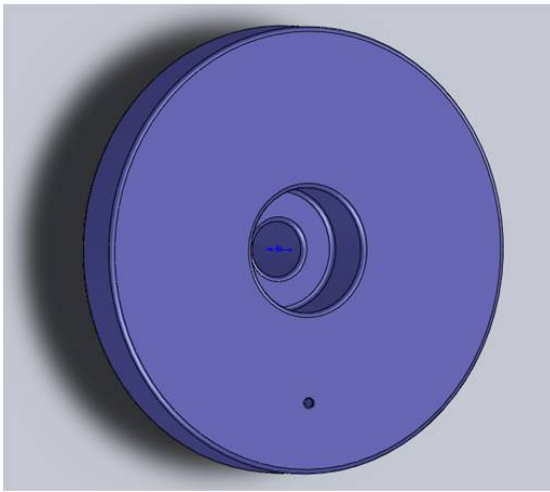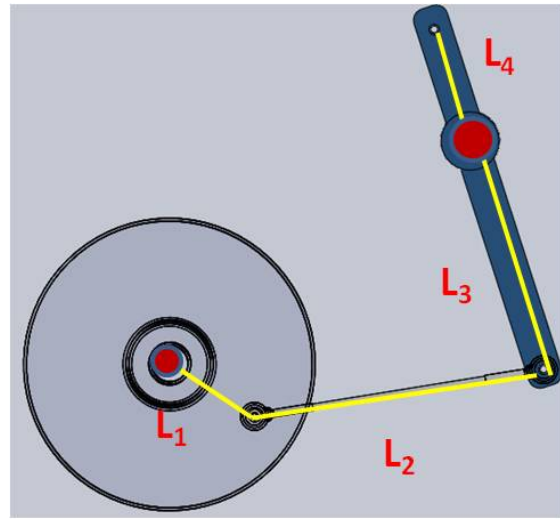
(a) L_4 and L_3 Element
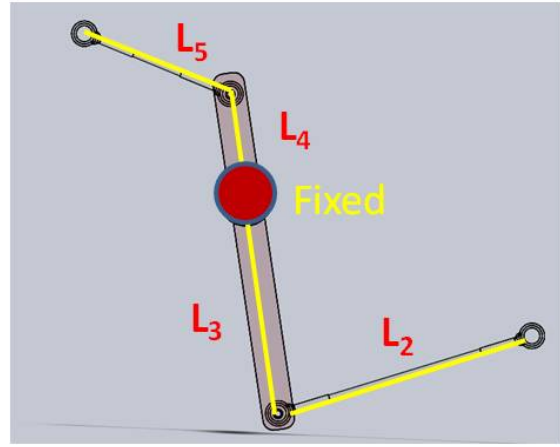
(b) Annotated Elements

Figure 3.30:   Push Rod Shown as L_5

(a) Flywheel

(b) Annotated Elements

Figure 3.31:   Driving Link L_1 as Rotating Flywheel

(a) Clamp Base   (b) Manufactured Reference Points   (c) Annotated Clamp Base
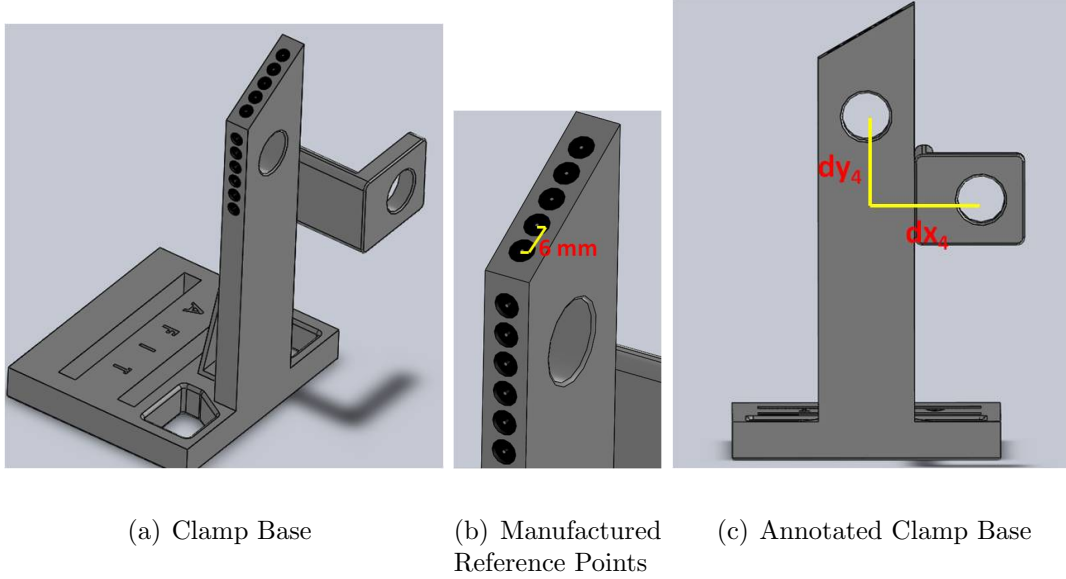
Figure 3.32:   Diving Link L_1 as Rotating Flywheel

order to serve as fixed reference points for Photomodeler to consider when examining the response of the wing. This reference point placement is yet another form of control in the experiment as the reference points that were manufactured on the upper portion are 30° from the horizontal, and the vertical points are 90° from the horizontal. Due to the fact that these do not translate during flapping, they inherently act as a 'standard' for the system when examining the data.

This is crucial for data comparison as the fixed, global reference frame will be used to compare and contrast the different wings and/or conditions that the flapper was to perform under. Needless to say, these reference points exist at a standard 6 mm apart (center to center). This was set in order to tabulate the residuals of the system- as Photomodeler outputs its residuals in units of 'pixels'. Due to the fact that photomodeler only considers its points in units of spatial separation (pixel separation), this standardized reference point placement that has been manufactured onto the aforementioned part will shed light on the physical distance that is represented by the pixel count of each of the photos for the purpose of tabulated residual calculation from point to point.
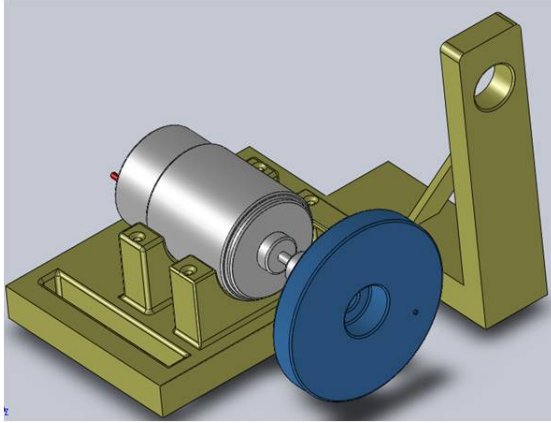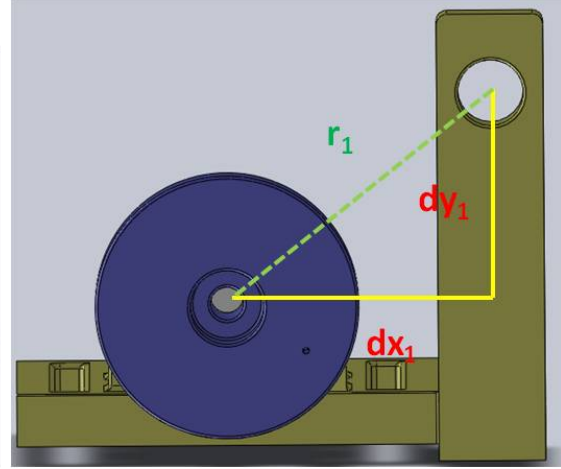
(a) Motor Mount   (b) Annotated Motor Mount

Figure 3.33:   Motor Mount and Associated Annotations

This flywheel had to be attached to the motor- which also had to be mounted onto a measured and standardized fixture- as this fixture would essentially define the key parameters dx_1 and dy_1, much the same as dx_4 and dy_4 was defined by the elements depicted in Figure 3.31. Figure 3.33 shows this 'motor mount' with the motor and flywheel attached.

The motor chosen for this study had to be both controllable and adjustable. Previous work done by Norris [1] elicited an brushed RC car motor whose main method of speed control was manual adjustment of power input. It was decided that this would not suffice as it was necessary to be in complete control of the speed. One of the main issues with the motors currently available is that most of them are meant to spin at a much higher rate than what is required for this study. Furthermore, at such low angular velocities (compared to what most motors are designed for) proved problematic to locate. The subject of gear-reduced motors was considered as many remote helicopter motors are required to spin at high angular velocities- yet have their actual output be geared down for both control and power.

Consideration was given to the purchasing of a new motor that would be both controllable and efficient, leading to a more advanced motor known as a 'brushed'

motor. It was determined that and $MPI\ HIMAXX^{TM}$ 600 Watt Geared Brushless Motor (Figure 3.34 be purchased in lieu of the setup left by Norris. This motor required batteries to power, and had a 4.28:1 gearing ratio.

Figure 3.34:   MPI HIMAXX 600 Watt Brushless Motor

In addition to the purchase of a new motor to drive the flapper, it was necessary to also purchase a speed controller. It was suggested by MPI HIMAXX to purchase a $PHEONIX^{TM}$ ICE 75 Brushless Motor Speed Controller. This would allow for complete control of the motor, as it retained the ability to program in various revolutions per minute (RPM) rates for the motor. In addition to its programmability, the speed controller featured a data logging ability that was able to track such motor functions as RPM and voltage input.

The system discussed here was calculated with with the rigid body, frictionless assumption. In the final construction, it was sought to preserve as much of these assumptions as possible. The push rods and printed parts could be expressed as rigid bodies as in the manufacturing process, their properties were designed to exhibit such qualities. One issue however did plague the construction process and that was the concept of friction.

In order to call the analysis presented in Chapter 2 'valid', careful consideration was given to this topic. The push rod/ball joints were designed to be as frictionless as possible as that was their intended property when they were designed, however it was necessary to further ensure this fact by both applying a simple lubricant and to sand out the round plastic ends to more easily slide over the ball joints. This process was continually repeated until there was no conceivable resistance associated with the interface of the push rod end and the ball joint. This was verified by allowing the

push rod to 'hang' off of the ball joint, and if the weight of the rod-end was enough to move itself to 'dangle', then the joint could be considered as frictionless.

The next area of concern was that of the fixed/rotating points of the system, conveyed as the upper red dots that connect L_6 and the L_4/L_3 element. Attempts were made to machine/construct such frictionless elements without success. It was determined that the purchase of ball bearings was in order, as their primary function is to allow for resistance free rotation. Six 8mm (outer) 5 mm (inner) bearings were purchased from $Boca\ Bearing^{TM}$, two of which are depicted in Figure 3.35.


Figure 3.35:   Boca Bearings Used For Frictionless Rotation

These bearings were located on various places on the flapper as depicted in Figure 3.5.

It can be noticed that in Figure 3.5, the leftmost hole that held the bearings had two placed within it. This was due to the fact that the back half of the L_6 element was designed with no tolerance between the element and bearing interface. This eliminated the need to use glue or screws to hold the L_6 element in place. The redundant bearings ensured little wear on the L_6 element at the bearing/element interface, and it also provided yet another surface for friction to hold the element in a constant position.

The other two sets of bearing placement only required one bearing each due to the fact that the system was designed to fit tightly together, and was designed to ensure as much- thus the L_4/L_3 element had the concern of movement removed from it.
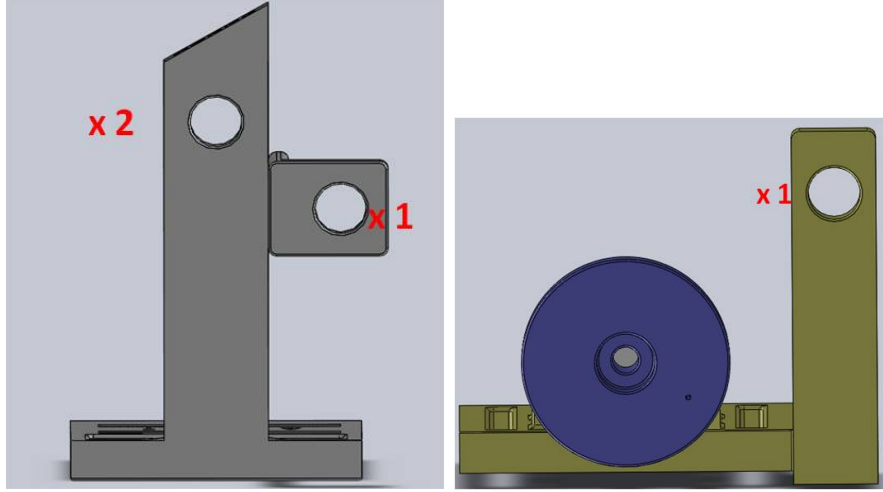
(a) Bearing Placement for L_6 and L_4/L_3 Elements

(b) Bearing Placement for L_4/L_3 Element

3.6 Summary

This chapter served to provide insight into the inner workings of the manufactured elements of this study. Several avenues were taken to create a biologically inspired flapping micro air vehicle wing in an iterative fashion in order to arrive at the final design depicted in Figure 3.22. Furthermore, separation techniques were discussed here to illuminate the precautions taken to ensure that an entire wing was considered in this study; limiting interference/damage to the wing itself as much as possible. System identification was performed by executing a modal analysis to investigate the properties inherent to both the manufactured and biological wings as a method of comparison in much the same fashion conceived by Norris et al. [1]

These wings eventually made their way into the DeLeón Flapper, whose kinematic properties were discussed at length in the previous chapter. Here, the manufacturing techniques and part assemblies were shown- shedding light on the manufactured part's features that lead one to reconsider their association with the aforementioned kinematics.

IV. Experimental Methodology

The second section concerning procedures for this research deals with the execution of the tests themselves. Standardization of methods was deemed crucial for the successful comparison of specimens to each other; specifically in the arena of the flapping. It was discovered (and will be discussed further within the context of this chapter) that not all specimens could withstand the flapping motion that was seen by the biological specimens; specifically the engineered wings. This not only sheds light on the fallibility of design methods, but it also grants a new respect for what nature has already optimized. In conclusion, this chapter aims to grant a full understanding of both the construction and execution of this project in its entirety; illuminating both fallacies and possible areas of improvement for future testing.

4.1 Preliminary/Preparational Actions of the Camera

Chapter 2 illuminated some essentials concerning one of the main investigative tools for this study: Photomodeler. As mentioned, camera calibration is one of the most crucial steps to take before making any calculations concerning the 3D positions of points in space. Before the proceeding experiments could be executed, it was necessary to perform a calibration project of the camera in use. The camera utilized for this study was a $Nikon^{TM}$ D80 digital camera. The lens used for this study was a $Promaster^{TM}$ Digital XR EDO *Aspherical* LD (IF) 17-50 mm 1:2.8 Macro ϕ 67.

Photomodeler provides the means to calibrate a camera via subroutine within the software called a 'Calibration Project', and its aim is to retrieve the parameters spoken of in Chapter 2 for the specific camera at a set number of settings. Photomodeler suggests that a calibration project be executed every time a camera setting has been changed, but for standardization purposes, it was deemed more prudent to maintain the camera settings for each test executed. There are 3 'basic settings' that Photomodeler considers:

- Zoom/Focus: This setting is lens specific and a change in these settings is often not detected within the Photomodeler software as it simply contributes to the

Figure 4.1:   Nikon D80 and Lens

'clearness' of a picture. If the focus is off, often times the captured image will appear blurry and cannot be used for practical applications such as 3D image correlations. Though Photomodeler rarely detects an issue if this parameter has changed, it is important that this parameter remain a constant for scaling purposes. If the focus or zoom were to change, the camera would detect a change in pixel size per image unit (for example 6mm in physical space would change from 500 pixels to 700 pixels in the camera's computational space).

- F-Stop/Shutter Speed: Not to be confused with the aperture stop, the f-stop allows for a limitation in the light allowed in the field of view (ie *field stop*). This is a unit less quantification of how much light will be allowed into the realm of the camera. The longer that a shutter is open, the more light will be allowed into the system, however the issue with this is that the image must be completely still. This does not grant room for error for this particular project as the camera is hand held and can be prone to slight movements. In addition, due to the fact that this project will employ stroboscopes to 'freeze' and image, a faster shutter speed is desired to capture an image that is actually illuminated

rather than in between strobe flashes such as in Figure 4.2 where the top half of the picture has not been captured due to the fact that the camera shutter was not able to capture the flash at the exact moment of illumination. Though this was an issue for some photos, it can be seen in Figure 4.2 that the image that 'would have been' was clear and discernible (64 degree flapping angle of engineered wing flapping at 12.5 Hz in vacuum). To decrease this probability of 'partial pictures', one could consider increasing the shutter speed however this would eliminate much needed light from the system. Several test trials were executed with different f-stops to gain the most desired effect/picture clarity.
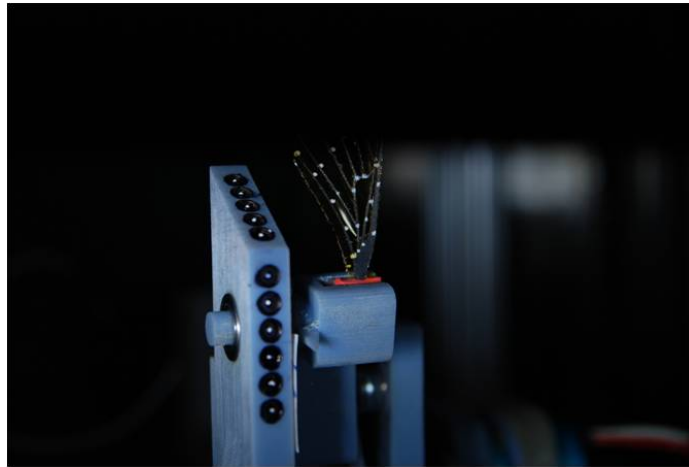
Figure 4.2:   Partial Picture Due to Being Between Strobe Flashes

It was crucial that this parameter remain fixed during testing due to the fact that often times one could not detect a slight change in settings with the naked eye, however Photomodeler easily detected a difference and thus would not allow for data manipulation/program execution unless a calibration project had to be executed at that specific setting.

- Aperture: The aperture is a term used to denote the opening of the camera lens that allows light rays to enter into the system. If the aperture is too narrow, the result will be an image that is too dark, but will have a greater depth of perception. A wide aperture will result in a bright image but will only produce a 'focused' image on the part that the camera thinks is the point of focus,

102

Table 4.1:   NIKON D80 Settings for This Study

Parameter	Setting
Zoom	42
Aperture	20
F-stop	4.0

granting little depth of vision. Just like the f-stop, several iterations had to be made as to the correct setting for this parameter. Figure 4.3 shows an example of the engineered wing having a too wide of aperture (when observing the 16 deg downward flapping angle in vacuum) wherein the tip of the wing is very well focused and 'blurry' near the base- and thus deemed unusable since the base reference points could not be discerned. Had the aperture been narrower, the depth would have been easier to capture however the light coming into the system would have been insufficient to discern the image as a whole
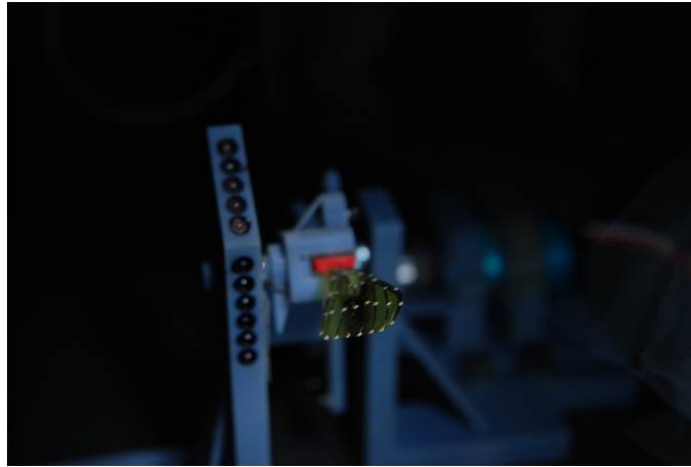
Figure 4.3:   Unusable Image Due to Lack of Depth

For this study, the following settings were utilized:

Once the correct settings were determined, it was necessary to execute a calibration project. Photomodeler provided both the means and instructions to do as much. Several **calibration grids** of various sizes were provided by the software, as these grids are recognized by the program. It is important to select a grid that emulates the

size of the area of interest [3] in that a 3ft by 3ft grid would be both impertinent and impractical for this study since the area of interest lies within a 8 in by 8 in arena. Figure 4.4 is an image that was used for calibration and depicts the calibration grid at a tilt.
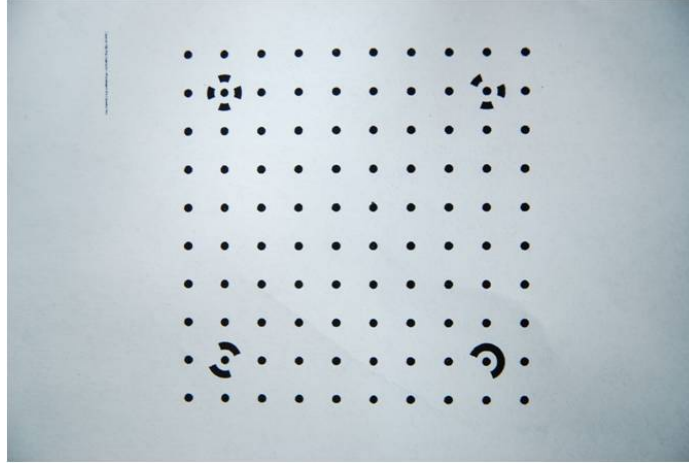

Figure 4.4:   Calibration Grid

12 different photos were taken at 12 different angles [30] and uploaded into Photomodeler's calibration software. Calibration was executed and the total root-mean squared residual was produced for the project. According to the literature, a residual beneath one pixel was ideal. The best that could be obtained for this project was (=.285 pixels) which was considered acceptable for this study.

Once calibrated, the camera was prepared for the experiment.

4.2   Experimental Setup

The basic premise of this study is comparison: the manufactured wing to the biological wing, however, there is a chance here to also consider the aeroelastic question, a topic that has presented itself throughout this literature and within many more. In order to examine this, it is not only pertinent to flap these wings in air, but also in vacuum. This will serve to evaluate the inherent differences between purely inertial deformations and displacements and those that present themselves only in the presence of aerodynamic effects. Figure 4.5 shows the experimental setup as a whole.
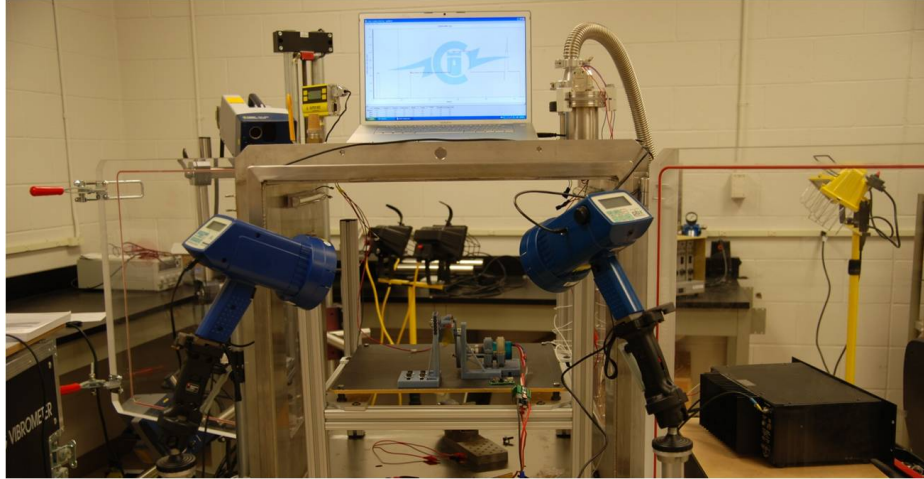
Figure 4.5:   Experimental System Post Testing

One may notice that their are several elements present in the system. This section will serve to examine each of the required elements not discussed thus far.

The first piece of equipment to consider is one that grants the ability to evaluate in both air and vacuum, be it the vacuum chamber, which is a the center of Figure 4.5 and will contain both the signal generator (for modal analysis) and the flapper. The same Abbess Instruments Vacuum Chamber was used by Norris [1], however due to the new flapper, slight modifications had to be made to accommodate the motor. As it turned out, the Phoenix ICE 50 speed controller held within it electrolytic capacitors which cannot handle vacuum conditions. As a result, it was determined that all speed control had to happen *outside* of the the chamber and thus the speed controller had to be removed. This was done by utilizing one of the vacuum chamber's built in ports that allowed wires to pass through from ambient to the chamber conditions as can be seen in Figures 4.2 and 4.2. An epoxy resin was used to seal the wires from allowing air to leak into the chamber while pulling vacuum.

On either side of the chamber in Figure 4.5, two blue light guns can be observed on stands facing flapper inside the vacuum chamber. These are the stroboscopes that have been referred to throughout this report, and their primary function is to display a 'frozen' image for the purpose of photographing a test subject while flapping. The
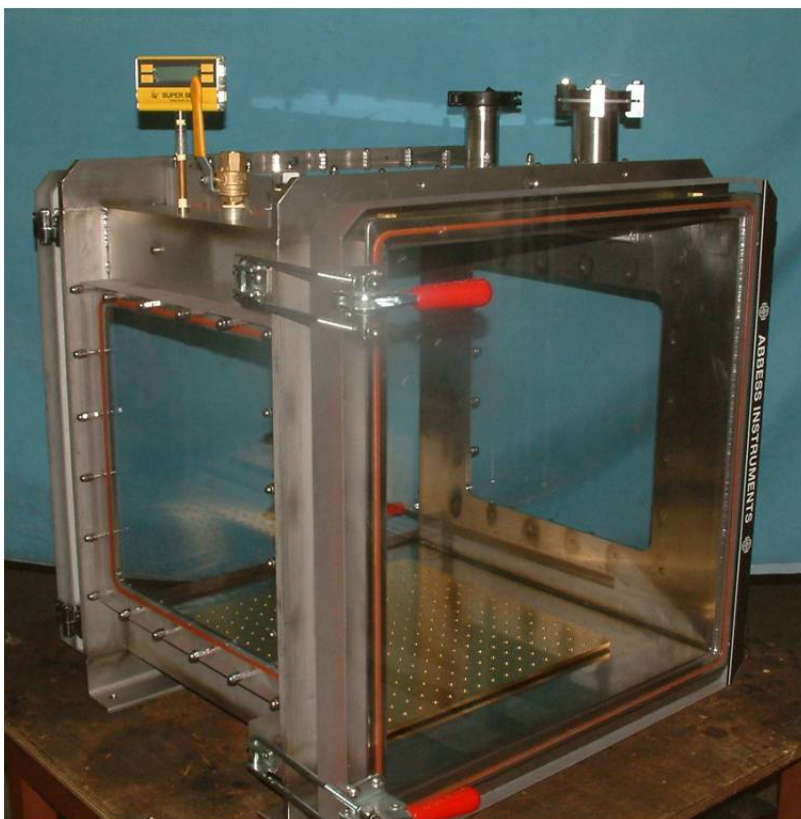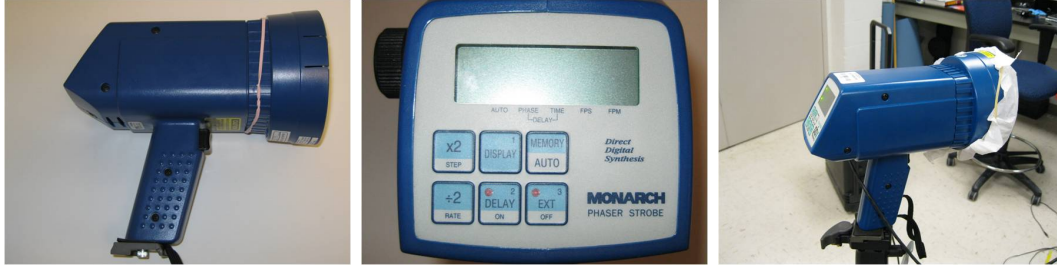
(a) Vacuum Chamber

(b) Wires Passed From Outside
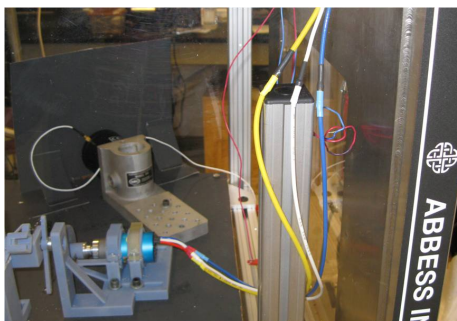
(c) Wires Inside for Speed Controller

Figure 4.6:   Vacuum Chamber and Modifications

(a) Side View of Monarch Stroboscope

(b) Digital Interface

(c) Prepared Stroboscope

Figure 4.7:   Stroboscopes

stroboscopes (2) used for this experiment were $Monarch^{TM}$ Phaser Strobes of which one is shown in Figure 4.7

In Figure 4.2, a white cloth may be seen over the lamp. This was done to one of the strobes in order to diffuse/damp some of the concentrated light. Previous trials of this experiment revealed that when the vacuum chamber was sealed (as it was for all experiments) the glass that the chamber was composed of reflected the light of the stationary strobe (on the stand) and would distort the images. The other strobe remained uncovered as it was not constrained by a stand (as is depicted in Figure 4.5) but was free to move in order to assist in obtaining clearer pictures for the experiment.

The stroboscopes retained the ability to measure/mimic the phases of moving objects. This was done via an Optical LED sensor that obtained feedback from a strip of reflective tape on the Flywheel. Every time this tape passed the field of the sensor's LED light, the signal generated by the reflection fed phase information to the stroboscope. This setup is best depicted in Figure 4.8 The features made available by the stroboscopes proved both convenient and useful as the sensor acted as an input to the stroboscope's actions. In addition to staying synced with the sensor, the interface of the stroboscope (as seen in Figure 4.2) provided feedback as to what the frequency of flashing was as the sensor read the input. This was a measure of verification that the speed controller was in fact spinning the motor at the prescribed speed. As well as providing frequency feedback, the stroboscopes held the option of setting a phase

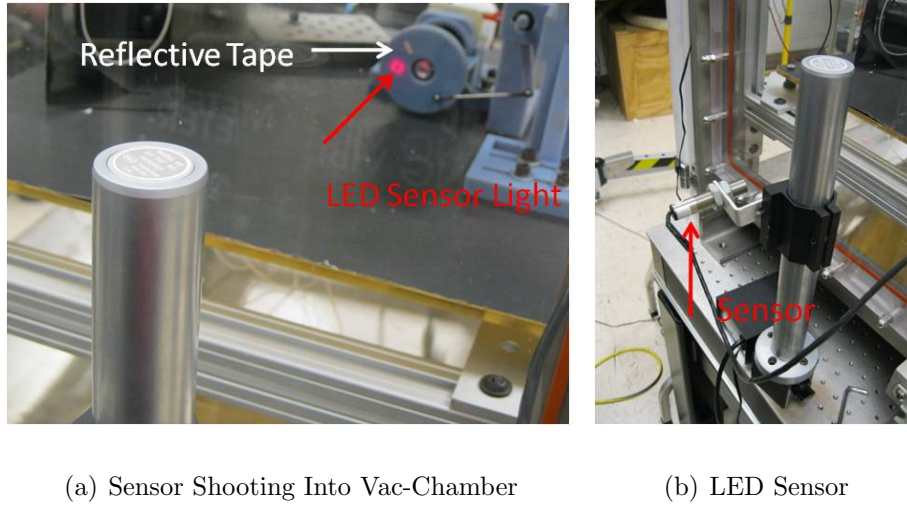(a) Sensor Shooting Into Vac-Chamber   (b) LED Sensor

Figure 4.8:   Stroboscope Phase Sensor

delay for the flashing: a feature that ultimately allowed for the data necessary for this study to be gathered at the specified points (to be discussed and enumerated in the next section) in the angular displacement of the flapper.

The stationary stroboscope acted as the driving stroboscope in that the stationary strobe was where all of the settings were set. The hand held stroboscope was plugged into the driving strobe and told to consider the input from the driving strobe as the 'driving input' much like the LED sensor was considered the input for the driving stroboscope. The driving strobe was where the adjustments were made to the phase delay during the experiment. Once the stroboscopes were placed and charged, the experiment could be executed.

4.3   Experimental Procedure

This section will serve to enumerate and discuss the physical steps taken in the execution of the experiment. All steps save for the first, which is more of a preparational step, take place after both wings have been prepared (engineering wing has been manufactured or the biological wing has been separated and marked. Both have had a modal analysis performed- the engineered in both air and vacuum, and the biological in just air).

1. Obtaining Phase Settings: As mentioned in the previous section, it was necessary to standardize the phase delay at which would display the investigated angles about the stroke, which can be seen in Figure 4.9.
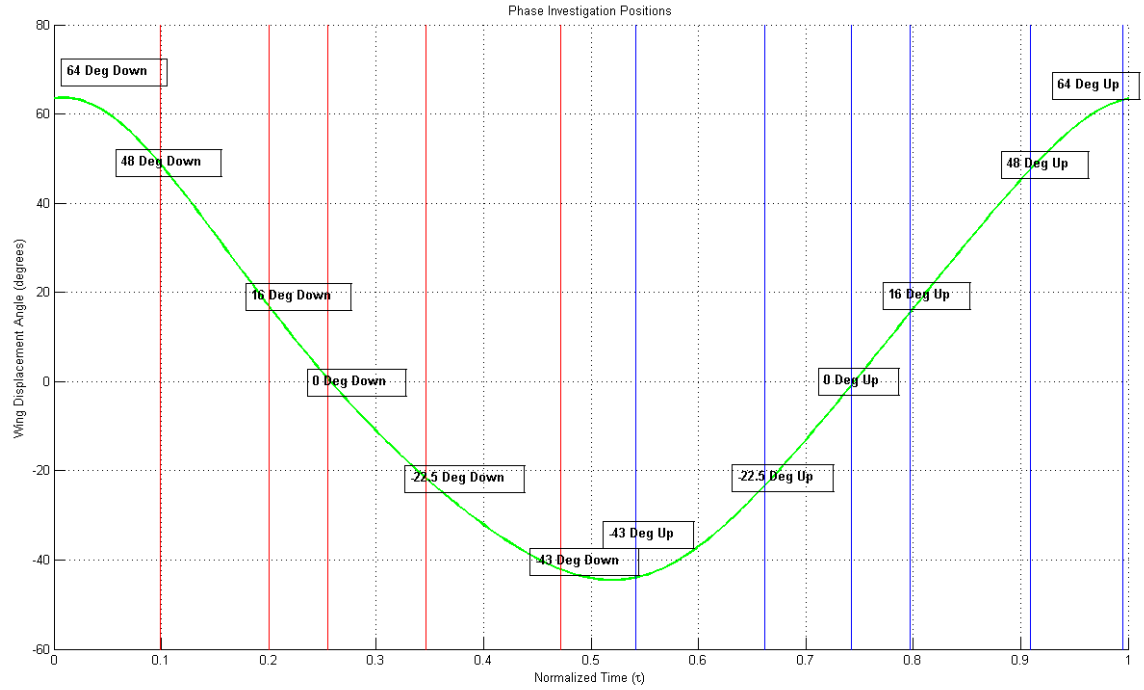

Figure 4.9:   Stroke Angle Investigative Angles

To obtain the necessary phase settings for the strobe, it was necessary to observe the angle via the system described in Figure 3.28 wherein the angle that the flapper exhibited for that particular phase had to be exactly that of what was to be observed in Figure 4.9. Table 4.2 will tabulate the set phases for this study:

Once these values were determined, it was then possible to continue to the next part of the experiment.

2. After securing the wing in question into the flapper, the vacuum chamber had to be sealed and the pump switched on. The chamber would indicate its level of vacuum via the 'SuperBee' convection enhanced Pirani vacuum gage module

109

Table 4.2:   Phase Settings on Stroboscope

Angle (deg)	Downstroke Pase (deg))	Upstroke Phase (deg)
64	39.16	0.10
48	56.03	338.07
16	97.84	303.16
0	115.65	282.71
-22.5	147.12	248.54
-43	186.85	214.79

manufactured by $InstruTech^{TM}$ (shown in Figure 4.10) which measures vacuum levels in units of TORR, which is an SI unit of pressure

Figure 4.10:   SuperBee Vacuum Gage

3. Testing could not begin until the system reached beneath 1 Torr. Once this was achieved, it was possible then to attach the speed controller to a computer with the $CastleCreations^{TM}$ software loaded onto it. This allowed for the setting of the motor RPM- which was to be held constant. This action also allowed for the setting of the data gathering rate. Once the data for the speed controller was cleared, it was then possible to disconnect the speed controller and re-connect the speed controller to the battery for operation. Testing of these wings did not exceed **12.5 Hz**. The reason for this was not that the wings did not survive (for both wings could flap in air at the originally prescribed 26 Hz), but as testing wore on, the biological wing could not survive 26 Hz in vacuum- as it would show signs of heavy use after 6 minutes of flapping. This fact was confirmed after

110

several attempts were made to execute the experiment under these conditions, but unfortunately the flapping frequency had to be continually decreased in order that the experiment could be executed with the same wing.

Pictures were taken in the manner described by Figure 2.16 for each of the flapping angles investigated at each of the phases denoted in Table 4.2. Often, between the upstroke and downstroke, it was pertinent to stop testing to perform and 'information dump' where both the camera's memory was freed by moving the newly taken pictures onto a computer. This proved crucial due to the fact that half of a stroke usually produced upwards of 500 pictures as it was pertinent to take multiples of a single shot to ensure that the image was fully captured. Additionally, the data from the speed controller could be downloaded via the associated software. This was done mainly to verify that the motor did in fact maintain its RPM throughout the test.

4. As soon as the test in vacuum was completed, power was cut to the flapper and all information pertaining to the test could be downloaded and removed from the recording systems (speed controller and camera). As downloads were completed, the vacuum chamber was allowed to slowly return to atmospheric conditions via a valve located on the roof of the chamber.

5. Testing in air began as soon as the chamber was finished filling. One important factor that should be considered is that though the chamber was full of air, it was necessary and pertinent that the glass door of the chamber **remain closed**. Though not obvious or essential for the test, any distortion that may be inherent in the presence of the glass should be maintained throughout the test. This may hinder results and make capturing data more difficult but this element of difficulty and/or distortion should be maintained for the simple purpose of comparison. Without the presence of the glass door, gathered data may or may not be 'better' in a sense of being more accurate, but even if the data is skewed due to possible light refraction because of the glass, it is important that *all* data be skewed in the same way.

4.4 Data Gathering Process: Details on Photomodeler Operations

For this study, the data gathering process was not rooted in the gathering of images that corresponded to certain angles, rather it was the calculation of the three-dimensional qualities that could be inferred from those images that held the results for the experiment. Dave Curtis [30] proclaimed that Photomodeler was an arduous and time consuming task, however he unfortunately did not indicate the exact degree of time consumption and prudence required when executing the data gathering process. As it turns out, the connatural properties of photogrammetry, especially at such a small scale, necessitate both caution and circumspection as the slightest amount of indiscretion may illicit farce data. It is thus necessary to elucidate the process of data gathering in Photomodeler here for future study.

To begin, it should first be mentioned that in order to obtain trustworthy data, it was determined that three trials should be run for each of the angles shown in Figure 4.9. These three 'trials' or repetitions served as a basis for averaging. This was deemed the most prudent method of progression due to the fact that previous attempts at Photomodeler often yielded slightly different results when considering the same test subject for two reasons:

- Though camera positions were standardized in the manner of Figure 2.16, the 'point picking' process that will be discussed in this section, enabled room for human error as often times a single reference point could often span up to 40 pixels at the settings that were standard for the camera. Theoretically, a reference point would remain standard for the size of one pixel, however due to constraints of both the application of reference points (as described in Chapter 3) and the capturing of said points at several angles (a process that required a hint of creativity in picture taking) which often involved several aberrant camera positions, disallowed for the capturing of the 'single pixel' reference point.

- During testing, a technically 'frozen' image was not actually frozen. Small displacements could be seen from shot to shot as the flapping of the wing proved

unsteady. These small displacements could not be standardized for this experiment and thus a picture taken at the same position but not at the same time proved slightly different (as will be seen in Chapter 5), leading one to admit that the approach made by Curtis [30] perhaps was more accurate in that he synchronized cameras to take a picture at the same time rather than just using one and changing its position.

Needless to say, this section will serve as yet another recipe on the methodology and execution of this experiment. The specific steps will be shown as to how one would obtain raw data from from the taken 2D images.

1. Photo Selection: The first step in this process does not directly deal with Photomodeler, rather this first step is a prepatory step. Before one can use the tools available my the software, photographs must be carefully selected from those that were taken by the experiment above as multiples would be taken at the same position/angle. Figure 4.11 depicts two pictures of the biological wing flapping downward at 12.5 Hz in air at the flapper's 0° mark. In Figure 1 one can clearly discern all reference points. Figure 1 is not much different save for the fact that the reference points near the base of the wing are not as easily discerned as those in Figure 1. This was an important concept to grasp as an acceptable picture may not have clarity of all reference points (some of them may appear blurry) however could be easily observed. A clear picture could show most points but not all- and that is not usable for this experiment as the **position** of all points must be found when looking at a picture.

   Having said that, some pictures deemed acceptable for analysis held blurry reference point representations at the tip of the wing with very clear points at the base. These pictures were used not for their inherent clarity, rather it was the discernibility of the points that was important, and due to the distinct separation of points at the wingtip, these were easier to recognize than those at

113
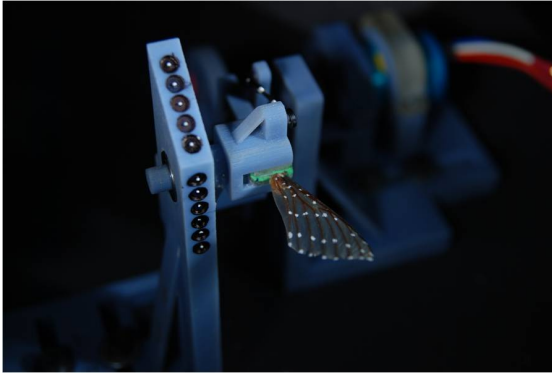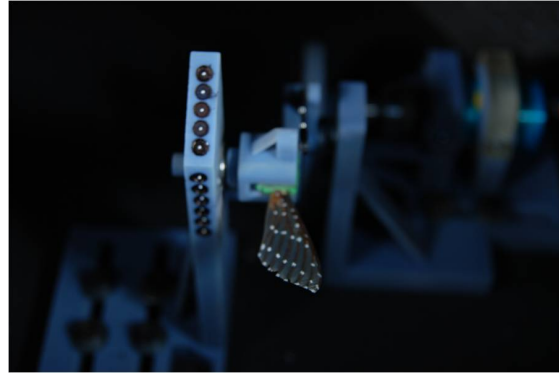
(a) Acceptable Image (b) Unacceptable Image

Figure 4.11:   Comparison of Images for Photomodeler

the base since the points at the base were very close together and often would get lost in an image amongst the wing features.

Three or four images were selected for each of the three trials for each angle, making the grand total of pictures used for one analysis of one wing 72 as there were (3 repetitions) for (12 separate angles) for (2 trials- air and vacuum). It was important that though some pictures were not used in the analysis- these 'extras' remain saved due to the fact that during analysis a previously deemed 'good' picture may not turn out to be as helpful. For this study, each wing had roughly 2400 pictures taken of it, and only 72 of those were used.

2. Once usable pictures were selected, the photogrammetry process could begin. The first step after opening the program and selecting the pictures in the folder that will be used for the analysis, was to 'pick' the reference points on the wing and flapper base. Though each picture was taken at a different angle, it was crucial that the points be picked in the **exact same order** each time for each photograph. Figure 4.12

If any one of these was out of order, it opened the door for unusable results as the final data was imported into MatLab as a text file, and the order of the points was very important for the analysis of the data.

114
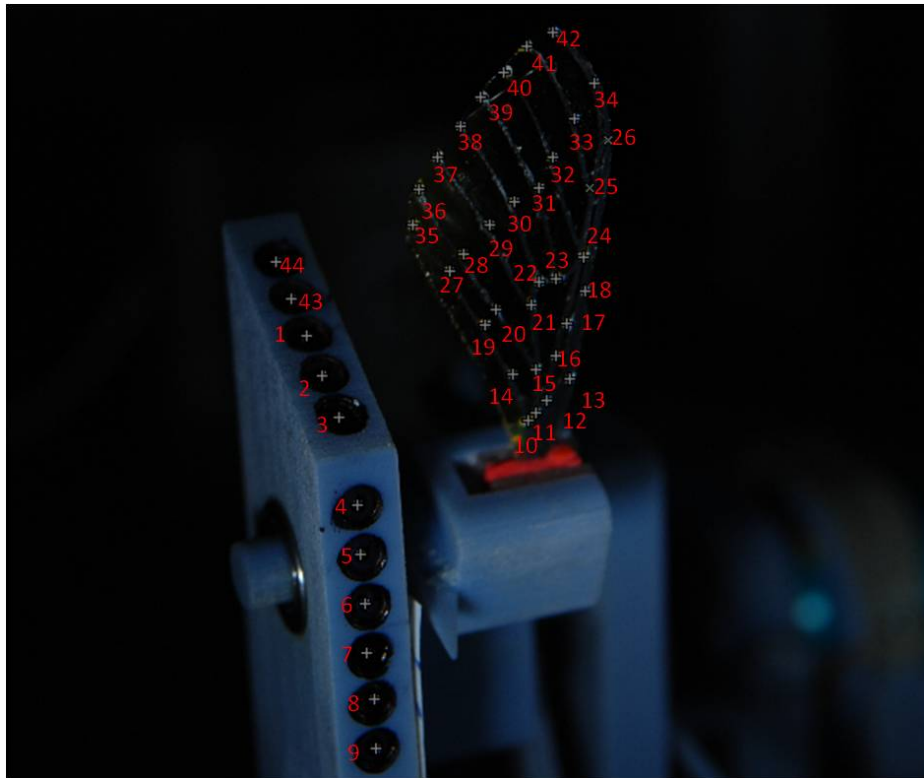
(a) Bottom of Wing Points
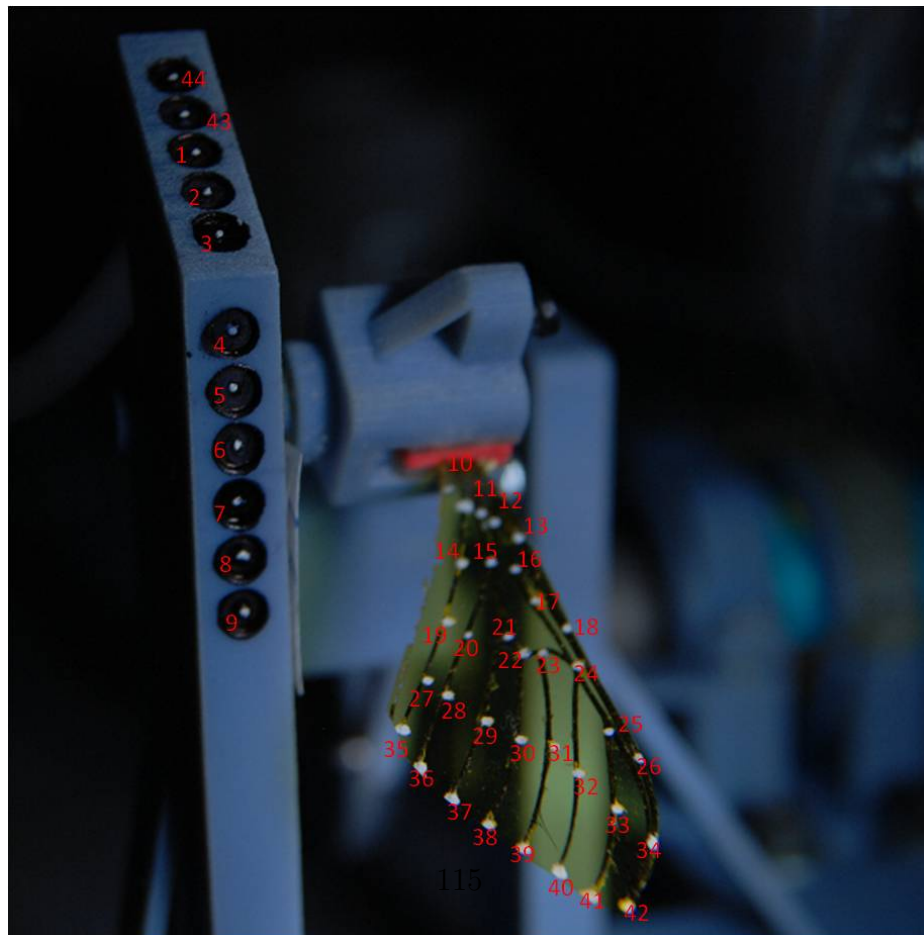
(b) Top of Wing Points

There were two options for point selection, and they are shown in Figure 4.13. The green circle denotes a 'self identification' of a reference point. This allows a user to place the cursor over what he/she thought was a reference point and identify it as one. This left plenty of room for human error as this was a hand identification. The red circle points towards the most efficient and trustworthy method of point selection in that this is Photomodeler's function known as *Sub-Pixel Target Mode* wherein the software will attempt to discern what it identifies as the center of a reference point by differentiating it from the surrounding selected area. Put simply, a user just needs to select a general area around a single reference point and Photomodeler will identify that reference point as such. Though efficient and the most widely used for this study, there were several pictures that would not allow the utilization of such a feature as the reference points were barely discernible and thus has to be user identified using that which was discussed previously in the green circle.
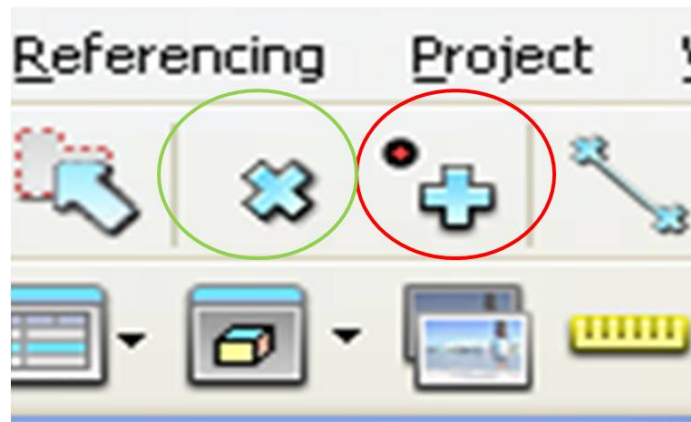
Figure 4.13:   Point Picking Options

3. Once the points were identified for each of the three photographs selected for that analysis, it came time to **reference** each of the selected reference points for each photograph to each other. This demonstrates the principle of triangulation that was discussed in Chapter 2 in that the user had to identify for the program which points were which between all three.
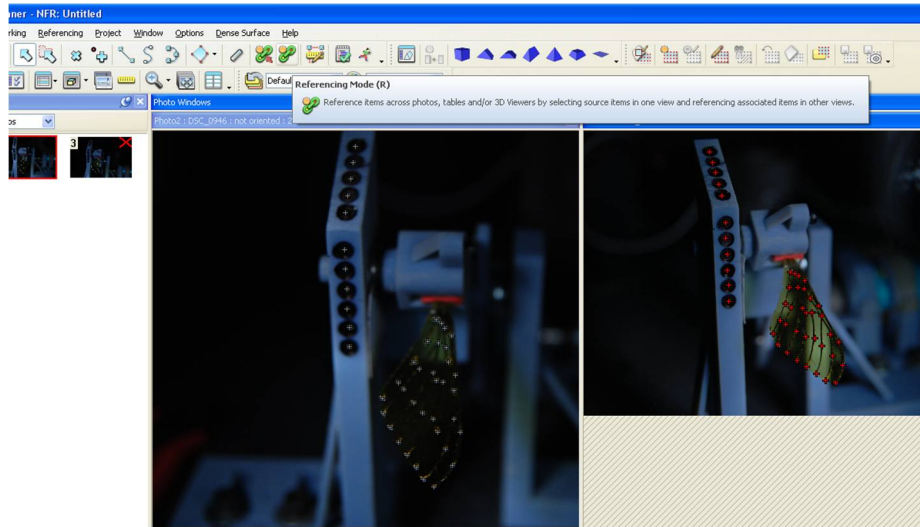
Figure 4.14:   Reference Mode Demonstration

The *Reference Mode* inquires about the position of each reference point from point to point by using one picture as the basis and requesting information about all the others. This acts as a guide and is helpful in verifying that all points were chosen in the same order.

4. Once the points were referenced to one another, it was possible then to **Process** the images and their corresponding referenced points. This can be considered the heart of photomodeler's functions due to the fact that this is exactly where the triangulation that was previously referred to takes place. Here, Photomodeler will attempt to use the referenced points to extract the camera positions that were used to take the photos. An image of this can be seen in in Figure 4.15, as it is a representation of Photomodeler's answer to the camera positions.

It can be seen in Figure 4.15 that Photomodeler understands that the pictures were taken in the manner of Figure 2.16. This provides a descent check that the processing has run as it should have in that if the cameras are in uncommon/incorrect positions, then it is possible that the setup before processing was erroneous. This commonly occurred when extra reference points were added or incorrect references were made from point to point.
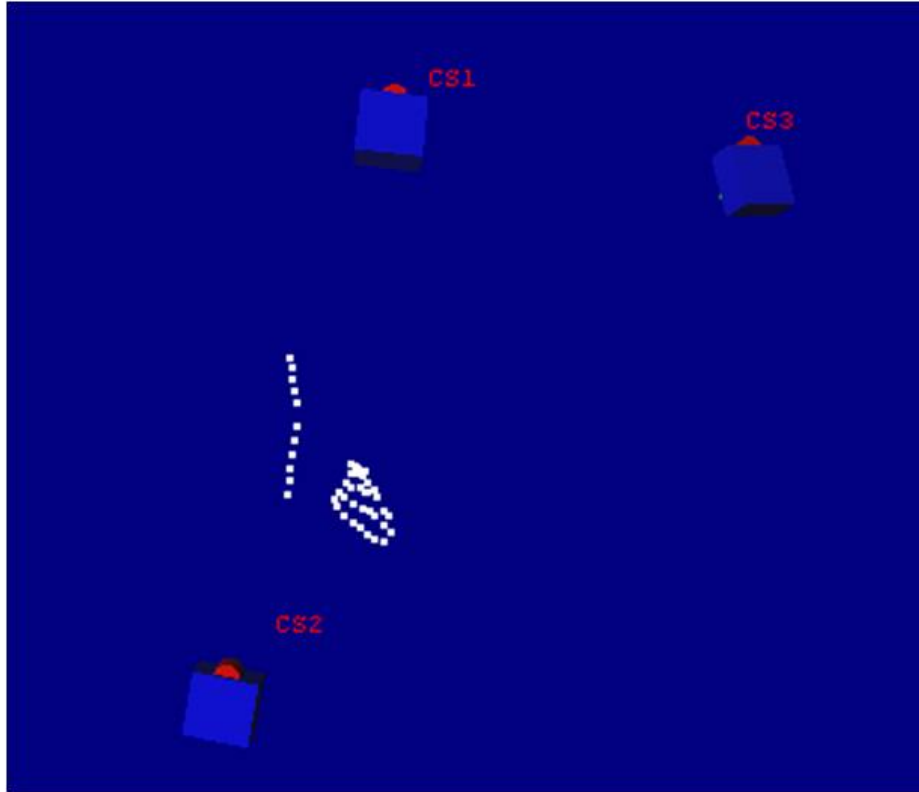
Figure 4.15:   Camera Positions as Seen by Photomodeler

There were several occurrences when processing was not able to execute, especially when observing the angles that were difficult to capture, especially the 16 degree and 0 degree angles. Often times the software was unable to understand some of the references as some of the photographs were mediocre in quality at best. To remedy this issue, there were several avenues to consider for a solution:

- Re selection of photographs: In taking multiple pictures at the same basic position, it was sometimes helpful for the user to slightly move the camera while photographing the same shot as a slight adjustment could in fact make the difference between seeing all reference points clearly and not. By keeping all the extra shots, it was possible to re-examine the photograph selection and perhaps re-execute the above steps before processing.

- Consider deleting a photograph from processing consideration: The discussion on the concepts behind Photomodeler in Chapter 2 shed light on the

118

subject of 'binocular vision' in that technically, only two images at different positions are required to resolve the three dimensional image. Though this route often hindered accurate results, it was considered a necessary evil due to the fact that gathering data at all angles was crucial for the comparison of these wings.

- Decrease solution tolerance: Within the preferences, there are several options that directly relate to the solution tolerance. Normal settings for this study entailed a 0.005 solution tolerance and a 0.001 bundle stability measure. Should a set of photographs fail to process, this was a 'last ditch' attempt to obtain processed data. This decrease in overall tolerance or solution accuracy certainly was not of the first solution to be considered, however $\cong 23\%$ of the projects concerning the 0 and 16 degree angles had to be treated this way.

5. Following successful processing, it helped to observe the solution to make sure that the picture looks as it should. This could be done by observing what Photomodeler saw as the 3D representation of the point positions as shown in Figure 4.15. Once the solution was observed, it was helpful to examine the residuals on a point to point basis. Photomodeler will report the highest residual (per reference point in units of pixels) and point towards the photograph that has the highest residual at that point. It was then pertinent as suggested by Curtis [30] to reconsider/re-examine that point's placement.

6. Once the processing results were obtained after re-consideration (if that in fact needed to occur), it was necessary to define the axes and origin of the system via the *Scale/Rotate* feature under the *Processing* tab. This feature of the software proved immensely useful in comparing results as it set the standard for comparisons. The axes that were defined in this study were the **z-axis** which was described by a line between points 9 and 4 (in that order) or 'bottom to top' and the **y-axis** wish is described by line between points 3 and 1 (in that order) or 'front to back'. Via the design of the flapper, it can be seen that

119

the **z** and **y** axis is not orthogonal, rather they are separated by a 30 degree angle (as discussed in Chapter 3). Photomodeler extrapolates the position of the **x-axis** that will make all axes orthogonal and thus disallowed the definition of all three axes. The origin of the system was defined as point 1. Figure 4.16 gives a graphical description of the axes used for this study.
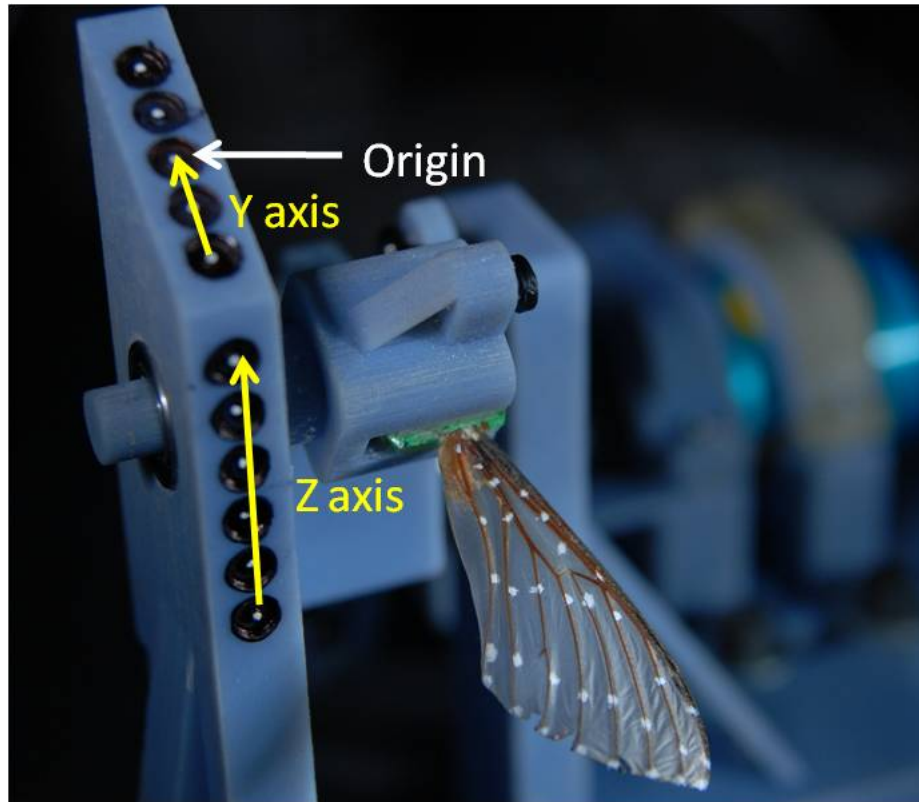
Figure 4.16:   Axes and Origin Defined in Photomodeler

7. Following the axis selection, it was necessary to obtain the pertinent information relating to the reference points to export into Matlab. The following table describes the information that was exported into a **.txt** file for eventual data manipulation.

8. Once all data was extracted, it was necessary to export it into MatLab for point processing and comparison.

Table 4.3:   Exported Data From Photomodeler

Paramater	Description
ID	Point identification number (1-44)
X ()	Point X position in Space
Y ()	Point Y position in Space
Z ()	Point Z position in Space
Photo	Photograph that has the highest residual at that point
Res (pixels)	Highest residual at that point

4.5 Data Handling and Algorithm Details

This section serves to illustrate the process of data acquisition and handling as the raw data simply consists of the following: 6 sets of points and associated information (See Table 4.3). Each set of points consist of 3 separate repetitions of all 44 points. To manipulate and examine this data, it was conceived that treatment of each set of data should be standardized and generalized as the data manipulation sequence should be able to be applied to any data set that be thrown its way.

The original goal of this project was to execute a 'point to point' comparison of the reference points on the wings (as their placement was standardized in the manner seen in Chapter 3), however as it will be seen, some of the differences are so vast in terms of flapping behavior (especially in the case of the wing-to-wing comparison), the process of comparing the reference points on one wing to another seemed impractical as there was almost no conceivable practical method of comparison. In addition, throughout the testing process, fallacies were observed in the resolution of the spanwise direction of the wing due to limitations in data gathering, thus effectively changing the size (spanwise dimension) of the wing. It was deemed pertinent to explore different avenues that shed light on the behaviors of the wings tested (or more importantly the differences in behavior between them). The following cases were tested:

- 2 Wings (biological and engineered)

- Under 2 conditions (air and vacuum)

- For 2 strokes (upstroke and downstroke)

- Which held 6 angles of investigation each

- Each angle was executed for 3 trials

  For a total of **144** cases.

4.5.1 Data Organizing and Allocation. The first task for data manipulation was to organize the data in a manner that could be utilized. In order to do this, it became necessary to take the lumped data- and break it up into the separated angles, and the upstroke and downstroke. This was done by using structured arrays- first splitting the data into sections containing only angles themselves (with each of their three trials) into x-y-z sections. Figure 4.17 is a flowchart depicting this described process.
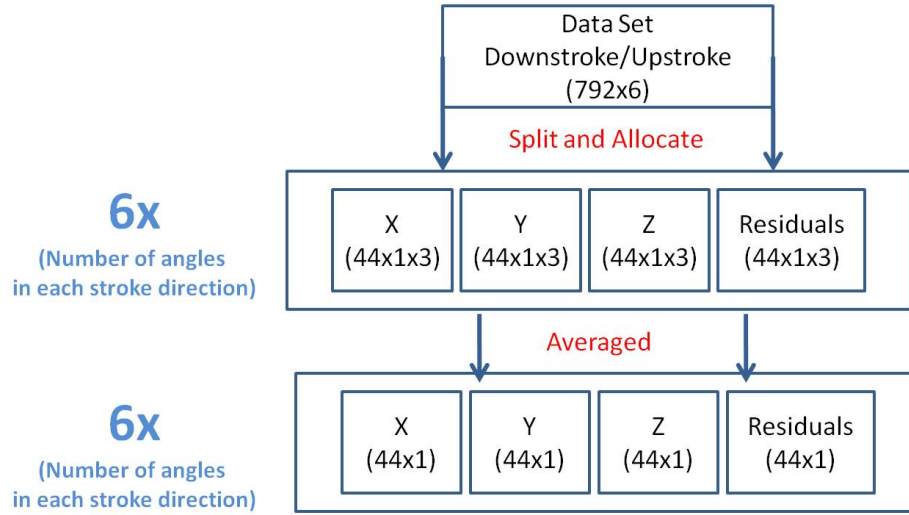
Figure 4.17:   Data Organizing and Allocation Flowchart

Once the aforementioned process was carried to completion, it was then possible to perform several operations on the separated data. It should be restated that the reason that three separate trials were executed was that an average could be taken to represent the true position of the reference points. After each angle data set was extracted from Photomodeler, a 'check' was performed using a subroutine called

SingleShow.m to make sure that the data did not appear too scattered from the averages. Figure 4.18 is an example of this operation.
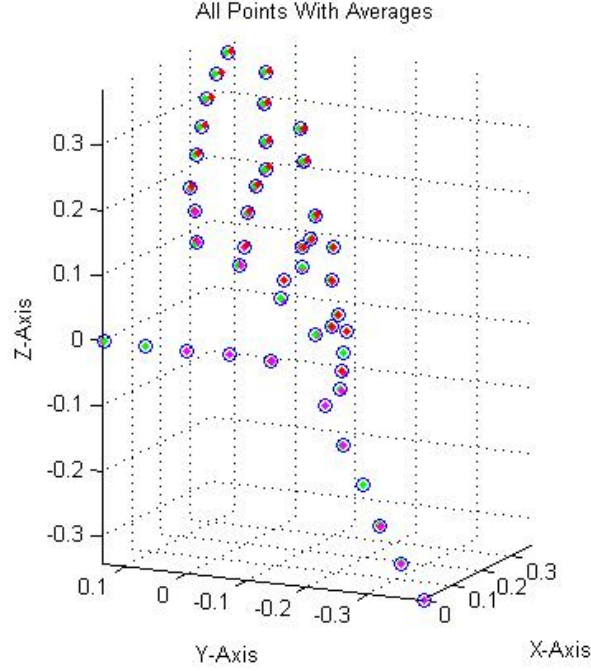
Figure 4.18:   Check of 48 Degree Engineered Wing in Air

In Figure 4.18, each reference point is represented as three separately colored reference points (red,green, magenta) surrounded by a blue circle. The multi-colored reference points each correspond to one of the three trials executed and extracted from Photomodeler. The blue circle is representative of the average position of these points as described by the following equation:

$$[\bar{P}] = \frac{p_1 + p_2 + p_3}{3} \tag{4.0}$$

Where [P] represents a position parameter (x,y,z).

Once the averages were computed for each of the data sets (there being 8 data sets - 2 separate wings - under 2 conditions (air and vacuum) for 2 strokes (upstroke and downstroke). It was then possible to manipulate the data for comparison pur-

123

poses. Figure 4.19 is a continuation of the program depicted in Figure 4.17 showing the several avenues of data manipulation taken.
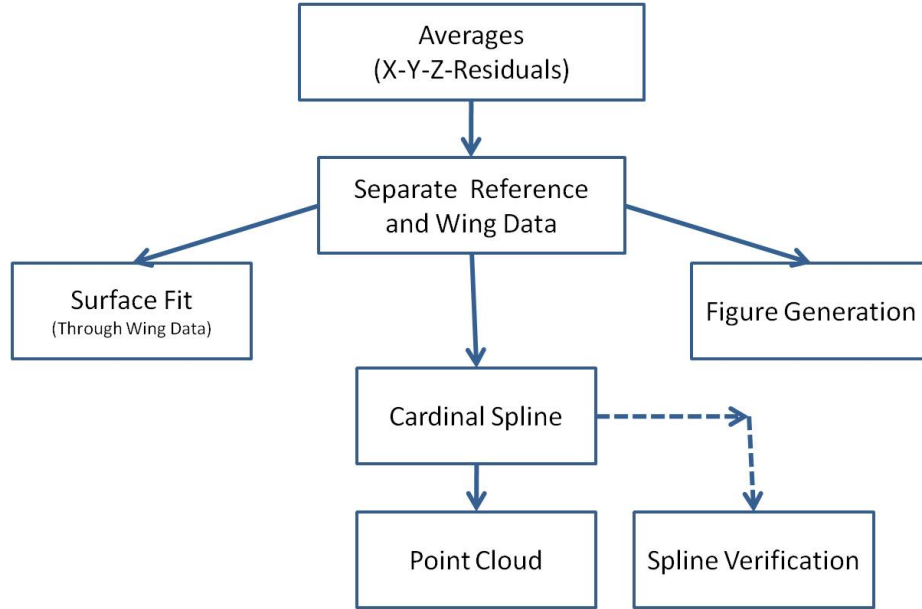
Figure 4.19:   Data Manipulation Flowchart

The flowchart shown in Figure 4.19 warrants some explanation as it generates most of the parameters that will be manipulated for a 'wing to wing' and 'air to vacuum' comparison.

The first topic to discuss in relation to Figure 4.19 would be the box to the left labeled the *Surface Fit*. This was generated using MatLab's Surface Fitting Toolbox (sftool) wherein the averaged position of the reference points associated with the wing alone were fitted using a *Cubic Interpolant* fit. This was chosen due to the fact that for all the options available for surface fitting, this option yielded the least amount of error (according to the [sftool]'s fit result function that calculates the largest error associated with a fit). This was performed to supply an aid for wing deformation visualization (rather than just looking at a picture).

The second topic to discuss in relation to Figure 4.19 is the *Cardinal Spline* box. For this thesis, 'spline' refers to the interpolation of data in between the experimentally gathered data. The purpose of this action was to perhaps generate the

3D position of a deflected wing for every point in its stroke. This would be helpful if one were to attempt a fluid-structure analysis of a flapping wing– only the structural deformations would be known, eliminating the need for the time consuming iterative process associated with an FSI simulation. In addition to gaining the wing deflection at every point in a stroke, a successfully splined data set could potentially shed light on the inherent twist associated with a stroke. Originally, it was conceived to utilize a **cubic spline interpolant** which is a stock program built into MatLab's list of available toolboxes. Attempts were made to utilize this function, however discontinuities in the splined data (as seen in Figure 4.20) were shown to be present, along with aberrant, non existent behaviors such as a wing changing dimensions during the stroke (in other words, instead of interpolating the data as a stroke, the cubic spline would often 'dip' as is seen in the green lines in Figure 4.20 instead of following the stroke).
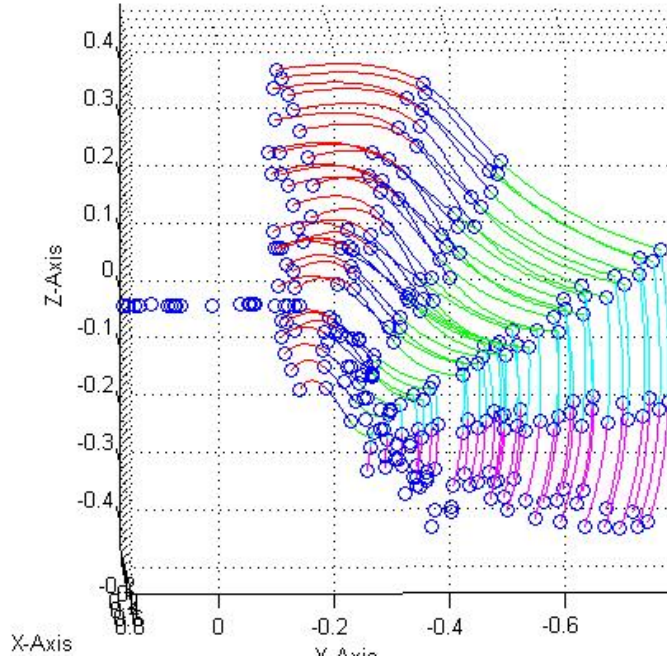
Figure 4.20:   Discontinuities Present in Cubic Spline Interpolation

It was deemed necessary to investigate new avenues of three dimensional interpolation between the points, which landed on a program known as a *Cardinal Spline*.

125

4.5.2 Cardinal Spline. A cardinal spline interpolant is not a new method of splining, rather it utilizes the averaging methods incorporated in such processes as 'overlapping' data. This means that a cardinal spline interpolant observes the 3 dimensional positions of a 'current point' of investigation/consideration and the previous and next point. The interpolant then averages the positions using a parameter known as a **Tension** value. This **Tension** value is typically between zero and one and it acts literally like the tension in a string or wire. A higher tension value would simply yield a straight line in between the points to be splined as it would simulate an 'infinitely tense' wire. Interestingly enough, the cardinal spline would treat these discontinuous lines as one function much like the cubic spline, but of a higher order. A lower tension value would yield a more 'relaxed' wire, forcing the solution to take a longer path. This can be seen in Figure 4.21 [32].
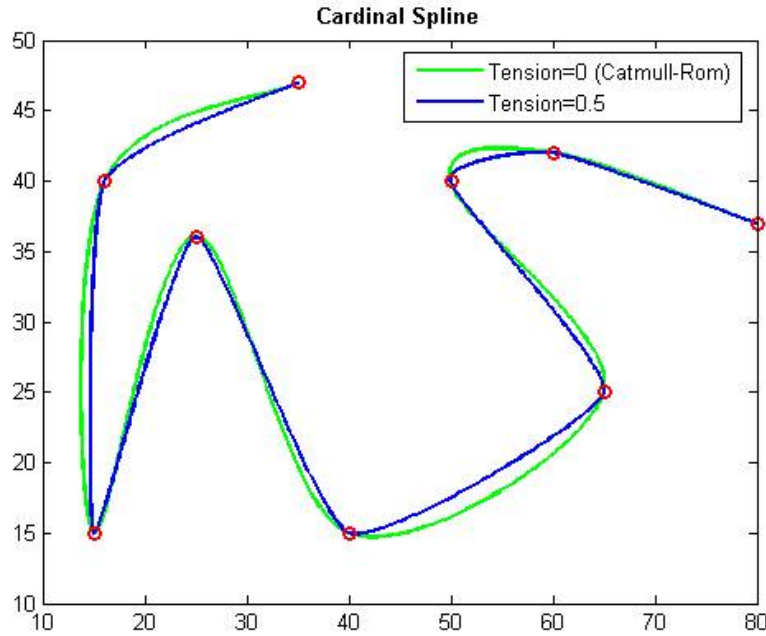
Figure 4.21:   Cardinal Spline Example [32]

The program of choice to use for this study was not designed here, but rather it was downloaded from mathworks.com as one of their available programs created by

126

Dr. Murtaza Khan [32]. The theory was applied in the manner detailed in Appendix C. The splined data would generate a list of points that will be called a *point cloud*.

The *point cloud* could then be constructed (as seen in Figure 4.19) by splining through each of the 33 points on the wing at each angle (thus point 17 on the wing at 64 degrees was connected to the corresponding point 17 on the 48, 16, 0, -22.5 and -43 degree angles). This would allow for the *point cloud* to be added on to for every interpolating spline, thus creating a curved line that was 6*npoints (or as it has been referred to as [u]) long for each of the x-y-z coordinated essentially creating 33 separate 3x6*u sets of data that could be used for the comparison analysis.

Once these values were obtained, it was then possible to utilize this data for comparison purposes. Figure 4.22 sheds light on some of the final operations that were to be performed for this analysis.
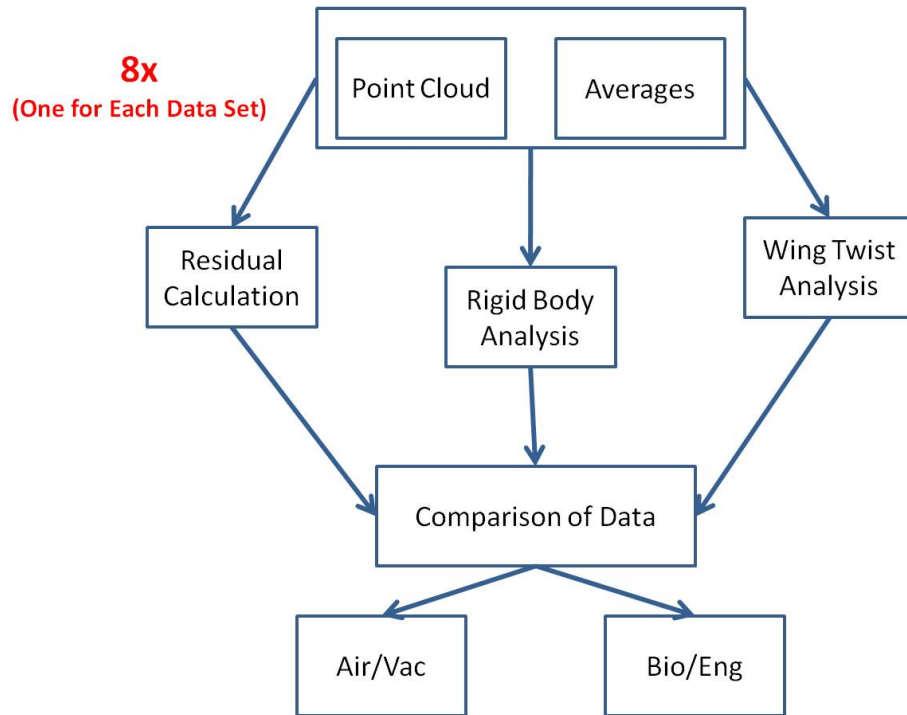
Figure 4.22: Data Manipulation and Comparison Flowchart

4.5.3 Residual Calculation. Before any comparisons or calculations could be made, it was necessary to first understand which reference points on the wing could

127

be considered reliable or trustworthy. As discussed in previous sections, a point-to-point comparison would not be as efficient or useful when comparing the wings as a *characteristic* comparison due to the simple fact that at times Photomodeler would lack resolution in the spanwise direction (due to the limited ability of the camera angles used to capture the images). Instead of examining all points, it was conceived that a more useful and pertinent comparison could be made by examining a few points that could define the characteristics of the wing such as twist and deflection/flapping angle. This would eliminate all issues concerning dimensionality due to the simple fact that it would not even be considered.

Before these points could be selected however, a residual calculation was performed. As mentioned, Photomodeler outputs its residuals in units of pixels, which to someone using Photomodeler makes sense as a reference point is defined on a single pixel, however in physical sense it is almost meaningless as a pixel count is dependent on the resolution of the camera and camera position. It was determined that in order to obtain the conversion from pixels to a physical parameter, it was necessary to re-consider Figure 3.32 which showed the standardized (non-translating) reference points which were separated by 6 mm center to center. Photomodeler allows for the observance of the 'pixel position' as it were for each photograph. In order to convert from pixels to mm, it was necessary to observe the pixel count in both the x and y direction between two of these reference points. Photographs, taken at a standardized location (the lower left location in Figure 2.16 for each of the 6 angles was observed and the positions of the centers of the reference points were observed and tabulated as shown here:

$$Ref_a = \begin{bmatrix} 1249 & 1814 \\ 1167 & 1731 \\ 1386 & 1418 \\ 1371 & 1463 \\ 1229 & 918 \\ 1357 & 938 \end{bmatrix} \qquad Ref_b = \begin{bmatrix} 1347 & 1679 \\ 1170 & 1587 \\ 1388 & 1281 \\ 1371 & 1342 \\ 1217 & 770 \\ 1351 & 808 \end{bmatrix} \tag{4.0}$$

The term $Ref_a(i, j)$ refers to the position the first reference point considered (a) for all six angles (i) in the x-y position (j) respectively- in units of pixels. To obtain the magnitude of the length between them, the following had to occur:

$$d_{ab} = \|Ref_a - Ref_b\| \tag{4.0}$$

Which yielded the differences in the x and y positions for all angles. Following, the magnitude of these two values had to be taken to yield the spatial length that separated them. This was done via the following:

$$dist = \sqrt{d_{ab}(1)^2 + d_{ab}(2)^2} \tag{4.0}$$

Which represented the pixel count for that particular angle that would define 6 mm. This conversion could then be applied to the average residuals at each point to yield residuals in units of (mm). The results of this analysis ultimately lead into the next topic of discussion: The twist angle comparison along the span as a function of the flapper's intended angle. Once conceivable issue that can be seen here is the fact that as the residuals stand, their units exist in (mm). .5 mm of error can be considered a small error for some applications, but it was deemed necessary to consider the actual *effect* that said errors would have on the solution in terms of 'percentage' of effect. The wing itself is 58 mm, however this dimension does not represent the range of values in (mm) that the measurements for some aspects of this study would exhibit.

In order to quantify the affected dimensions, it is necessary to consult Section 4.5.4, which was essentially formed by observing the residuals in units of (mm) to determine which points held the most reliability on the wing.

Using the results of Section 4.5.4 which will be seen to observe the torsional deflections of the wing (by observing the angular difference of the leading edge relative to the trailing edge), it is conceivable to obtain a range of angular deflections associated with the motion of the flapping wing. These angles could be considered a chordwise deflection (3 positions along the spanwise axis), which can be averaged to obtain a general feel for how the specimen would deflect. The maximum and minimum deflection angles could be obtained from this 'average deflection along the stroke' to yield a range angle θ_{range}.

$$\theta_{range} = \theta_{max}^{avg} - \theta_{min}^{avg} \tag{4.0}$$

Which can be applied to the general arc length equation:

$$s_{range} = r_{chord} \cdot \theta_{range} \tag{4.0}$$

The parameter [r_{chord}=18.1533 mm] is the average chord of the wing. Determination of [r_{chord}] was carried out by only considering the points associated with the spanwise calculated torsional angles (to be discussed in Section 4.5.4). Figure 4.23 sheds light on the methods employed to gather the average chord of the wing.

The arc length s_{range} represents the range of deflections (in mm) that will be the parameter that will be scaled against the residuals (in mm) to obtain a 'percent of effect' on the results in the following manner:

$$Residual(\%) = \frac{Residual(mm)}{s_{range}(mm)} \cdot 100 \tag{4.0}$$
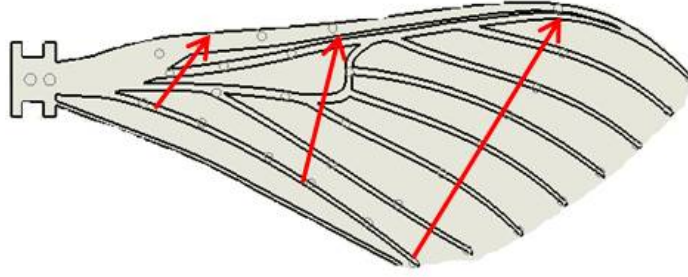
Figure 4.23:   Demonstration of Average Chord Calculation

Table 4.4: S_{Range} Values for Biological Wing

Biological	Downstroke	Upstroke
Vacuum	2.0331 mm	1.2593 mm
Air	4.3927 mm	0.7205 mm
Engineered		
Vacuum	15.4193 mm	2.6544 mm
Air	7.8483 mm	2.0720 mm

Table 4.4 represents the respective arc lengths associate with the above calculations, and are the s_{range} values for each corresponding cases. This information is helpful in determining the overall error associated with the quantitative data involved with this study. Section 4.5.6 shows the methods employed to resolve the level of error associated with the hard data gained from the Photomodeler methods.

4.5.4   Orientation Angle Determination (Torsional Deformations).   It was conceived that due to the fact that a series of reference points (points in space) was the product of the data organization, it was necessary to consider the topic of vector mechanics. Theoretically speaking, a vector can be defined by two points. Should two vectors share a single point, then those vectors can ultimately define a plane. Taking the crossproduct of the two vectors that share that single point will yield a vector at the common point that is orthogonal to the plane defined by the previous two vectors. Normalization of this vector gives potential to comparison to other vectors. If one were to do the same for a standardized, global axis system (that has been normalized), it would create a normalized, global vector for comparison. The angle with respect to

131

the dot product of this would yield the directional cosine of the angle between them, which essentially represents the **orientation** of that plane with respect to a global axis.

$$\vec{u_n} \cdot \vec{u_{global}} = cos(\theta_{twist}) \tag{4.0}$$

To visualize this in a simplified manner, Figure 4.24 shows how this may work, where both vectors are normalized and matched up to each other. The global reference and the measured wing vector of course does not have to share any sort of common point, but their characteristics in relation to each other are what should be of note (See the above equation)
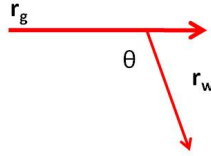
Figure 4.24:   Demonstration of Vector Treatment

The point at which the local vector was formed was the common point of the two vectors used to make the plane that existed on the flapping wing. This would be essentially indicative of the wing's deflection in the spanwise direction. Figure 4.25 is a two dimensional illustration of this concept as it essentially uses the information presented in Figure 4.24 an applies it to a top view of the wing (a view along the spanwise direction/corssectional view).

As was mentioned, it was necessary to consider 'reliable' points for this analysis that still would capture the twist associated with the given plane along the span of the wing. After observing the highest residuals (least certain of the data), points were selected that would be used to form the normalized 'orientation vectors'. Figure 4.26 gives a graphical depiction of the selected points based on the best (or most reliable) data that would serve to capture the twist associated with the flapping wing.

To prove that these points are the most pertinent, it is necessary to examine the residual plots as seen in Appendix B. To represent this 'reliability' the points shown
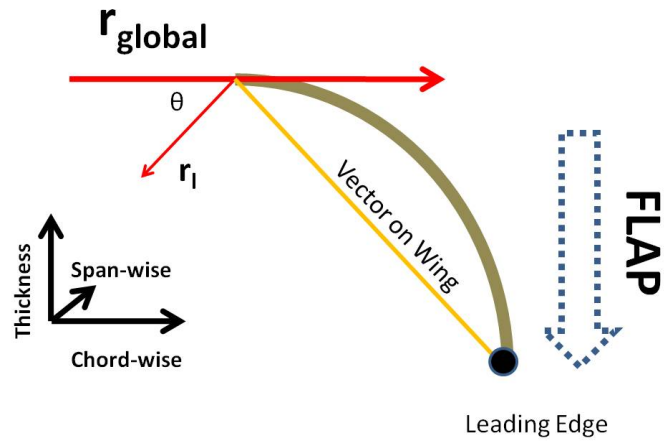
Figure 4.25:   Demonstration of Wing Orientation Vector Treatment
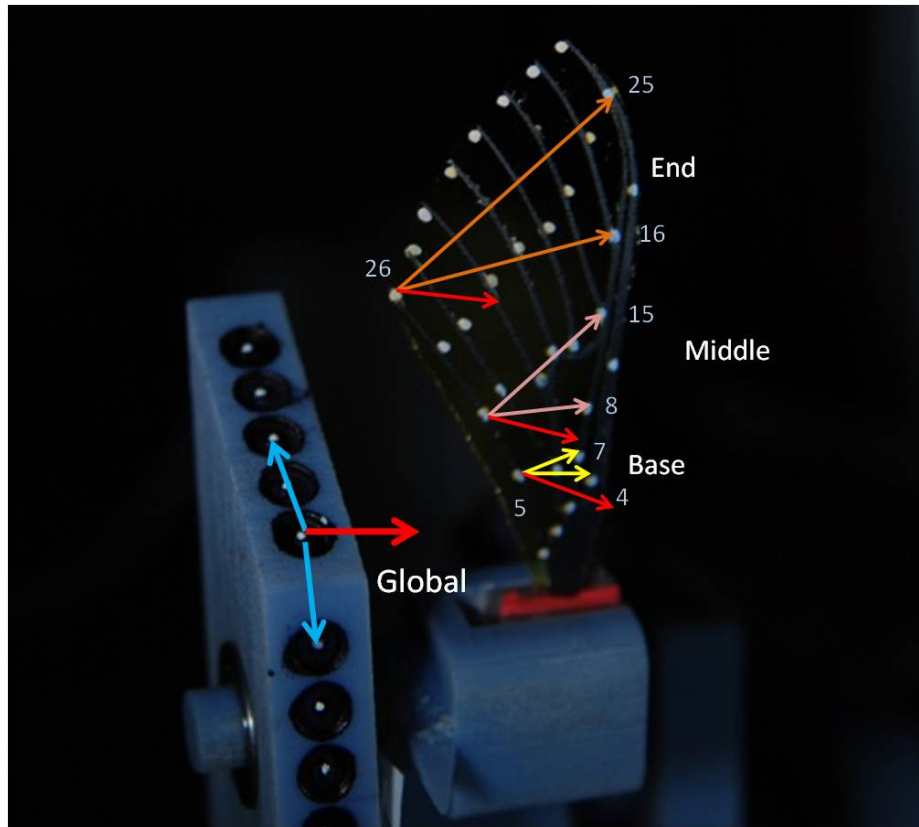
Figure 4.26:   Vectors Formed on Wing to Determine Spanwise Orientation/Torsional Deformation

to form the vectors in Figure 4.26 were pulled from their corresponding positions in the residual plots, averaged about their first dimension (ie the average was taken for

all 6 observed angles) and then averaged again for all four trials per wing (2 upstroke
and 2 downstroke in air and vacuum per wing). Figure 4.27 sheds light on the level
of certainty associated with the points chosen to represent the twist at each portion
of the span.
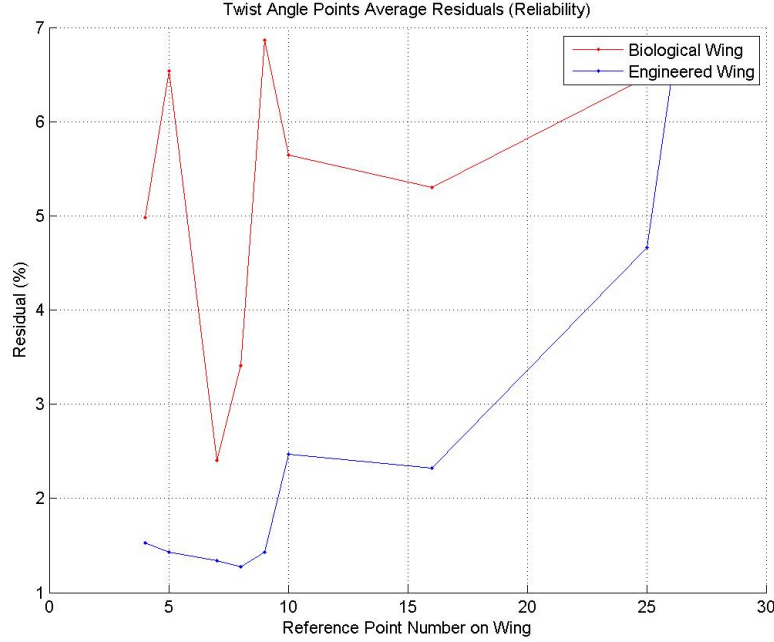
Figure 4.27:   Certainty Associated With Points Chosen to Represent Planes

It can be seen in Figure 4.27 that the highest level of uncertainty exists at less
than 7% (which corresponds to a quarter of a millimeter at point 26 on the engineered
wing). All others lie far below this level, thus granting confidence that these points
can be used to accurately depict the orientation of the wing's leading and trailing
edges along the spanwise direction with respect to the globally defined axis.

*4.5.5   Flapper Angular Displacement vs. Wing Angular Displacement: A Like-
ness to Rigid Body Motion.*   Similar to that of the previous analysis, it was deemed
pertinent to investigate the effect of the flapping in the spanwise direction, that is to
compare the angle that the flapper saw as opposed to that of what the wing emulated.
This sheds light on the SW deflections inherent in the flapping motion. This analysis

134

is somewhat simplified in that it requires little or no effort to construct the vectors for investigative purposes. Needless to say, it is necessary to show here the vectors utilized as the normalized global vector can be represented by the **y-axis** alone. The vector in question would be the one represented by points 4 and 9 on the wings as it finds itself on the leading edge of the wing. Figure 4.28
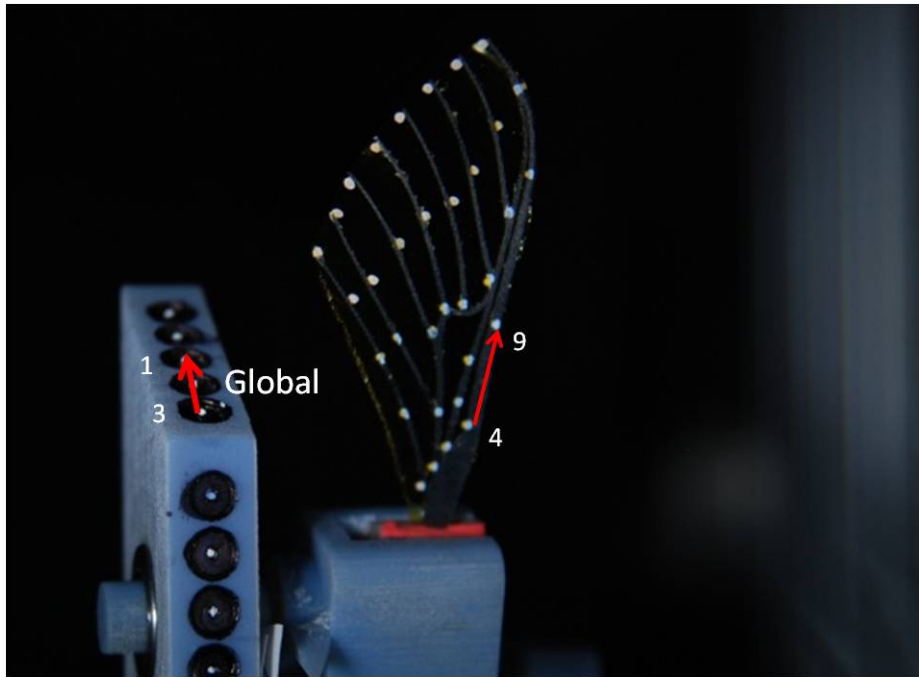
Figure 4.28:   Depiction of Vectors Used to Observe Wing Angular Displacement

This progresses much in the same manner as the spanwise-planar orientation operations in that the dot product of the normalized global and wing vectors will yield the angular cosine of the displacement angle. These displacements could then be compared to the rigid body analysis seen in Chapter 2. It turns out that there was some slight modifications that had to be made to the results of this data however. If one were to differentiate the values from Table 4.2, one would notice that for the most part the difference between the phases lies in and around 32 degrees. This means that there is about a 10% difference between phase delays/flapping angular displacement positions. The Cardinal Spline takes care of these 10% differences by interpolating in between them. The only area that the spline does not address is the

(a) Downstroke at -43 deg

(b) Upstroke at -43 deg
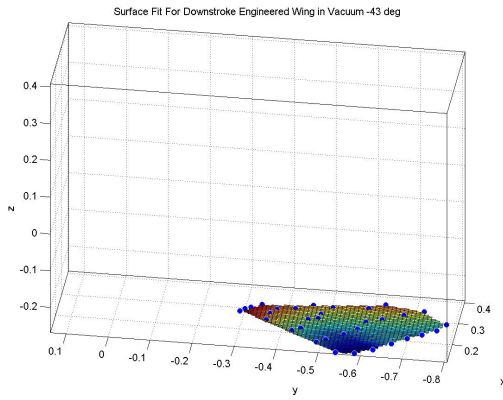
(c) Surface Fit of Downstroke at -43 deg
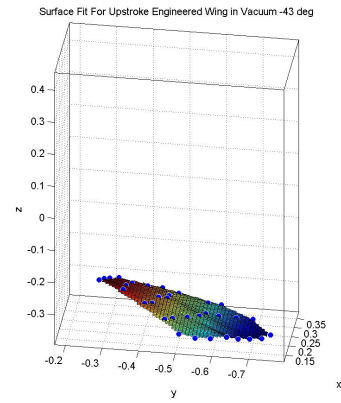
(d) Surface Fit of Upstroke at -43 deg

Figure 4.29:   Downstroke and Upstroke Comparison of Engineered Wing in Vacuum

transition between the upstroke and downstroke. In the data there is a discontinuity
at this point in the stroke. To obtain the data between strokes is a mission perhaps
for future study, but this discontinuity proves problematic in that it makes the data
appear erroneous. Figure 4.29 sheds light on this dilemma for the engineered wing in
vacuum.

As can be observed in 4.29, there does in fact exist a difference in the wing
displacements, even though each of them theoretically exists at -43 degrees. As a
result, it was determined that the data needed to be 'padded' in that 5% of the total
number of data points would be set to a non-number as there existed no data at those

points. This will be shown as an area with no data present in the results section that is emphasized by vertical lines. This operation was preformed purely for aesthetic reasons, but it does raise a few questions as to the nature of this transition.

4.5.6 Error Analysis. Chapter 5 will display the results of the above operations. Results however are always subservient to the uncertainty associated with the data gathering methods. Fortunately, Photomodeler provides the residual values on a point-to-point basis. Section 4.5.3 discussed the treatment of these residuals to turn them from units of 'pixels' into a 'percent of torsional deflection'. Figure 4.27 extrapolates the point residual values (in %) associated with the points that are resposible for providing this thesis with the bulk of its conclusions.

The residuals associated with the points shown in Figure 4.27 will also contribute to the overall error in this analysis. It is important to shed light on the calculation of the error (to be shown in the form of error bars in the torsional deformation plots in Chapter 5) since this will ultimately determine the accuracy of the conclusions to be made in Chapter 6. In order to calculate the error, the first parameter to be considered is the % uncertainties in Figure 4.27. There exist 9 points plotted in that figure, however as can be seen from Figure 4.26, the points work together three at a time to form the orthogonal vecotr used in the calculations, so all three contribute to the error. It can thus be said that since all three points contribute to the error, then all three % uncertainty values ($\%_{uncertainty}$) must be summed to yield a total error for the orthogonal vector:

$$\%^i_{uncertainty} = \sum \%^i_j \tag{4.0}$$

Here, the parameter (i) denotes the plane region (base, middle, tip) which is composed of 3 (j) points. The total percent uncertainty can then be multiplied by the total range of displacements associated with that deflected region to yield an error

137

Table 4.5:   Total Error for All Cases in Torsional Deflection

Bio Downstroke	Base	Middle	Tip
Vacuum	1.21 deg	0.69 deg	1.28 deg
Air	1.34 deg	1.40 deg	4.58 deg
Bio Upstroke			
Vacuum	1.39 deg	0.43 deg	0.66 deg
Air	0.40 deg	0.48 deg	0.64 deg
Eng Downstroke			
Vacuum	1.07 deg	2.68 deg	9.26 deg
Air	0.47 deg	1.29 deg	5.17 deg
Eng Upstroke			
Vacuum	0.22 deg	0.44 deg	2.17 deg
Air	0.19 deg	0.32 deg	1.21 deg

value (in degrees) for that particular data set. Table 4.5 shows the actual values to be used as error bar plots in Chapter 5.

Table 4.5 displays several variances associated with the estimated error for this analysis. Though some of these may seem insignificant, they do in fact pose issues for those cases that did not show high amplitudes of torsional deflection.

4.5.7 Spline Verification.   As will be seen in Chapter 5, the splined data that was treated in the manner described above is utilized to gain insight into many of the results gained from this data. Though the splined data technically grants a glimpse of an almost continuous look into the behavior of the flapping wing, it is important to realize that the spline is the program's version of a *calculated estimate* of the behavior in between the hard data. Conveniently, the Cardinal Spline places a specified number of points in equal spacing from each other between each of its segments. This is how it is possible to estimate a twist angle that was not conceived from the raw data, rather the estimate. Furthermore, this treatment allows for 'easy indexing' as the number of points between hard data segments is known.

Because the spline fit represents the basis behind many of the plots in Chapter 5, it is necessary to examine the actual 'level of estimation' in the manner of a percentage error. Figure 4.9 grants insight into the several data sets taken, but during testing it was deemed pertinent to examine an extra angle, be it the **-11.25** degree in the upstroke of the biological wing for both air and vacuum. Though this angle was ultimately not used in the calculation of the results or the spline treatment, its gathering found purpose in the verification of the spline- i.e. comparing hard data to the 'estimated data'. This would grant a certain aura of trust concerning the interpolated data.

In order to perform this task, it was necessary to obtain the three data sets of the -11.25 degree angle (three data sets for averaging) from Photomodeler. Once gathered, the data was processed in the manner of Figures 4.17 and 4.19 to obtain a point cloud of only 1 set (as opposed to the 6 x npoints of the splined data). It would have been an appropriate to make a point-to-point comparison as often the wing found a tendency to slightly shift in the spanwise direction, however the twist angles described in Section 4.5.4 could possibly grant a more informative look into the actual 'trustability' of the spline fit.

Figure 4.30 displays this 'trustability' of the spline fit in the manner of comparing the twist at the splined -11.25 upstroke angle and the gathered -11.25 upstroke angle of the biological wing. It can be seen that the most difficulty is seen in the center of the wing, but surprisingly enough the tip appears to behave quite well in terms of the percentage difference. The results here are what ultimately lead to the determining of the appropriate value for the 'Tension' discussed in Section 4.5.2. The Tension value that yielded the lowest overall percentage error was the one selected for the data presentation in this thesis.

This percent error sheds light on the fallibility found in the splined data presented in this report. Since the splined data yielded less than 2.5% error from the
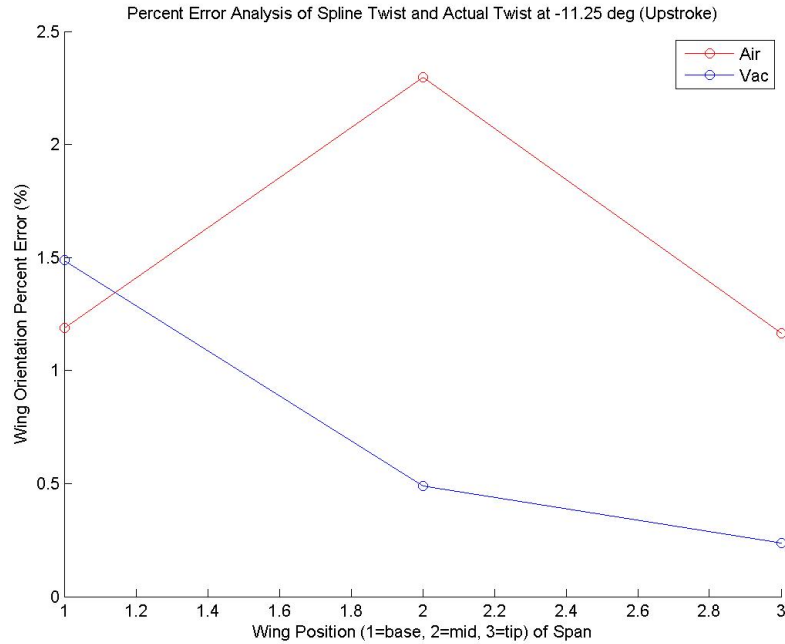
Figure 4.30:   Percent Error in the Spanwise Planar Orientation With The Cardinal Spline Vs. Gathered Data

gathered data, it is safe to say that this splined data is usefull in the presentation of results.

4.6   Summary

This section served to highlight some of the physical actions that had to be taken for the successful execution of this study. Preliminary actions were taken to ensure that the data gathered from photogrammetry was as accurate as possible by means of camera calibration. The test structure was discussed as a means of ensuring that all experimental procedures were as standardized as possible, eliminating any room for leeway in the comparison of the two wings. Following, the actual experimental procedure there was lengthy discussion on the methods that would need to take place should this experiment be repeated.

Once data was gathered, it was necessary to discuss the details that went into the data harvesting process associated with photogrammetry and the Photomodeler

interface. Once gathered, it is necessary to discuss at length the algorithm details associated with the data manipulation process, shedding light on some of the methods employed to eliminate any fallacies associated with the data visualization and comparison process.

V. Results and Discussion

The aim of this section is to discuss the research findings associated with the evaluation of both the biological and manufactured wing under flapping conditions in both air and vacuum at 12.5 Hz. It may be helpful during the analysis to observe the following items:

- Section 4.5 which gives details on the data handling processes.

- Appendix A which grants access to some of the actual data pieces used in the analysis (photographs used in photogrammetry process) and their corresponding surface fitted data sets. This serves to better visualize the wings' flapping behavior when observing the comparative analysis.

- Appendix D which shows the raw and averaged data sets. These plots were not necessary to include in the analysis section but the information that they display was helpful in understanding how the data was treated and what in fact the flapping wing looks like during each of its strokes. It is important to keep in mind that the averaged data is what was used for the comparative processes that are to occur in this chapter.

  This section will display the following:

- The splined data visualization will be displayed for the purpose of observing the behavior of the data sets themselves (for example: make observation on the behavior of the biological wing in vacuum for both the upstroke and down stroke).

- Comparisons will be made for the spanwise orientation of the leading edge to the trailing edge as it compares to air and vacuum, beginning with the biological wing and then moving to the engineered wing.

- Once observations have been made concerning the behaviors of the Air/Vacuum differences of each of the wings as they compare to themselves, it will then be necessary to compare the behavior of the wings as they compare to each other under the same conditions.

- Following the wing comparison, the spanwise orientation of the leading edge to the trailing edge data will be displayed as a 'full stroke' in order to compare the downstrokes and upstrokes of each of the wings in both air and vacuum as it will aid in visualizing the biological wing's complexities

It should be stated before results are discussed that previous research proffered several findings, three of which will be compared to the findings presented in this focus of inquiry. These findings are as follows:

- Norris observed a damping to the SW bending of the flapping wing due to the presence of air

- Combes and Daniel observed the same when executing a flapping analysis

- Though Combes and Daniel are biased towards the inertial dominance of the motion, both researchers agree that air does in fact have a significant effect on the motion of the wing

5.1 The Splined Data and Observations

Chapter 4 discussed the curve fitting (or splining) of the three dimensional reference points as the wing moved through its flapping motion using a Cardinal Spline. For this particular analysis, the tension value was set to **Tension=0.75**. This disallowed for the data to be 'too taught' but it also kept the splining under control in that too much 'slack' yielded results that could be considered useless as too high a tension would sometimes make a wing change dimensions during the course of the flapping motion. The determination of the tension process was an iterative one that was based on the percent error discussed in Chapter 4.

All six data points per half stroke were used in the splining process, however, keep in mind that plots will yield different colors for every segment that was evaluated under the Cardinal Spline. The rationale for this procedure is for aesthetic and evaluative purposes since it aided in the recognition of the raw data sets that were generated from the experimental process discussed in Chapter 4. The separation

clearly was not equal (especially in the case of the engineered wing) but for this study, a standardized **40 points** between segments was utilized in order to observe the data.

To begin, the biological wing was splined for both air and vacuum. Figure 5.1 represents the splined data set for the biological wing in the down stroke in vacuum. Both figures are of the same data, but for visualization purposes, it was considered pertinent to observe the wing behavior from two views.

Figure 5.1 grants a glimpse of this downstroke behavior. The side view does not capture however the seemingly aberrant behavior of the top view, as one would normally expect the data to travel parallel throughout the stroke. This concern can be addressed however by recognizing that the set axes reference points (plotted in blue circles) do not translate back and forth, calling into question the 'zig-zag' pattern seen by the top view of Figure 5.1. What was brought to focus was the fact the the back and forth-non parallel nature of the data is a result of the passive twist exhibited by the flapping wing. This became apparent when observing high speed video of the wing flapping in the DeLeón Flapper which quite literally shed light on the inherent twist of the wing present during the flapping motion.

Figure 5.2 displays the other half of the Bio-Vacuum analysis. What is important to observe here is that Figure 5.1 and Figure 5.2 are different. The fact that the observed torsional deformation seems a little more dramatic in the upstroke may suggest an elaboration on the wing's dynamic behavior wherein throughout the course of the stroke amplitude, the wing *may not* necessarily behave the same in the downstroke as does the upstroke; a difficult feat to mimic when designing a wing based off of biological design. Wooton [22] discussed the possibility of anisotropic, almost mechanically designed, behavior associated with the construction and formulation of the proteins as they form the 'veins' that provide the rigid (but flexible) structure of the wing. The twist will be discussed in more detail later in this chapter.
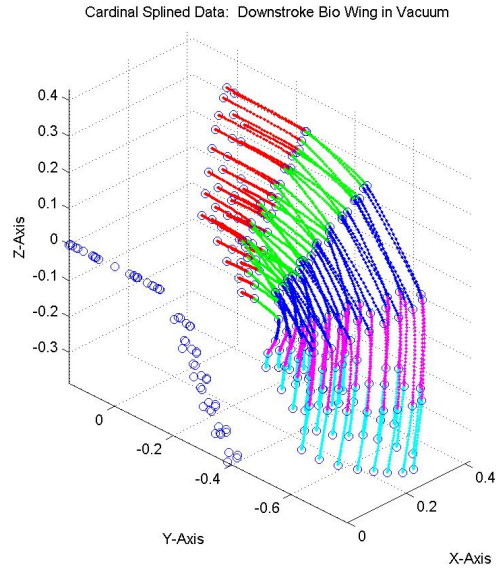
(a) Side View
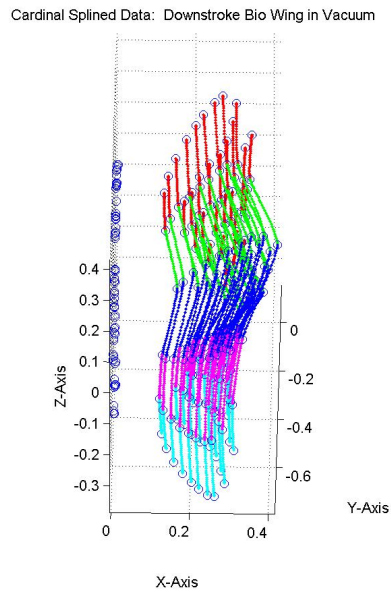
(b) Top View

Figure 5.1:   Splined Data for Biological Wing Flapping in Vacuum in the Down-
stroke

145
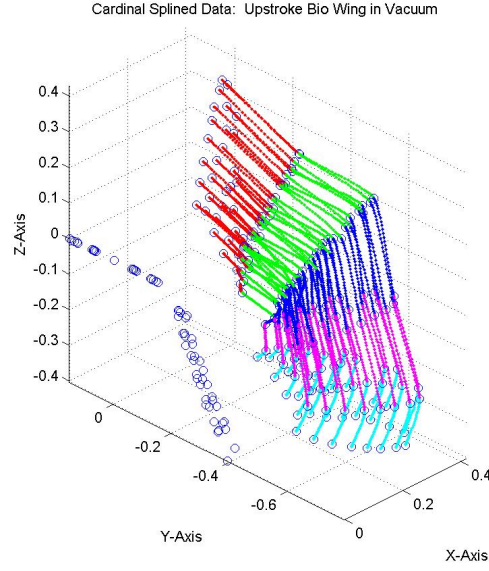
(a) Side View
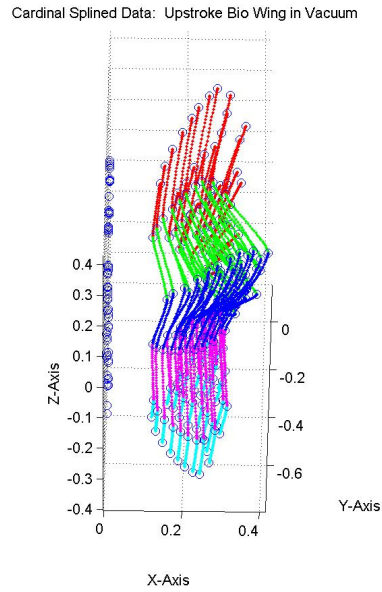
(b) Top View

Figure 5.2:   Splined Data for Biological Wing Flapping in Vacuum in the Upstroke

Figure 5.3 displays the splined data of the biological wing in the downstroke flapping in air. Surprisingly, it can be seen in Figure 5.3 that the top view shows very

146

little of the 'zig-zag' motion as compared to that of the downstroke in vacuum. As discussed in Chapter 1, observations by Norris [1] and Combes and Daniel [7] showed that the air acted as a damper to the amplitude of the dynamic behavior of the wing.

As a result, Combes and Daniel claim to have had to place a 10% damping coefficient on the wings during their FEA flapping tests based on observations rooted in photogrammetry as was done here. Though these spline fit figures only serve as an observational, non-analytical tool, it is important that some of these considerations be made so when the analytical portion comes to fruition, as some of these behaviors will become more clear.

Figure 5.4 depicts the biological wing flapping in the upstroke in air. From the top and side views, little can be inferred as to the difference between the downstroke and upstroke in air of the biological wing as there is not an apparent change in the 'zig-zag' observations made by the Bio-Vacuum analysis. Though different, this may in fact be helpful for engineers to understand due to the simple fact that this degree of difference is somewhat curbed by the presence of air.
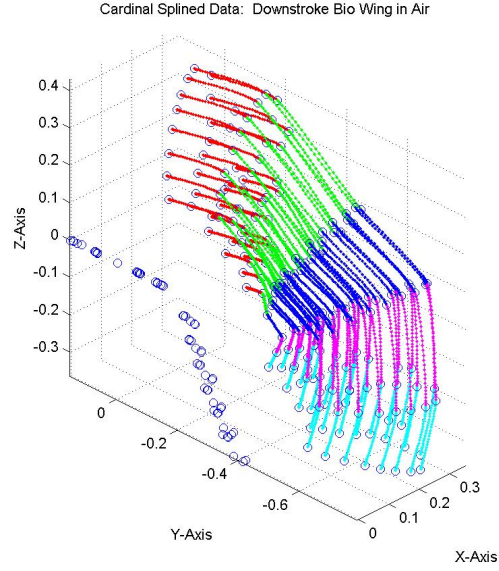
(a) Side View
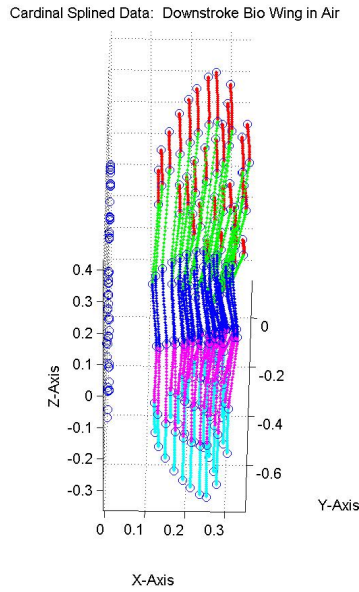
(b) Top View

Figure 5.3:   Splined Data for Biological Wing Flapping in Air in the Downstroke

What these depictions of the biological wing in air and vacuum indicate is the importance of the **aeroelastic question** investigated by Norris [1] and Sims [4] in
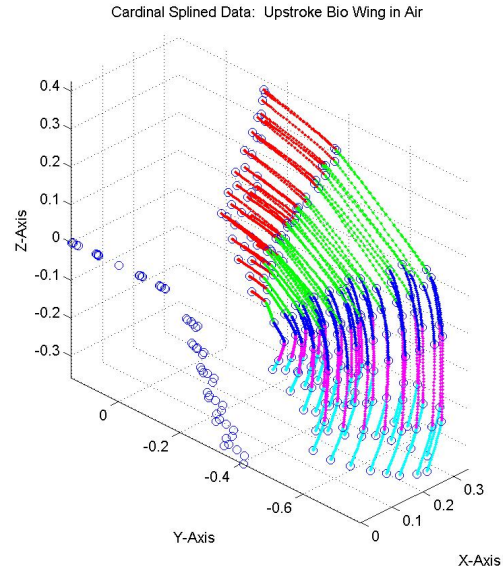
(a) Side View
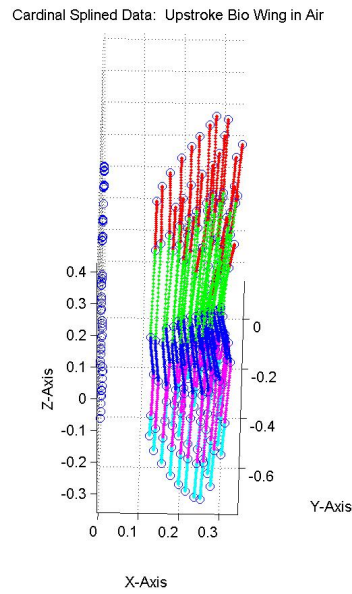
(b) Top View

Figure 5.4:   Splined Data for Biological Wing Flapping in Air in the Upstroke

which there is a clear presence of *both* an aerodynamic and inertial effect that dictates the dynamic behavior of the wing.

Cardinal Splined Data: Downstroke Engineered Wing in Vacuum

(a) Side View

Cardinal Splined Data: Downstroke Engineered Wing in Vacuum
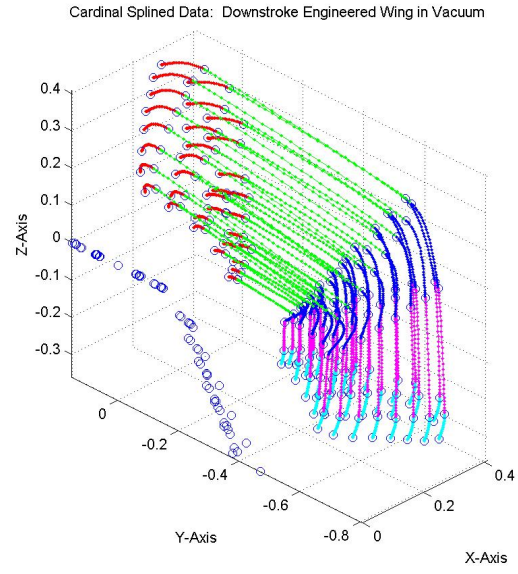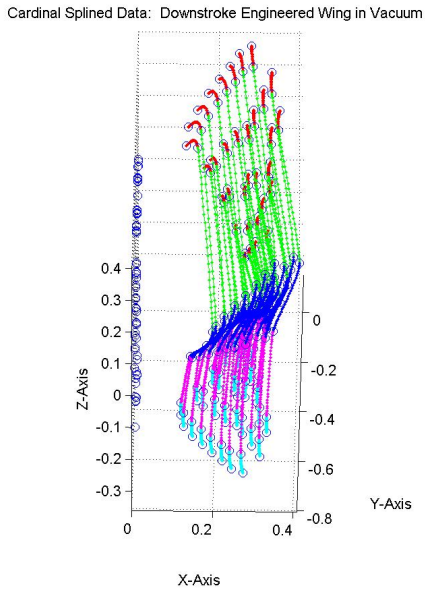
(b) Top View

Figure 5.5: Splined Data for Engineered Wing Flapping in Vacuum in the Down-stroke

150

Figure 5.5 displays the downstroke of the engineered wing in vacuum. Upon observation of Figure 5.5, it becomes very clear that though the modal analysis predicted that the results of the engineered wing would yield similar results to that of the biological one, the behavior when subjected to the flapping conditions was in stark difference. The first observation that should be made about Figure 5.5 other than the almost discontinuous level of torsional deformation about the leading edge, is the complete lack of even distribution along the stroke path's amplitude; especially at the top of the stroke. It would appear from initial observations that there was a mistake in the data gathering process, but after repeated testing, it became apparent that the small angular and translational displacements of the wing at the beginning of the stroke was an inherent dynamic property of the wing. When looking at the two perspectives here, it is clear that at the 48 degree position that the engineered wing experiences more flexion and twist than translation- a clear difference from the biological wing who exhibited a more even distribution along the stroke path.

Figure 5.6 depicts the engineered wing flapping in vacuum for the upstroke. Without so much as a glance, it is very clear that the behavior of the wing in the upstroke is in stark difference to that of the wing in the downstroke. It would appear that the engineered wing experiences far less flexion in the upstroke- a major difference from the biological wing that appeared to twist more on the upswing (much like a paddle in water).

It is clear that the data displayed in Figure 5.6 does in fact experience some torsional deflection, but certainly not to the degree as was seen in the downstroke. Original conceptions at rationalizing this behavior pointed towards the accelerations due to the kinematics of the flapper, and as was seen in the regression analysis that the DeLeón Flapper failed in comparison to the biological design. Interestingly, what Figure 2.7 does show is a failure to reach the amplitude of accelerations exhibited by the other flappers. This is only restated as a possible explanation for the behavior seen in Figure 5.6 as compared to Figure 5.5, which appears to retain a far more diverse leading edge to trailing edge displacement throughout the stroke amplitude.

151
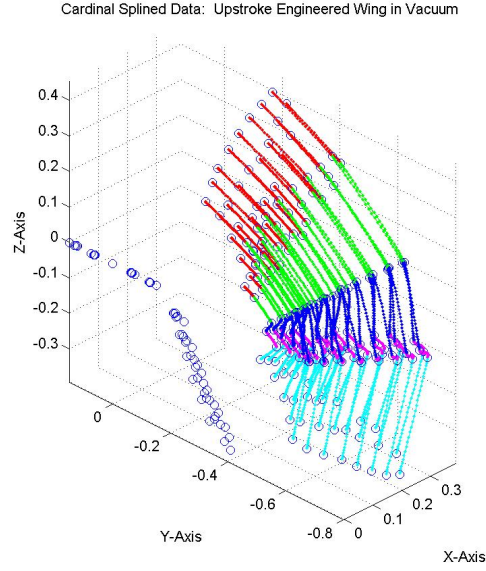
(a) Side View
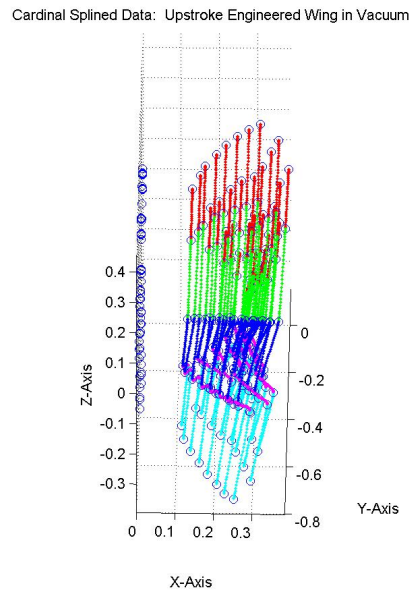
(b) Top View

Figure 5.6:   Splined Data for Engineered Wing Flapping in Vacuum in the Upstroke

This outcome questions the engineered wing's design due to the simple fact that though similar in stiffness to the biological wing for the first mode, the engineered

Table 5.1: Modal Analysis of Biological to Engineered				
Wing	**Weight) (UnMarked)**	**Weight (Marked)**	**1st Mode (Air)**	**1st Mode (Vac)**
.16 mm Carbon	61.7 mg	62.0 mg	59.06 Hz	78.13 Hz
Biological (D)	73.3 mg	68.5 mg	64.75 H Hz	115.00 Hz

wing appears to retain a lower second mode (torsional) as compared to the biological. The effect of this lack of stiffness in the torsional mode can be seen through these results wherein the engineered wing's orientation plane retains much higher values for this torsional mode as is reiterated in Table 5.1 which is taken from Chapter 3.

Figure 5.7 depicts the engineered wing flapping in air for the downstroke. It can be seen here that the same 'whipping' motion at the top of the stroke is seen by the down stroked wing at the beginning (48 deg) however the violent twisting associated with the flapping motion in vacuum of the engineered wing appears to be damped similar to the biological wing.

The torsional deflection does in fact seem to still occur however and as is seen in Figure 5.8, which depicts the upstroke of the engineered wing in air. It is clear that in this portion of the stroke, the mid-stroke twist is a little more extravagant, however it would appear that the twist angle is the reverse of what was originally conceived as being the 'proper' form of displacement in that the wing appears to 'flip up' on the upstroke (not what would be seen by the biological wing). Clearly this owes itself to the inertial behavior of the wing's structure as air would have damped/reversed this motion.

5.2 Comparison to Air and Vacuum: The Deviation of Angular Orientation About The SW Axis and Angular Displacement

Each wing's data was subjected to the methods of SW orientation analysis as described in Chapter 4 in the Algorithm Details. Three separate planes were analyzed based off of three reference points that could define a plane of which the vector normal to that plane could be evaluated. The directional cosine was evaluated with respect
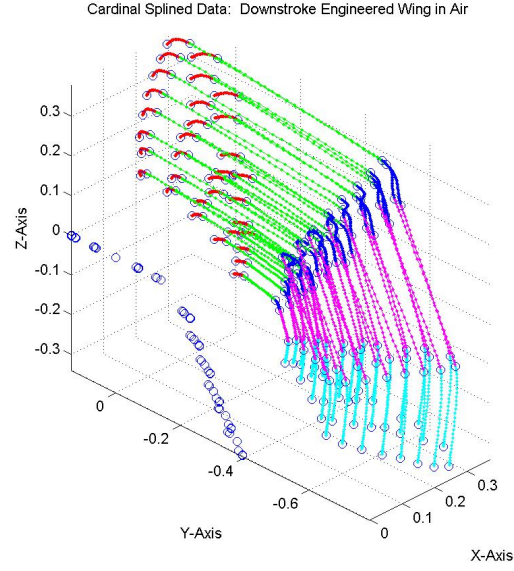
(a) Side View
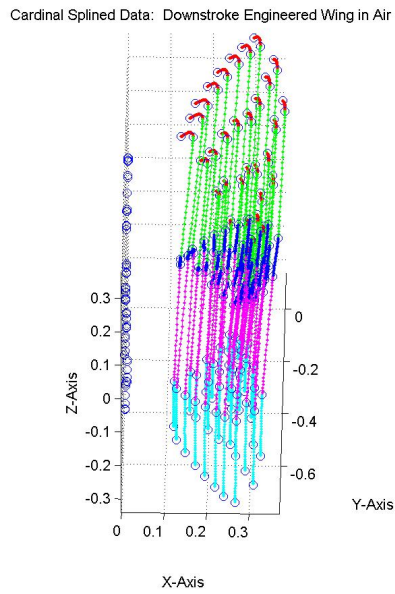
(b) Top View

Figure 5.7:   Splined Data for Engineered Wing Flapping in Air in the Downstroke

to a standardized normalized 'global' axis system and the resulting angle represented

the angle away from parallel to the global axis. Error bars are displayed at the actual
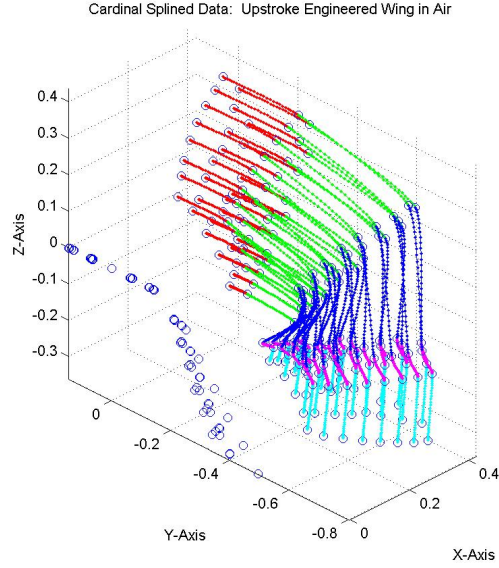
(a) Side View
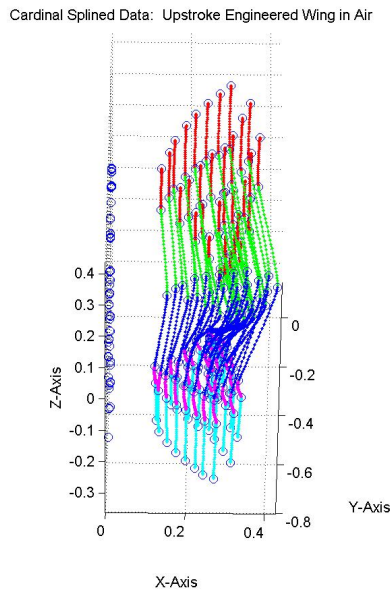
(b) Top View

Figure 5.8:   Splined Data for Engineered Wing Flapping in Air in the Upstroke

data points. This was done to point out that the spline does conform through the actual, experimental data, and to illustrate the error associated with the taken data.

The orientation associated with the biological wing was evaluated in three positions for both the upstroke and downstroke. Figure 5.9 depicts these angles of the biological wing flapping in air and vacuum. The continuous lines represent the splined data and the blue dots correspond to the data points associated with the spline for verification of spline purposes.

Observance of Figure 5.9 would indicate that a higher amplitude of deflection from global axis was seen by the downstroke of the wing in air (red), but for the upstroke the air appears to drop far below that of the vacuum, indicating that perhaps rather than acting as a damper to the deflection mentioned in the last section, it would seem that the presence of air amplifies it. Both air and vacuum's data appears to slightly drop in amplitude in the upstroke, which is indicative of the wing flattening out or 'flexing back' on the upstroke. Later in this section, a few brief observations will be made on the differences between downstroke and upstroke.

Further discussion of Figure 5.9b indicates that there seems to exist an out lier which is represented by the red thick line (which is the base of the wing- or the bottom most plane). The data would appear to state that the base of the wing experiences a far more dramatic flexion than that of the other two evaluative planes, rather a change in flexion from point to point appears present. It is also necessary to point out that the axis for the upstroke is, more of a deflection as in Figure 5.2. The error associate with the upstroke seems high, especially for the tip, however, it would appear that at the extremes, the error does not affect the general trends shown in terms of the behavior of the wing.

Figure 5.10 sheds light on the behavior of the engineered wing when subjected to both air and vacuum. It would appear here that there is a stark difference in the amplitude of deflection (orientation from the global) between air and vacuum for the downstroke. What is important to realize for the downstroke is that like in the biological wing, the air data appears to amplify the deflection about the spanwise axis. Unfortunately this high magnitude of deflection re-confirms data presented earlier in
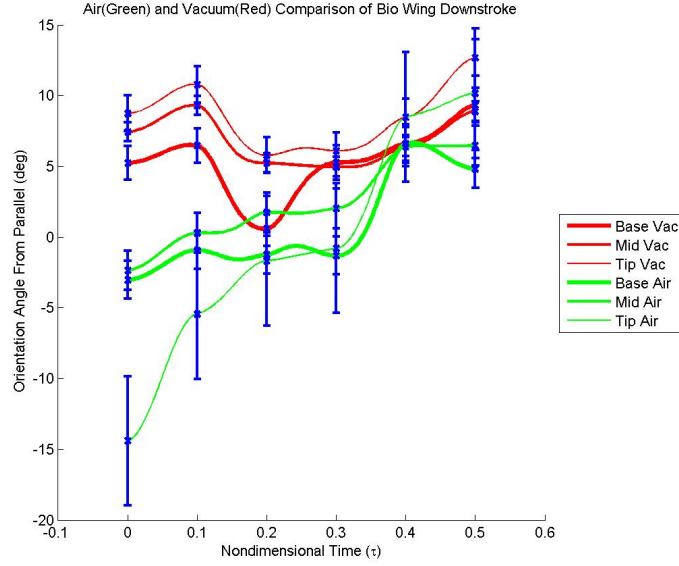
(a) Downstroke
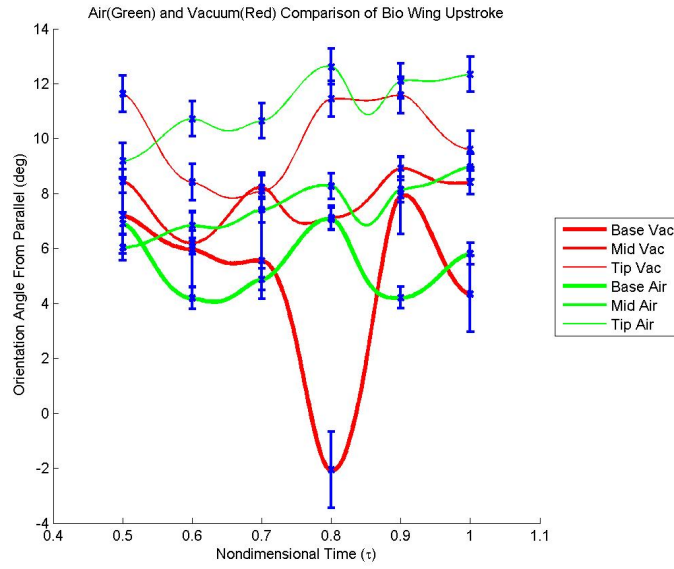
(b) Upstroke

Figure 5.9:   Planar Orientation of Biological Wing Splined Data in Air (Red) and Vacuum (Green) with Hard Data Points (Blue) for All Three Planes

that the engineered wing is behaving contradictory of what is expected in that when observing the biological wing, which in the downstroke appeared to 'scoop' the air, and then allow the air to pass over it easily on the upstroke. Error present in this display appears to have little bearing on the engineered wing, mainly due to the high amplitudes of deflection seen by the wing, especially in the downstroke.

Figure 5.10 does appear to exhibit qualities of common phase (regardless of amplitude for both the air and vacuum separately). This shows that the wing deflects as a unit as the solid line is the furthest from the base, and thus more spectacular amplitudes of twist can be seen at the tip of the wing (thinner lines) than at the base.

An additional observation that can be made for both Figures 5.9 and 5.10 is this appearance of the consistency along the span (or lack thereof) which demonstrates this planar deflection. Even in terms of error, it would appear that the wing would still behave in this seemingly uniform matter. It would appear that for both wings, the three lines that represent the data in vacuum appear to lie closer to each other in magnitude when in vacuum where as more of a spread is seen in air. This sheds light on the effects of air on the wings (specifically the biological wing) in that air contributes to a deflection that is not uniform along the span. The only place that this could be argued is the downstroke in air of the biological wing as seen in Figure 5.9a wherein both data sets appear to be reasonable close to one another, especially when compared to the plot next to it that has vector cosines that are not at all close. This again illuminates this idea of 'scooping' that is associated with the flapping wing in the downstroke and the passive 'flip' associated with the upstroke that allows the air to pass over the wing with minimal 'scooping' as that would contribute to a force in the downward direction. This complexity associated with the biological wing is rather disconcerting in the realm of manufacturing, as previously stated.

In terms of the angular displacement as seen by the flapper compared to the displacements seen by the wing (as discussed in Section 4.5), Figure 5.11 sheds light on this topic. The red vertical lines here illustrate the previously discussed 'padded'
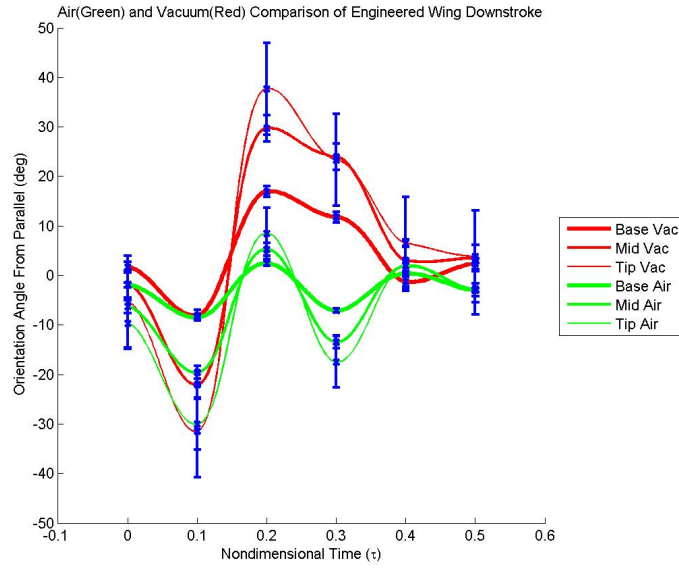
(a) Downstroke
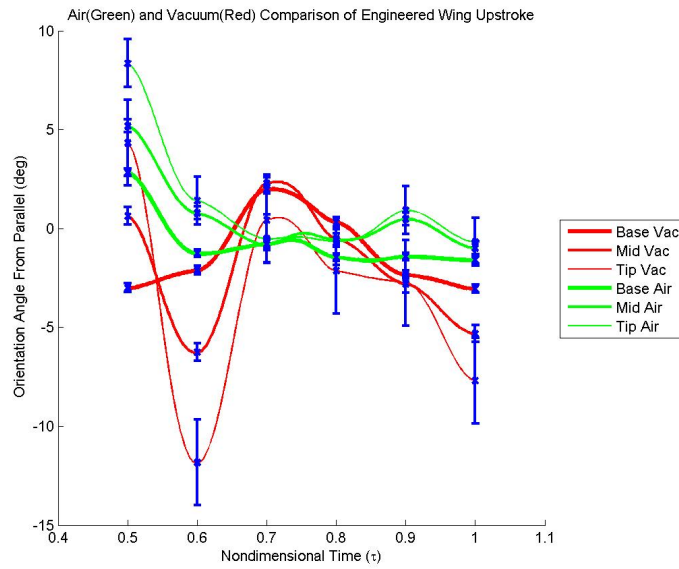
(b) Upstroke

Figure 5.10: Orientation of Engineered Wing Splined Data in Air (Red) and Vacuum (Green) with Hard Data Points (Blue) for All Three Planes

data wherein the transition between downstroke and upstroke was not captured in this study.
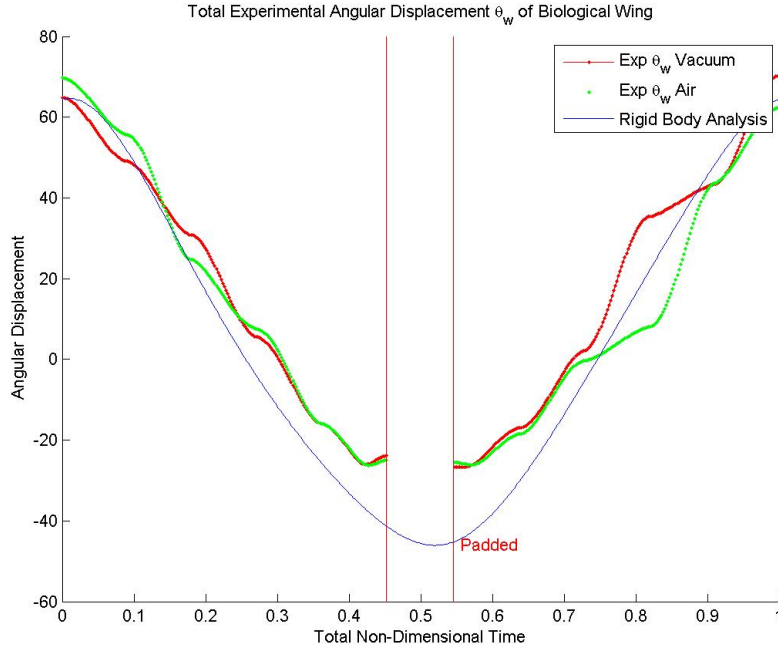
Figure 5.11:   Biological Wing Angular Displacements in Air (Red) and Vacuum (Green)

Figure 5.11 shows that the wing does not quite follow the rigid body analysis exactly, however the behavior of the wing seems to stay consistent with the RBA. The biological wing would appear to deform away from the almost sinusoidal behavior that was seen in the rigid body analysis for two possible reasons:

1. The spline fit places unseen/imaginary deformations/beam-like deflections due to 'too much slack' associated with the tension value

2. The wing actually experiences deflections that are not linear in the course of the flapping motion.

In the end, though different, this analysis shows that in the realm of angular displacements and/or spanwise bending, the wings exhibit no unexpected behavior in terms of the flapping motion or the angular displacement in flapping during the

160

strokes. It would appear that the amplitude of the stroke is not fully realized by the data presented when compared to the rigid body motion as this fact is clear at the transition between downstroke and upstroke. The same can be said for the engineered wing's angular displacement as seen in Figure 5.12, which appears to exhibit very strange behavior in terms of flapping amplitude.
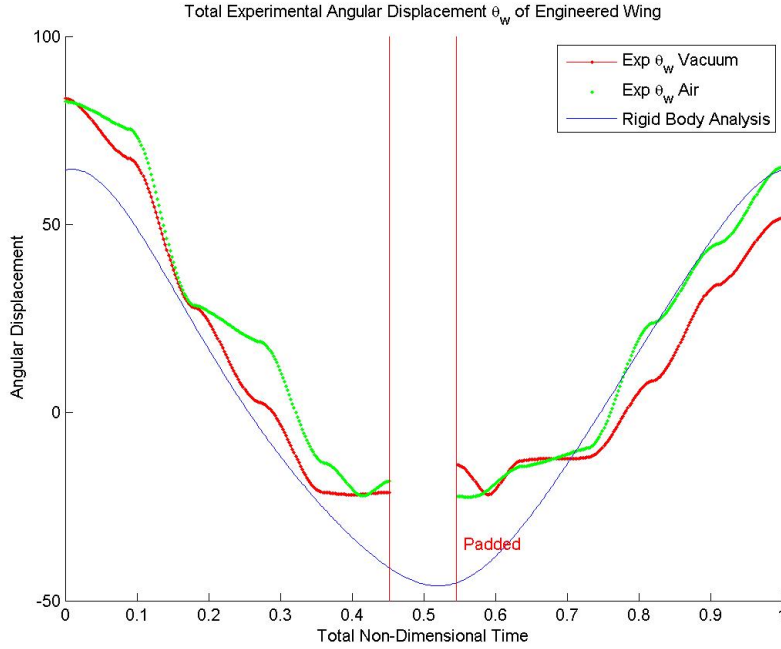
Figure 5.12: Engineered Wing Angular Displacements in Air (Red) and Vacuum (Green)

During testing, this behavior was indeed observed, especially in vacuum which often would cause wings to break due to the apparent lack of damping in the spanwise bending regime. Furthermore, it would appear that the beginning of the stroke exhibited a far higher amplitude of angular displacement. This may be due to the fact that the foam boundary condition had a tendency to wear out during testing. It is important to note that in the case of the biological wing, the presence of the shoulder made the fit very tight, whereas the engineered wing was essentially two dimensional and had more 'wiggle room' in its clamp.

161

What is even more interesting about the behavior of the engineered wing under flapping is the behavior of the angular displacement immediately following the transition as it would appear that the angle increases then decreases (lending itself back to the customary behavior that is closer to the RBA). This behavior may be the result of yet another 'whipping' effect generated by the change in direction of the flapping as was seen at the top half of the downstroke. Simply stated, this behavior was not observed by the biological wing as will be shown when compared.

5.3   Comparison to Biological and Engineered Wings: The Planar Orientation Along the Span and Angular Displacements

Figure 5.13 depicts the comparison of both wings flapping in vacuum. Upon immediate observation, it becomes clear that there is a stark difference in the behavior of the engineered wing as compared to the biological. On the downstroke, the biological wing appears to exhibit far less twist as compared to the engineered wing, which completely envelopes the bio-data. Furthermore, in the upstroke, the engineered wing appears to completely reverse direction (observe y-axis) in terms of the chordwise deflection.

It would appear that if the biological wing were taken to be the standard, the engineered wing lacks support in the chordwise direction which may be a function of construction or material properties, but in all, the performance appears poor at best when considering the aforementioned possibility of the 'scoop' as seen exhibited by the biological wing. It is helpful to compare this data with Figure 5.14 which depicts the same operation but in air.The presence of error in both cases makes the upstroke data difficult to discern however since all of the error bars appear to overlap. This presents challenges when attempting to draw conclusions about overall behavior of the wings when compared to each other.

The air observation proves itself interesting simply due to the fact that again the 'spread' associated with the deflection of the wing in air is still present in both data sets as in the deflection in the spanwise direction is less uniform than in vacuum.

162
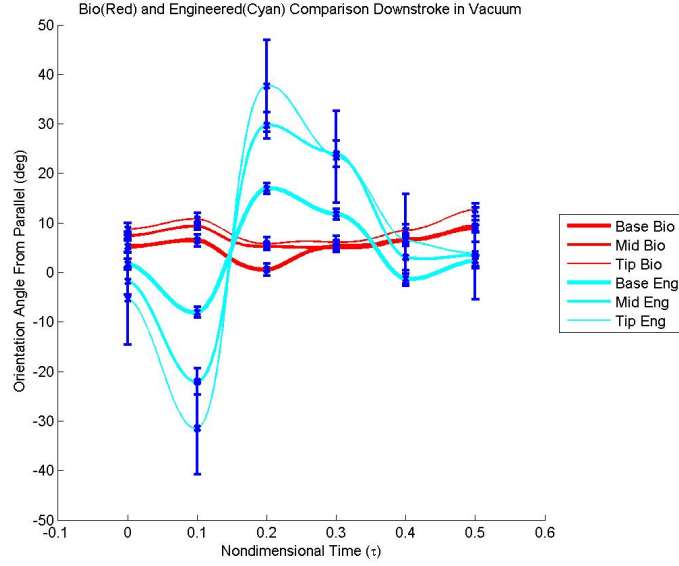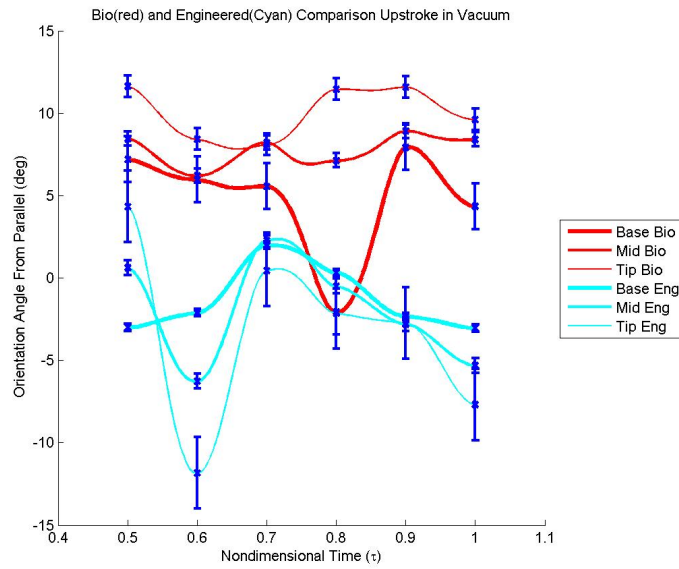
(a) Downstroke

(b) Upstroke

Figure 5.13:   Planar Orientation of Biological Wing (Red) and Engineered Wing (Cyan) Splined Data in Vacuum with Hard Data Points (Blue) for All Three Planes
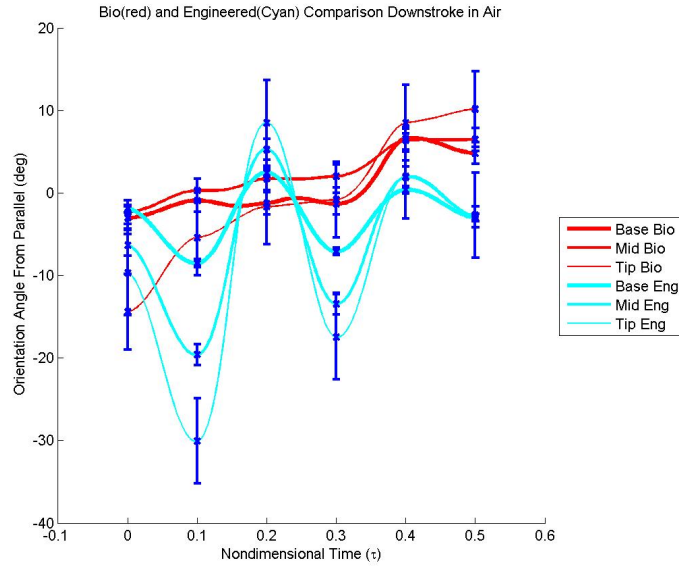
(a) Downstroke
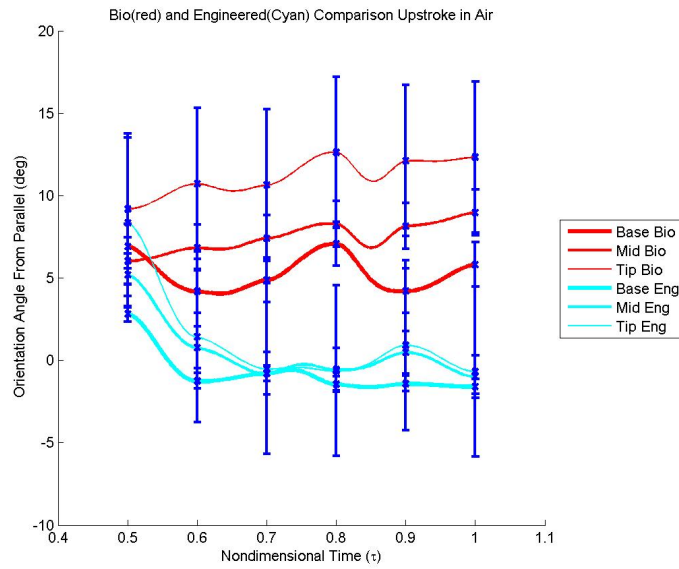
(b) Upstroke

Figure 5.14:   Twist of Biological Wing (Red) and Engineered Wing (Cyan) Splined Data in Air with Hard Data Points (Blue) for All Three Planes

Once again the engineered wing appears to lack the stiffness in the chordwise direction to maintain the lack of relative deflection as observed by the biological wing.

Speaking more on the uniformity of deflection along the spanwise direction, it would appear when examining the two wings together that uniformity is maintained more in the case of the biological wing. Again, this may be due to the fact that the construction is different, or the biological wing exhibits far more three dimensional qualities (such as vein thickness, hollowness, and wing camber) and the engineered wing only mimics in weight, two dimensional geometry, and modal qualities in air. Needless to say, the observation of Figure 5.15 compares the rigid body motion of the biological and engineering wing in vacuum.
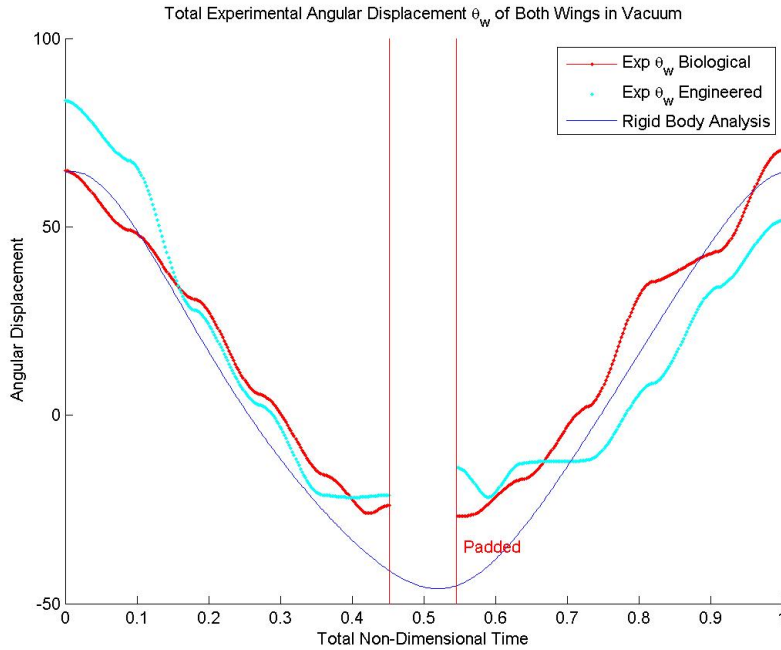
Figure 5.15:   Biological (Red) and Engineered (Green) Wing Angular Displacements in Vacuum

Compared to the engineering wing, the biological wing more closely emulates the rigid body motion as the engineering wing (as discussed) may have been at a disadvantage in its construction and 'not as snug' boundary condition.

5.4 Brief Comparison of Upstroke and Downstroke of Biological Wing

The purpose of this section is to observe the differences in the torsional deformations of the biological wing; comparing the upstroke and downstroke. This analysis was performed for the purpose of future construction.It is important to note that the biological wing appears to have an antisymmetric motion associated with the upstroke and downstroke. Figure 5.16 points towards the differences in strokes.

The first observation of Figure 5.16a suggests that although not exact, the aforementioned conjecture of the asymmetric twist can be put to rest. Other than the slightly greater amplitude of twist seen in the upstroke, it would appear that in vacuum the wing does in fact have a downstroke similar to that of the upstroke in terms of this twisting motion. The 'purely inertial' answer to the Aeroelastic Question would say that the wing will behave like this in air as well, wherein the symmetric downstroke/upstroke should appear not as prominently as the presence of air damping has been a continuous parameter.

Figure 5.16b demonstrates problematic or challenging results. Brief inspection would indicate that the effect of air causes the biological wing to behave far differently than that of the wing in vacuum. Though flapped at the exact same frequency, air seems to illicit a unique and complex reaction from the natural wing as the downstroke exhibits a tighter, more uniform twist along the span, 'scooping' the air beneath it, and the upstroke sees a non-uniform, higher amplitude twist which is indicative of allowing air to pass over the wing (as previously discussed), essentially dodging the need to move through the medium of air and exposing less surface area to the 'oncoming' velocity of air to essentially cut down on drag produced by the moving wing.

This presents a rather unique problem for future engineers who wish to properly emulate the efficient, elegant motion of the wing. Chapter 1 made mention of the 'novel principles' exhibited by naturally occurring, flapping wings [18]. This comparison shown in Figure 5.16 brings these novel principles to light as the wing naturally does this, even when exposed to simplified flapping. If a higher frequency had been

166
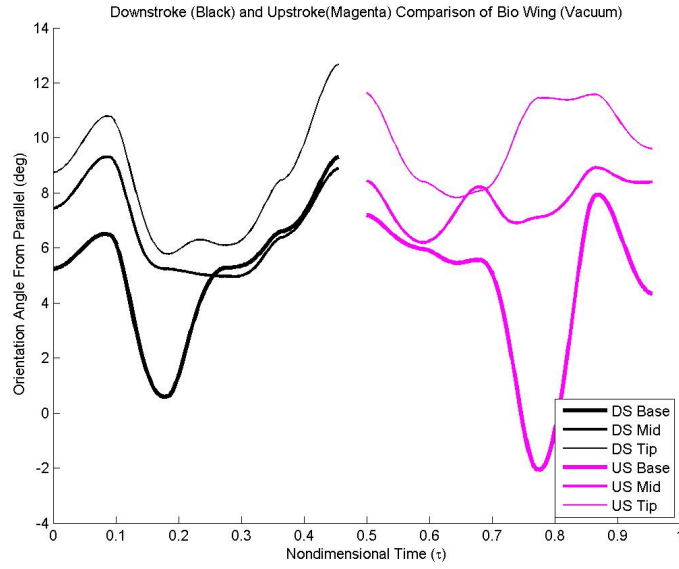
(a) Vacuum
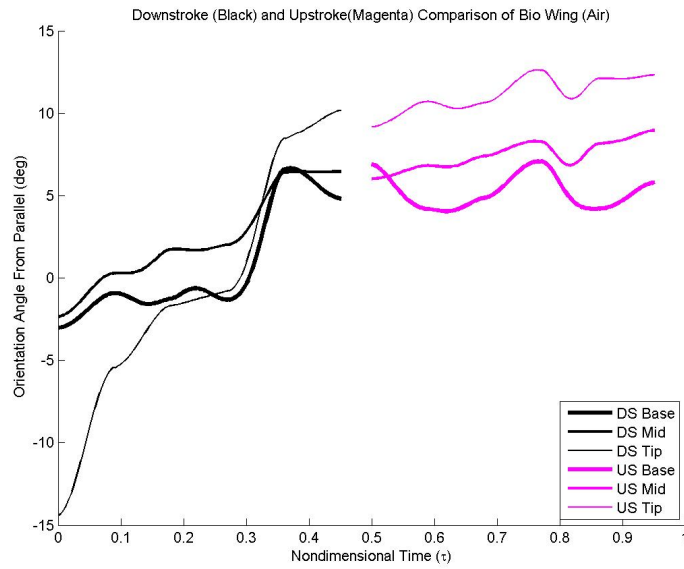
(b) Air

Figure 5.16: Comparison of Deflection for Upstroke and Downstroke of Biological Wing

studied, there is no doubt that even more dramatic effects would be observed in terms of twist and deflection, paving way to future studies as materials get smarter and methods become more refined. As for now, humanity demonstrates its callowness in terms of understanding the unique and intricate complexities wrought of years and years of evolution. This should grant a deeper appreciation for what was originally thought as a trivial problem as few have deemed this area of study pertinent for study and understanding.

As an almost novel presentation, Figure 5.17 is shown in the similar fashion of the last two as the comparison of downstroke and upstroke of the engineered wing. It can be seen here that the deflection amplitudes here exist at much higher values than those seen in the biological wing.

This is evermore evident here as the amplitudes of deflection appear to be damped by the presence of air- a behavior not observed in such magnitude by the biological wing. Here, the presence of air does not seem to affect the non-uniformity of deflection as was seen by the biological wing, but rather for the engineered wing it would appear that the uniformity is not necessarily affected nearly as much as the amplitude. The plots displayed in Figure 5.17 show an even clearer picture of the lack of similarity between the engineered and biological wing.

5.5 Summary

This section served to display the experimental results that came about through the procedures detailed in Chapters 3 and 4. The splined data was instrumental in visualizing some of the behaviors that were eventually quantized via the orientation and angular displacement analyses. The data here strongly suggests that though the engineering wing closely resembled the biological wing in 2D geometry, size, weight, and first bending mode, it exhibited noticeable differences in its dynamic behavior. The amplitude of planar orientation was the most clear indicator of this claim in that it clearly showed a far greater amplitude of this change in planar orientation that the biological wing did not (as could be inferred by a much lower second mode from
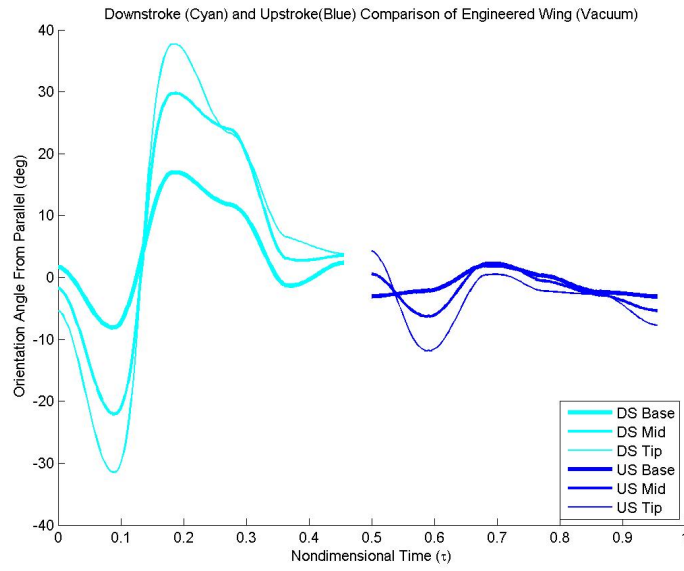
(a) Vacuum
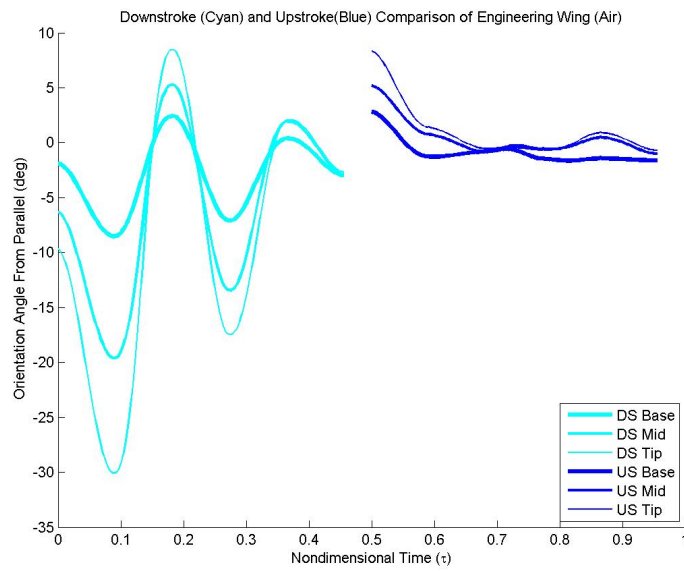
(b) Air

Figure 5.17:   Comparison of Deflection for Upstroke and Downstroke of Engineered Wing

the modal analysis), nor did it exhibit the complex 'novel' behavior that can be best described as the **'downstroke scoop'** in air.

The concept of the downstroke scoop was best seen in the juxtaposition of the downstroke and upstroke in air, as a smaller change in planar orientation is seen in the downstroke and a much higher one exists in the upstroke. This complex behavior was not observed in vacuum, tempting one to reevaluate the claims made in Chapter 1 concerning the **Aeroelastic Question** in that so many believe the wing's behavior to be dominated by inertial effects. The results depicted here would beg to differ, suggesting a strong presence of aerodynamic effects.

VI. Conclusions

The purpose of this research study is the recognition of the complexities and structural aspects of the FWMAV. As the title of this project indicates there were two areas of interest which involve manufacturing and evaluation. This research secures the necessity for these two arenas to be coupled due to the fact that manufacturing is always subservient to the testing. Clearly this research calls for future studies to focus on more investigation into the realm of construction and mechanical considerations as was shown in the results.

The following sections will illuminate some of the specifics of the above generally stated conclusions. For this project, two wings, the separated biological wing and the biologically inspired engineered wing, were flapped at 12.5 Hz in both air and vacuum to determine their dynamic characteristics when faced with said conditions, to include a clamped, rigid base condition [4].

6.1 Manufacturing of FWMAV Wings

An efficient manufacturing technique of FWMAV wings has been developed. A single, biologically inspired MAV wing was constructed with the *Manduca Sexta* as the inspiring specimen. The main features that were chosen to be emulated were the wing/vein geometry, weight, and modal properties as these were considered very pertinent in the realm of proper emulation and construction considerations.

The manufacturing technique proved to be an iterative process as in the beginning, 3-D printing was chosen as the revolutionary materialization method due to its ability to manufacture near-exact geometries in all three dimensions which will allow for considerations to be made of both vein geometries and thicknesses. This method failed due to all-too high inertial loading and material densities, producing wings that were not applicable for MAV usage. The next few iterations explored the realm of differing materials that exhibited various properties, however the filleted vein geometry was abandoned due to a distinct lack of 'manufacturability.' The next iterations considered were two dimensions for manufacturability. Through this process

the research indicated that laser etching was the most efficient and repeatable process of manufacturing.

Understanding the outcomes of the first two iterations lead to newly conceived methods of mimicry. Significant steps were taken in the formation of the vein geometry by using CT and photographed examples of wings which lead to the final manufacturing technique. This technique utilized 3-layer, cured carbon fiber that was arranged in a 90-0-90 formation wherein the stiffer direction was chosen to run the span of the wing. In terms of the membranous material, 20 micron Kapton film was used due to its availability and low density. The combination of these two produced a flat, rigid wing that allowed for both spanwise and chordwise flexion, yet held its rigidity and modal properties which ended up being similar to those of the Hawkmoth wing in air.

6.2   Manufacturing of Evaluation Techniques

As a result of the different steps utilized in the inquiry process, this project yielded a new technique of characterization and evaluation of FWMAV wings. Norris [1] and Sims [4], [11] believed that the modal analysis that employed small displacements and rotations normal to the surface of the wings evaluated was the most efficient and accurate method to carry out said evaluations. This study extended the Norris and Sims characterization by employing these small displacements used by the others to verify design, and then evaluate the design under large displacements and rotations by simulating flapping conditions.

Simplified flapping conditions were applied to a wing using an in-house constructed flapper that retained the ability to mimic both frequency and flapping amplitude. A careful kinematic analysis suggested that the flapping device came closest to emulating the angular displacement exhibited by the *Manduca Sexta* which is based on data gathered by Willmont and Ellington. However, in terms of velocities and accelerations, the new AFIT flapper did not mimic the behaviors as exhibited by other, previous flappers based on a careful regression analysis. As a result of these find-

172

ings, the fallibility in the realm of accelerations of the new AFIT flapper opened up a window of accessibility for study in that the amplitude of acceleration was shown to be far less than other flappers, allowing for more wings to be tested and survive the violent flapping motion seen by the Hawkmoth.

Using Photomodeler, a program that employs algorithms based on photogrammetry and three dimensional triangulation, the three dimensional characteristics of the wing deformations were determined by effectively 'freezing' the flapping wing at 12 different phases within the stroke. Photogrammetry was enabled by the placement of reference points on the wings that proved non intrusive and extremely useful for data analysis. This method was applied to both a biological wing and the aforementioned engineered wing.

6.3   Modal vs. Flapping Analyses

The modal analysis proved to be very useful in providing a standardized, repeatable, and reliable process of evaluation of the two different wings that were tested. The results clearly demonstrated that though the goal of nearly matching the first resonant frequency of the biological specimen, the engineered wing in almost no way exhibited the same behavior when subjected to the flapping conditions set forth in the procedure.

It would appear that the engineering wings not only lacked the chordwise stiffness essential to maintain the shape or behavior seen by the biological wing (which indicative of the much lower second mode when compared to the biological wing), but it also indicated the absence of the unidentifiable features necessary to emulate the complex 'scoop' in the downstroke as was seen by the flapping biological wing in air. This motion could be associated with the torsional characteristics seen by the modal analyses. The motion as seen by the Hawkmoth by no means exhibits the small displacements and rotations associated with the modal analysis which provided the window of access to evaluate a wing is such a manner, however the similarities/dis-

similarities associated with the results do in fact bring to light the importance of mimicking *both* the torsional and bending modes of the wing.

6.4 Material Time Dependency

Norris *et al.* [1] stated that a moth wing should be tested and evaluated within 3 hours of separation before profound effects could be seen on the material properties. To curb this issue even further, Norris tested his wings within 20 minutes [4] however for this study, it was determined that the same wing be tested for both air and vacuum, making the total time elapsed for the experiment for the biological wing to be 1 hr, 42 mins. This was considered a necessary evil due to the fact that standardization for comparison purposes was so important- and thus the same wings was used. The conclusion of the test proved that the wing did in fact exhibit an increasing stiffness as time wore on, thus introducing yet another form of complexity to the issue of biological inspiration as the stiffness and material properties will change with time.

6.5 Photomodeler

Though processes revolving around the usage of Photomodeler proved to be difficult and extremely time consuming, it did prove useful in the characterization of the wing behavior. Challenges in resolution and depth were discovered, especially for the 16 degree and 0 degree angles of flapping in the spanwise direction. Often wings would be resolved by Photomodeler as being various spanwise dimensions (longer or shorter). Resolution in the vertical and horizontal directions proved to be extremely reliable, allowing for analyses to take place concerning the planar deflection about the spanwise axis of the wing relative to the stationary global axis.

6.6 Data Analysis

In order to eliminate concern about the previous statements about the lack of spanswise resolution , it was determined that the analysis of the chordwise behavior was the most pertinent area of investigation. Three planes along the span of the

wing were chosen to use vector analysis for the purpose of deformation angle evaluation. This method proved useful in the examination of the behavior surrounding the flapping motion. Additionally, comparisons to rigid body motion were made by examining a vector represented by points on the leading edge of the wing to determine what the wing demonstrated in terms of its angular displacement as opposed to what the system (flapper) saw as its position in the stroke.

6.7   The Importance of Aerodynamics

It should come as no surprise that the engineered wing failed to compare to the biological specimen, despite similar geometry and structural qualities (especially in the first vibrational mode). This significant finding demonstrates the wide area of inquiry that focuses on the effects of aerodynamics in this study. Trials of the biological wing in vacuum showed a passive rotation that was very similar in the upstroke as was the downstroke. This symmetry in strokes due to purely inertial loading would normally yield zero lift if that behavior was observed in air as well, but as was seen at the end of Chapter 5, this certainly was not the case.

In both cases (air and vacuum), passive rotation was observed in both wings but in air, the biological wing appeared to exhibit a non-uniform, spanwise deflection that was not observed in vacuum, effectively spreading data over a wider range of torsional deflection angles. This may be due to the presence of air in that the tip of the wing (which can be seen to be geometrically wider) presents a greater area to the medium of air, allowing the motion to have more of an effect on the deflection of the wing within that area. Furthermore, in air the wing exhibits far different torsional deflection behavior in the upstroke than in the downstroke- deforming more perhaps to allow for the 'scooping' of air to create lift, then leading to the reduction of negative lift in the upstroke. This behavior is significant to consider due to the fact that this naturally occurring motion was once thought to be the product of the Hawkmoth's shoulder joint/naturally occurring boundary conditions. As mentioned, this presents

quite the issue for those who wish to engineer such an efficient FWMAV wherein the boundary conditions will be far less complex– owing to the abilities of the wing.

6.8 Future Study

As is with any research, investigations start with a question; which inevitably spawns myriad further questions, regardless of the results obtained. The original question that was posed for this research was this:

What are the structural aspects that are required to influence a manufactured wing to behave as its inspiring specimen? Furthermore, what are some of the most effective methods of evaluation of this behavior?

Needless to say, the second question poses the least stringency in its answer. The goal of this research was to in fact evaluate dynamic behavior, however as was mentioned several times throughout the entirety of this thesis, the flapper that was manufactured to simulate flapping conditions left much to be desired, as it did not mimic all of the features inherent to that of the inspiration; the *Manduca Sexta.* Thus, one area of future study that should be thoroughly investigated is that of the inspiring boundary conditions of flapping. If one could successfully implement the mechanical flapping device that accurately mirrored those of the Hawkmoth, one could even more accurately evaluate the behavior of both the biological wing along with any other wings that have been created in its image.

In addition to a new flapping mechanism that eliminates the 'clamped' [4] boundary condition, the evaluation of behavior in the flapper was executed via photogrammetry. Though apparently effective in capturing behaviors inherent to the wing's dynamic motion, difficulties in resolution and data gathering were presented via limitations in both camera operation and data harvesting (the Photomodeler process which proved to be extremely time consuming). There are two possible avenues to take to remedy this issue:

- The difficulties with capturing resolution in the spanwise direction could have been eliminated if either high speed video were used for several synchronized

cameras, both in and out of the vacuum chamber. Furthermore, it would be helpful if the cameras were allowed to translate on tracks within the chamber. This would allow for capturing at several shot angles that were not attainable in this study (since the camera was hand-held, outside of the chamber), along with the elimination of the need for strobe lights as they appeared rather difficult to use.

- Photomodeler provides coded targets (reference points) for data harvesting that have numbers assigned to them. If these targets could somehow be applied to the wings without being intrusive (affecting weight or modal properties), they would make the photogrammetry process far simpler and quicker, eliminating the need to 'point pick' as was detailed before.

In short, Photomodeler itself did not appear faulty, rather it was the application of Photomodeler that proved to leave room for error (as was seen by the residuals).

The first part of the question above leaves the most room for discussion. This is due to several factors:

- The material properties of the biological wing have yet to be determined and implemented. The obtaining of these may aid in the determination of necessary factors associated with the proper implementation of the structural qualities utilized by nature to attain flapping flight.

- The first mode was the area of most interest to mimic as it was considered the most prominent during the modal analysis and was closest to what could be considered the flapping frequency. In short, this did not prove to be the case due to the fact that the behavior observed in the torsional regime of the engineered wing was different from that of the biological. More attention should be paid to the first *two* modes instead of just the first.

- The three dimensional characteristics of the wing, though considered originally, were not implemented in this study; specifically in the realm of vein geometry and possible camber (that would in effect increase stiffness without the need

for concern of material stiffness). It is possible that if somehow the three dimensional geometry of the veins were implemented exactly as those seen in the inspiring specimen, that the inherent 'scoop' seen in the wing could be mimicked.

- More investigation should be done concerning the interface between the veins and the membrane. CT imagery shown in Chapter 1 denotes the offset nature of the veins to the membrane, but crossectional cuts reveal that perhaps the attachment is not as simple as being 'glued' on.

- Last, but possibly most importantly, the boundary conditions that are applied to the wing must be evaluated more closely. Though this does not deal with the wing directly, the complex shoulder joint was not present in this study; rather it was the rigid clamp that was employed. Though this served its purpose in standardized comparison, it should be recognized that this lack of boundary consideration may have influenced the overall behavior of the wing in that it may have not behaved in its true form. The boundary condition must be modified somewhat to represent the interconnection of the rigid wing to the flapper, though as stated: the current setup proved adequate for comparison purposes.

In all, these few questions shed light on several areas of improvement for future study, allowing for even further pertinent investigations. It is the sincere hope of this researcher that in a short time, all of the data presented in this thesis be replaced with even more pertinent data that was more accurately/efficiently obtained; as this thesis represented one of the first stepping stones in the chronology of the life cycle of the MAV. There is no doubt that this initial 'iteration' will serve as a basis for thinking- to be disproved and attacked for the remainder of its existence. However hopes run high that this research will at least make a small dent in the realm of the successful creation of the efficient, effective, and incredible 'bug-sized' unmanned aircraft.

Appendix A. Physical Pictures of Flapping Wings and Their Surface Fits

This Appendix serves to show some of the physical pictures taken during the experimental process for each of the wings tested. Though this serves very little purpose from an analytical standpoint, it does in fact assist in observing the point positions since as discussed in Chapter 5, some of the tests did not yield expected results. An actual visual image certainly assists in this process of evaluation and visualization.

To further aid in the observational process, it was deemed necessary to also depict the surface fitted averaged raw data as some of the pictures are difficult to discern or draw conclusions from. It was neccessary that although some of the surface fitted data cannot be seen as well from all angles to standardize MatLab's output viewpoint as it will aid in understanding the differeces between the tabulated/surface fitted data.
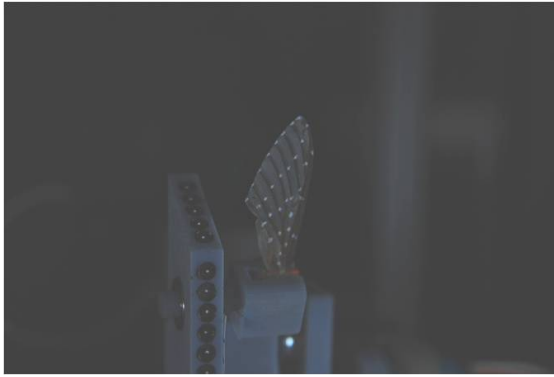
(a) 64 deg
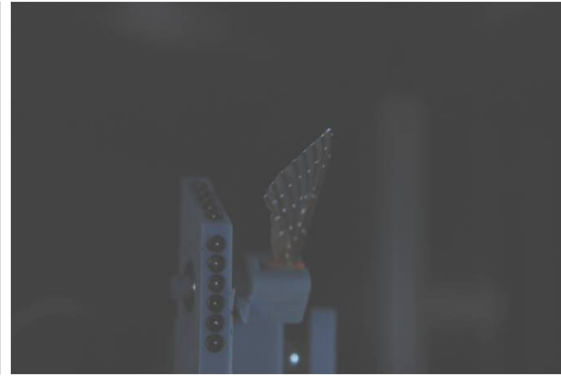
(b) 48 deg

(c) 16 deg
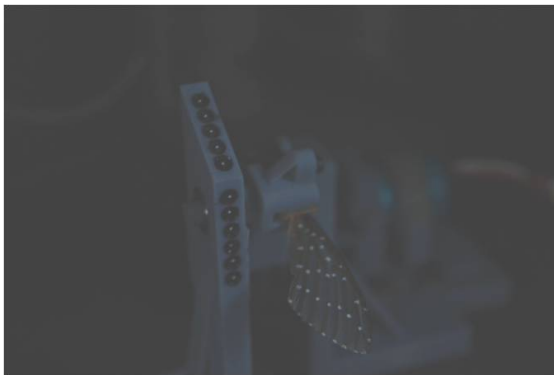
(d) 0 deg

(e) -22.5 deg

(f) -43 deg

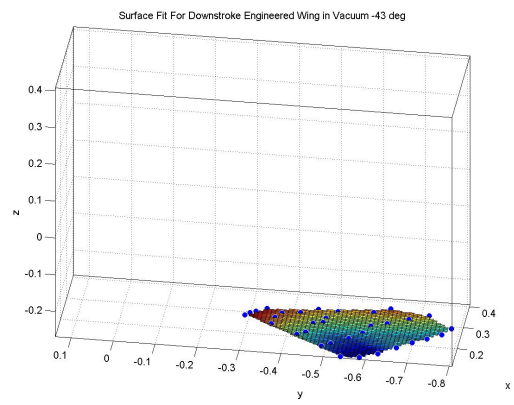Figure A.1:   Downstroke of Biological Wing in Vacuum
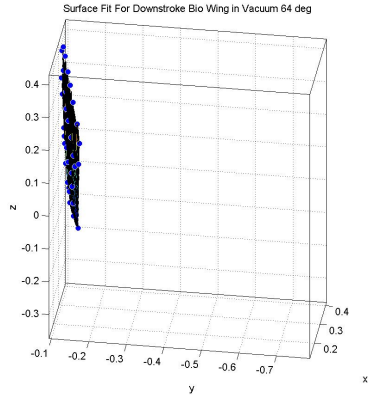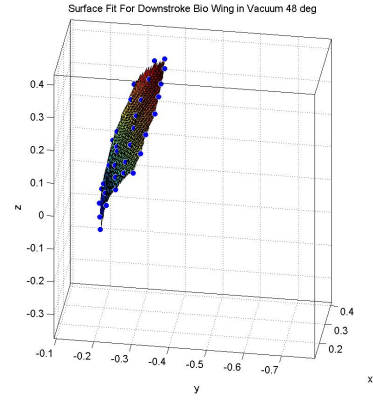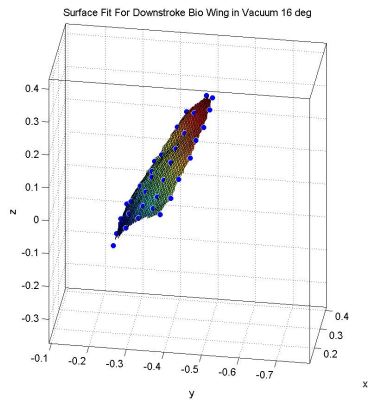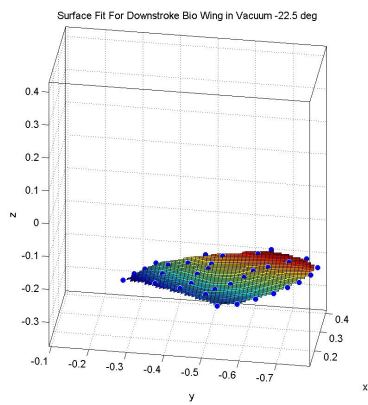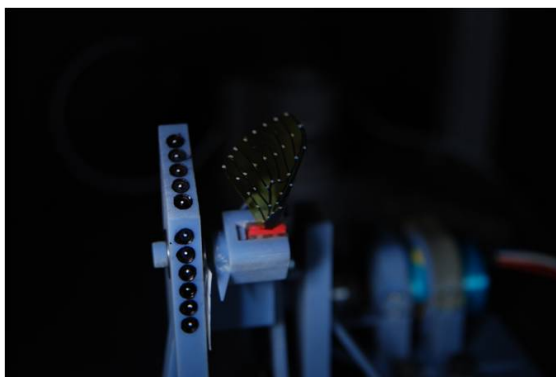
(a) 64 Deg
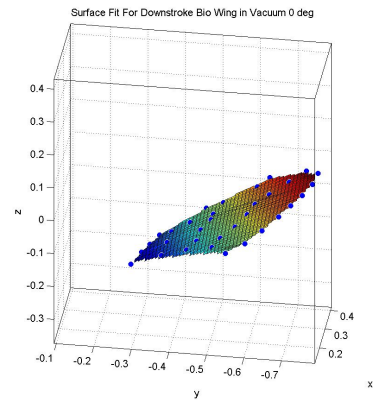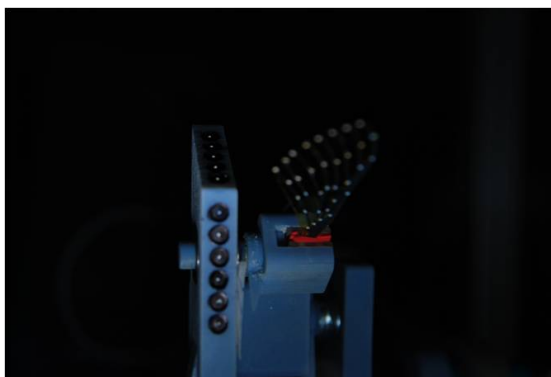
(b) 48 Deg

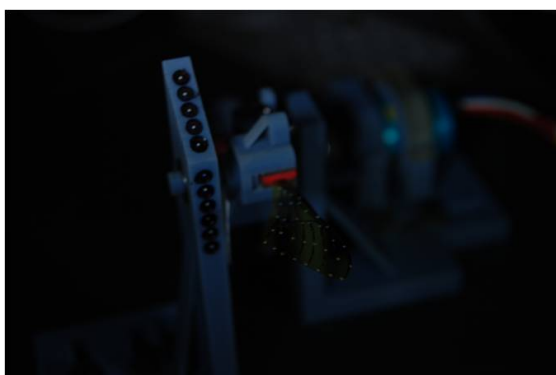(c) 16 Deg
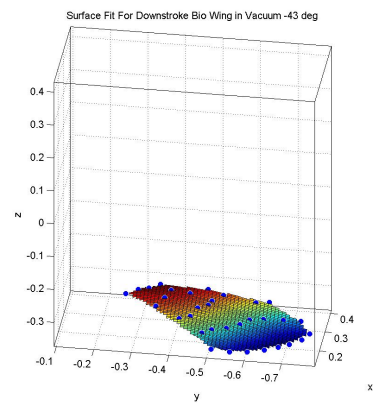
(d) 0 Deg

(e) -22.5 Deg

(f) -43 Deg

Figure A.2:   Surface Fit of Downstroke of Biological Wing in Vacuum
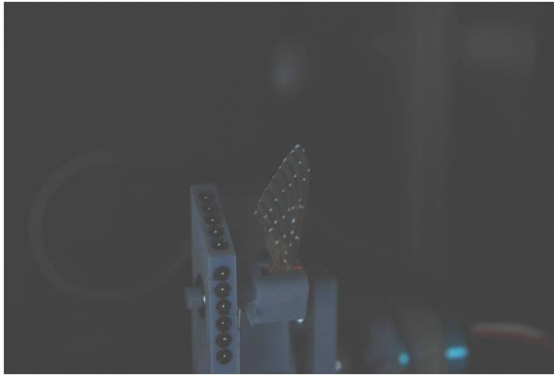
(a) 64 deg

(b) 48 deg

(c) 16 deg
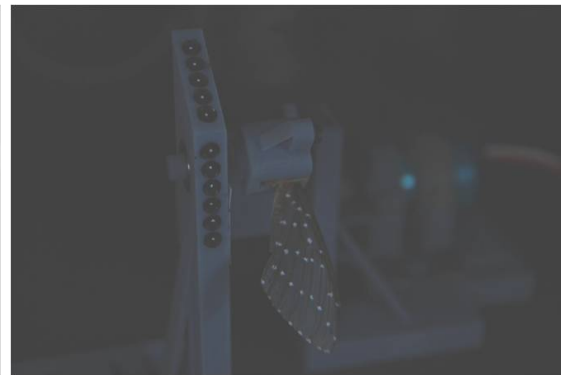
(d) 0 deg
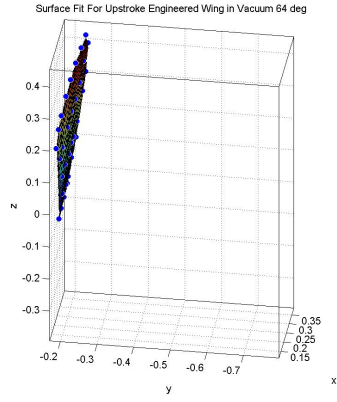
(e) -22.5 deg

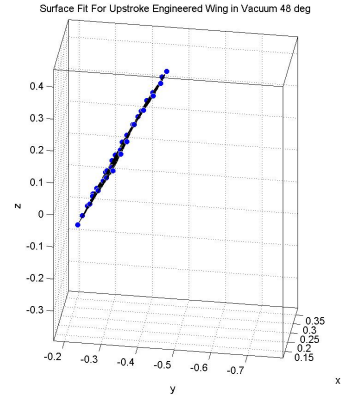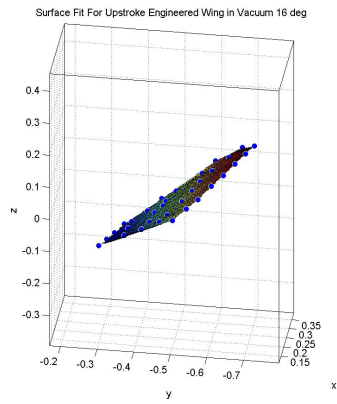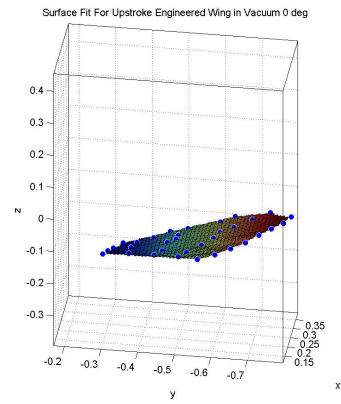(f) -43 deg

Figure A.3: Upstroke of Biological Wing in Vacuum
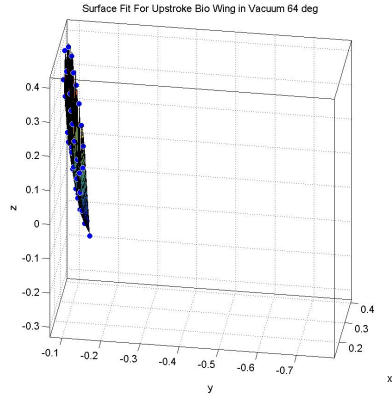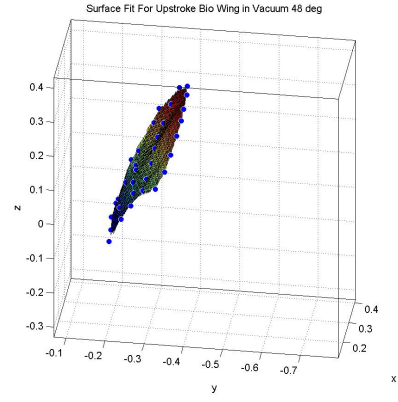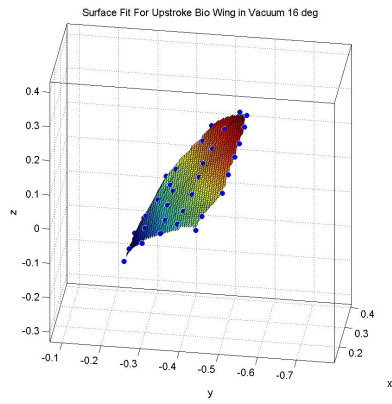
(a) 64 Deg
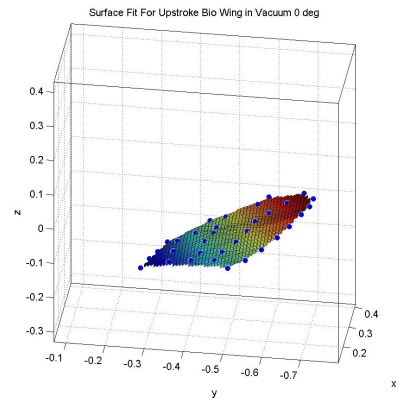
(b) 48 Deg

(c) 16 Deg
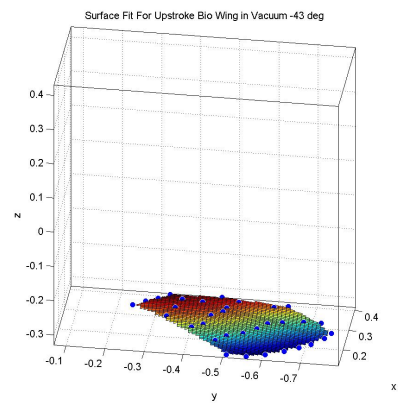
(d) 0 Deg

(e) -22.5 Deg

(f) -43 Deg

Figure A.4:   Surface Fit of Upstroke of Biological Wing in Vacuum
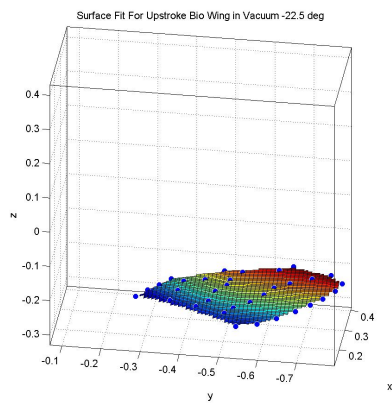
183
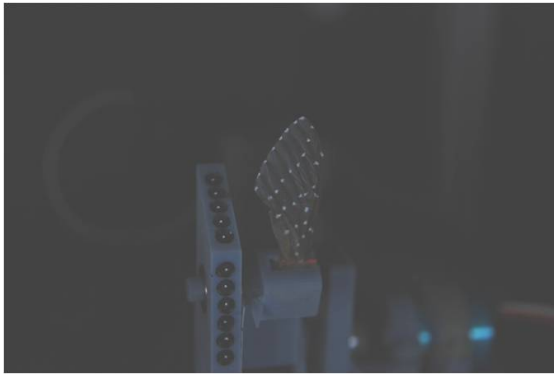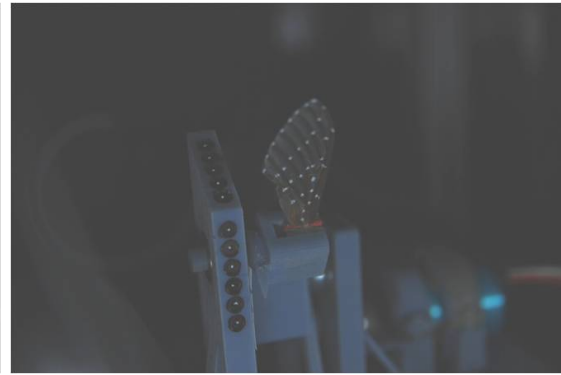
(a) 64 deg

(b) 48 deg

(c) 16 deg

(d) 0 deg

(e) -22.5 deg

(f) -43 deg

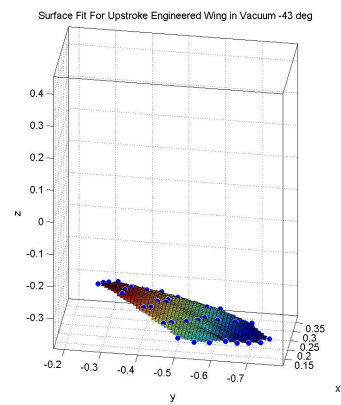Figure A.5:   Downstroke of Biological Wing in Air
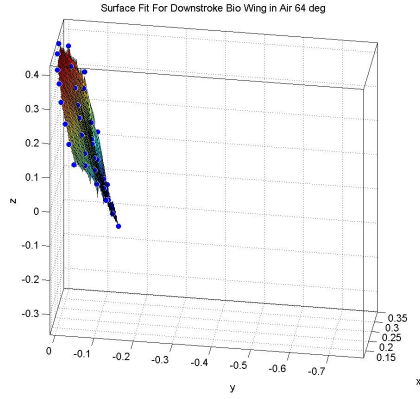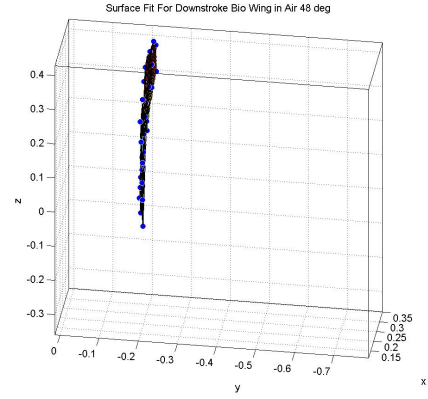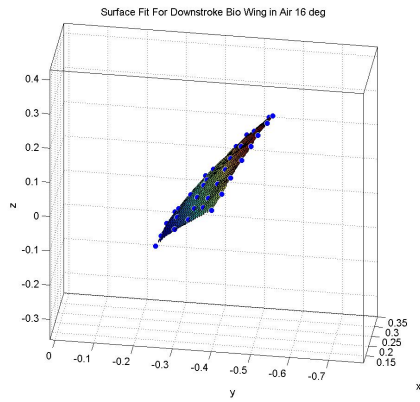
(a) 64 Deg
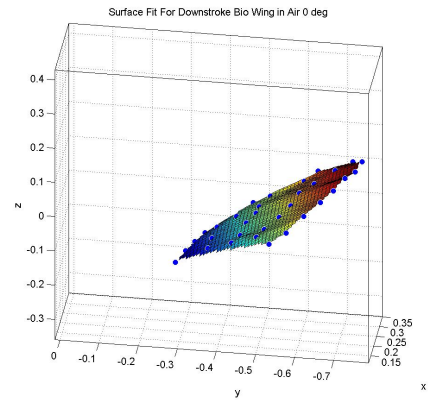
(b) 48 Deg

(c) 16 Deg
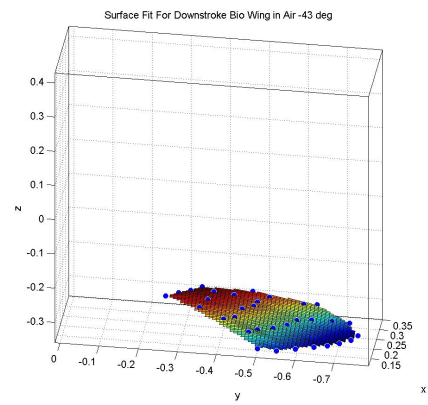
(d) 0 Deg

(e) -22.5 Deg

(f) -43 Deg

Figure A.6:   Surface Fit of Downstroke of Biological Wing in Air

185
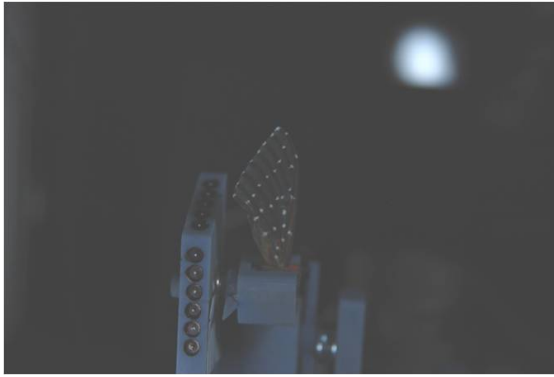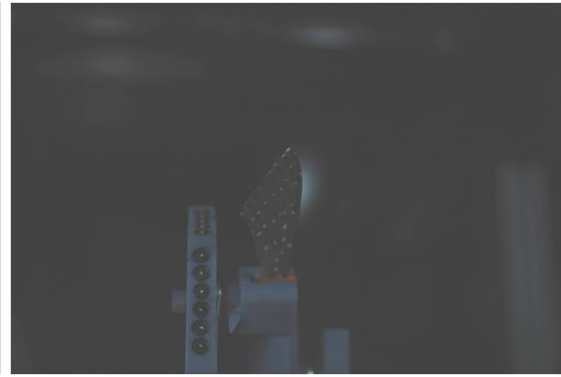
(a) 64 deg

(b) 48 deg
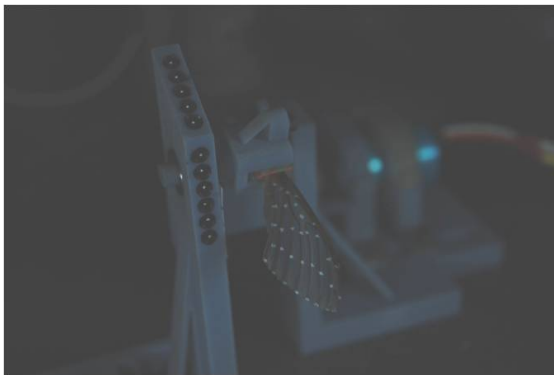
(c) 16 deg
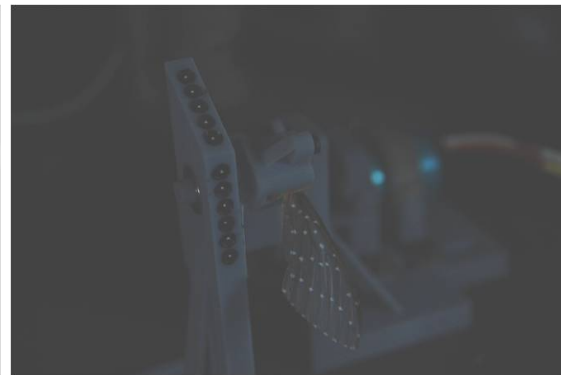
(d) 0 deg

(e) -22.5 deg

(f) -43 deg

Figure A.7:   Upstroke of Biological Wing in Air
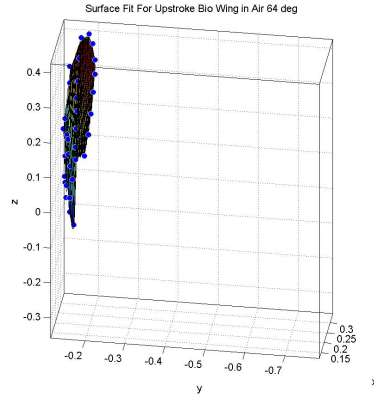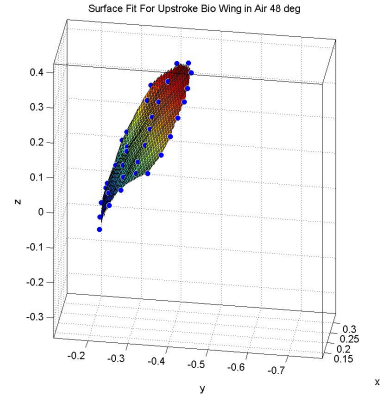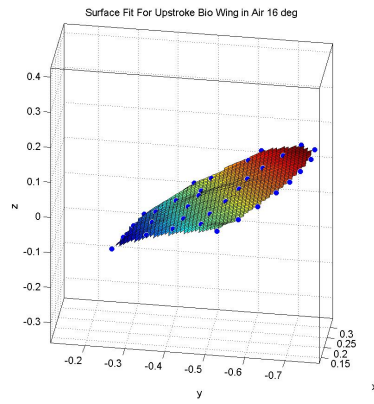
(a) 64 Deg
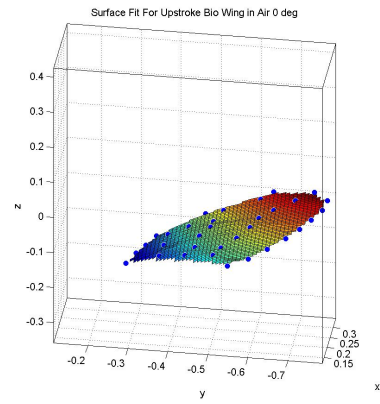
(b) 48 Deg
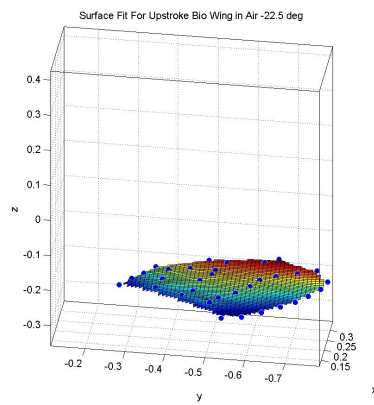
(c) 16 Deg
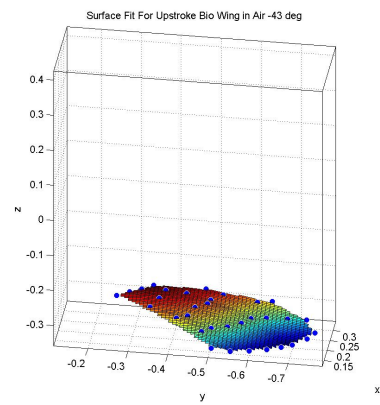
(d) 0 Deg

(e) -22.5 Deg

(f) -43 Deg

Figure A.8:   Surface Fit of Upstroke of Biological Wing in Air
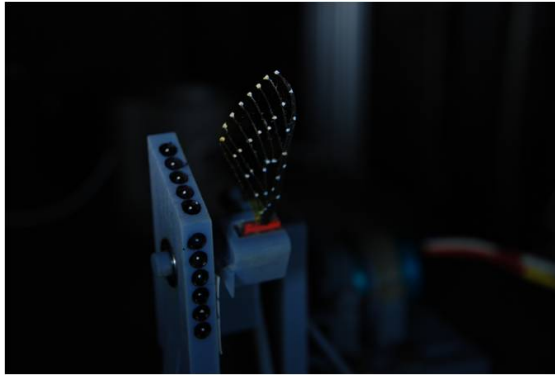
(a) 64 deg

(b) 48 deg

(c) 16 deg

(d) 0 deg

(e) -22.5 deg

(f) -43 deg

Figure A.9:   Downstroke of Engineered Wing in Vacuum
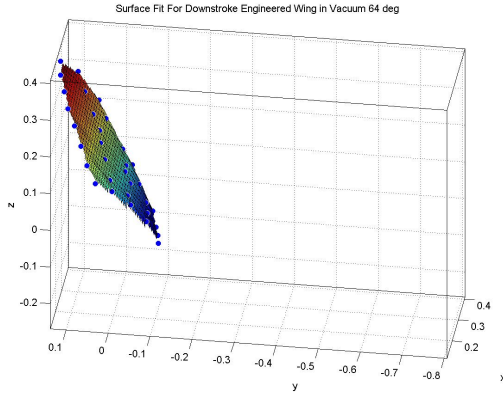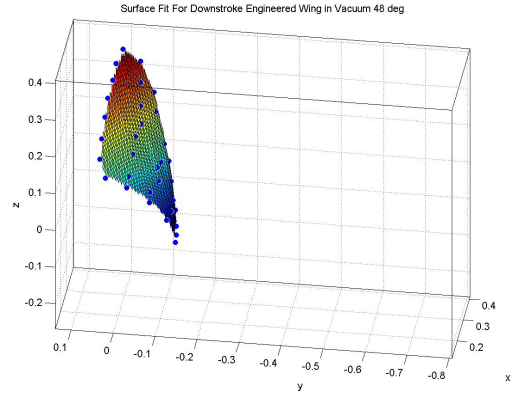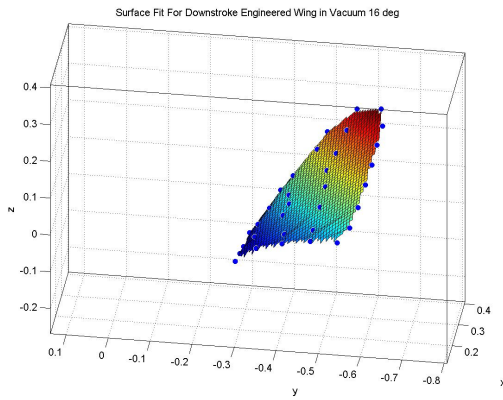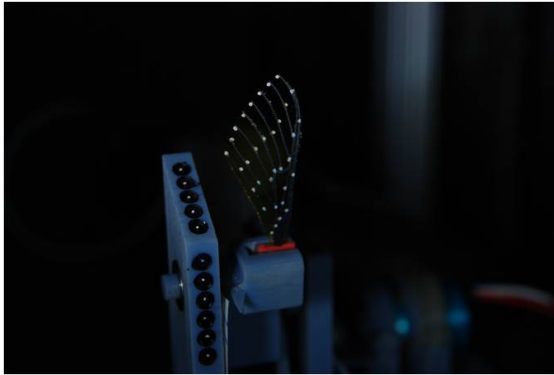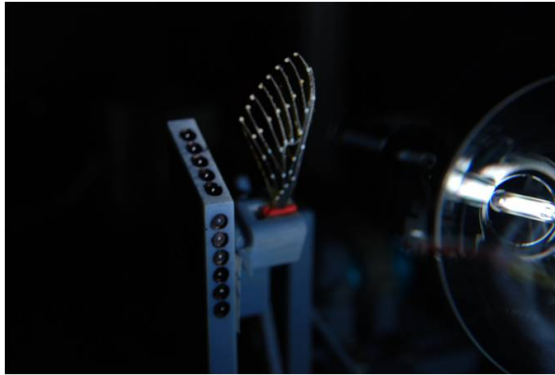
(a) 64 Deg
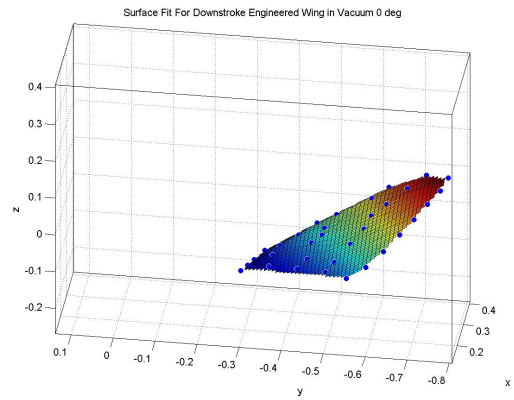
(b) 48 Deg

(c) 16 Deg

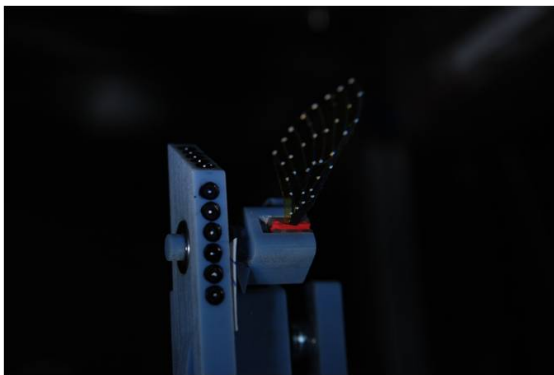(d) 0 Deg

(e) -22.5 Deg

(f) -43 Deg

Figure A.10:   Surface Fit of Downstroke of Engineered Wing in Vacuum

189

(a) 64 deg

(b) 48 deg

(c) 16 deg

(d) 0 deg

(e) -22.5 deg

(f) -43 deg

Figure A.11:   Upstroke of Engineered Wing in Vacuum

(a) 64 Deg

(b) 48 Deg

(c) 16 Deg

(d) 0 Deg

(e) -22.5 Deg

(f) -43 Deg

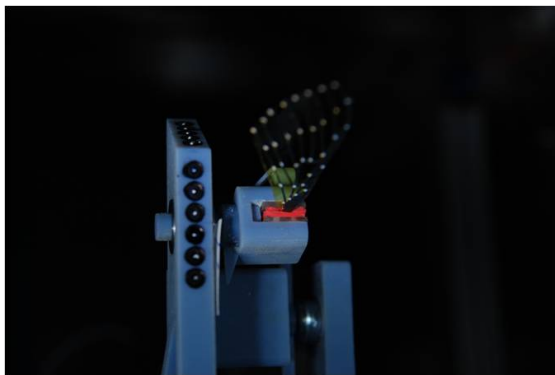Figure A.12:   Surface Fit of Upstroke of Engineered Wing in Vacuum
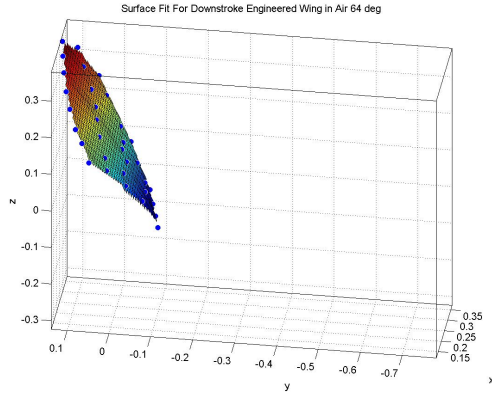
191

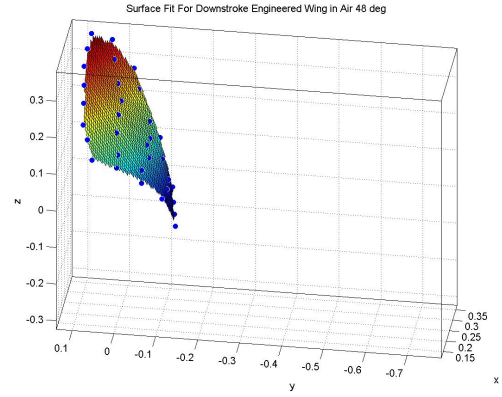(a) 64 deg

(b) 48 deg

(c) 16 deg
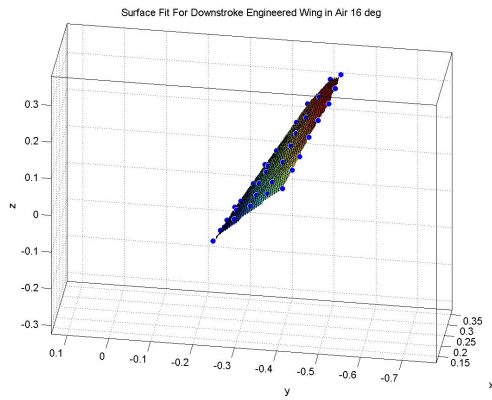
(d) 0 deg

(e) -22.5 deg

(f) -43 deg

Figure A.13:   Downstroke of Engineered Wing in Air

(a) 64 Deg

(b) 48 Deg

(c) 16 Deg

(d) 0 Deg

(e) -22.5 Deg

(f) -43 Deg

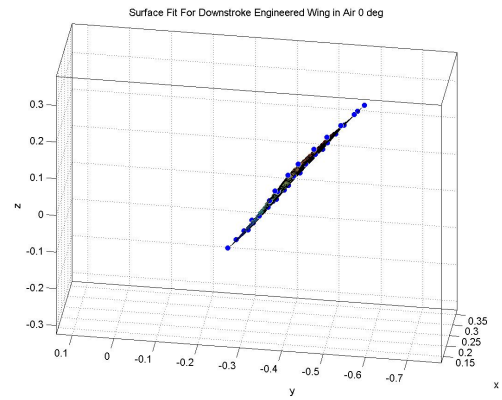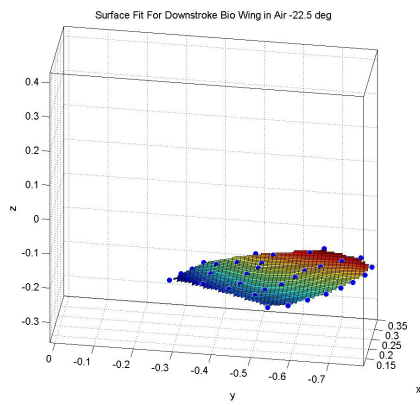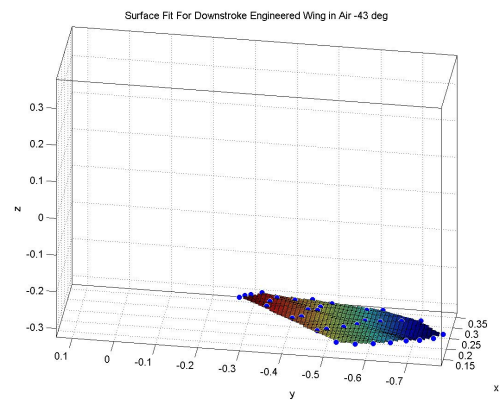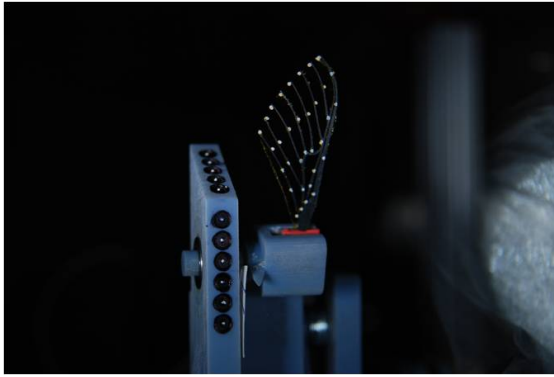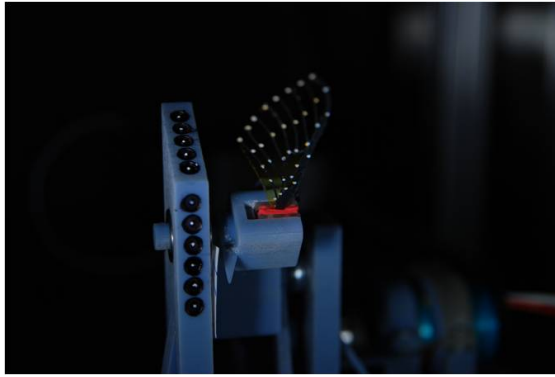Figure A.14:   Surface Fit of Downstroke of Engineered Wing in Air

193

(a) 64 deg

(b) 48 deg

(c) 16 deg

(d) 0 deg

(e) -22.5 deg

(f) -43 deg

Figure A.15:   Upstroke of Engineered Wing in Air

194
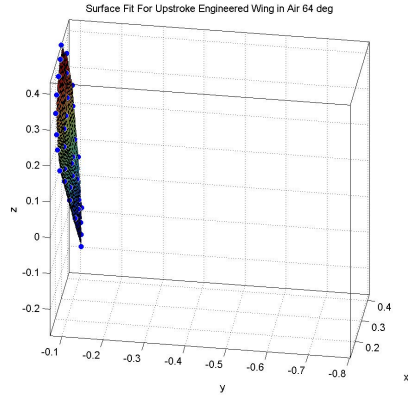
(a) 64 Deg
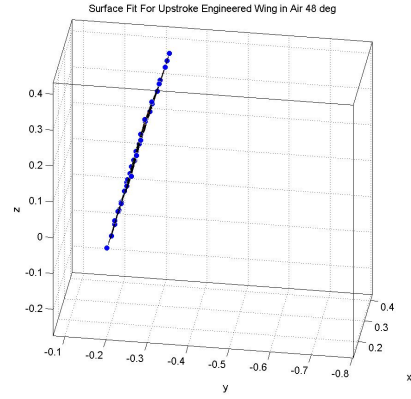
(b) 48 Deg
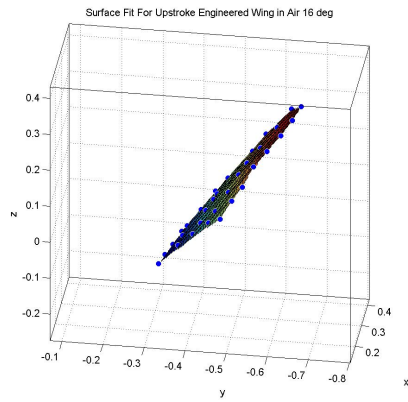
(c) 16 Deg
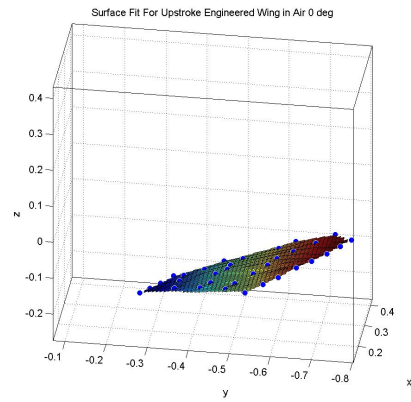
(d) 0 Deg
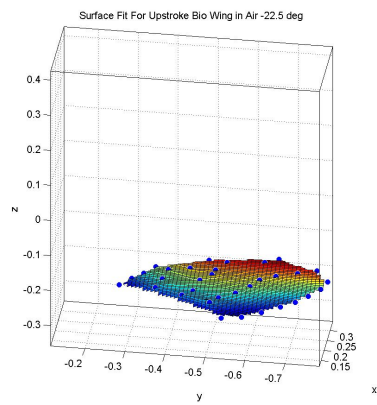
(e) -22.5 Deg
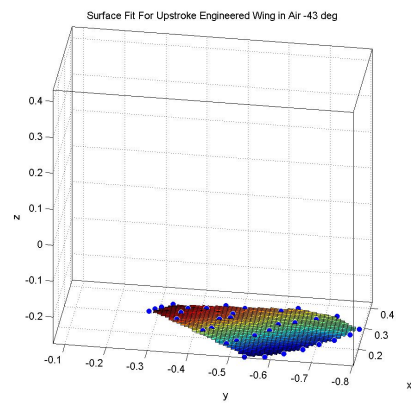
(f) -43 Deg

Figure A.16:   Surface Fit of Upstroke of Engineered Wing in Air

195

Appendix B.   Residuals

In order to determine the 'reliability' of the points used to compare the engineered and biological wings (on the vector basis) it was deemed necessary to examine the point-to point residuals as produces from Photomodeler. The red Vertical lines indicate the positions of the solid (nontranslating) reference points. In between these are the points on the wings that will be considered.
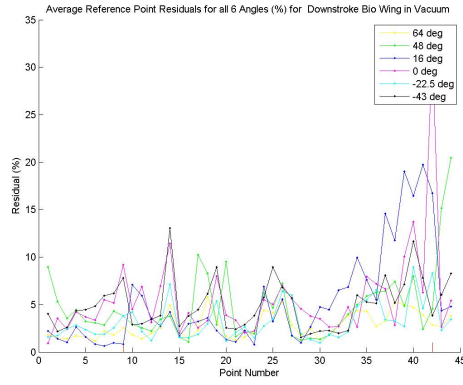
(a) Downstroke Vacuum
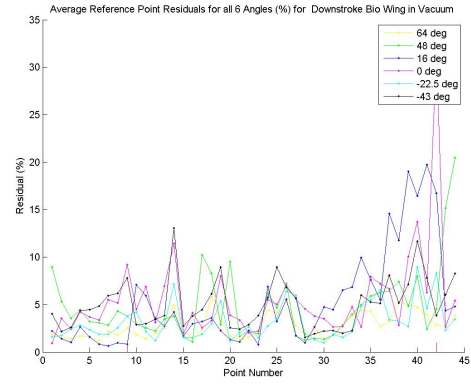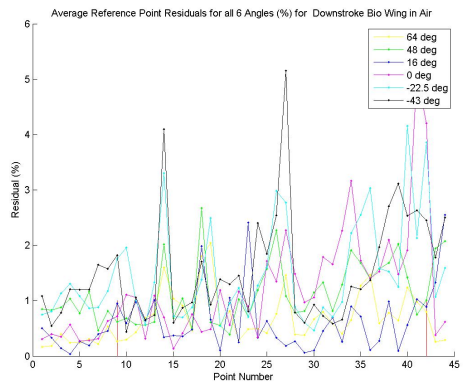
(b) Upstroke Vacuum
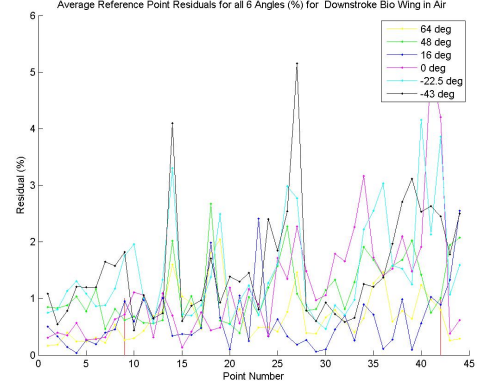
(c) Downstroke Air

(d) Upstroke Air

Figure B.1:   Point Residuals of Biological Wing
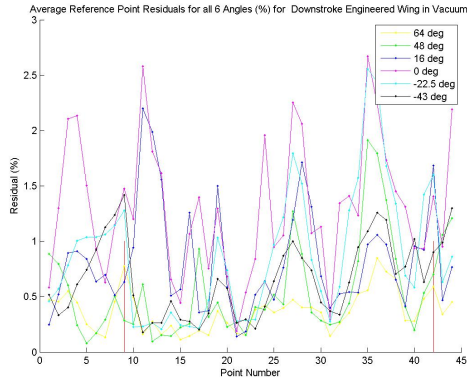
(a) Downstroke Vacuum
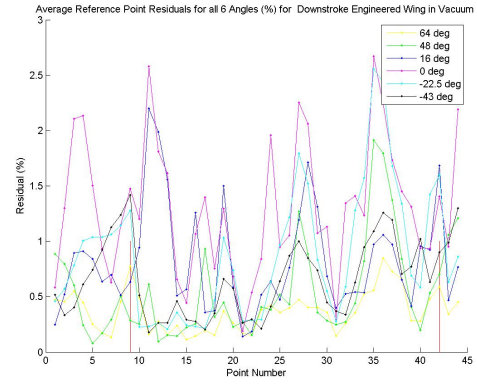
(b) Upstroke Vacuum
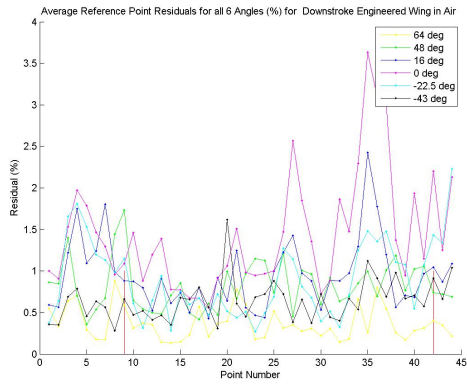
(c) Downstroke Air
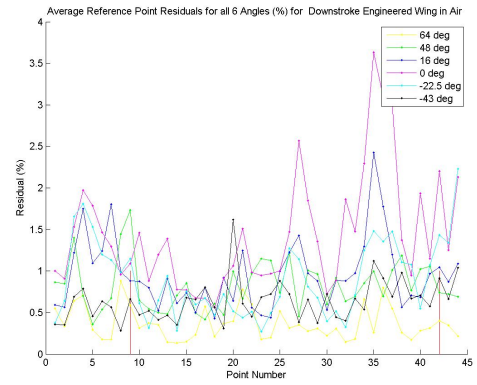
(d) Upstroke Air

Figure B.2:   Point Residuals of Engineered Wing

Appendix C. Cardinal Spline Theory

The aim of this appendix is to display the theory that is rooted in the implementation of the **Cardinal Spline Interpolant** as it applies to its implementation in this thesis. Though this was mentioned in the text, it should be reiterated that the code used was not in-house, rather it was gained from mathworks.com courtessy of Dr. Murtaza Khan [32].

Given the independent variable (call it [u] which can be stated as 'the number of points between points to be splined') and a tension (call it [T]), it is possible to evaluate the dependent variable at four different points at a time (P0,P1,P2,P3) where P1 and P2 are the 'end points' at the end of the curve and P0 and P3 are what is used to calculate the slope of the curve endpoints [32]. The cardinal matrix is constructed based off of the given tension value [T] as such:

$$s = \frac{1-T}{2} \tag{C.1}$$

Which is used for the Matrix M_{card}:

$$M_{card} = \begin{bmatrix} -s & 2-s & s-2 & s \\ 2 \cdot s & s-3 & 3-(2 \cdot s) & -s \\ -s & 0 & s & 0 \\ 0 & 1 & 0 & 0 \end{bmatrix} \tag{C.2}$$

A matrix of inputs is then constructed which will b called [G]

$$G = \begin{bmatrix} P0 & P1 & P2 & P3 \end{bmatrix} \tag{C.3}$$

This [G] matrix will of course be in three separate arenas (be it there are three dimensions for this analysis) so a [P] vector must be constructed for each of the dimensions. The independent variable (or also known as the parameter value- say put 30 points in between wach hard data point) can then be constructed as such:

199

$$U = \begin{bmatrix} u^3 & u^2 & u & 1 \end{bmatrix} \qquad (C.4)$$

These can then be combined to form what can be refered to as the 'spline matrix' or as it shall be called [Pu], which is essentially the array of splined points based off of the aforementioned averaging methods:

$$Pu = U * M_{card} * G \qquad (C.5)$$

This can then be applied to the every point based off of the same parameters for as many 'sets' of points, so it is possible to spline an infinite number of points as long as they are fed in or 'overlapped' four points at a time (as described above). This was possible in this study due to the fact that since 6 separate angles were investigated for one half of a stroke (downstroke and upstroke), it is safe to say that the splined data will be based off of 5 separate intervals that were each averaged twice. In order of this to occur, it was necessary to redistribute the averaged data sets (as described in Figure 4.17) to fit with the rules of this (Catmull-Rom) Cardinal Spline. Redistribution entailed splitting the averaged wing data (isolated from the stationaly reference points) into the the **x-y-z** coordinates. They needed to be organized in a manner that repeated the first and last points at the end points in the manner of:

$$P_x = [s_w(1).ux, \quad s_w(:).ux, \quad s(end).ux] \qquad (C.6)$$
$$P_y = [s_w(1).uy, \quad s_w(:).uy, \quad s_w(end).uy] \qquad (C.7)$$
$$P_z = [s_w(1).uz, \quad s_w(:).uz, \quad s_w(end).uz]$$

Where the term $s_w(1).u(x, y, z)$ denotes the averaged reference points on the wing at angle 1 (64 degrees) split into the x,y,z coordinates. This would essentially create an [8x33] matrix as there were originally 6 angles with 33 reference points

present. This 'data padding' by placing the repeated end points at each ends of the $P_{x,y,z}$ data sets allows for the spline to average its slope with itself which disallows any unusuall behavior to occur at the end points (64 degree and -43 degree positions) which was seen by the cubic spline interpolant.

Appendix D. Raw Data Display

The aim of this appendix is to display the data as it occurs in its raw form. This represents the full half-strokes as they move from the raw point cloud to averaged, managable data sets that were used in the analysis of the flapping wing. This was not presened in the text because the plots tens to take up room that was deemed iinapropriate for reaching any type of conclusion, but these pictures shoud be included in order that a reader can see the unmanipulated data as a means to perhaps explain some of the observed behaviors seen in the results.

All Points With Averages for Downstroke Bio Wing in Vacuum

(a) Downstroke Vacuum

All Points With Averages for Upstroke Bio Wing in Vacuum
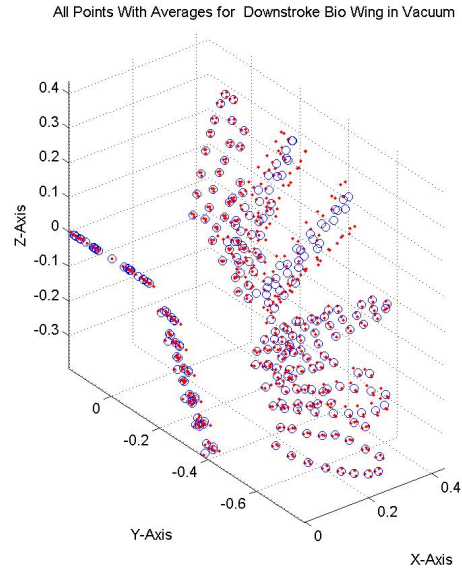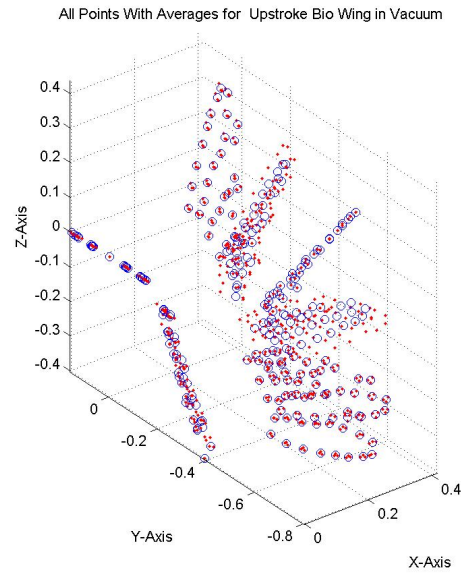
(b) Upstroke Vacuum

Figure D.1:   Raw Data of Biological Wing in Vacuum
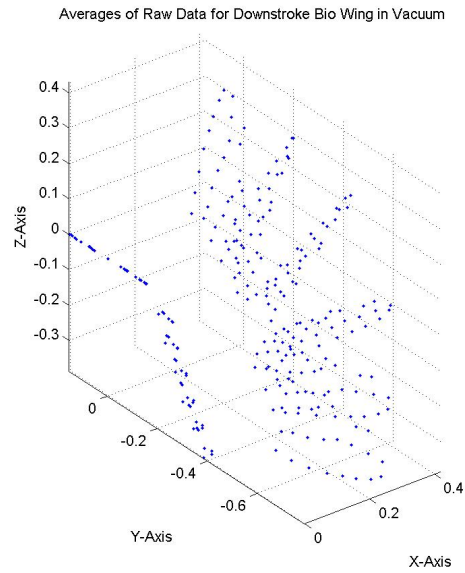
(a) Downstroke Vacuum
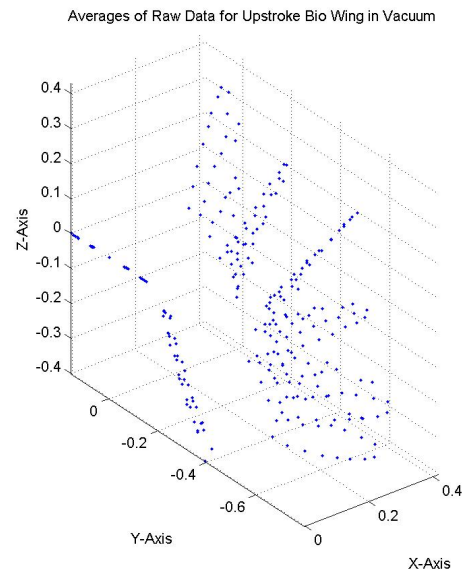
(b) Upstroke Vacuum

Figure D.2:   Averaged Data of Biological Wing in Vacuum
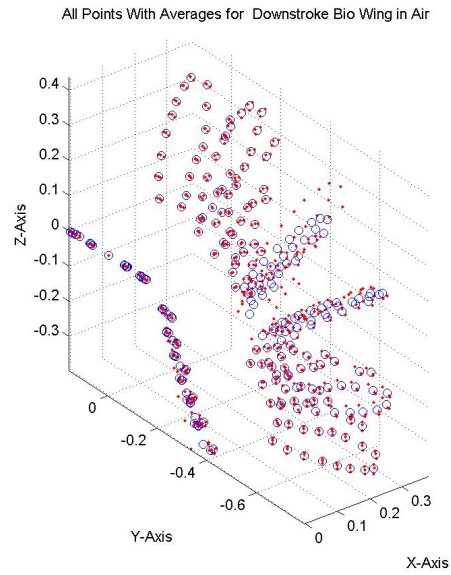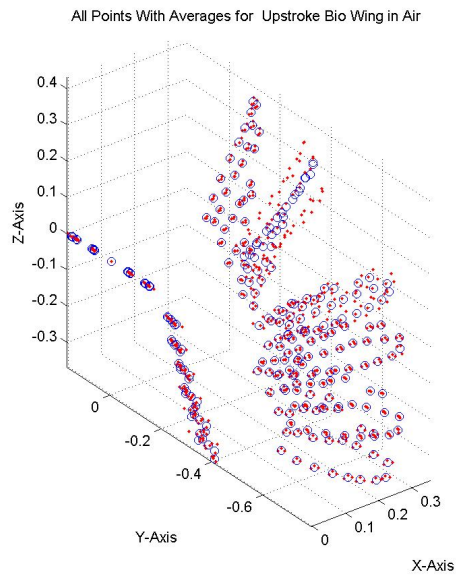
(a) Downstroke Air

(b) Upstroke Air

Figure D.3:   Raw Data of Biological Wing in Air
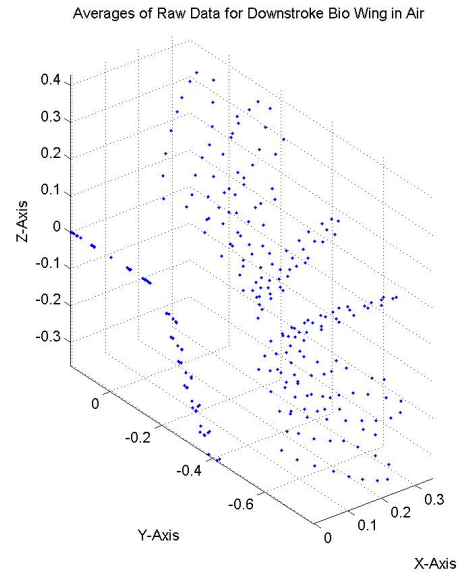
(a) Downstroke Air
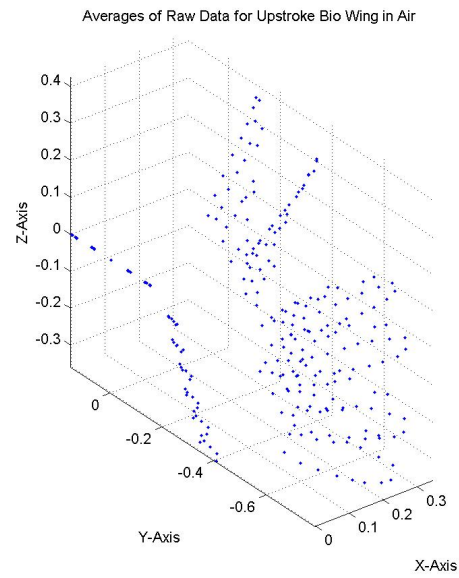
(b) Upstroke Air

Figure D.4: Averaged Data of Biological Wing in Air

All Points With Averages for Downstroke Engineered Wing in Vacuum

(a) Downstroke Vacuum

All Points With Averages for Upstroke Engineered Wing in Vacuum
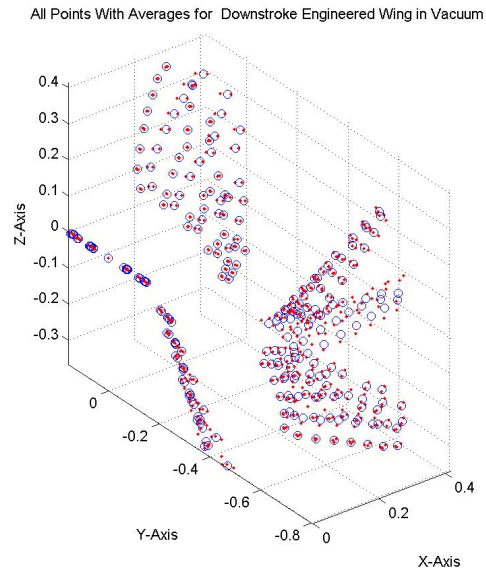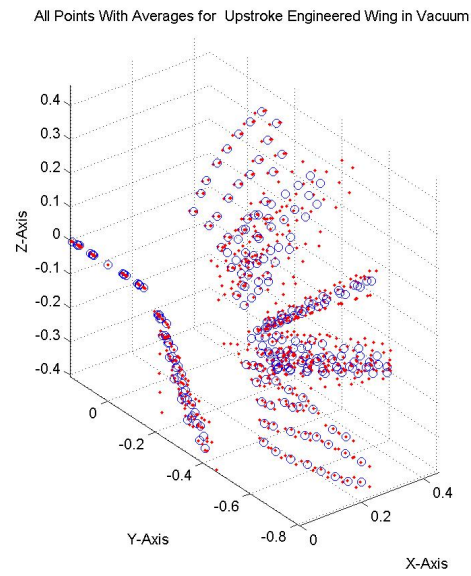
(b) Upstroke Vacuum

Figure D.5:   Raw Data of Biological Wing in Vacuum

207

Averages of Raw Data for Downstroke Engineered Wing in Vacuum

(a) Downstroke Vacuum

Averages of Raw Data for Upstroke Engineered Wing in Vacuum
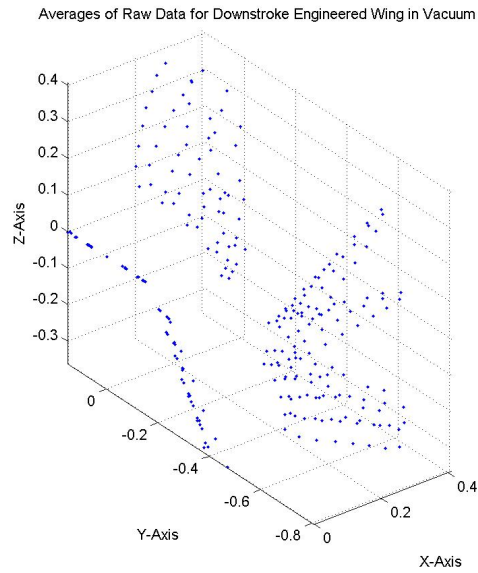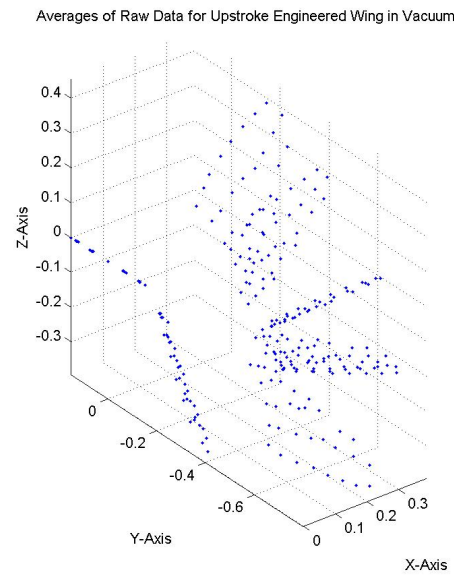
(b) Upstroke Vacuum

Figure D.6:   Averaged Data of Engineered Wing in Vacuum
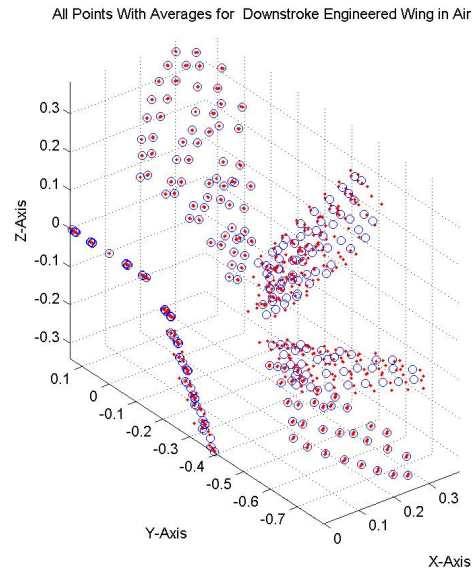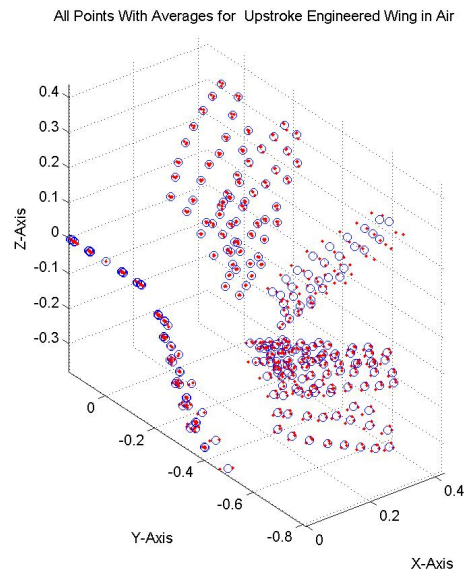
(a) Downstroke Air

(b) Upstroke Air

Figure D.7:   Raw Data of Engineered Wing in Air

209
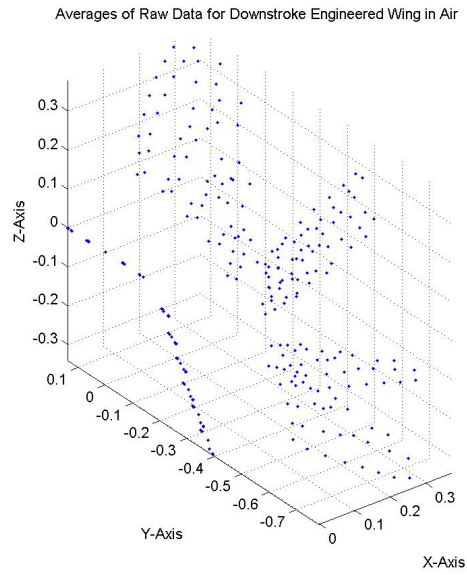
(a) Downstroke Air

(b) Upstroke Air

Figure D.8:   Averaged Data of Engineered Wing in Air

210

Appendix E. Modal Analyses

The crux of this thesis was to re-examine the realm of the structural characterization of the *Manduca Sexta* wing and compare it to that of one that was designed and constructed by man with nature in mind. Previous research [1], [4], [11] held the modal analysis as the end all-be all of structural characterization. Initial conjectures that revolved around this thesis viewed these claims with skepticism since the small displacements inherent in the modal analysis do not find themselves as a part of the functionality of these wings.

Despite doubt, it was deemed pertinent to characterize the biological wing under these several conditions via the modal analysis. This action secures its necessity due to the fact that before this study, there was no solid method of structural characterization beyond what was seen in Combes and Daniel [6] and [7] and Norris [1]. Proper credit should be given to those who pioneered this realm of investigation, and as such the procedures concerning the modal analysis detailed in Chapter 3 were applied to the following:

- A dry wing that was allowed to sit for 12 hours in air. Execution in Air

- A freshly removed wing with scales attached. Execution in Air and Vacuum

All of these wings were removed in the manner detailed by Chapter 3 in which the shoulder was included (as opposed to Norris' cut location which did not include the shoulder). It is an unfortunate truth that the number of specimens available for testing was lacking. The analysis presented here was performed for the purpose of observing both resonant frequencies and mode shapes, and to compare them to those found in the work of Norris et al.

Table E.1: Modal Analysis of Norris Biological Wing (with Wing Scales)

Wing	1st Mode Bending	2nd Mode Torsion	1st Mode Saddle	2nd Mode BiSaddle
Norris Wing (Air)	59.75 Hz	84.0 Hz	107 Hz	142.0 Hz
Norris Wing (Vac)	85.0 Hz	105.0 Hz	138.0 Hz	170.0 Hz
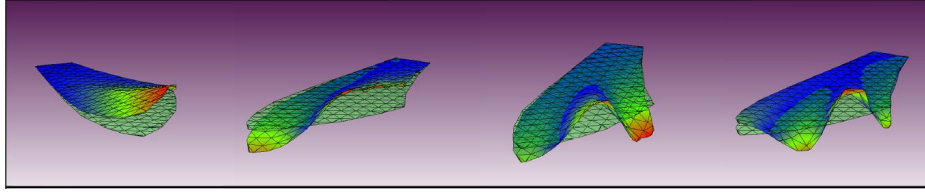
Figure E.1:   First Four Modes of a Hawkmoth's Forewing [1]
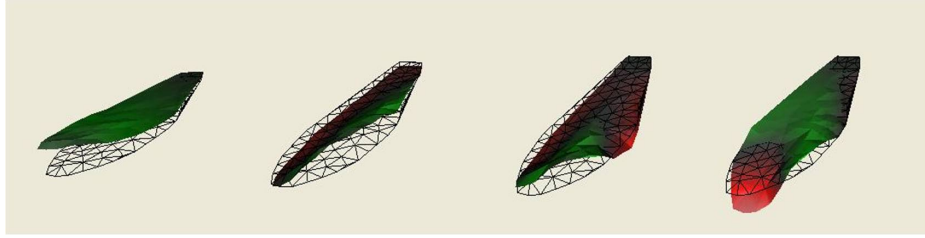
Figure E.2:   First Four Modes of a Dry Hawkmoth's Forewing With Shoulder

Table E.2:   Modal Analysis of Dry Biological Wing (with Wing Scales)

Wing	1st Mode Bending	2nd Mode Torsion	1st Mode Saddle	2nd Mode BiSaddle
Dry Wing (Air)	60.625 Hz	104.375 Hz	159.375 Hz	206.25 Hz

It can be seen in Figure E.2 that the mode shapes of the dry wing with scales are comprable to those observed by Norris' fresh wings without the shoulder. The resonant frequencies appear to exist slightly above those of what was seen by Norris' work in Air according to Table E.2.

A fresh wing was first tested in air then in vacuum, all within 40 mins. The results are shown in Table E.3

Table E.3:   Modal Analysis of Freshly Removed Biological Wing with Wing Scales in Air

Wing	1st Mode Bending	2nd Mode Torsion	1st Mode Saddle	2nd Mode BiSaddle
Fresh Wing (Air)	46.875 Hz	84.375 Hz	141.25 Hz	191.25 Hz

The fresh wing in vacuum did not yield results similar to anything that has been seen before save for the first mode. It would appear that when examining the only two modeshapes are seen. The only ones that appear to be present are the first bending

212
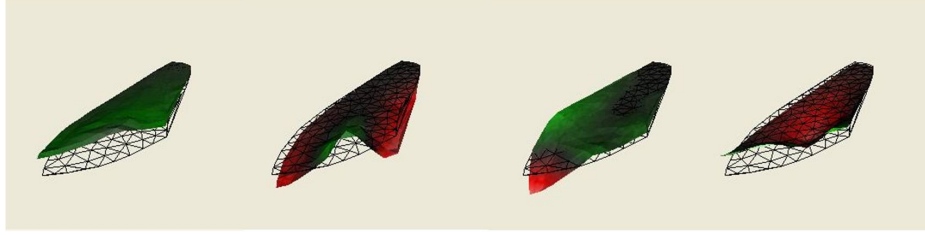
Figure E.3:   First Four Modes of a Fresh Hawkmoth's Forewing in Air

and the saddle mode, and it would appear that they exist at resonant frequencies similar to those seen in Norris' work.

Table E.4:   Modal Analysis of Freshly Removed Biological Wing with Wing Scales in Vacuum

Wing	1st Mode Bending	2nd Mode Torsion	1st Mode Saddle	2nd Mode BiSaddle
Fresh Wing (Air)	84.375 Hz	N/A	152.5	N/A

Appendix F. The Kinematics of the DeLeón Flapper

This appendix serves to present the kinematic analysis of the DeLeón Flapping mechanism discussed in Chapters 4 and 5.

F.1 Basis of Investigation

Before total implementation, it is necessary to consider the theory associated with the inner workings of the flapping mechanism shown in Figure 2.1. Figure F.1 will aid in the overall visualization of the variables used in this analysis.
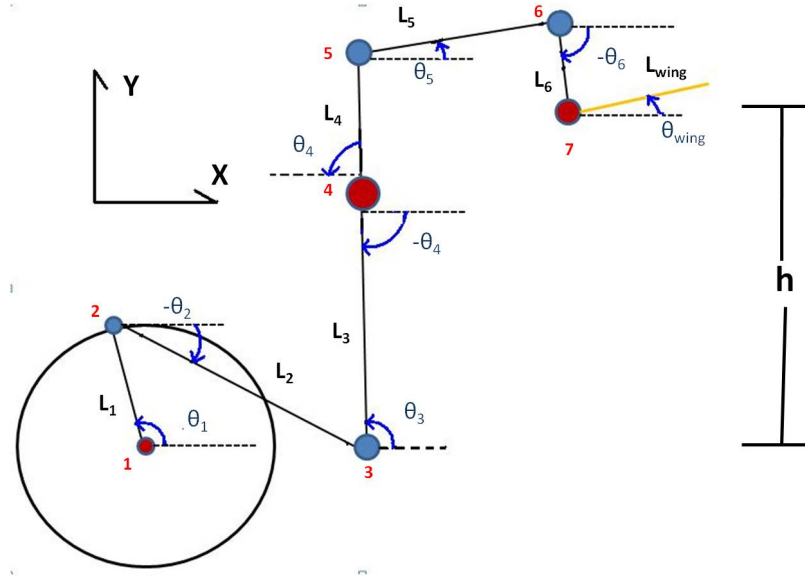
Figure F.1:   Illustration of the Variables Associated With the DeLeón Flapper

It should be noted that in Figure F.1, the blue dots represent freely rotating/-translating links and the red dots denote a fixed hinge in which rotation is permitted, however translation is constrained.

The actual dimensions of this setup are as follows (presented for MatLab analysis).

To begin this analysis, one must first be made aware of the *type* of analysis that is to be performed here. It is always necessary to consider the internal and

Table F.1:   DeLeòn Flapper Element Dimensions

Element	Length (in)
L_1	0.835
L_2	2.511
L_3	2.000
L_4	1.000
L_5	1.540
L_6	0.500
dx_1	2.511
dy_1	1.000
dx_4	1.540
dy_4	1.000

inertial properties inherent in any system, however for the current setup (as will be seen in Chapter 3) the effects of mass and momentum will be ignored due to the amount of available power supplied at the crank (Link L_1) and the materials chosen to construct the illustrated system shown in Figure 2.1 which at this moment can be considered massless. In fact, the motor chosen to conduct the experiments was so powerful, the aerodynamic forces associated with the wing and its presence can be considered negligible. These statements allude to a type of treatment known as **rigid body motion** (RBM) which does not concern itself with the kinetics associated with a system, rather it is firmly rooted in the kinematics associated with a given system.

The system illustrated in 2.1 and F.1 exhibits the following three of the types of motion:

1. *Translation*: The movement of all particles associated with a given structure or element find themselves moving with respect to a still or different translating reference frame. "When a rigid body is in translation, all points of the body have the same acceleration at any given instant in time" [33]

2. *Rotation about a fixed axis*: Here, all particles move parallel to each other in a circular motion around a fixed axis which can be said to be the center or rotation. This is not the same as curvilinear translation in which the magnitude and direction of a translating body change at any given instant.

3. *General Plane Motion*: A very prominent portion of this particular analysis, this is simply the concept that all bodies move in the same plane with respect to each other. Though it will be later seen that each member does not coexist/move in the same plane, the system in question can be considered as such to exhibit planar motion. Both translation and rotation can exist in planar motion

Members 1, 3, 4, 6, 7 (wing) all exhibit items two and three, which are due to the fixed nature of one of their ends. Members 2 and 5 however exhibit curvilinear translation (item 1) in which neither of their two ends are fixed, rather they are allowed to both translate and rotate. They are only constrained by the motion exhibited by the other members that they are attached to. Interestingly enough, though there are a total of eight bars in this system, the big center dot can be considered a division point between two four-bar linkages. Four bar linkage systems are well known and many of their characteristics are already present in various forms of literature. The proceeding presentation will shed light on the kinematics associated with the given system.

F.2   Mathematical Considerations

To begin, it is necessary to consider the lower half of the described system in Figure F.1. To illustrate this treatment, please consider Figure F.4 in which the progression towards the four bar treatment can be seen for visualization purposes.

In Figure F.2 the crank has been allowed to rotate, but only the lower half of the entire system is shown. Figure F.2b removes some of the unnecessary extraneous objects to show that in fact the four bar mechanism does exist here, and it is Figure F.2c that simply flips and annotates Figure F.2b for the purpose of calculation. It should be noted that the green vector $\vec{r_p}$ does not exist, rather it is there for the purpose of aiding in the understanding of future calculations. Additionally, the grey linkage r_1 does not explicitly exist, but its presence is implied due to the fixed nature of the links [1] and [4] displayed as red numbers. It was conceived to include the parameter θ_3 as it is included in preceding figures, however its presence is neither mandated nor necessary in the following calculations. Validation of the proceeding

(a) Original Orientation

(b) Crank Rotated (Four Bar Visualization)

(c) Annotated Crank-Rocker

Figure F.2:   Four Bar Flapper Visualization

methods could be obtained once the mechanism was designed in SolidWorks^{TM} using the builtin motion analysis functions.

To begin, it is necessary to examine the concept of a closure equation, which simply put, expresses the condition that a loop of a linkage closes on itself. It is

helpful to consider the presence of $\vec{r_p}$ when performing the analysis appropriately, as it effectively links all four of the bars into two triangles. This is illustrated here:

$$\vec{r_p} = \vec{r_1} + \vec{L_3} = \vec{L_1} + \vec{L_2} \qquad (F.1)$$

Equation F.1 treats the links L_i as vectors. This is done in order to maintain consistency for equation treatment, however it is necessary to clarify that even though $\vec{L_i}$ is treated as a vector, the physical links L_i maintain their shapes and lengths throughout the analysis and are fixed. Rearranging Equation F.1, it is possible to solve for $\vec{L_2}$. This is necessary since the $\vec{L_2}$ vector represents the aforementioned behavior of curvilinear translational motion. This is due mainly to the fact that this analysis uses L_1 as the driving link (as noted).

$$\vec{L_2} = \vec{r_1} + \vec{L_3} - \vec{L_1} \qquad (F.2)$$

which in Cartesian coordinates translates to:

$$L_2 \cos \theta_2 = r_1 \cos \theta_{r1} + L_3 \cos \theta_4 - L_1 \cos \theta_1 \qquad (F.3)$$

$$L_2 \sin \theta_2 = r_1 \sin \theta_{r1} + L_3 \sin \theta_4 - L_1 \sin \theta_1 \qquad (F.4)$$

It should be realized that in Equations F.3 and F.4, all the link lengths are known and fixed, but more importantly, θ_{r1} does not change with respect to time at all, and θ_1 is controlled as the driving angle (and thus is known for all time) leaving the system with two equations and two unknowns of θ_2 and θ_4. Though the parameter θ_2 influences θ_4, it is θ_4 that is of most interest. In order to solve this system of equations, Waldron and Kinzel [34] suggest to square both sides of Equations F.3 and F.4 and then add them. This will allow for the identity $sin^2(\theta) + cos^2(\theta) = 1$ to be utilized. The end result (after simplification) is represented here:

$$L_2^2 = r_1^2 + L_1^2 + L_3^2 + 2r_1 L_3(\cos\theta_{r1}\cos\theta_4)$$

$$-2r_1 L_1(\cos\theta_{r1}\cos\theta_1 + \sin\theta_{r1}\sin\theta_1) + 2L_1 L_3(\cos\theta_1\cos\theta_4 + \sin\theta_1\sin\theta_4) \quad\text{(F.5)}$$

The manipulation carried out in Equation F.5 effectively allows θ_4 (the goal parameter) to be isolated in terms of the known lengths and prescribed variable θ_1. Again Waldron and Kinzel [34] provide on the next step, which is to simplify the calculations performed above by breaking the equation up as such:

$$A\cos\theta_4 + B\sin\theta_4 + C = 0 \quad\text{(F.6)}$$

Where the terms A-C can be defined as follows:

$$A = 2r_1 L_3 \cos\theta_{r1} - 2L_1 L_3 \cos\theta_1$$

$$B = 2r_1 L_3 \sin\theta_{r1} - 2L_1 L_3 \sin\theta_1$$

$$C = r_1^2 + L_1^2 + L_3^2 - L_2^2 - 2r_1 L_1(\cos\theta_{r1}\cos\theta_1 + \sin\theta_{r1}\sin\theta_1)$$

In order to solve Equation F.6, it is possible to utilize the standard trigonometric identity for half angles shown here:

$$\sin\theta_4 = \frac{2\tan\frac{\theta_4}{2}}{1 + \tan^2\frac{\theta_4}{2}} \quad\text{(F.7)}$$

$$\cos\theta_4 = \frac{1 - \tan^2\frac{\theta_4}{2}}{1 + \tan^2\frac{\theta_4}{2}} \quad\text{(F.8)}$$

Substituting these identities into Equation F.6 and simplifying, one may yield the following:

$$(C - A)\left(\tan^2 \frac{\theta_4}{2}\right) + 2B\left(\tan \frac{\theta_4}{2}\right) + (A + C) = 0 \qquad \text{(F.9)}$$

Which allows for the isolation of θ_4 by solving for $\tan \frac{\theta_4}{2}$ using the well known quadratic formula as such:

$$\tan \frac{\theta_4}{2} = \frac{-2B \pm \sqrt{4B^2 - 4(C - A)(C + A)}}{2(C - A)} = \frac{-B \pm \sqrt{B^2 - C^2 + A^2}}{C - A} \qquad \text{(F.10)}$$

Thus stating that:

$$\theta_4 = 2\arctan\left(\frac{-B \pm \sqrt{B^2 - C^2 + A^2}}{C - A}\right) \qquad \text{(F.11)}$$

This is an important parameter that links the bottom four bar linkage with the top, essentially providing the essential formula to move onto the next objective which is to analyze the upper four bar. It may not be apparent, but the fact that the angle θ_2 was essentially eliminated from concern does not denote that its existence is any less important. This angle will become instrumental in calculating the velocities and thus must be solved for. Since θ_4 was solved for in the previous equation, it is now possible to reexamine the treatment of Equations F.3 and F.4. By dividing Equation F.4 by Equation F.3, one may then solve for θ_2 in the following manner:

$$\theta_2 = \arctan\left[\frac{r_1 \sin\theta_{r1} + L_3 \sin\theta_4 - L_1 \sin\theta_1}{r_1 \cos\theta_{r1} + L_3 \cos\theta_4 - L_1 \cos\theta_1}\right] \qquad \text{(F.12)}$$

Using MatLab, the preceding equations were evaluated and the result produces the plot depicted in Figure F.3

220
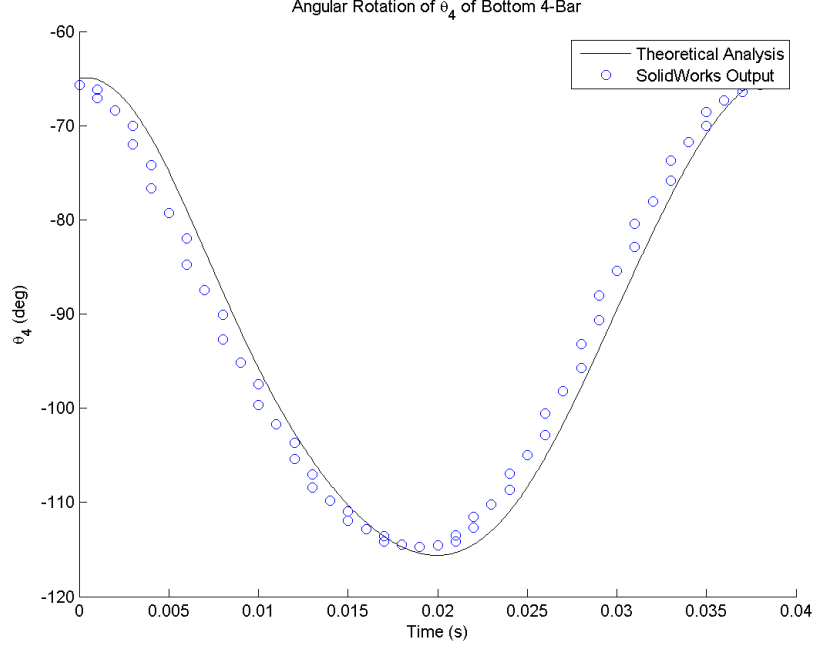
Figure F.3:   Bottom Four Bar Mechanism Angular Displacement (θ_4) Response

It can be noticed that in Figure F.3 that the phase is slightly off. This is due to the fact that the SolidWorks analysis did not exactly start at a θ_1 of zero, but the estimation is adequate for the purpose of this study. Now that this angle has been solved for, it is possible to repeat this process for the top linkage set, with L_4 being the driving link. This can be visualized in Figure F.4. Due to the orientation of the system in Figure F.1, the top half requires little or no re-orientation to examine the four bar setup.

As mentioned, the goal of this analysis is to obtain the angle θ_{wing} as a function of θ_1. Since L_3 and L_4 are essentially the same link and are rigidly connected, it is safe to say that $\theta_4^- = \theta_4^+$. This indicates that the top and bottom are equal and thus if it is possible to obtain θ_{wing} in terms of θ_4, then the system will be solved for the translational portion of this analysis. To begin, it should be noticed that the same properties of the upper half and lower half exist, specifically in that the green vector is not existent, along with the link r_4 (which is there by the nature of the setup) however the analysis requires their presence. The analysis will proceed as before:

221
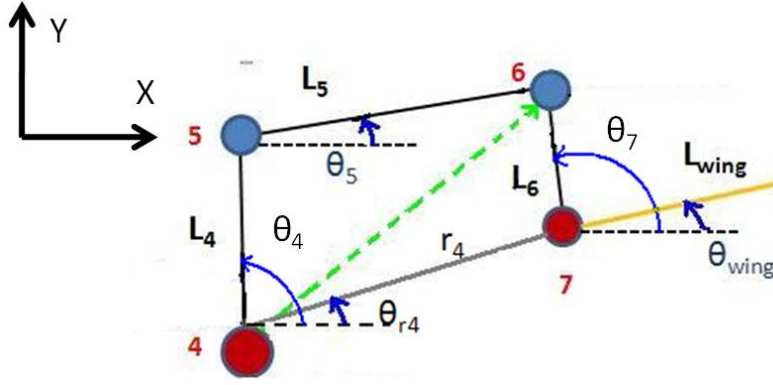
Figure F.4: Top Half of DeLeón Flapper with Annotations

$$\vec{r_p} = \vec{r_4} + \vec{L_6} = \vec{L_4} + \vec{L_5} \tag{F.13}$$

$\vec{L_5}$ is found next since it will exhibit curvilinear translation:

$$\vec{L_5} = \vec{r_4} + \vec{L_6} - \vec{L_4} \tag{F.14}$$

which in Cartesian coordinates translates to:

$$L_5 \cos \theta_5 = r_4 \cos \theta_{r4} + L_4 \cos \theta_4 - L_6 \cos \theta_7 \tag{F.15}$$

$$L_5 \sin \theta_5 = r_4 \sin \theta_{r4} + L_4 \sin \theta_4 - L_6 \sin \theta_7 \tag{F.16}$$

It should be realized that in Equations F.15 and F.16 the term θ_7 is introduced. Simply put, this term is representative of the angle of L_6 with respect to the normal. $\theta_{wing} = \theta_7 - 90^o$ so the representation is more simple to manipulate. Performing the same operation that produced Equation F.5, the following is produced:

$$L_5^2 = r_4^2 + L_4^2 + L_6^2 + 2r_4 L_6 (\cos \theta_{r4} \cos \theta_7) - 2r_4 L_4 (\cos \theta_{r4} \cos \theta_4 \tag{F.17}$$
$$+ \sin \theta_{r4} \sin \theta_4) + 2L_4 L_6 (\cos \theta_4 \cos \theta_7 + \sin \theta_4 \sin \theta_7)$$

222

The manipulation carried out in Equation F.17 effectively allows θ_7 to be in terms of θ_4 as was shown before. This time the variables will be different, but the concept is the same as for the lower four bar linkage:

$$D \cos \theta_4 + E \sin \theta_4 + F = 0 \tag{F.18}$$

Where the terms D-F can be defined as follows:

$$D = 2r_4 L_6 \cos \theta_{r4} - 2L_4 L_6 \cos \theta_4$$

$$E = 2r_4 L_6 \sin \theta_{r4} - 2L_4 L_6 \sin \theta_4$$

$$F = r_4^2 + L_4^2 + L_6^2 - L_5^2 - 2r_4 L_4 (\cos \theta_{r4} \cos \theta_4 + \sin \theta_{r4} \sin \theta_4)$$

In order to solve Equation F.6, it is possible to utilize the standard trigonometric identity for half angles shown here:

$$\sin \theta_7 = \frac{2 \tan \frac{\theta_7}{2}}{1 + \tan^2 \frac{\theta_7}{2}} \tag{F.19}$$

$$\cos \theta_7 = \frac{1 - \tan^2 \frac{\theta_7}{2}}{1 + \tan^2 \frac{\theta_7}{2}} \tag{F.20}$$

Substituting these identities into Equation F.18 as before:

$$(F - D)\left(\tan^2 \frac{\theta_7}{2} \right) + 2E\left(\tan \frac{\theta_7}{2} \right) + (F + D) = 0 \tag{F.21}$$

Which allows for the isolation of θ_7 by solving for $\tan \frac{\theta_7}{2}$ using the well known quadratic formula as such:

$$\tan\frac{\theta_4}{2} = \frac{-2E \pm \sqrt{4E^2 - 4(F-D)(F+D)}}{2(F-D)} = \frac{-E \pm \sqrt{E^2 - F^2 + D^2}}{F-D} \qquad \text{(F.22)}$$

Thus stating that:

$$\theta_7 = 2\arctan\left(\frac{-E \pm \sqrt{E^2 - F^2 + D^2}}{F-D}\right) \qquad \text{(F.23)}$$

And as mentioned:

$$\theta_{wing} = \theta_7 - 90^o \qquad \text{(F.24)}$$

As was before in Equation F.25, the angle θ_5 must be solved for by dividing Equations F.16 by F.15 and solving for θ_5:

$$\theta_5 = \arctan\left[\frac{r_4 \sin\theta_{r4} + L_6 \sin\theta_7 - L_4 \sin\theta_4}{r_4 \cos\theta_{r4} + L_6 \cos\theta_7 - L_4 \cos\theta_4}\right] \qquad \text{(F.25)}$$

The result of this analysis can be seen in Figure F.5.

It can be seen here that the response of the top half of the four bar mechanism matches closely to what SolidWorks has deemed as the correct response. This provides a vote of confidence in the analysis. This is an important realization due to the fact that this is what can be used to compare to other previously conceived designs as was seen in Figure 2.2.

Once the angular position of the flapping element with respect to the driving angle (θ_1) is determined, it can be conceived that the velocity of the wing member can be found as a function of the crank velocity $\dot{\theta}_1$ or as can be stated: ω_1. It becomes necessary once again to examine Figure F.2 as it will be easier to treat this as two four bar mechanisms. The identity $\dot{\vec{r}_p} = \dot{\vec{r}_1} + \dot{\vec{L}_3} = \dot{\vec{L}_1} + \dot{\vec{L}_2}$ should hold true, thus aiding
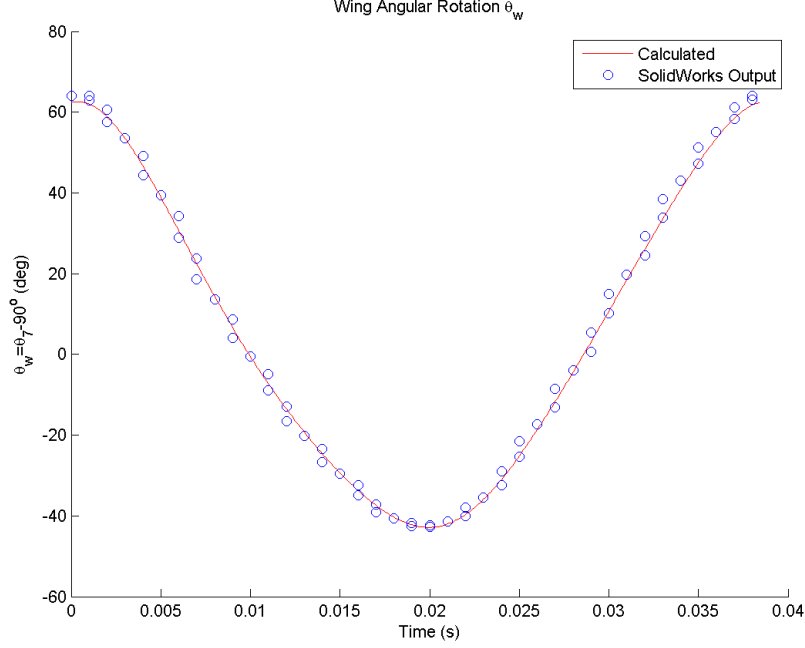
Figure F.5: Angular Displacement of Top Four Bar Mechanism (θ_w) Response as Compared to SolidWorks

in the manipulation of the following process to be discussed. Taking the derivatives with respect to time of Equations F.3 and F.4 will yield the following:

$$L_1\omega_1 \sin\theta_1 + L_2\omega_2 \sin\theta_2 = L_3\omega_4 \sin\theta_4 + r_1\omega_{r1} \sin\theta_{r1} \tag{F.26}$$

$$L_1\omega_1 \cos\theta_1 + L_2\omega_2 \cos\theta_2 = L_3\omega_4 \cos\theta_4 + r_1\omega_{r1} \cos\theta_{r1} \tag{F.27}$$

It should be noticed here that due to the setup of the linkage (specifically the fixed points) $\omega_{r1} = 0$ and $\omega_1 = fixed$ (or prescribed as 26 Hz), simplifications can be made by eliminating any treatment of the driving parameters associated with θ_1. This leaves the system as the familiar two equation - two unknown setup, however there are several more variables to consider here, so by eliminating the ω_{r1} term, one may rearrange the previous equations for the known values (ω_1 and θ_1) and place the system into matrix form:

225

$$\begin{bmatrix} -L_2 \sin\theta_2 & L_3 \sin\theta_4 \\ -L_2 \cos\theta_2 & L_3 \cos\theta_4 \end{bmatrix} \begin{Bmatrix} \omega_2 \\ \omega_4 \end{Bmatrix} = \begin{Bmatrix} L_1 \omega_1 \sin\theta_1 \\ L_1 \omega_1 \cos\theta_1 \end{Bmatrix} \qquad \text{(F.28)}$$

The result of this analysis can be seen in Figure F.6.
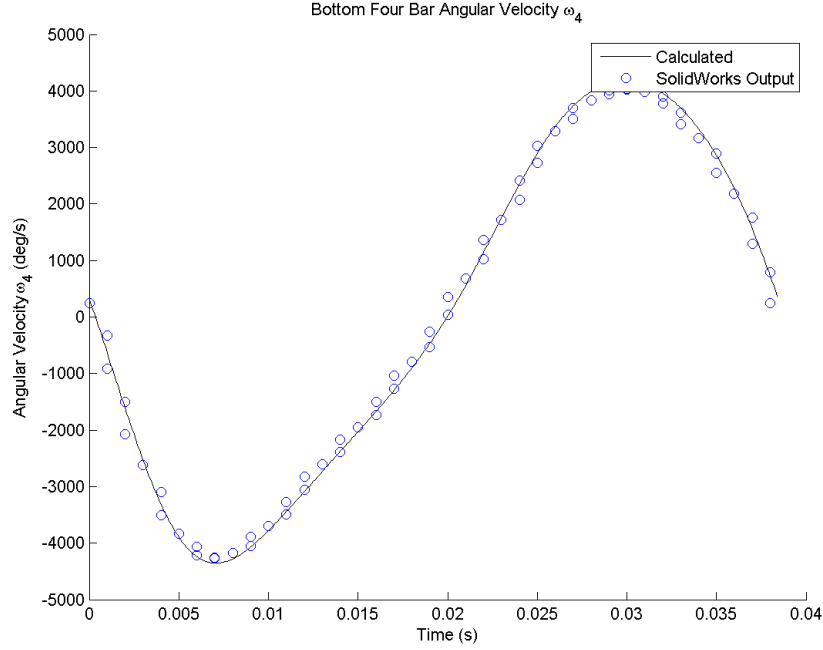
Figure F.6:   Angular Velocity of Wing for Bottom Four Bar Mechanism ω_4 Response as Compared to SolidWorks

These results can be used to solve for the two unknown angular velocities for the bottom four bar linkage. The upper four bar proceeds in much the same manner, utilizing the behavior of ω_4 as the driving angular velocity of the driving link L_4. To begin, consider the variables unique to those in Figure F.4 as applied to Equations F.26 and F.27:

$$L_4 \omega_4 \sin\theta_4 + L_5 \omega_5 \sin\theta_5 = L_6 \omega_7 \sin\theta_7 + r_4 \omega_{r4} \sin\theta_{r4} \qquad \text{(F.29)}$$

$$L_4 \omega_4 \cos\theta_4 + L_5 \omega_5 \cos\theta_5 = L_6 \omega_7 \cos\theta_7 + r_4 \omega_{r4} \cos\theta_{r4} \qquad \text{(F.30)}$$

By eliminating the ω_{r4} term, one may yield an expression similar to that which was gained for the bottom four bar mechanism:

$$\begin{bmatrix} -L_5 \sin\theta_5 & L_6 \sin\theta_7 \\ -L_5 \cos\theta_5 & L_6 \cos\theta_7 \end{bmatrix} \begin{Bmatrix} \omega_5 \\ \omega_7 \end{Bmatrix} = \begin{Bmatrix} L_4\omega_4 \sin\theta_4 \\ L_4\omega_4 \cos\theta_4 \end{Bmatrix} \qquad \text{(F.31)}$$

This produces all angular velocities for the entire mechanism. The most important angular velocity however is that of the wing (or ω_{wing}) which is going to be the same as that of ω_7, though it exhibits different angular displacements. This is due to the fact that inherent in the design of the mechanism, the point of pivot coincides with the central rotational axis of the wing and thus requires no special treatment as was seen with the angular displacement of θ_7 to θ_w in Equation F.24. Had the wing been offset from the pivot as was in the design conceived by Anderson et al. [28], the behavior of the wing would require special treatment in this analysis or the offset portion would have to be assumed as negligible (which is not a factor in the biological specimen). The result of this analysis can be seen in Figure F.7.

For comparison purposes, the experimental data obtained from [5] was applied to a 4th order polyfit in MatLab; and idea conceived by Willmont and Ellington. It was also necessary to apply a 6th order polyfit to both the data gained from the Combes and Daniel flapper and the Norris Flapper. Once the values for the function-fitted data was obtained, it was possible to differentiate it to obtain some assemblence of an angular velocity term as was represented from the raw data via the following relation;

$$\omega = \frac{d\theta}{d\tau} = \frac{\theta_2 - \theta_1}{\tau_2 - \tau_1} \qquad \text{(F.32)}$$

This relation could then be applied to all data that was represented in Figure 2.5 to yield Figure 2.6: the comparison of angular velocities as conceived by all previous designs and experimental data:
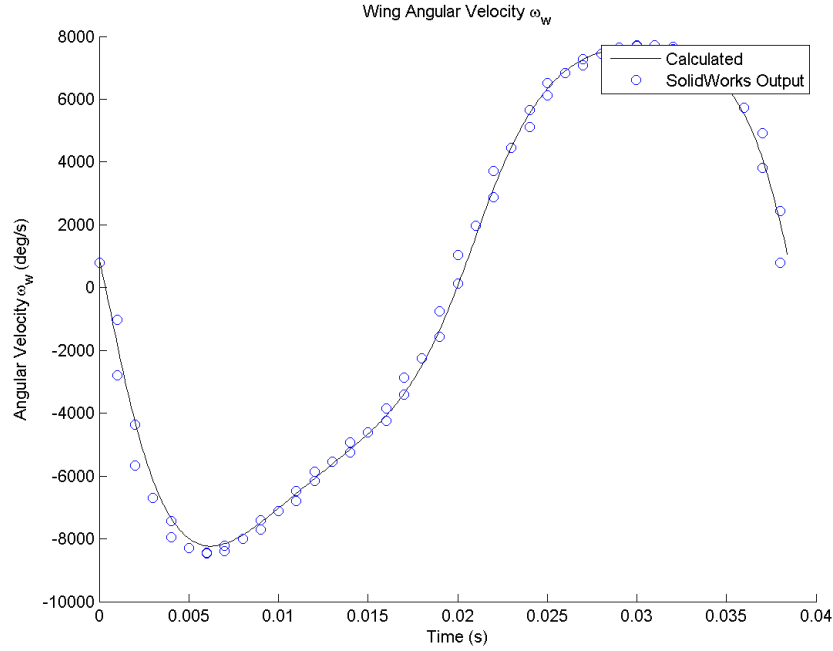
Figure F.7:   Angular Velocity of Wing for Top Four Bar Mechanism Response as Compared to SolidWorks

The third and final directive for this analysis, and possibly one of the most important, is the treatment of the accelerations inherent in the system. This analysis is crucial since it may lead to eventual requirements/information about the motor torque required to run the study (future study). To begin, Equations F.26 and F.27 can be differentiated with respect to time. This can be seen here:

$$L_1\alpha_1 \sin\theta + L_1\omega_1^2 \cos\theta_1 + L_2\alpha_2 \sin\theta_2 + L_2\omega_2^2 \cos\theta_2 = L_3\alpha_4 \sin\theta_4 + L_3\omega_4^2 \cos\theta_4 \quad \text{(F.33)}$$

$$L_1\alpha_1 \cos\theta - L_1\omega_1^2 \sin\theta_1 + L_2\alpha_2 \cos\theta_2 - L_2\omega_2^2 \sin\theta_2 = L_3\alpha_4 \cos\theta_4 + L_3\omega_4^2 \sin\theta_4 \quad \text{(F.34)}$$

Fortunately, for this particular study, the angular acceleration for the driving link will be zero (constant angular velocity), so as with velocity, this above system

can be broken into matrix form, separating the already known angular velocities and positions from the unknown angular accelerations:

$$
\begin{bmatrix} -L_2 \sin\theta_2 & L_3 \sin\theta_4 \\ -L_2 \cos\theta_2 & L_3 \cos\theta_4 \end{bmatrix} \begin{Bmatrix} \alpha_2 \\ \alpha_4 \end{Bmatrix} = \begin{Bmatrix} L_1\omega_1^2 \cos\theta_1 + L_2\omega_2^2 \cos\theta_2 - L_3\omega_4^2 \cos\theta_4 \\ -L_1\omega_1^2 \sin\theta_1 - L_2\omega_2^2 \sin\theta_2 - L_3\omega_4^2 \sin\theta_4 \end{Bmatrix}
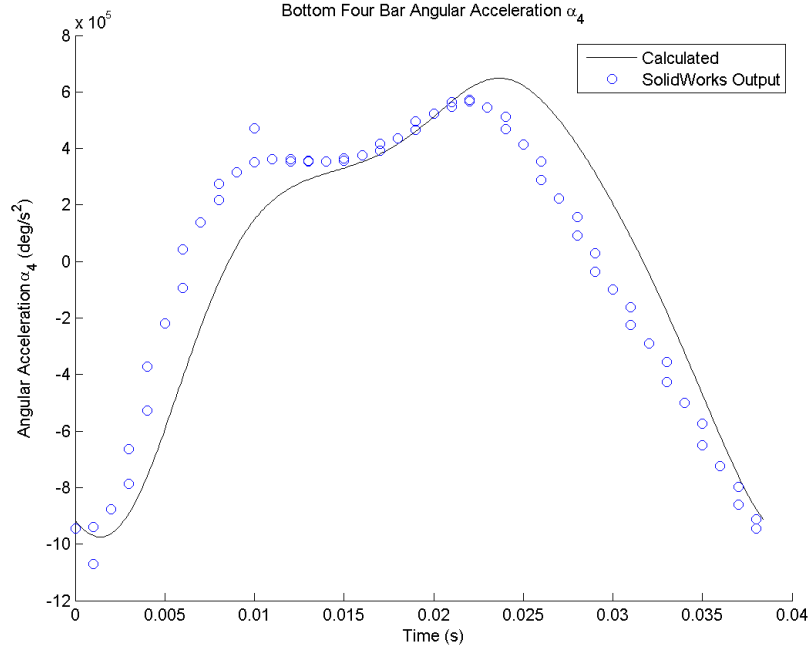$$
(F.35)

Figure F.8:   Angular Acceleration of the Bottom Linkage Compared to SolidWorks

The result of this for the angular accelerations associated with joints 2 and 4. Since α_4 was just calculated, this can be translated to the upper four bar linkage. The system is to be solved with the following:

$$
\begin{bmatrix} -L_5 \sin\theta_5 & L_6 \sin\theta_7 \\ -L_5 \cos\theta_5 & L_6 \cos\theta_7 \end{bmatrix} \begin{Bmatrix} \alpha_5 \\ \alpha_7 \end{Bmatrix} = \begin{Bmatrix} L_4\alpha_4 \sin\theta_4 + L_4\omega_4^2 \cos\theta_4 + L_5\omega_5^2 \cos\theta_5 - L_6\omega_7^2 \cos\theta_7 \\ L_4\alpha_4 \cos(_4) - L_4\omega_4^2 \sin\theta_4 - L_5\omega_2^2 \sin\theta_5 - L_6\omega_7^2 \sin\theta_7 \end{Bmatrix}
$$
(F.36)

Results are depicted in Figure F.9 wherein agreement can be seen between this analysis and the SolidWorks analysis except at near the end points. This lack of coherence in the back half was simply a function of a lack of resolution in the SolidWorks analysis. Thus, it is safe to say that this is representative of the angular acceleration of the wing; an important parameter when considering some of the possible kinetics that will not be discussed here.
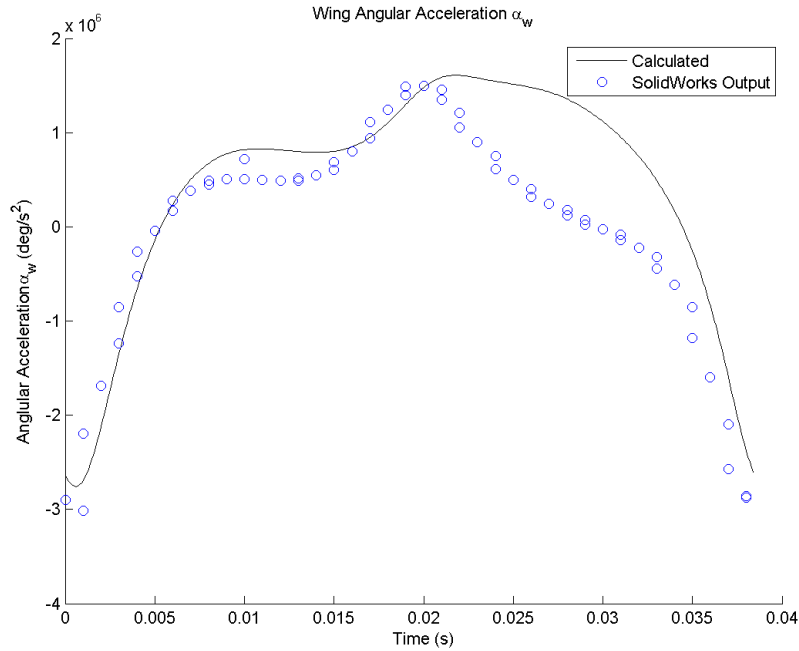

Figure F.9:   Angular Acceleration of the Wing Compared to SolidWorks

Thus concluding the kinematic analysis of the DeLeón Flapper.

Bibliography

1. Norris, A., Palazotto, A., and Cobb, R., "Structural Dynamic Characterization of and Insect Wing: Toward the Development of Bug Sized Flapping Wing Micro Air Vehicles," *American Institute of Aeronautics and Astronautics*, 2006, AIAA-2010-2790.

2. Geodetic Services Inc., "The Basics of Photogrammetry," 2006, URL http://www.geodetic.com/whatis.htm.

3. Photomodeler, "Core Technology," 2010, URL http://www.photomodeler.com.

4. Sims, T., *A Structural Dynamic Anaysis of a Manduca Sexta Forewing*, Master's thesis, Air Force Institute of Technology, Wright-Patterson AFB, OH, March 2010, AFIT/GAE/ENY/10-M22.

5. Willmott, A. P. and Ellington, C. P., "Mechanics of Flight in the Hawkmoth Manduca Sexta I: Kinematics of Hovering Forward Flight," *Journal of Experimental Biology 200*, 1997.

6. Combes, S. and Daniel, T., "Flexural Stiffness in Insect Wings I. Scaling and the Influence of Wing Venation," *Journal of Experimental Biology*, Vol. 206, 2003.

7. Combes, S. and Daniel, T., "Flexural Stiffness in Insect Wings II. Spatial Distribution and Dynamic Wing Bending," *Journal of Experimental Biology*, Vol. 206, 2003.

8. Tobias, A., *Experimental Methods to Characterize Nonlinear Vibration of Flapping Wing Micro Air Vehicles*, Master's thesis, Air Force Institute of Technology, Wright-Patterson AFB, OH, March 2005, AFIT/GAE/ENY/07-M23.

9. Stanford, B., Shyy, W., and Ifju, P., "A Numerical and Experimental Investigation of Flexible Micro Air Vehicle Wing Deformation," *American Institute of Aeronautics and Astronautics*, 2006, AIAA 2010-4941.

10. Han, J. and Chang, J. W., "Flow Visualisation and Force Measurement of an Insect Wing Based on Dragonfly Hovering," *American Institute of Aeronautics and Astronautics*, 2010, AIAA 2010-4941.

11. Sims, T., Palazotto, A., and Norris, A., "A Structural Dynamic Analysis of a Manduca Sexta Forewing," *International Journal of Micro Air Vehicles*, Vol. 2, No. 3, September 2010.

12. McMichael, J. and Francis, M., "Micro Air Vehicles- Toward a New Dimension in Flight," *Unmanned Systems*, Vol. 15 No. 3, 1997.

13. Madangopal, R., Khan, Z. A., and Agrawal, S. K., "Biologically Inspired Design of Small Flapping Wing Air Vehicles Using Four-Bar Mechanisms And Quasi-steady Aerodynamics," *Journal of Mechanical Design*, Vol. 127, 2005.

14. Michelson, R. C. and Reece, S., "Update on Flapping Wing Micro Air Vehicle Research," *13th Bristol International RPV Conference*, 1998.

15. Singh, B., Ramasamy, M., and Chopra, I., "Experimental Studies on Insect-Based Flapping Wings for Micro Hovering Air Vehicles," *American Institute of Aeronautics and Astronautics*, 2005, AIAA-2005-2293.

16. Willis, M., "Personal Correspondence 1-5 July 2010," 2010, Independent Study, Air Force Institute of Technology.

17. Shyy, W., Lian, Y., Tang, J., Viieru, D., and Liu, H., *Aerodynmics of Low Reymolds Number Flyers*, Cambridge University Press, New York, NY, 2008.

18. Weis-Fogh, T., "Quick Estimates of Flight Fitness in Hovering Animals, Including Novel Mechanisms for Lift Production," *Journal of Experimental Biology 59*, 1973, pp. 169–230.

19. Wooton, R. J., "The Insect Flight Skeleton: Towards a New Technology?" *44th AIAA Aerospace Sciences Meeting and Exhibit*, 2006, AIAA 2006-36.

20. DeLeón, N., O'Hara, R., and Palazotto, A., "Manufacturing of Engineering Biologically Inspired Flapping Wings," *25th Annual US-Japan Composites Conference*, 2010.

21. O'Hara, R., DeLeon, N., and Palazotto, A., "Structural Identification and Simulation of the Manduca Sexta Forewing," *American Institute of Aeronautics and Astronautics*, 2011, 2011 SDM Conference.

22. Wooton, R. J., "Support and Deformability in Insect Wings," *Journal of Zoology London*, Vol. 193, 1981.

23. Wooton, R. J., "Functional Morphology of Insect Wings," *Annual Review of Entomology*, Vol. 37, 1992.

24. Ennos, A. R., "Inertial and Aerodynamic Torques on the Wings of Diptera in Flight," *Journal of Experimental Biology*, Vol. 142, 87-95, 1989.

25. Ennos, A. R., "Inertial Cause of Wing Rotation in Diptera," *Journal of Experimental Biology*, Vol. 140, 161-169, 1989.

26. Combes, S. and Daniel, T., "Into thin air: contributions of aerodynamic and inertial-elastic forces to wing bending in the hawkmoth *Manduca Sexta*," *Journal of Experimental Biology*, Vol. 206, 2003.

27. Willmott, A. P. and Ellington, C. P., "Measuring the angle of Attack of Beating Insect Wings: Robust Three Dimensional Reconstruction From Two-Dimensional Images," *Journal of Experimental Biology 200*, 1997.

28. Anderson, M. L., O'Hara, R. P., and Cobb, R. G., "Design, Fabrication, and Testing of an Insect-Sized MAV Wing Flapping Mechanism," *49th AIAA Aerospace Sciences Meeting*, 2011.

29. Tanner, B. C. W., Regnier, M., and Daniel, T. L., "A spatially explicit model of muscle contraction explains a relationship between activation phase, power and ATP utilization in insect flight," *Journal of Experimental Biology*, 2008, 211.

30. Curtis, D. H., *Laser Dot Projection Photogrammetry and Force Measurement for Flapping Wing Micro Air Vehicles*, Master's thesis, Air Force Institute of Technology, Wright-Patterson AFB, OH, March 2009, AFIT/GAE/ENY/09-M05.

31. Objet Industries, *Eden 500 User Guide*, Objet Industries Ltd, Billerica, MA, 2008.

32. Khan, M., "Cardinal Spline (Catmull-Rom) Spline," 2010, URL http://www.mathworks.com/matlabcentral/fileexchange/7078-cardinal-spline-catmull-rom-spline.

33. Beer, F. P. and E. Russell Johnston, J., *Vector Mechanics for Engineers; Dynamics*, McGraw-Hill Book Company, New York, NY, 5th ed., 1988.

34. Waldron, K. J. and Kinzel, G. L., *Kinematics, Dynamics, and Design of Machinery*, John Wiley and Sons, INC, 2nd ed., 2004.

Vita

Lieutenant Nathanial E. DeLeón graduated from St. Charles Prepatory High School in Columbus, Ohio in 2004. He entered undergraduate studies at the The Ohio State University where he graduated with a Bachelor of Science degree in Aerospace Engineering in June of 2009. At that same time he comissioned as a distinguished graduate from Air Force Reserve Office Training Corps Detachment 645 into the United States Air Force.

Following his undergraduate career and comissioning , he was granted the opportunity to immediately attend the Air Force Institute of Technology as a first assignment to graduate with a degree in Aerospace Engineering. During his tenure at AFIT, Nathanial also served as a CrossFit Level 1 Certified Instructor at Crossfit Wright-Patt gym.

<div align="center">

Permanent address: 2950 Hobson Way
Air Force Institute of Technology
Wright-Patterson AFB, OH 45433

</div>

1. REPORT DATE *(DD–MM–YYYY)*	2. REPORT TYPE		3. DATES COVERED *(From — To)*
24 March 2011	Master's Thesis		Aug 2009 — Mar 2011

4. TITLE AND SUBTITLE

Manufacturing and Evaluation of a Biologically Inspired Engineered MAV Wing Compared to the *Manduca Sexta* Wing Under Simulated Flapping Conditions

5a. CONTRACT NUMBER

5b. GRANT NUMBER

5c. PROGRAM ELEMENT NUMBER

6. AUTHOR(S)

DeLeón, Nathanial E., 2d Lt, USAF

5d. PROJECT NUMBER

212/127

5e. TASK NUMBER

5f. WORK UNIT NUMBER

7. PERFORMING ORGANIZATION NAME(S) AND ADDRESS(ES)

Air Force Institute of Technology
Graduate School of Engineering and Management (AFIT/EN)
2950 Hobson Way
Wright-Patterson AFB, OH 45433-7765

8. PERFORMING ORGANIZATION REPORT NUMBER

AFIT/GAE/ENY/11-M07

9. SPONSORING / MONITORING AGENCY NAME(S) AND ADDRESS(ES)

Air Force Office of Scientific Research, AFOSR
Dr. Douglas Smith, (douglas.smith@afosr.af.mil), (703) 696-6219
875 North Randolph St, Suite 325, Rm 3112, Arlington, Va.,22203
Air Force Research Lab, AFRL
Dr. Richard Snyder, (richard.snyder@wpafb.af.mil), (937) 785-8473
2210 8th St, B146 R220, WPAFB, OH

10. SPONSOR/MONITOR'S ACRONYM(S)

AFOSR, AFRL

11. SPONSOR/MONITOR'S REPORT NUMBER(S)

12. DISTRIBUTION / AVAILABILITY STATEMENT

APPROVED FOR PUBLIC RELEASE; DISTRIBUTION UNLIMITED.

13. SUPPLEMENTARY NOTES

This material is declared a work of the U.S. Government and is not subject to copyright protection in the United States.

14. ABSTRACT

In recent years, researchers have expressed a vested interest in the concepts surrounding flapping wing micro air vehicles (FWMAVs) that are capable of both range and complex maneuvering. Most research in this arena has found itself concentrated on topics such as flapping dynamics and the associated fluid-structure interactions inherent in the motion, however there still remains myriad questions concerning the structural qualities intrinsic to the wings themselves. Using nature as the template for design, FWMAV wings were constructed using carbon fiber and Kapton and tested under simplified flapping conditions by analyzing 'frozen' digital images of the deformed wing by methods of photogrammetry. This flapping motion was achieved via the design and construction of a flapper that emulates several of the kinematic features that can be seen in naturally occurring flyers. The response to this motion was then compared to the inspiring specimen's wings, the North American Hawkmoth (*Manduca Sexta*), under the same flapping conditions in order to identify some of the key features that nature has deemed necessary for successful flight.

15. SUBJECT TERMS

Bio-inspired Flight, Flapping, Micro Air Vehicles, MAV, FWMAV, Structures, Hawk Moth, *Manduca Sexta*

16. SECURITY CLASSIFICATION OF:			17. LIMITATION OF ABSTRACT	18. NUMBER OF PAGES	19a. NAME OF RESPONSIBLE PERSON
a. REPORT	b. ABSTRACT	c. THIS PAGE			Dr. Anthony Palazotto, Professor, AFIT (ENY)
U	U	U	UU	254	19b. TELEPHONE NUMBER *(include area code)* (937) 785-3636 x 4599; anthony.palazotto@afit.edu

Standard Form 298 (Rev. 8–98)
Prescribed by ANSI Std. Z39.18